UNIVERSIDADE DE LISBOA
FACULDADE DE CIÊNCIAS

Structure and tectonics of the crust and Moho discontinuity of the Gloria Fault and Terceira Rift (S. Miguel) along the Nubia-Eurasia plate boundary

" Documento Definitivo"

Doutoramento em Geologia
Especialidade de Geodinâmica Interna

Luís Filipe Rodrigues Batista

Tese orientada por:
Professor Doutor Pedro Terrinha
Professor Doutor Christian Hübscher

Documento especialmente elaborado para a obtenção do grau de doutor

2019

UNIVERSIDADE DE LISBOA

FACULDADE DE CIÊNCIAS

Structure and tectonics of the crust and Moho discontinuity of the Gloria Fault and Terceira Rift (S. Miguel) along the Nubia-Eurasia plate boundary

Doutoramento em Geologia

Especialidade de Geodinâmica Interna

Luís Filipe Rodrigues Batista

Tese orientada por:

Prof. Dr. Pedro Terrinha

Prof. Dr. Christian Hübscher

Júri:

Presidente:

● Doutora Maria da Conceição Pombo de Freitas, Professora Catedrática e Presidente do Departamento de Geologia da Faculdade de Ciências da Universidade de Lisboa.

Vogais:

● Doutor Luis Filipe Fuentefria de Menezes Pinheiro, Professor Associado

Departamento de Geociências da Universidade de Aveiro;

● Doutor Joaquim Manuel Freire Luis, Professor Auxiliar

Faculdade de Ciências e Tecnologia da Universidade do Algarve;

● Doutor Rui Manuel Amaral Branco de Oliveira Quartau, investigador Auxiliar

Instituto Hidrográfico;

● Doutor João Nuno Vilhena de Sousa Lourenço, Presidente da Direção CoLab + Atlântico, qualidade de individualidade de reconhecida competência na área em que se insere a tese;

● Doutor João Daniel Casal Duarte, Professor Auxiliar

Faculdade de Ciências da Universidade de Lisboa.

● Doutor Pedro António Gancedo Terrinha, Professor Auxiliar Convidado

Faculdade de Ciências da Universidade de Lisboa (Orientador)

Documento especialmente elaborado para a obtenção do grau de doutor

Financiado pela Fundação para a Ciência e Tecnologia, SFRH/BD/81351/2011

e pela German Research Foundation, DFG, grant Hu698/19-1

2019

ABSTRACT

The crustal structure of two ~150 km long segments across two main tectonic plate boundaries in the North Atlantic, the Gloria Fault and the Terceira Rift are presented.

The Gloria Fault stands as a seismogenic fracture zone that generates high magnitude earthquakes, such as the M8.4 event in 1941. Vp and Vs waves were recorded during an active seismic refraction experiment using 18 Ocean Bottom Stations. The velocity model allows discrimination of five layers (L1 to L5), L1 for sediments, L2 for upper crust, L3 for lower crust, L4 for a layer of unknown origin and L5 for mantle. Poisson coefficient from Vp/Vs ratio allowed estimation of layers' densities. We speculate on L4 origin and nature from velocities and densities. Two possible models, L4 corresponds to a mixture of gabbro and peridotite or to hydrated mantle (serpentinized mantle).

The Terceira Rift seismic refraction line comprehends data from the S. Miguel Island. Velocities of S waves were not recorded. The model is based in Vp only. A five layer model is proposed, L1 for volcano-sedimentary layer, L2 for upper crust, L3 for lower crust and L5 for the mantle. L4 between L3 and L5 has a lensoid shape and its velocities suggest either a cumulate gabbro underplated layer or hydrated mantle.

A south dipping extensional shear zone aligned with the Monaco Graben was identified from the brittle upper crust and across the lower crust, L4 and mantle. This shear zone coincides with a cluster of seismicity located to the south of S. Miguel Island. To the north of S. Miguel seismicity is barely inexistent and a 20 km long recent landslide with a toe thrust is clearly imaged, suggesting northward tilting of the island caused by the extensional shear zone, the south flank of the Terceira Rift.

Keywords: Atlantic Ocean; Plate Boundary; Gloria Fault; Terceira Rift; Crustal structure and Mantle serpentinization.

RESUMO

Os Oceanos e os seus domínios são das zonas da Terra menos compreendidas pelo conhecimento humano. Estes ocupam quase ¾ da sua superfície e são vistos como o grande armazém de recursos do planeta. É por isso que o seu conhecimento é de extrema importância para a sustentabilidade da Humanidade e fundamental para o seu progresso. Por outro lado, é no Oceano que se localizam grande parte dos mecanismos recicladores e formadores de crusta responsáveis pela ocorrência uma elevada quantidade de processos geológicos geradores de grandes catástrofes naturais nomeadamente sismos, *tsunamis* ou erupções volcânicas.

Poder contribuir para o enriquecimento do conhecimento nestes domínios e poder contribuir com novas ferramentas para ajudar na compreensão e mitigação destes fenómenos foi a motivação que me levou a desenvolver este trabalho agora aqui apresentado.

A plataforma continental tem sido alvo da maior parte dos estudos efectuados no mar. A sua proximidade, para além de proporcionar um acesso mais fácil, é também a zona do oceano que está mais próxima das populações e que mais as influencia. A investigação do mar profundo, talude e planícies abissais é por isso menor e, dado a sua distância à costa, implica normalmente a necessidade uma série de procedimentos mais complexos e dispendiosos muitas vezes fora do alcance dos investigadores. A oportunidade de integrar uma equipa de investigadores da Universidade de Hamburgo e de participar na campanha oceanográfica M79 a bordo do navio Alemão METEOR possibilitou o acesso aos dados trabalhados e apresentados nesta dissertação.

A fronteira de placas entre a Eurásia e África, desde o golfo de Cádiz até ao arquipélago dos Açores, é conhecida como a Zona de Fractura Açores-Gibraltar (ZFAG). No seu troço entre os Açores e a Crista Madeira-Tore apresenta um traçado morfológico linear bem marcado, com cerca de 800 km denominado por Falha da Gloria (FG). Esta falha possui um movimento intraplaca relativo de desligamento direito, muito lento, entre 2 e 3.4 mm/ano, e é caracterizada por apresentar uma baixa actividade sísmica. Contudo, um dos maiores sismos registado neste tipo de ambientes transcorrentes foi o sismo de 1941 com uma magnitude M=8.4. A ligação do extremo oeste da Falha da Glória com a Crista Médio-Atlântica é feita através do Rift da Terceira que limita o Planalto dos Açores (PA) a nordeste, formando uma

junção tripla que liga três placas tectónicas, a placa Euroasiática, a placa Africana e a placa Norte-americana.

Embora o Planalto dos Açores seja uma das regiões mais estudadas no Atlântico Norte a sua origem e estrutura crustal são ainda matéria de debate. O espessamento do planalto tem sido atribuído essencialmente à existência de uma anomalia térmica que tem favorecido a subida de um volume considerável de magma que por sua vez aproveita o facto de estar numa zona de tectónica activa para ascender à superfície.

Na campanha de geofísica marinha M79-leg2 foram usados 18 OBS na execução de dois perfis sísmicos de refracção e reflexão de grande ângulo, ambos com direcção N-S: um com cerca de 150 km perpendicular à Falha da Glória à longitude ~21ºW e outro com cerca de 160 km perpendicular ao Rift da Terceira atravessando a Ilha de São Miguel na sua zona central. Simultaneamente foram adquiridos sobre os perfis de refracção três perfis de reflexão sísmica multicanal. Um na área da Falha da Glória e dois na área de São Miguel. A interpretação dos dados de sísmica de reflexão permitiu constranger a cobertura sedimentar nas áreas de estudo e assim melhorar a construção dos modelos de velocidades das ondas P e S, produzidos a partir da interpretação dos dados obtidos pela sísmica de refracção.

Na Falha da Glória, a interpretação das velocidades das ondas P e das ondas S, permitiu a construção de um modelo com 5 camadas. As camadas 1 a 3 correspondem respectivamente às camadas típicas dos sedimentos, crusta superior e crusta inferior, a camada 5, com velocidades das ondas P superiores a 7.5 km/s foi identificada como correspondendo a manto litosférico superior. A camada 4, com 4 km de espessura e velocidade das ondas P entre 7.1 km/s no topo e 7.4 km/s na base situa-se entre a base da crusta inferior e topo do manto típicos. As velocidades da camada 4 mostram que estamos na presença de material diferente do material típico que constituem a crusta inferior (gabros) e manto litosférico superior (peridotitos). Através das razões entre as velocidades das ondas P e S foi possível calcular coeficiente de Poisson para as várias camadas possibilitando estimar as densidades dos materiais que as constituem.

A comparação com análogos naturais e com medições laboratoriais anteriormente publicadas de velocidades de propagação de ondas P e S e respectivas densidades, sugere que a camada 4 possa tratar-se de uma mistura de litologias entre gabros e peridotitos com cumulados e manto hidratado (serpentinitos). A falta de evidências morfológicas para a existência de extrusão de magmática ajudou a concluir que devemos estar na presença de um processo hidrotermal e

metassomático com a circulação de água através da permeabilidade secundária resultante da actividade tectónica. Em São Miguel só foram detectadas nas secções dos OBSs velocidades das ondas P. O modelo resultante mostrou, para além de diferentes zonas de espessamento das camadas correspondentes à crusta superior e inferior, que existe uma camada anómala entre a crusta e o manto superior litosférico. Essa camada com velocidades Vp compatíveis com cumulados de gabro, pode estar associada a um processo de *underplating* que, segundo este estudo, ajuda a justificar o espessamento do Planalto dos Açores e é compatível com o que acontece em muitos dos locais de formação de ilhas oceânicas de origem volcânica.

Foi ainda possível identificar que ao largo do bordo sul da ilha de S. Miguel existe uma zona de deformação distensiva, inclinando para sul (cisalhamento simples) que deforma desde o fundo do mar até à parte analisada do manto superior litosférico. Verifica-se a deformação em regime frágil ou discreto nas camadas de materiais vulcano-sedimentares assim com no topo da camada da crusta superior. A parte inferior desta, juntamente com a crusta inferior camada 4, encontram-se também deformadas, embora ductilmente. Não há resolução suficiente para determinar se o manto está deformado dúctil ou fragilmente. Esta deformação rotacional impôs o basculamento da ilha para norte ao qual se encontra associado um deslizamento submarino recente de cerca de 20 km de extensão com transporte para norte e cavalgamento na sua extremidade.

A análise conjunta da sísmica de refracção e reflexão e da batimetria permitiu a ligação entre a parte norte do graben do Mónaco e a crista vulcânica (VR no manuscrito) a sul de São Miguel, constituindo um lineamento tectónico extensional de rifting, que aqui é interpretado como o bordo sul do Rifte da Terceira.

Este trabalho põe em evidência que nas áreas de estudo a composição da crusta e a descontinuidade da Moho não seguem os denominados padrões normais para a sua composição e estrutura apresentando características específicas nos diferentes contextos tectónico em que se inserem.

Palavras-chave: Oceano Atlântico; Fronteira de Placas; Falha da Glória; Rift da Terceira; estrutura da crusta e manto superior.

ACKNOWLEDGMENTS

Undertaking this PhD was a truly living experience and it would not have been possible to do without the support and guidance that I received from many people. I will always remember them.

I want to start acknowledging my supervisor Pedro Terrinha for always being there when I need it. His encouragement to keep me focus all these years was essential to overpass many difficult moments during this work. Without his wisdom, friendship and his simple way to transmit and simplify, this work probably never had arrived to the end. I thank him for that and also for the knowledge in geology that I've learned with him.

I also owe a great acknowledge to my co-supervisor Christian Hübsher who was always present and available and always showed interest and helped me when I needed. I am indebted to him for the invitation that allowed me to participate in the cruise where the data that made this work possible was collected.

A special thanks to Luis Matias and Alexandra Afilhado who taught me the methodology and how to work with the software I used in this work. All the support that they gave me was crucial to the ending of this work.

I would like to give a very big thank you to my good friend João Noiva. He was always present from the beginning of my work and his help was truly important and indispensable.

Many thanks also to Henrique Duarte for all the talks we had and his special way to see the world. "That lunch" was very important to me.

To Pedro Brito, Marta Neres, Sónia Silva, Carlos Ribeiro, Nuno Lourenço, Cristina Roque, Vasco Valadares, João Duarte and Vitor Magalhães thank you for all the help and support received.

I thank Fátima Abrantes and all the colleagues from the *Paleo*-group.

I also thank the geophysical colleagues.

This work was not possible without the data from the TRAGICA project and M79/2 cruise so I sincerely thank Captain Thomas Wunderlich and his crew of RV Meteor for their support. Also I thank all the scientific team who helped in the data acquisition.

Financially I want to acknowledge the Fundação para a Ciência e Tecnologia for my PhD grant (SFRH/BD/81351/2011) and to the German Research Foundation (DFG, grant Hu698/19-1) for the CASCADE project.

My thanks also go to Landmark Graphics Corporation via the Landmark University Grant Program.

I am also very grateful to the Portuguese Task Group for the Extension of the Continental Shelf (EMEPC), Institute Dom Luiz (IDL), University of Hamburg (UH), National Laboratory of Energy and Geology (LNEG) and the Portuguese Institute for Sea and Atmosphere, I. P. (IPMA, IP) which were the host institutions. They kindly supported me and my work.

Finally I want to leave a truly thank you from the bottom of my heart to the most important people of my life, My Family.

Mam and Dad thank you very much for being there and always believed in me. You are always in my heart. Thank you too my sister Patricia.

I kindly thank my mother and father in law who really make me feel welcome in the family and for their encouragement.

Graça e João a special thanks for you for the great time we have been spending together and for the enthusiastic words of motivation and the support that helped me to cross the goal line.

Thanks to my nephews Sofia, Sara, Santiago, Maria Inês e Alice. I hope you can see me as an example.

Filipe and Miguel you are the reason of my life and everything I do is always with you in my heart. I hope you can be proud of me.

Finally, thanks as big as the world to my wife, Sofia. She is the great woman behind me and the truly pillar of this work. She always believed and encouraged me. Thank you for being my wife, my friend, my companion, my everything…, thank you for being you.

TABLE OF CONTENTS

Omira, R., Ramalho, I., Terrinha, P., Baptista, M.A., Batista, L. & Zitellini, N., 2016. *Deep-water seamounts, a potential source of tsunami generated by landslides? The Hirondelle Seamount, NE Atlantic*, Marine Geology, 379, 267-280.

Omira, R., Neres, M. & Batista, L., 2019. Chapter 8 - The Gloria Transform Fault—NE Atlantic: Seismogenic and Tsunamigenic Potential. in Transform Plate Boundaries and Fracture Zones, pp. 157-167, ed. Duarte, J. C. Elsevier.

Hensen, C., Duarte, J.C., Vannucchi, P., Mazzini, A., Lever, M.A., Terrinha, P., Géli, L., Henry, P., Villinger, H., Morgan, J., Schmidt, M., Gutscher, M.-A., Bartolome, R., Tomonaga, Y., Polonia, A., Gràcia, E., Tinivella, U., Lupi, M., Çağatay, M.N., Elvert, M., Sakellariou, D., Matias, L., Kipfer, R., Karageorgis, A.P., Ruffine, L., Liebetrau, V., Pierre, C., Schmidt, C., Batista, L., Gasperini, L., Burwicz, E., Neres, M. & Nuzzo, M., 2019. *Marine Transform Faults and Fracture Zones: A Joint Perspective Integrating Seismicity, Fluid Flow and Life*, Frontiers in Earth Science, 7.

FIGURE INDEX

TABLE INDEX

ACRONYM LIST

A.D. – Anno Domini
AF1 – Altiprado Fault 1
AF2 – Altiprado Fault 2
ARG – Água Retorta Graben
ATJ – Azores Triple Junction
AZGF – Azores-Gibraltar Fracture Zone
AzP – Azores Plateau
BAS – Basalt
BSL – Below Sea Level
CFVS – Congro Fissural Volcanic System
CGUL – Geophysics Centre of the University of Lisbon
CJF - Cú de Judas Fault
cm – centimetre
D – Distance
DEPAS – Deutscher Geräte-Pool für amphibische Seismologie from University of Hamburg
DUN – Dunite
DDDZ – Deep Ductile Deformation Zone
EAFZ – East Azores Fracture Zone
EMEPC – Task Group for the Extension of the Continental Shelf
EMODnet – European Marine Observation and Data Network
FF – Falca Fault
FGV – Fogo Volcano
FRV – Furnas Volcano
freqhi – High frequency
freqlo – Low frequency
FTF – Feteiras Fault
g – gram
GAB – Gabbro
GEBCO – General Bathymetric Chart of the Oceans
GF – Gloria Fault
GoC – Gulf of Cadiz
GPS – Global Positioning System
HAP – Horseshoe Abyssal Plain
ibndps – Butterworth frequency bandpass filter
ICS – International Seismological Centre
IAP– Iberia Abyssal Plain
IPMA – Portuguese Institute for the Atmosphere and Sea
izerop – Zero-phase filter
Ka – Thousands of years
Ky – Thousands of years ago
km – kilometer
KT – King's Trough
kn – Knot
LF – Lombinha Fault
LHF – Lomba dos Homens Fa
LVF – Lomba do Vasco Fault
m - meter
M – Magnitude
Ma – Millions of years
My – Millions of years ago
MAP – Madeira Abyssal Plain
MAR – Mid-Atlantic Ridge
MCS – Multichannel Seismic
MG – Mosteiros Graben
MORVEL – Mid-Ocean Ridge
VEL – Velocity
MPa – Megapascal
MTR – Madeira-Tore Rise
MTD – Mass Transport Deposit
ms – Milliseconds
NOC – Normal Oceanic Crust
NPTS – Number of Observations
NR – Number of Rays
NVA - North Volcanic Alignment
NVS - Nordeste Volcanic System
OBH – Ocean Bottom Hydrophones
OBS – Ocean Bottom Seismometers
OCB – Ocean-Continent Boundary
OFZ- Oceanographer Fracture Zone
PFVS - Picos Fissural Volcanic System

Pg – Sub-basement crustal refractions
PgP – Sub-basement crustal reflections
PmP – Moho wide-angle reflections
Pn – Sub-Moho refractions
PSP – Partial Serpentinized Peridotite
PV – Povoação Volcano
RGG – Ribeira Grande Graben
s – second
SAP – Seine Abyssal Plain
SBCM – Sub-lithospheric Continental Mantle
SEGY – Society of Exploration Geophysicists 'Y' format
SER – Serpentinite
Shmax – Maximum Horizontal Stress
SVA – South Volcanic Alignment
SCV – Sete Cidades Volcano
SVP – Sound Velocity Profile
sp – Shotpoint
T – Tore seamount
T-D/V – Reduction Time = Time-Distance/Velocity
TF – Tronqueira Fault
TAP – Tagus Abyssal Plain
TR – Terceira Rift
TRMS – Time Root Mean Square
TWT – Two Way Travel Time
V – Velocity
VGF – Vale Grande Fault
Vp – P-wave Velocity
VR – Volcanic Ridge
Vs – S-wave Velocity
WRGF – West Ribeira Grande Fault
Yr – Year

1. CHAPTER 1 – INTRODUCTION

For a variety of logistic, strategic and financial reasons the deep structure of the North Atlantic deep sea still largely unknown. Surveying the deep sea solid earth, in the sense of deep waters far off the mainland (transfer time from the Azores to Europe mainland is more than 3 days), requires oceanic vessels. These are not only expensive but also usually have a busy schedule because they can also serve non-scientific purposes like working for private companies or other societal needs.

Most of the on North Atlantic Ocean continental margins and their adjacent deep sea research effort have been concentrated on their shallow and deep structure. This is mainly because their rift basins are potential sites for hydrocarbon generation and storage and also because they can be potential sources for natural hazards, such as large landslides, earthquakes and tsunamis.

However, the Azores plateau and the Gloria Fault are two lithospheric scale geological provinces that deserve priority, both from societal and pure scientific reasons.

The Azores plateau as outlined by a bathymetric contour of 2000 m below sea level (bsl) is not far from 150,000 km^2 (approximately twice the area of Portugal mainland). The total area of the Azores nine islands is 2,346 km^2 with approximately 247,000 inhabitants. All the islands are of volcanic origin, several of them with historical volcanism. Subaerial and submarine volcanic eruptions occurred in the last 70 years for instance, Capelinhos eruption in the Faial Island,,are well documented. Seismicity is very frequent although not of very high magnitude. Only 7 events with magnitudes between 6 and 7.1 account for 84.1% of the total seismic moment produced by thousands of earthquakes with M>3 (Caldeira *et al.*, 2017). Although dozens of earthquakes have been attributed a focal mechanism from which dynamics of fracturing can be related to oceanic plate kinematics, the actual depths are still poorly constrained and the nature of the crustal and uppermost lithospheric structure is also poorly constrained.

The Gloria Fault (GF) is a well-defined seismogenic fracture zone that lies on the eastern prolongation of the East Azores Fracture Zone extending for approximately 1000 km till the Madeira-Tore Rise. The GF is a fairly rectilinear seafloor structure characterized by dextral strike-slip kinematics. It hosts various elongated graben-like features, probably strike-slip

basins formed at releasing bends with more than 1 km of vertical basement drop. The GF has one main restraining bend feature that was the epicentre of the M8.4 1941 earthquake (Buforn *et al.*, 1988). In addition to this it has generated three more M>7 instrumental earthquakes. The western tip of the GF lies at ~65 km and ~100 km to Santa Maria and São Miguel islands of the Azores archipelago and ~550 km to the Portuguese mainland. Due to very high magnitude of the GF earthquakes it must be considered a natural hazard source. From the point of view of understanding the tectonics and seismotectonics the GF is mostly unknown because the nature of the oceanic crust in this part of the Atlantic is also unknown.

The objective of this dissertation is twofold. Firstly, to construct velocity models of the oceanic crust and uppermost lithospheric mantle from two key geological provinces of the North Atlantic Ocean that can provide valuable information on the geodynamics of the Eurasia-Africa plate boundary and Azores plateau; secondly to discuss adequate geologic models for these crustal models. This exercise is based on two original refraction profiles acquired during the TRAGICA cruise M79-leg 2, 2009, (Hübscher, 2013) and gravity data (Bonvalot, 2012) that are described in two following chapters. One of these chapters is on the Gloria Fault upper lithospheric structure (Batista *et al.*, 2017) and the second is on the upper lithospheric structure across the São Miguel Island that lies within the most active tectonic ride of the Azores plateau.

2. CHAPTER 2 – GEOLOGICAL SETTING

2.1. The opening of the Atlantic Ocean and the Gloria Fault

The Central Atlantic started spreading between the Vema (~10ºN) and the Azores-Gibraltar (~37ºN for its central sector) Fracture Zones in Early Jurassic times, possibly in the Pliensbachian-Toarcian transition, ~182 Ma (Schettino & Turco, 2009). This oceanic drifting was a direct consequence of the continental break up of Pangea that followed the post-Paleozoic cratonization phases that resulted from the final collision of Gondwana and Laurasia.

On the Africa side of the Atlantic Ocean this is an approximately 3,000 km long segment of a stable passive margin. On the North America side of the Atlantic Ocean the southern part of the equivalent African passive margin has been interrupted by the formation of a subduction zone and volcanic island arc (the Lesser Antilles Arc) that has been migrating from the East Pacific into the West Atlantic Ocean since approximately 100 Ma (Bouysse *et al.*, 1990).

The onset of the Pangea break up (Figure 2.1) is arguably associated with the formation of the Cape Verde hotspot and its northeastwards migration (Wilson, 1992). The radial dyke complex associated with this intra-continental hotspot has dykes larger than 1000km long and can still be observed in both parts of the Atlantic, namely in Mauritania, Morocco and United States of America.

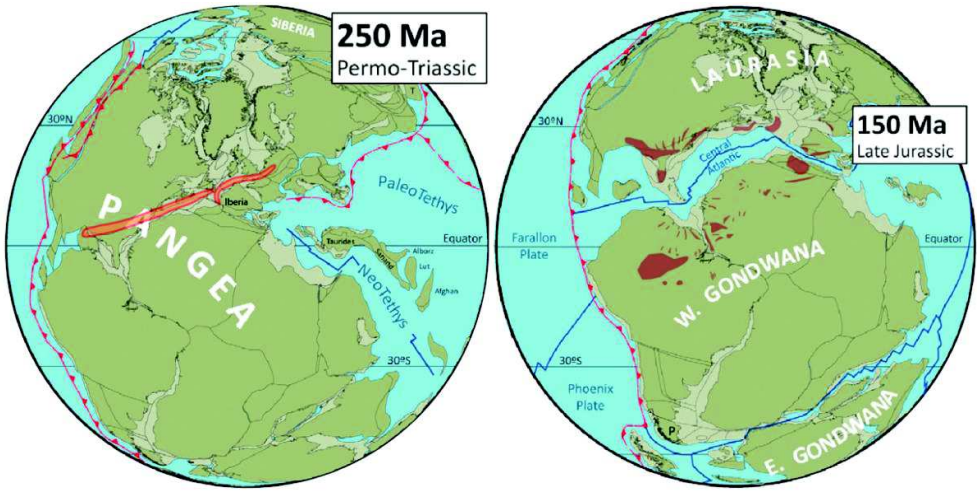

Figure 2.1: Plate reconstructions for Late Permian (Pangea tightest assemblage) and for Late Jurassic (modified from Torsvik *et al.* (2012) in Terrinha *et al.* (2019)).

The north limit of the Africa passive margin is the present day Azores-Gibraltar Fracture Zone (AGFZ) that has possibly been a complex transform-type plate boundary in the latest times of the formation of Pangea (Terrinha *et al.*, 2019 and references therein). The AGFZ is a plate boundary between the Africa and Eurasia lithospheric plates, to the south and to the north, respectively. Examples of seminal works on this plate boundary, its seismicity and their tectonic implications are McKenzie (1972), Purdy (1975), Grimison & Chen (1986), Buforn *et al.* (1988), among others.

The present day AGFZ extends for ~1,700 km from the eastern tip of the Azores Plateau to the Gibraltar Arc. The AGFZ is intersected by the magmatically over-thickened ridge, the Madeira-Tore Rise (MTR) (Peirce & Barton, 1991).

The MTR is punctuated by several volcanic seamounts most of which are of Cretaceous age (100-80Ma) to the north of the GF (i.e. Eurasia plate) and of Paleogene and mostly Neogene age to the south (i.e. in the Africa plate) (Geldmacher *et al.*, 2005, Geldmacher *et al.*, 2006, Merle *et al.*, 2018, Merle *et al.*, 2006). The Cretaceous magmatism is of alkaline affinity and it is speculated that it is associated with alkaline magmatism that occurs in the Estremadura Spur and in the Sintra-Lisbon region (Terrinha *et al.*, 2019, Neres *et al.*, 2014, Terrinha *et al.*, 2018).

In the Tagus Abyssal plain, Horseshoe Abyssal plain, and off southwest Iberia (also known as Gulf of Cadiz), i.e. between the MTR and Gibraltar Arc, the plate boundary is complex and cryptic. Some authors define it as a diffuse plate boundary between the Goringe Bank and the Coral Patch (Sartori *et al.*, 1994) where tectonic strain is accommodated by dextral transpressive strike-slip faults that define a shear zone with a minimum width of 80km (SWIM Faults in Zitellini *et al.* (2009)). The Accretionary Wedge Gulf of Cadiz (Figure 2.2) formed in the footwall of the Gibraltar orogenic Arc that moved westwards into the Atlantic Ocean as the west Neo-Tethys oceanic slab subducted. In these areas the seafloor basement has been described as consisting of serpentinized mantle overlain by deep ocean sediments.

Between the Azores plateau and the MTR the plate boundary is materialized by the Gloria Fault (GF) (Omira *et al.*, 2019, Batista *et al.*, 2017, Argus *et al.*, 1989). Until Batista *et al.* (2017) in this dissertation the only work on the nature of the oceanic lithosphere between the MTR and the MAR was carried out by Potts *et al.* (1986). The refraction study across the Tydeman fracture zone (Figure 2.2), at Chron 25 (~55 Ma) by these authors revealed low crustal seismic velocities within the fracture zone together with unusually low velocities of 7.2 – 7.5 km in the lithospheric mantle attributed to serpentinization of mantle; however, their

experiment could not reach normal mantle velocities above depths of 12 km. This survey was the first, wide-angle seismic surveys of fracture zone crust older than 25 Ma. It was carried out using 4 OBS, free-floating sonobuoys and was shot with explosives. Three OBS where disposed perpendicular to the fracture zone and two OBS where disposed parallel to fracture zone and two shot lines were executed with 25 shots each.

2.2. The Azores Plateau

The geology of the Azores plateau is very challenging as it is highly variable from whatever points of view as well as considerably unknown. This can apply to seafloor or subaerial morphology, along or perpendicular to volcanic ridges, to deep interior processes, surface processes or vertical processes such as mantle plume horizontal migration and its influence on triple junction displacement. Other vertical processes like gas flux depends on various parameters such as magmatic gas pressure, surface brittle deformation and seasonal atmospheric pressure variations. Surface movements are driven mainly by strong topographic gradients, seismicity and inflation-deflation related to magmatism and differential tectonic stress. The Azores is thus a fertile natural laboratory to virtually any earth science discipline.

In what respects lithosphere structure, which is the primary interest of this dissertation, there is little information about. Two end-members can be considered in what respects the plateau height: it can be dynamically sustained by a hot spot or mantle plume process or can be justified by overthickened lithosphere in isostasy. The existence of a mantle plume process is not denied by recent works on plate kinematics such as Silveira *et al.* (2006), Silveira *et al.* (2010), Miranda *et al.* (2015). However, Luis *et al.* (1998) and Luis & Neves (2006), sustain that the topographic anomaly can be justified solely by isostasy of overthickened crust and that the Azores spreading ridges are too immature to create significant topographic effects of thermal origin.

On the other hand, a recent numerical modelling by Arnould *et al.* (2019) indicates the existence of an asymmetric mantle plume (2,000 km south and 600 km north with respect to central Azores), the origin of which can be as deep as the lower mantle.

The Terceira Rift is the most recent spreading extensional magmatic belt located at the northeastern part of the Azores plateau. Onset of tectonic and volcanism can be as old as 3-4.6 Ma (Miranda *et al.*, 2015). Princess Alice bank and basin is the second and older spreading (extensional deformation zone) in the Azores plateau (Figure 2.2).

The East Azores fracture Zone has been inactive since the formation of the stable Azores triple junction, i.e. from magnetic anomalies C11-12 (c. 30 Ma) and C6c (c. 24 Ma) (Luis & Miranda, 2008). This is the time when continental Iberia became attached to Eurasia and, on the other hand, the Azores plateau became progressively welded to Africa and extensional deformation migrated northwards with development of extensional rifts and volcanic ridges.

Figure 2.2 (next page): Overview of the main morphologic features in the area of interest of the North Atlantic: AzP- Azores Plateau; SM- S. Miguel Island; SMa- Sta. Maria Island; T- Terceira Island; G- Graciosa Island; SJ- S. Jorge Island; Pi- Pico Island; Fa- Faial Island; Co- Corvo Island; Fl- Flores Island; A- Açor Seamount; PA- Princess Alice Seamount; MAR- Middle Atlantic Ridge; PAR- Princess Alice Ridge; NAFZ- North Azores Fracture Zone; FFZ- Faial Fracture Zone; PAFZ- Princess Alice Fracture Zone; PFZ- Pico Fracture Zone; WAFZ- West Azores Fracture Zone; OFZ- Oceanographer Fracture Zone; TFZ- Tydeman Fracture Zone;KT- Kings Through; MTR- Madeira-Tore Rise; GB- Gorringe Bank; CPR- Coral Patch Ridge; AWGC- Accretionary Wedge Gulf of Cadiz; IAP- Iberia Abyssal Plain; TAP- Tagus Abyssal Plain; HAP- Horseshoe Abyssal Plain; SAP- Seine Abyssal Plain; MAP- Madeira Abyssal Plain; Seismicity from the I.S.C. On-Line Bulletin (1915 – 2014; International Seismological Centre, 2011) and from IPMA (Portuguese Institute for the Atmosphere and Sea) . Red dashes represent the Gloria Fault. The white arc represents the current relative motion between Nubia and Eurasia, according to the MORVEL kinematic model (DeMets *et al.*, 2010). Isochrones from Müller *et al.* (2008). Bathymetry from EMODnet project (https://www.emodnet-bathymetry.eu) Altimetry from Digital Elevation Database (http://srtm.csi.cgiar.org.).

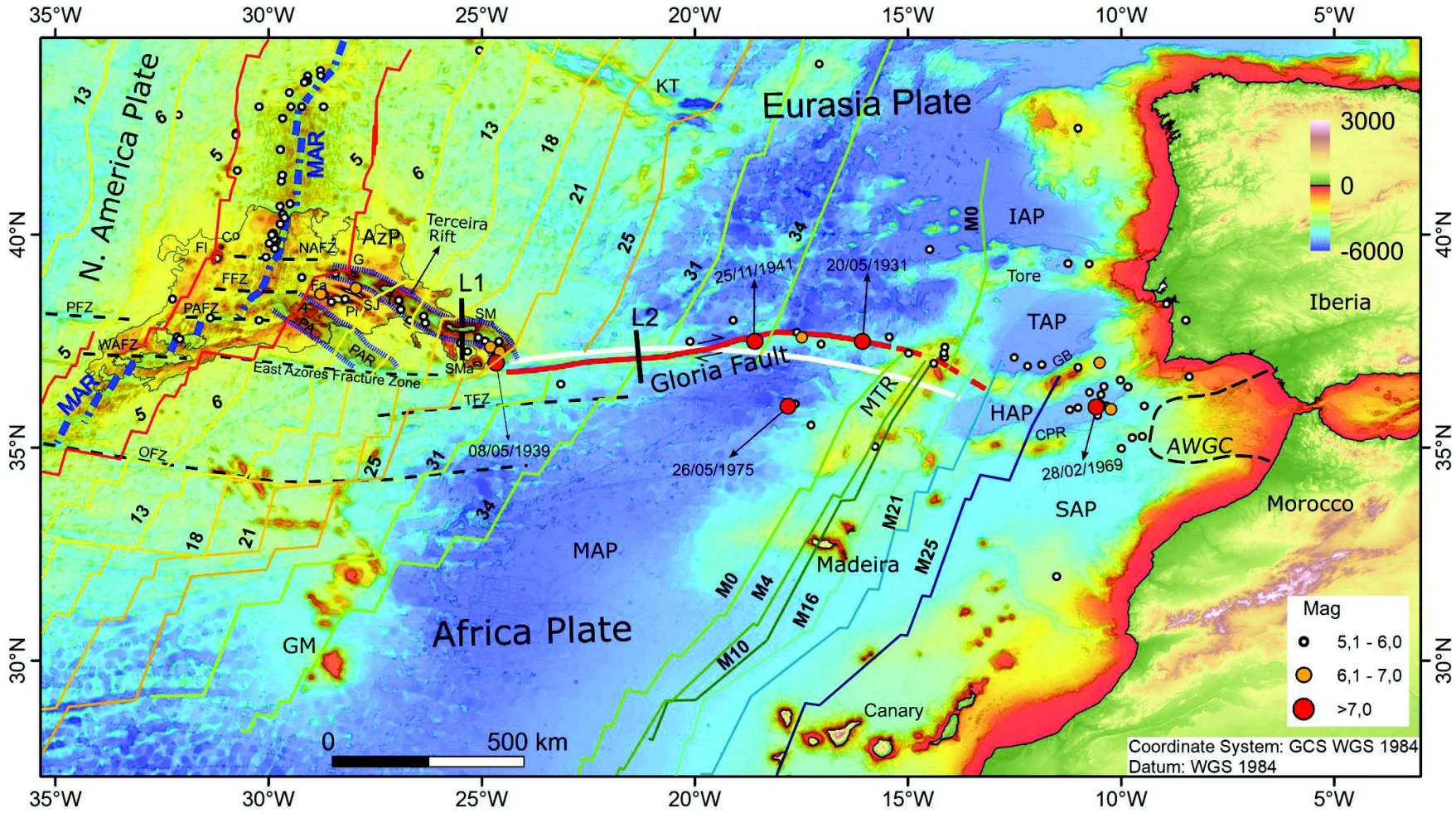
35°W
30°W
25°W
20°W
15°W
10°W
5°W
40°N
35°N
30°N
N. America Plate
Eurasia Plate
Africa Plate
MAR
AZP
Terceira Rift
L1
L2
Gloria Fault
East Azores Fracture Zone
KT
IAP
TAP
HAP
SAP
MAP
MTR
AWGC
CPR
GB
Tore
Iberia
Morocco
Madeira
Canary
GM
FZ
PFZ
PAFZ
WAFZ
NAFZ
FFZ
OFZ
TFZ
PAR
SM
SMa
SJ
Pi
Fa
Co
Fl
G
A
P1
P2
M0
M4
M10
M16
M21
M25
25/11/1941
20/05/1931
08/05/1939
26/05/1975
28/02/1969
3000
0
-6000
Mag
5,1 - 6,0
6,1 - 7,0
>7,0
0
500 km
Coordinate System: GCS WGS 1984
Datum: WGS 1984

3. CHAPTER 3 – DATA & METHODS

To investigate the oceanic crust and upper lithospheric mantle structure it is necessary to use seismic refraction, which is the best indirect way to retrieve information from levels at such depths. The seismic reflection acquisition can get information all the way through the Moho depending on the energy used and the geometry of acquisition but the costs for that are enormous. The Wide Angle Refraction acquisition is normally the geophysical method to reach those targets that can be completed with a more accessible MCS acquisition. For this work we used the data acquired during the METEOR cruise M79-Leg2 August 26 to September 21, 2009 (Hübscher, 2013). During the cruise a refraction line was acquired in the region off São Miguel Island, across the Terceira Rift, running perpendicular to the island and close to the most active Fogo volcano and a second seismic refraction line was acquired across a section of the Gloria Fault, further east. In addition to this, reflection seismic profiles were acquired on the top of the refraction lines and were also used to complement the understanding of the geology of the shallower crust and sedimentary packages (Figure 3.1).

3.1. Multichannel Seismic Reflection

Three Multichannel Seismic (MCS) profiles were used in this work. Seismic line MCS w51 (Figure 3.1) was shot perpendicular to the GF and MCS M79_23 and M79_09 was shot on the north and south of São Miguel Island respectively. Both lines were shot on the top of the refraction lines (Figure 3.1). The seismic signals were generated by an array of two GI-Guns with a generator volume of 45 in^3 and an injector volume of 105 in^3 each. For data recording a 600 m long asymmetric digital streamer was used, containing 144 channels with an average increment of 4.2 m. Shots were released every 25 m at a speed of 5 kn. Four Concord Navigator birds were used to keep the streamer cable at the desired depth of 3 m (Hübscher, 2013). Seismic interpretation was performed using the Landmark software.

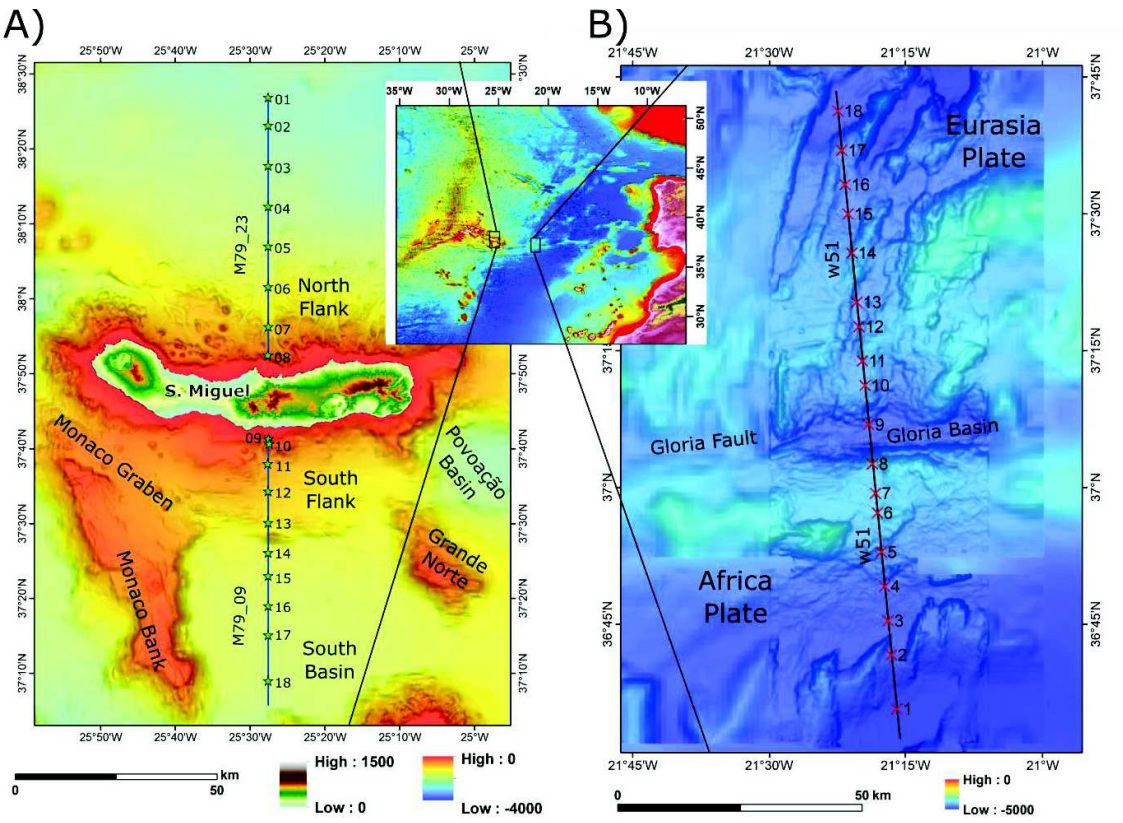

Figure 3.1: Location of the two wide angle refraction profiles and the coincident MCS profiles. Azores bathymetry from M79 cruise and EMODnet project; Gloria Fault bathymetry from EMEPC.

3.2. Ocean Bottom Seismic Refraction Stations

To record the seismic energy 18 Ocean Bottom Seismometers (OBS) were deployed in the studied area (Figure 3.1, Table 3-1 and Table 3-2). The 18 OBS were divided in 10 vertical component ocean bottom seismometers (OBS), 5 ocean bottom hydrophones (OBH) and 3 three component ocean bottom seismometers DEPAS (Deutscher Geräte-Pool für amphibische Seismologie from University of Hamburg). In DEPAS OBS channel 1 recorded the z-Geophone and channels 2-4 recorded the hydrophone with different amplifications. The 10 OBS recorded the vertical component with different amplifications. The 5 OBH recorded only the hydrophone. Two 32 litres BOLT guns generated seismic signals shooting every 60 s with 120 bar air pressure and 4 kn speed over ground, giving a short distance of 120 m. The distance between OBS was ~8 km generating a total profile length of 150 km for the Gloria and 160 km for the São Miguel.

Table 3-1: São Miguel OBS location.

Ocean-bottom recorder	Deployment		Recovery		Water depth [m]	Type
	Longitude	Latitude	Longitude	Latitude		
1	25°27.60'W	38°26.88'N	25°27.60'W	38°26.88'N	2893	OBS
2	25°27.59'W	38°23.15'N	25°27.59'W	38°23.16'N	2844	OBH
3	25°25.58'W	38°17.77'N	25°27.58'W	38°17.78'N	2709	OBS
4	25°27.59'W	38°12.33'N	25°27.40'W	38°12.27'N	2463	DEPAS
5	25°27.59'W	38°07.02'N	25°27.21'W	38°06.89'N	2280	OBS
6	25°27.58'W	38°1.62'N	25°27.45'W	38°01.48'N	1899	OBS
7	25°27.57'W	37°56.29'N	25°27.66'W	37°56.22'N	1332	OBH
8	25°27.62'W	37°52.48'N	25°27.63'W	37°52.48'N	555	OBS
9	25°27.54'W	37°41.29'N	25°27.52'W	37°41.29'N	204	OBS
10	25°27.44'W	37°40.65'N	25°27.44'W	37°40.65'N	374	OBH
11	25°27.65'W	37°37.99'N	25°27.84'W	37°38.04'N	895	DEPAS
12	25°27.58'W	37°34.31'N	25°27.95'W	37°30.09'N	1076	OBS
13	25°27.59'W	37°30.09'N	25°27.61'W	37°30.10'N	1470	OBH
14	25°27.58'W	37°26.08'N	25°27.58'W	37°26.08'N	1755	OBS
15	25°27.59'W	37°23.02'N	25°27.59'W	37°23.01'N	1929	DEPAS
16	25°27.59'W	37°18.99'N	25°27.43'W	37°19.09'N	2037	OBS
17	25°27.58'W	37°15.11'N	25°27.45'W	37°14.83'N	2192	OBH
18	25°27.59'W	37°08.99'N	25°27.59'W	37°08.99'N	2200	OBS

Table 3-2: Gloria OBS location.

Ocean-bottom recorder	Deployment		Recovery		Water depth [m]	Type
	Longitude	Latitude	Longitude	Latitude		
1	21°15.881'W	36°35.689'N	21°16.46'W	36°35.424'N	4931	OBS
2	21°16.461'W	36°41.586'N	21°17.36'W	36°41.058'N	4486	OBS
3	21°16.819'W	36°45.351'N	21°17.41'W	36°44.964'N	4566	OBH
4	21°17.199'W	36°49.130'N	21°17.79'W	36°48.749'N	4455	DEPAS
5	21°17.563'W	36°52.885'N	21°17.59'W	36°52.884'N	4151	OBS
6	21°18.017'W	36°57.183'N	21°18.40'W	36°56.704'N	3766	OBS
7	21°18.232'W	36°59.314'N	21°18.67'W	36°58.850'N	3835	OBS
8	21°18.529'W	37°02.541'N	21°18.79'W	37°02.686'N	3824	OBH
9	21°18.960'W	37°06.847'N	21°19.14'W	37°06.508'N	4465	OBS
10	21°19.366'W	37°11.154'N	21°19.32'W	37°11.011'N	3936	DEPAS
11	21°19.607'W	37°13.831'N	21°19.40'W	37°13.634'N	3935	OBS
12	21°20.020'W	37°17.592'N	21°19.83'W	37°17.255'N	4100	OBH
13	21°20.275'W	37°20.285'N	21°19.93'W	37°20.065'N	4097	OBS
14	21°20.777'W	37°25.638'N	21°20.81'W	37°25.662'N	3879	OBH
15	21°21.224'W	37°29.954'N	21°20.93'W	37°29.810'N	4235	DEPAS
16	21°21.574'W	37°33.207'N	21°21.08'W	37°33.022'N	4250	OBS
17	21°21.905'W	37°36.875'N	21°21.38'W	37°36.726'N	4208	OBH
18	21°22.336'W	37°41.247'N	21°16.46'W	36°35.424'N	4931	OBS

3.2.1. Raw data

The OBS raw data for the Gloria area was in the s2x format. To be used in the interpretation software it was necessary to convert first to SEGY format and then to z-format (Figure 3.2). The z-format is an internal format to usage in the Zelt software and consists of two files: *.data and *.hdr. The *.dat file contains the wavelet information and *.hdr contains the pick information of the trace. Both files are created with the sgy2z application from the Zelt software package. To convert in the SEGY format it was used the application s2x-seg from SEGY write software version 2.37 (13/09/2007) from SEND GmbH. The data from São Miguel was already received in the SEGY format so it was just applied the procedure to convert SEGY into the z-format. To perform those conversions some additional data was necessary: the navigation shooting file and the OBS deployment coordinates. An offset file that contains the distances from OBS location to the shot points was also required so for each OBS a file with that information was create using the nav2offset application developed by CGUL (Geophysics Centre of the University of Lisbon).

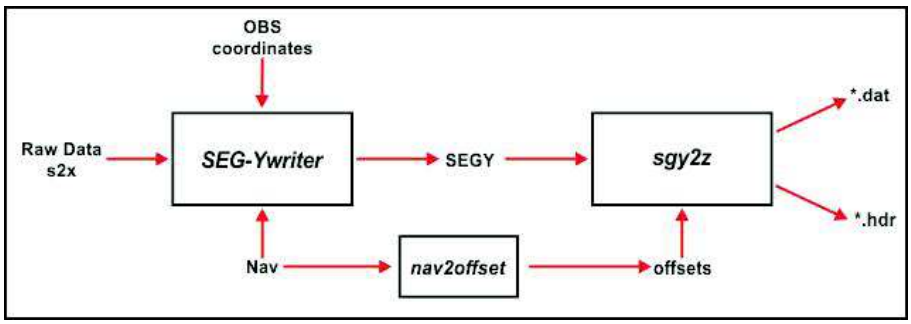

Figure 3.2: Flow diagram for format conversion from s2x to Zelt-format.

With the raw data converted in the z-format it is possible to run the *zplot* program and visualize the OBS data for quality control. A parameter file is necessary for run the *zplot*. Some of the parameters can be exchanged interactively in the plot screen for better visualization. As major parameters visualization we applied a 5-20 Hz Butterworth frequency bandpass filter (ibndps=1; freqlo=5; freqhi=20), a velocity reduction of 6 km/s (vred=6), a 0.25 clipping (clip=0.25) with the positive peaks shaded (ishade=2) and a trace normalized display (iscale=0) (Figure 3.3). All the plotting parameters are described in the *zplot* and *xzplot* documentation (see the web page http://terra.rice.edu/department/faculty/zelt/rayinvr.html).

iscale:	0	irec:	0	itxdps:	1	tlinc:	0.500	spick:	0.04	nskip:	1	ndecim	1
amp:	1.000	itx:	0	izerop:	0	clip:	0.25	ixaxis:	1	xmm:	300.0	tmm:	175.0
rcor:	0.50	imute:	0	freqlo:	5.0	vred:	6.00	itype:	0	xmin:	-50.000	tmin:	2.000
sf:	2.53982	iseg:	0	freqhi:	20.0	ishade:	2	pick:	1	xmax:	30.000	tmax:	7.000

OBS04-1

Figure 3.3: Interactive plotting parameters for channel evaluation. Same of the principal parameters are marked by a red circle.

A first evaluation on the raw data of São Miguel revealed several problems: i) corrupted information on the trace headers of OBS08; ii) extra shots resulting from an acquisition problem and shooting while going around the island from south to north (Figure 3.4); iii) some missing shots in OBS04; iv) repeated shots in OBS13.

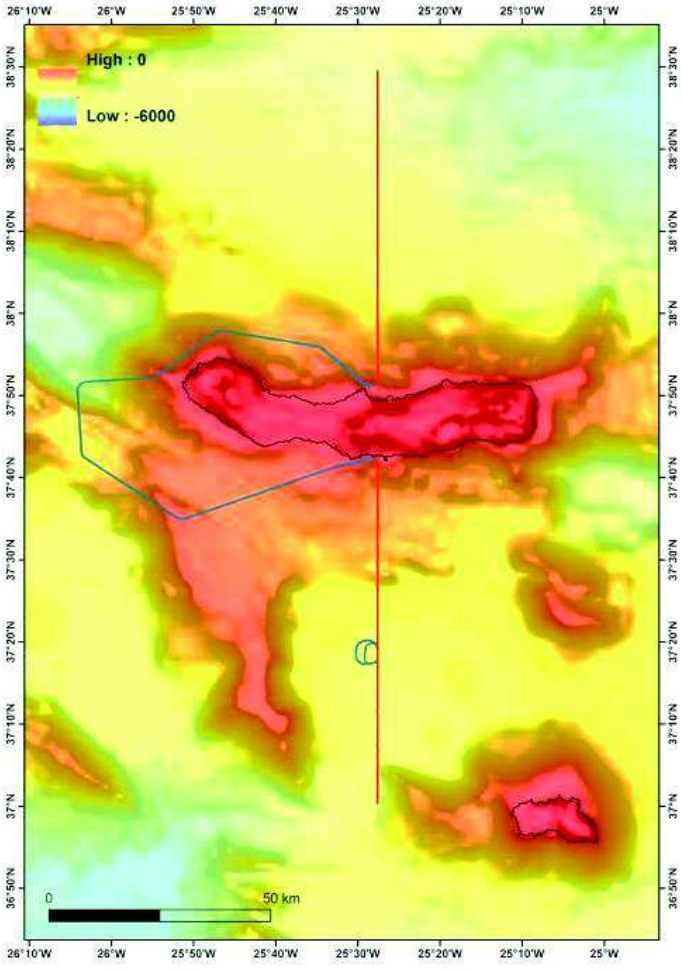

Figure 3.4: Navigation track off S. Miguel. The blue track represents the shots necessary to be removed and the red track the shots to be preserved.

The problem with OBS08 results from the conversion of the original acquisition format to the SEGY format. At this stage it is not possible to fix this problem because we do not have the original raw data and so OBS08 will be out of the model building process. For the other problems it was necessary to evaluate which shots were necessary to remove. As we can see in Figure 3.4 we had to eliminate the shots from the loop on the south section of acquisition and the turning around the island. With the relation shot-trace it was possible to cut and concatenate the correct sequences (Table 3-3).

Table 3-3: OBS cutting parameters.

OBS	Name	OBS raw file	shot	trace	OBS work file	Nº of traces
1	astra	N01-astra1_cat.su.sgy	1-358 1082-1550 2200-2941	1-358 595-1063 1713-2454	obs01_cut_fim	1569
2	pest	N02-Pest1_cat.su.sgy	1-358 1082-1550 2200-2941	1-358 595-1063 1713-2454	obs02_cut_fim	1569
3	becks	N03-Becks1_cat.su.sgy	1-358 1082-1550 2200-2941	1001-1358 1595-2063 259-1000	obs03_cut_fim	1569
4	freewilly	N04-Free-Willy1_cat.su.sgy	1-358 1082-1324 2269-2941	674-1031 1268-1510 1-673	obs04_cut_fim	1274
5	carlsberg	N05-Carlsberg1_cat.su.sgy	1-358 1082-1550 2200-2941	1-358 595-1063 1713-2454	obs05_cut_fim	1569
6	duff	N06-Duff1_cat.su.sgy	1-358 1082-1550 2200-2941	1-358 595-1063 1713-2454	obs06_cut_fim	1569
7	hunger	N07-Hunger1_cat.su.sgy	1-358 1082-1550 2200-2941	1-358 595-1063 1713-2454	obs07_cut_fim	1569
9	ganter	S09-Ganter1_cat.su.sgy	1-358 1082-1550 2200-2941	1-358 595-1063 1713-2454	obs09_cut_fim	1569
10	krieg	S10-Krieg1_cat.su.sgy	1-358 1082-1550 2200-2941	1-358 595-1063 1713-2454	obs10_cut_fim	1569
11	nessie	S11-Nessie1_cat.su.sgy	1-360 1084-1550 2200-2941	1-360 363-829 1479-2220	obs11_cut_fim	1569
12	jever	S12-Jever1_cat.su.sgy	1-360 1084-1550 2200-2941	1-360 363-829 1479-2220	obs12_cut_fim	1569
13	tod	S13-Tod1_cat.su.sgy	1082-1550 2200-2941	1-469 1119-1860	obs13_cut_fim	1211
14	karlsquell	S14-Karlsquell1_cat.su.sgy	1-360 1084-1550 2200-2941	1-360 363-829 1479-2220	obs14_cut_fim	1569
15	obsi	S15-Obsi1_cat.su.sgy	1-361 1085-1550 2200-2941	1-361 363-828 1478-2219	obs15_cut_fim	1569
16	polar	S16-Polar1_cat.su.sgy	1-360 1084-1550 2200-2941	1-360 363-829 1479-2220	obs16_cut_fim	1569
17	binky	S17-Binky1_cat.su.sgy	1-361 1085-1550 2200-2941	1-361 363-828 1478-2219	obs17_cut_fim	1569
18	rothaus	S18-Rothaus1_cat.su.sgy	1-361 1085-1550 2200-2941	1-361 363-828 1478-2219	obs18_cut_fim	1569

Except for OBS04 and OBS13 all the remaining OBS contain 1569 traces. The correspondent navigation files for each OBS were also needed to be corrected for the number of traces. Figure 3.5 shows the differences before and after cutting the extra shots.

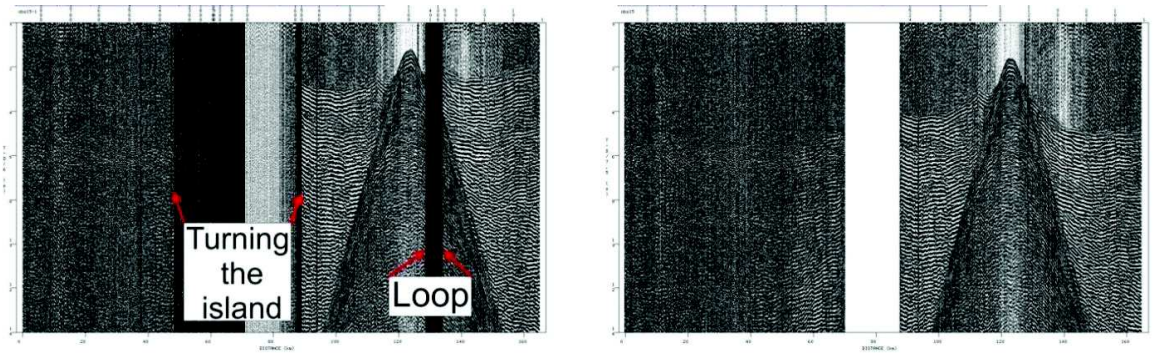

Figure 3.5: A plot of the OBSN15 before (left) and after (right) the trace cleaning, i.e. removal of spurious traces.

3.2.2. Relocation

After deployment and according to the depths of the working area (around 4000 m in the Gloria area and nearly 3000 m for some OBS in the São Miguel area) the OBS can take about 1:30h to 2h to reach the ocean floor. Because of this diving time and the existence of water currents the OBSs suffer some drift from the deployment position until their position on the bottom. It was necessary to correct this drift and estimate the real bottom position. Without this correction we can introduce some critical errors in the final model. To perform this correction the following proceedings were applied to the raw data:

-do the first-break picking and use the first arrivals information as time distance reference.

-calculate the new location.

-perform a quality control test to ensure that the final results are within acceptable values.

To perform the first break picking we had to adjust the plotting parameters and certify that we get the best signal information. As major visualization parameters we applied a velocity reduction of 1.75 km/s (vred=1.75), a 0.10 clipping (clip=0.10) with the negative trace shaded (ishade= -1), a trace normalized display (iscale=0) with a reduction on the amplitude to 0.099 (amp=0.099). To ensure we get all the significant frequencies of the signal we applied a 1-21

Hz Butterworth frequency bandpass filter (ibndps=1; freqlo=1; freqhi=21) as a zero-phase filter (izerop=1) (

Figure 3.6). After performing the picking we removed the bandpass filter to see if the picks were in place and there were no errors (Figure 3.7).

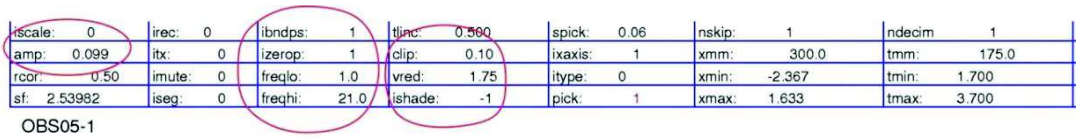

Figure 3.6: Plotting parameters to execute the first break picking. Same of the principal parameters are marked by a red circle.

All the OBS channels were converted and plotted and a visual evaluation was made to choose the best channel for the picking process. In all the OBS the first channel was the one that offered the best quality signal for the picking (Figure 3.8 and Figure 3.9).

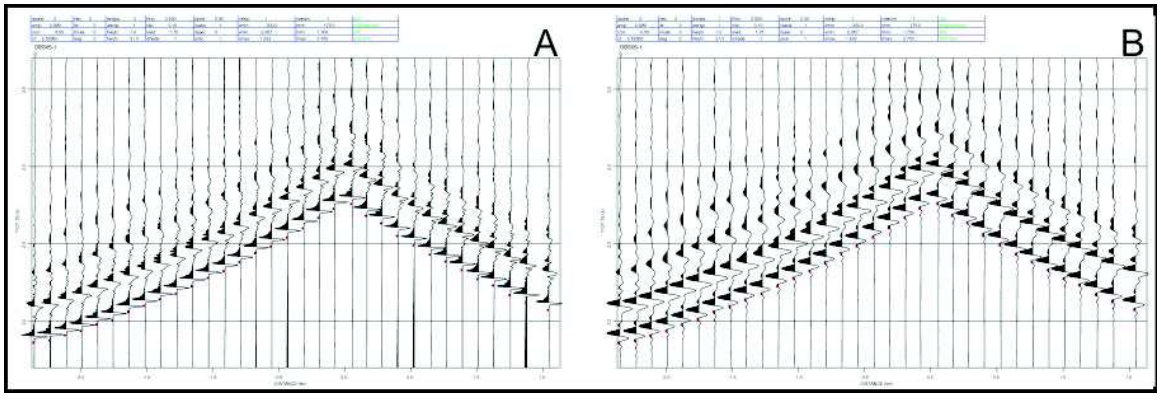

Figure 3.7: Zoom from the seismic section where is possible to see a few traces with de direct wave to do an evaluation of the picks position: A - display without Butterworth frequency bandpass filter; B - display with Butterworth frequency bandpass filter (1-21 Hz).

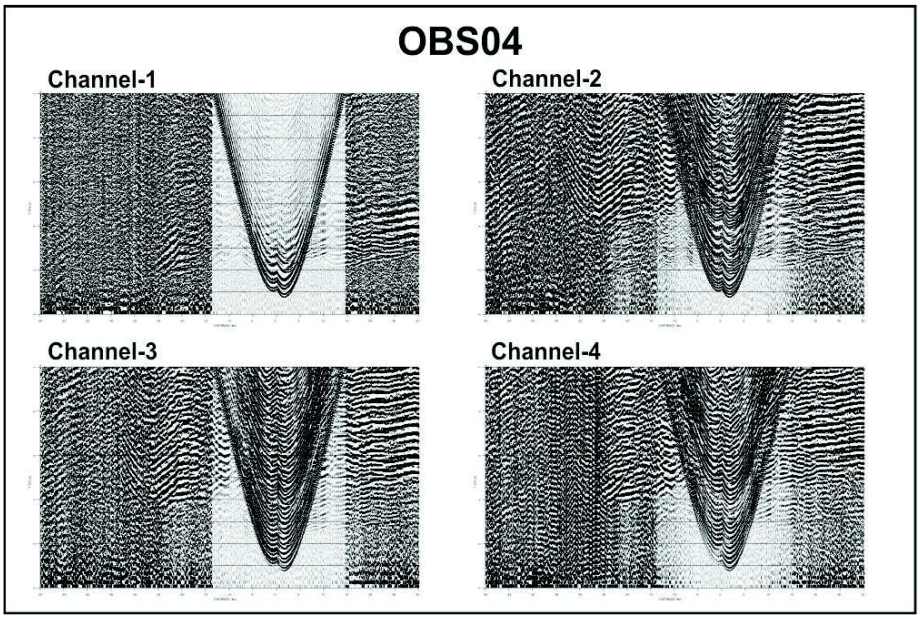

Figure 3.8: Comparison of Zplot seismic sections from different channels of OBS04 to evaluate the best channel to perform the picking. Channel-1: vertical component; Channel-2, 3 and 4: hydrophone with different amplifications.

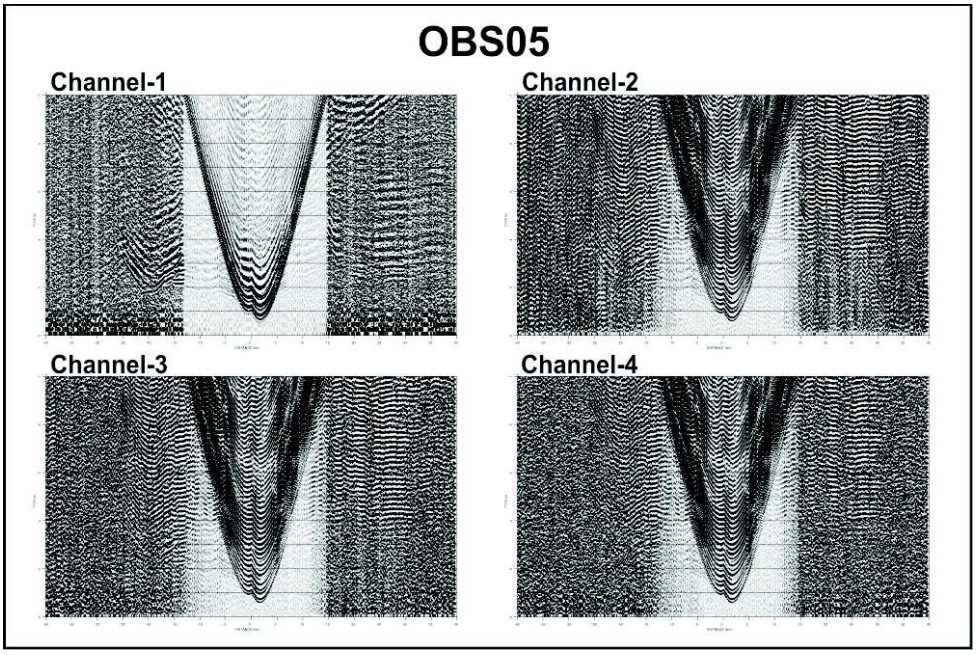

Figure 3.9: Comparison of Zplot seismic sections from different channels of OBS05 to evaluate the best channel to perform the picking. Channel-1, 2, 3 and 4: vertical component with different amplifications.

The OBS's seismic sections should yield two symmetric branches of a hyperbole if devoid of location errors. As show in Figure 3.10 the signal is asymmetric and the travel time is shorter from south (shooting was performed from north to south). This gives us additional information that the OBS could not be on the planned position. To correct for the location we used the application *zobscorr* by CGUL. With this application we got a new location by adjusting the position interactively. To run this program we need the information of the first break picking, the sound velocity in water, the OBS's depths from deployment and the initial point coordinates. The OBS's depths are from EMEPC bathymetry information and as initial point we use the middle point between deployment and recover location.

To determine the sound velocity in water we used different data sets from the Gloria fault area: a compilation from Levitus temperature and salinity database, the multibeam data from M79-2 cruise and an SVP dataset from EMEPC. The data were adjusted to the target depth (4000 m deep) and converted in to a weighted average velocity value (Figure 3.11).

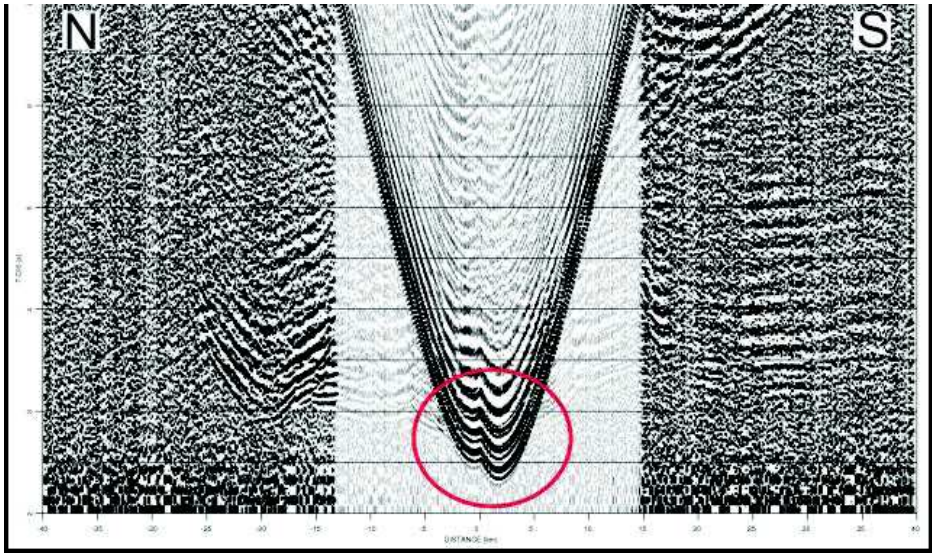

Figure 3.10: A zplot seismic section for OBS05-1. The red circle shows an asymmetric first arrival signal. (vertical scale: time in s; horizontal scale: distance in km)

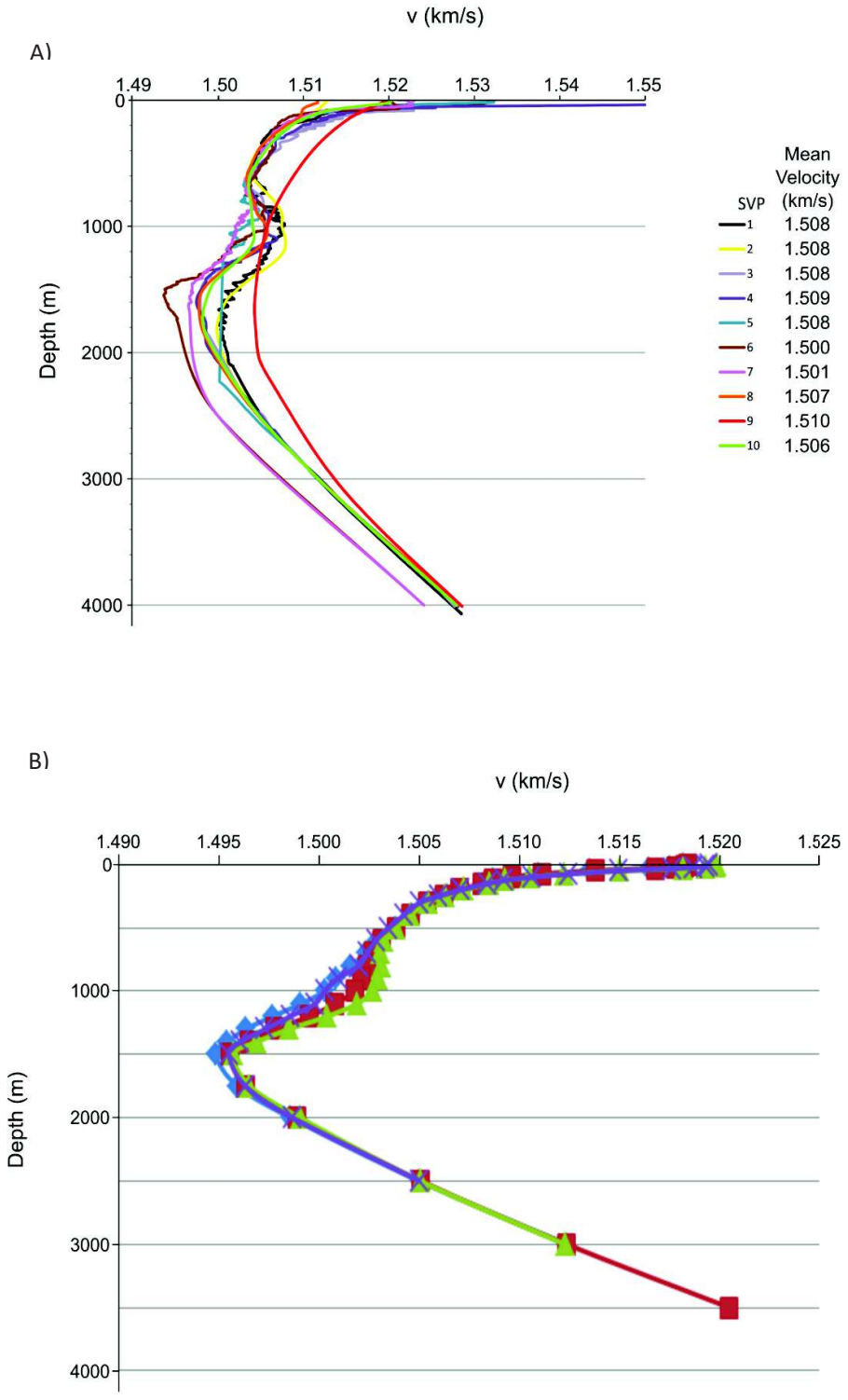

Figure 3.11: Sound Velocity Profiles used to calculate the average sound propagation velocity in water for the OBS location correction. A) Profiles used to Gloria Fault area: the first eight profiles were provided from EMEPC, the ninth profile is from cruise M79-2 multibeam data and the tenth profile is from Levitus database. The mean velocity was defined down to 4000 m depth. B) Profiles from Levitus database used on the São Miguel area. The mean velocity was defined down to 3500 m depth.

The mean value from all profiles in São Miguel was 1.5014 km/s and for Gloria Fault 1.5065 km/s. Since the software sensitivity just goes to the second decimal division, we used the water velocity of 1.500 and 1.510 km/s respectively.

For each OBS the time-distance between shots and initial point was calculated and compared with the values from the first break picking file to estimate the initial error. The next step uses a grid in the area of interest and computes the error for each grid vertex. The grid step is given interactively by the user in order to find the best error value for the new position. All the new positions with an error below 50 ms and the small displacement from the refraction profile were accepted. The program was forced to find a final location for the OBS on the same side of the recovered position with respect to the refraction profile. For some OBS's we had to change the initial point location to get acceptable results. In Figure 3.12 it is possible to observe the grid and the contours with the error value (in ms) and the final location (red circle) for the OBS04. The smallest error for this OBS was 31 ms, the distance between the final location and the refraction profile was 136 m, the distance between deployment and the final location was 441 m and the displacement from the initial point (red triangle in Figure 3.12) was of 112 m.

In Figure 3.13 we see the improvement of the data after the relocation process. At this point we have the OBS relocated and time corrected.

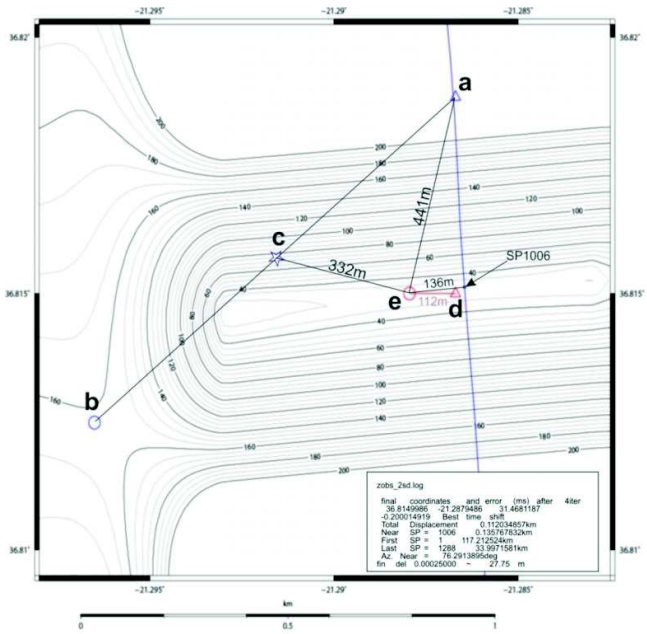

Figure 3.12: Relocation of OBS04. The blue line represents the shooting navigation; a) blue triangle- Deploy location; b) blue circle- recover location; c) blue star- mean location between deploy and recovery; d) red triangle-initial point; e) red circle-final location. In OBS04 it was necessary to select an initial point different from the mean location starting point (c).

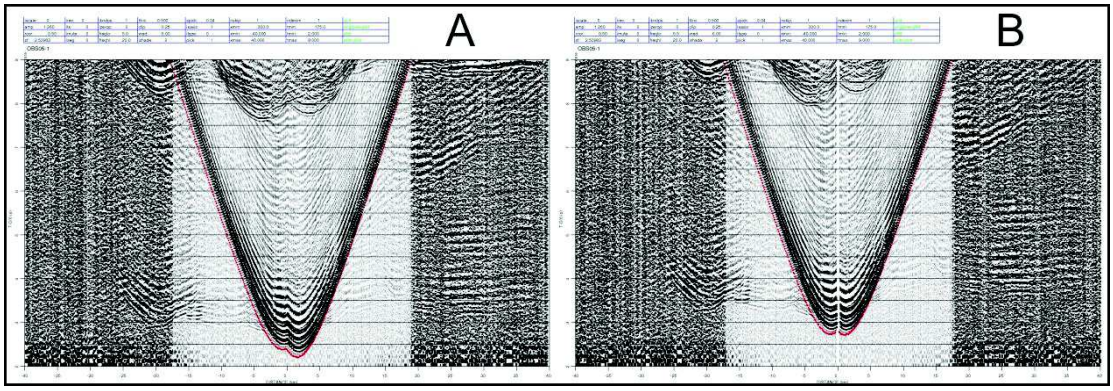

Figure 3.13: Difference of the relocation process in the OBS05-1: (A) before relocation and (B) after relocation.

For quality control we use the Ray Tracing software "*RAYINVR"* from Zelt package. This software allowed 2-D ray tracing and travel time inversion. We compared the Theoretical solution for the new location with the observed data (Figure 3.14).

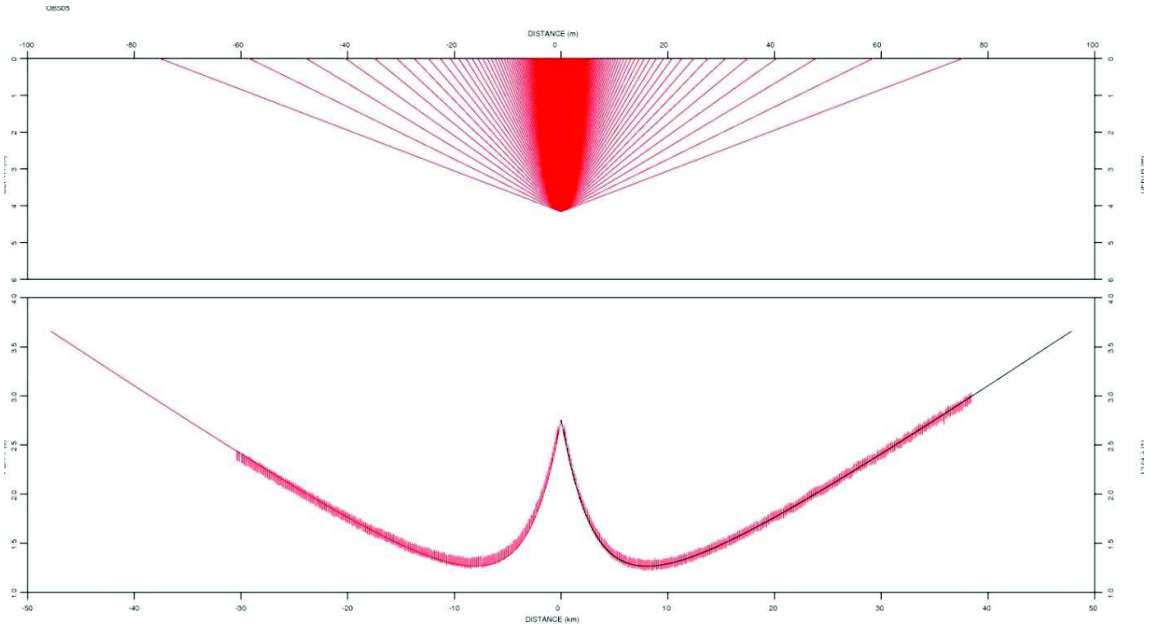

Figure 3.14: Ray tracing for OBS05 after the relocation process. The continue line represent the theoretical value (in s) and the vertical dashes represent the observe data.

After running all this procedure and calculate the best location for all OBSs a visual plot for the differences between the two positions allowed to see if there were large differences that could be important for the ray inversion. The new locations are plotted with the yellow plus in the maps below (Figure 3.15). For the Gloria Fault data, the displacement of the new location when compared with the nearest shot position was less than 500 m for eleven OBS's; between 500 m to 1000 m for six OBS's; and 1100 m of displacement for one OBS. For S. Miguel one OBS had 750 m of displacement, two OBS had 300 m and the rest of them had displacements below 250 m. As we can see the depth has an important role in the displacement of the instruments.

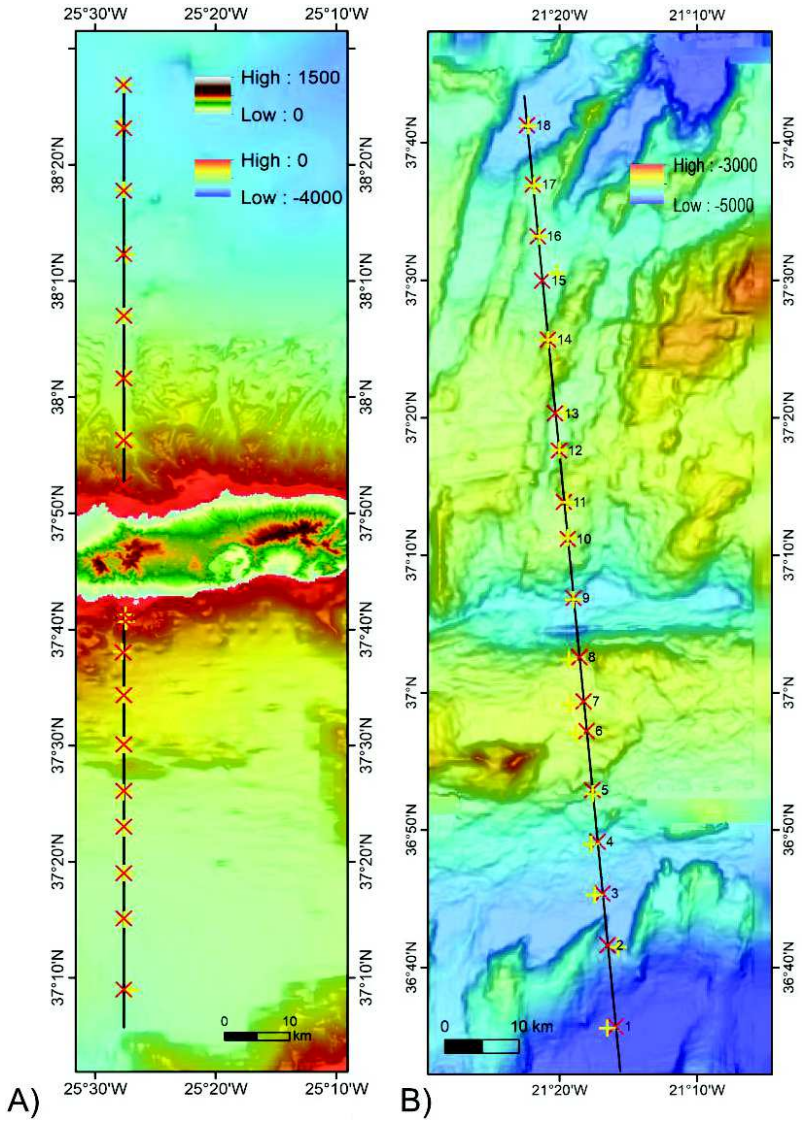

Figure 3.15: Differences between deploy location and final location after correction. A) S Miguel area; B) Gloria Fault area. Red marks: deploy location; Yellow marks: final location.

3.2.3. Inversion

The general methodology and modelling strategies discussed in (Zelt & Ellis (1988), Zelt (1999), Zelt (1994), Zelt & Smith (1992), Zelt & Forsyth, 1994) were followed to interpret the OBS data.

Ray Tracing software "*RAYINVR"* from Zelt package was used for 2-D ray tracing and travel time inversion. A compilation of the method is described in Afilhado (2006).

All pickings on the OBS seismic section can be found in annex 1,2 and 3 and the discussion is done furtherer in chapters 4, 5 and 6.

4. CHAPTER 4 – CRUSTAL STRUCTURE OF THE EURASIA-AFRICA PLATE BOUNDARY ACROSS THE GLORIA FAULT, NORTH ATLANTIC OCEAN

Luis Batista, Christian Hübscher, Pedro Terrinha, Luis Matias, Alexandra Afilhado, Thomas Lüdmann

(This chapter is presented in a paper format, as published in Geophysical Journal International, Batista et al, 2017).

This chapter provides new data, information and interpretation of the structure and nature of the oceanic crust and Moho discontinuity along a 150 km long seismic refraction profile across the Gloria Fault, i.e. across a segment of the Eurasia-Africa plate boundary in the North Atlantic

We show the existence of a 4 km thick layer between the lower crust and lithospheric upper mantle, which is interpreted as hydrated mantle as a result of serpentinization. This result is discussed on the basis of obtained Vp, Vs, the Poisson's coefficient and comparison with a natural analogue observed in the Ophiolite suite of Trodos. We also show evidence of slumped material and of upward fluid flow with two possible origins, i) from within the sedimentary units and ii) from the oceanic basement.

Summary

The oceanic crustal and uppermost lithospheric mantle structure across the Gloria Fault transcurrent plate boundary between Africa and Eurasia in the Northeast Atlantic is investigated based on seismic reflection, seismic refraction and wide-angle reflection data. This experiment used 18 ocean bottom stations along a N-S 150 km long traverse together with acquisition of a multichannel seismic reflection profile.

Modelling of P and S seismic waves and gravimetric anomalies allowed estimation of P-wave and S-wave velocity, density, Poisson's ratio and discussion of a compositional model. A five layer model is proposed in which layers 1 to 3 correspond to normal sediments through typical oceanic crust layers 2 and 3. Layer 5 yielded mantle velocities above 7.9 km/s. Layer 4 with 4 km of thickness has Vp velocities between 7.1 and 7.4 km/s and is clearly separated from typical oceanic crust and mantle layers. Comparison with natural analogues and published lab measurements suggest that layer 4 can be a mix of lithologies that comply with the estimated P and S velocities and computed Poisson's ratio and densities, such as, olivine cumulates, peridotite, gabbro and hydrated mantle. We favour the tectonic process that produces secondary porosity from which results serpentinization due to seawater circulation in fractures.

Structural and seismic stratigraphic interpretation of the reflection profile shows that Neogene to recent tectonic deformation on this segment of the plate boundary concentrated on the southern side of the Gloria fault, i.e. the Africa plate.

Keywords: oceanic transform and fracture zone processes, transform faults, crustal structure, Atlantic Ocean, composition and structure of the oceanic crust.

4.1. Introduction

The Gloria Fault (GF) is an oceanic fracture zone that defines the Eurasia-Africa plate boundary for more than 1300 km from the eastern tip of the Azores plateau to the Madeira-Tore Rise (Figure 4.1), approximately one third of the Azores-Gibraltar Fracture Zone (AGFZ) (e.g. Argus *et al.*, 1989, DeMets *et al.*, 2010, Grimison & Chen, 1986, Luis & Miranda, 2008, Serpelloni *et al.*, 2007, Verzhbitskii *et al.*, 2010).

The GF generated instrumental earthquakes with magnitudes M = 7.1 and M = 8.4, in 08/05/1939 and 25/11/1941 (Buforn *et al.*, 1988), implying surface ruptures in the order of 250 - 300 km. Seismicity of this magnitude constitutes a hazard that should be taken in consideration by scientists and civil authorities regarding the assessment of seismic and tsunami hazard. The crustal and uppermost lithospheric mantle structure of this plate boundary remains unknown to date and unravelling it is important to help understanding the causes and origin of seismicity, its rheological behaviour and geodynamic setting.

Our overarching objective is to produce a compositional model for the crust and upper lithospheric mantle of the abyssal oceanic basins that flank the GF at around 21º15'W. To achieve this, a velocity model for P and S seismic waves (Vp and Vs seismic velocity models respectively) is produced by processing the data acquired by 18 Ocean Bottom Stations (OBS) during an active seismic refraction experiment along a 150 km long transect (Figure 4.2). Poisson's ratio and density values are derived from Vp and Vs models and the compositional model is discussed. Interpretation of the seismo-stratigraphy of a multichannel seismic profile allowed discussion on the stratigraphy and tectonics in the area.

These results provide new information on the structure of the Northeast Atlantic deep oceanic basins and GF far from the influence of ocean-continent transition and mid-Atlantic ridge along a fracture zone that has recorded one of the largest magnitude earthquakes ever recorded in fracture zones. Also considering the recently reported evidence of fluid convection from the oceanic basement across the Horseshoe Abyssal Plain east of the GF (Hensen *et al.*, 2015), our results can contribute for further understanding of the relationship of fluids and seismicity along transform fault type plate boundaries. This objective is accomplished by linking the refraction data with multichannel seismic reflection data acquired along the same section.

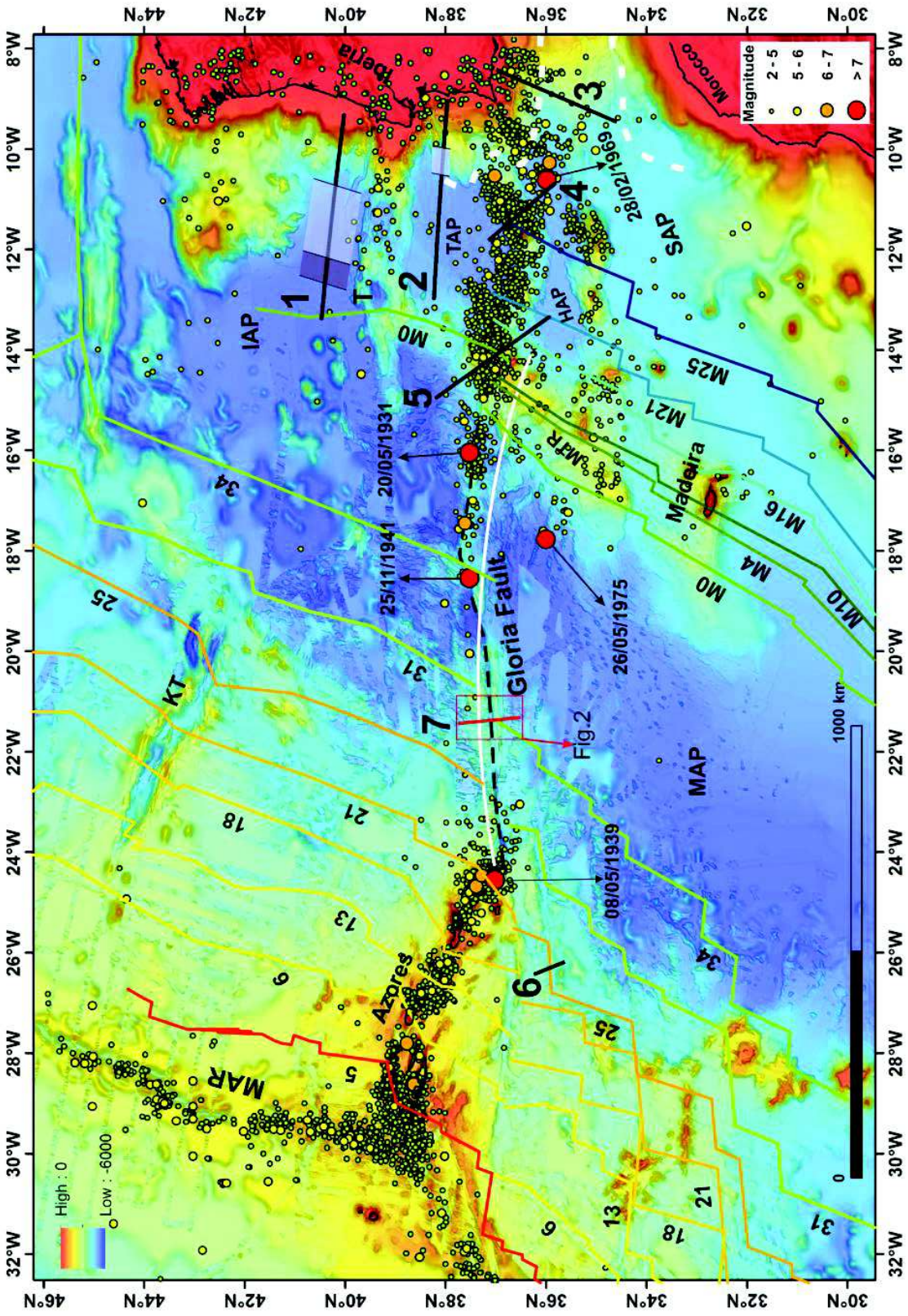
Magnitude
2 - 5
5 - 6
6 - 7
> 7
Iberia
Morocco
IAP
TAP
HAP
SAP
MAP
MAR
KT
Gloria Fault
Madeira
Azores
28/02/1969
20/05/1931
25/11/1941
26/05/1975
08/05/1939
Fig.2
1000 km
0
High : 0
Low : -6000

Figure 4.1 (page before): Location map. The black lines show the location of seismic refraction lines: 1- Dean *et al.* (2000) dark grey area represents the peridotite ridge and light grey area indicates the Ocean-Continent transition zone; 2- Afilhado *et al.* (2008) light grey area refers to the Ocean-Continent transition zone; 3- Sallarès *et al.* (2011); 4- Sallarès *et al.* (2013), white dashed line marks the Ocean-Continent Boundary (OCB) for those authors ; 5-Peirce & Barton (1991); 6-Potts *et al.* (1986); red line 7-This study. MAR–Mid-Atlantic Ridge; MTR–Madeira-Tore Rise; KT-King's Trough; T–Tore seamount; IAP–Iberia Abyssal Plain; TAP–Tagus Abyssal Plain; HAP–Horseshoe Abyssal Plain; SAP-Seine Abyssal Plain; MAP-Madeira Abyssal Plain; Seismicity from the I.S.C. On-Line Bulletin (1915 – 2014, International Seismological Centre, 2011) and from IPMA (Portuguese Institute for the Atmosphere and Sea) . Black dashes represent the Gloria Fault. The white arc represents the current relative motion between Nubia and Eurasia, according to the MORVEL kinematic model (DeMets *et al.*, 2010). Isochrones from Müller *et al.* (2008). Bathymetry from EMEPC (Task Group for the Extension of the Continental Shelf) and from GEBCO (General Bathymetric Chart of the Oceans).

4.2. Geological setting

The GF is an oceanic fracture zone (from 24ºW to 15ºW) that accommodates mainly as a dextral strike-slip fault the movement of Africa with respect to Eurasia (Argus *et al.*, 1989, Buforn *et al.*, 1988, Jiménez-Munt & Negredo, 2003, Udías *et al.*, 1976, Neres *et al.*, 2016). However, the trace of the GF does not follow perfectly the expected relative motion between these two plates, according to the MORVEL kinematic model (white line in Figure 4.1), and complex tectonics are expected. The GF has been described as consisting of the three rectilinear segments: i) the western one is 300 km long and strikes WSW-ENE ; ii) the central one is 150 km long and strikes SW-NE, and iii) the eastern one is 250 km long and strikes WNW - ESE. These segments and the bends that connect them create different strain regimes strike-slip faulting in the first segment, compression in the second and strike-slip faulting with a small portion with extension in the third segment with predicted slip rates varying from 3.2 mm/yr (for transcurrent motion) and 2.0 mm/yr (for transpressive motion) (Neres *et al.*, 2016)

Historical records does not yield any information of major seismogenic activity of the GF since 1500 A.D. (Udías *et al.*, 1976). However, Buforn *et al.* (1988) based on the instrumental seismicity, showed that most of the stress is released in the central section of the fault by large magnitude earthquakes along a fairly simple fracture with strike-slip motion. There is a nearly complete absence of low to intermediate magnitude earthquakes since 1960. However, two of the largest earthquakes in the AGFZ are found here, the M = 8.4 (25/11/1941) and the M = 7.1 (8/5/1939) events. It can be argued that this section of the Africa-Eurasia plate boundary is still affected by the post-event seismic gap, characteristic of some large earthquakes.

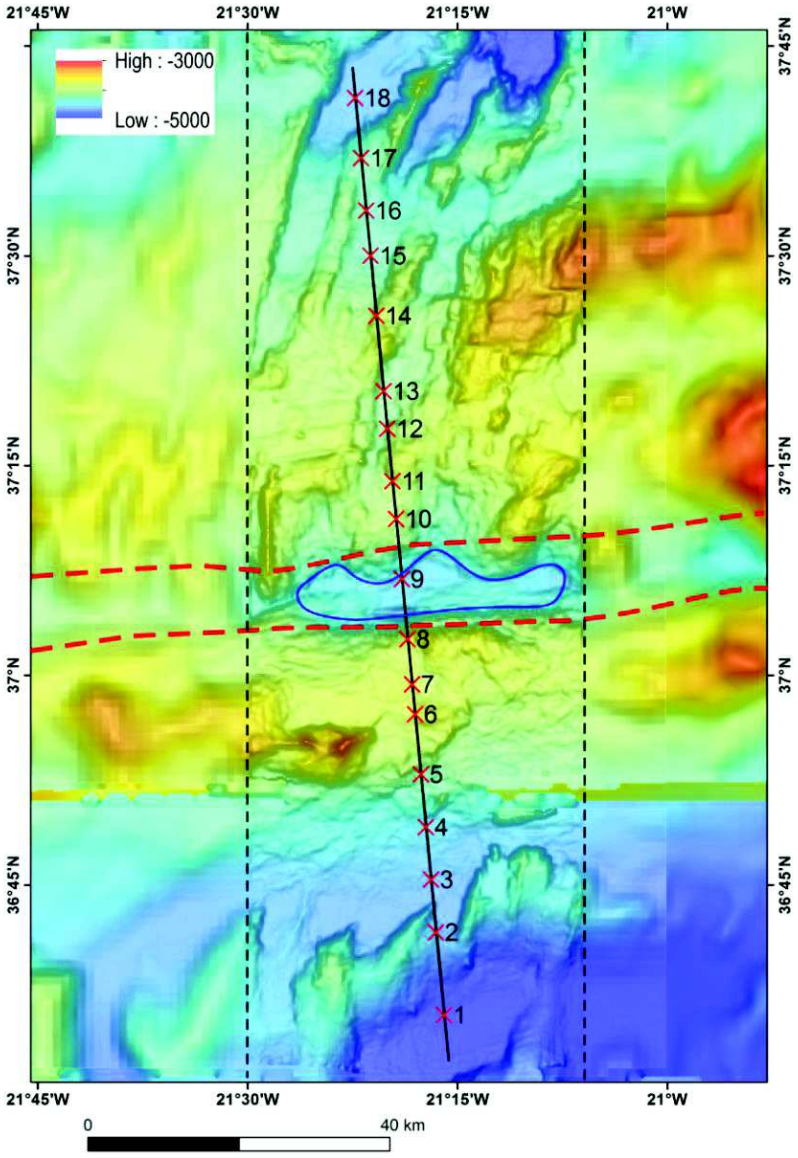

Figure 4.2: Map of the study area with location and identification of the OBS (red crosses) and reflection seismic profile (black line). The high-resolution swath bathymetry (delimited by black dashes line) is a courtesy from EMEPC (Task Group for the Extension of the Continental Shelf). Blue line limited the GF M79 basin. Red dashes line indicates GF area.

The Africa-Eurasia plate boundary in the Atlantic Ocean is only defined as a discrete plate boundary between the Azores plateau and to the west of the Madeira-Tore Rise (MTR), i.e. along the GF, where both plates are presumably made of typical Atlantic oceanic lithosphere (Jiménez-Munt *et al.*, 2001, Bezzeghoud *et al.*, 2014). Between the MTR and the Gibraltar Straits the Africa-Eurasia plate boundary has been discussed by various authors on the basis of recently acquired geophysical data (Gueydan & Précigout, 2014). A distributed strike-slip plate boundary along a 600 km long dextral shear zone was proposed by Zitellini *et al.* (2009)

and the possibility of the roll-back from a subducted oceanic slab under the Gibraltar orogenic arc was proposed by Gutscher *et al.* (2002). Tectonic fabrics associated to the strike-slip and thrust regimes in the Gulf of Cadiz area were analysed and tested experimentally and shown to be coeval by Duarte *et al.* (2011). The tectonic strain and seismicity is decoupled on approximately W-E striking dextral faults and thrusts and SW-NE trending thrusts (Palano *et al.*, 2015, Rosas *et al.*, 2012, Terrinha *et al.*, 2009, Matias *et al.*, 2013, Custódio *et al.*, 2015). This area has also recorded seismic events of large magnitude, such as the 1st November, 1755 historical event with estimated magnitude 8.1-8.9 (Johnston, 1996) and the M=7.9 28th February, 1969 event (Custódio *et al.*, 2016, Stich *et al.*, 2010). Although the general tectonic strain regime from the Azores plateau eastern tip to the Gorringe Bank (roughly from 24ºW to 12ºW, respectively, see Figure 4.1) is dominated by strike-slip tectonics, large landslides prone to cause tsunami waves up to 10 m high occurred in the recent geological past on the Hirondelle seamount seismicity cluster (~13º W, see Figure 4.1 for location) as shown by Omira *et al.* (2016).

From a kinematic point of view, it is worthwhile noting that the GF was localized between two Mid-Atlantic Ridge segments from ~85 to ~60 My, acting as a typical oceanic transform fault. From ~60 to ~20 My Africa and Iberia moved together so it is expected that during this time interval no major differential movement of Africa with respect to Eurasia occurred on the GF. At ~20 My the westward displacement of Africa with respect to Eurasia in the Atlantic initiated as recorded by the offset of magnetic anomalies and kinematics of the geological structures (e.g., Hayward *et al.*, 1999, Rosenbaum *et al.*, 2002, Srivastava *et al.*, 1990).

To the east of the MTR the nature of the lithosphere is complex as it comprises the Seine Abyssal Plain (SAP), the Tagus Abyssal Plain (TAP), the Horseshoe Abyssal Plain (HAP) and the Gulf of Cadiz (GoC) region. The M-series magnetic anomalies are only well defined in the SAP, whilst the TAP, the HAP and the GoC region (whose lithosphere is made of exhumed serpentinized mantle and highly extended continental crust) do not show a clear magnetic pattern (Afilhado *et al.*, 2008, Martínez-Loriente *et al.*, 2014, Sallarès *et al.*, 2011, Sallarès *et al.*, 2013). This area is certainly a complex domain since it not only accommodates the western end of the Alpine orogeny and its transition to a transcurrent plate boundary but also comprises a sleeve of the westernmost Tethys Jurassic ocean and its narrow oceanic slab underneath the Gibraltar arc (Duarte *et al.*, 2013, Martínez-Loriente *et al.*, 2014, Gutscher *et al.*, 2002, Sallarès *et al.*, 2011). Further north along the West Iberia Margin in the Iberia

Abyssal Plain (IAP) the oceanic crust displays 6.5 - 7 km of thickness underlain by 2 to 4 km thick layer of partially to fully serpentinized lithospheric mantle (Dean *et al.*, 2000).

The GF study area of this work is located in oceanic crust of ~60 My of age between magnetic anomalies C31 and C25 in the Eurasia plate and ~80 My on magnetic anomaly C34 in the Africa plate (Figure 4.1). The nearest studies regarding compositional models of the lithosphere were carried out across the Tydeman fracture zone and Josephine seamount in the MTR (profiles 6 and 5 in Figure 4.1, respectively) (Potts *et al.*, 1986 and , Peirce & Barton, 1991 respectively).

The refraction study across the Tydeman fracture zone, at chron 25 (~55 My), revealed low crustal seismic velocities within the fracture zone together with unusually low velocities of 7.2 - 7.5 km/s in the lithospheric mantle attributed to serpentinization of mantle peridotite by hydrothermal circulation (Potts *et al.*, 1986). Those authors defined a crustal thickness along the fracture zone between 3 and 5 km. However, their experiment could not reach normal mantle velocities above depths of 12 km.

A northwest-southeast refraction profile acquired across the Josephine seamount (Figure 4.1) indicates that the crust on both Eurasia and Africa sides of the MTR is oceanic and underlain by a layer with velocities between 6.8-7.0 km/s with a crustal thickness of 14-18 km (Peirce & Barton, 1991).

4.3. Datasets

The original available data for this study consisted in two coincident 150 km long seismic profiles, a multichannel seismic reflection profile (MCS w51) and a seismic refraction and wide-angle reflection profile. Both profiles were shot across the GF (see Figure 4.1 and Figure 4.2 for location) during the METEOR cruise M79-Leg2 in August 2009 (Hübscher, 2013).

The acquisition was simultaneous using as energy source two 32 lt BOLT air guns with 120 bar shooting air pressure. Seismic signals were generated every 60 s at 4 kn velocity over ground resulting in a shot spacing of approximately 120 m.

18 Ocean Bottom Stations (OBS) spaced every ~8 km and a digital streamer with 144 channels made up of six multiple arrays performing an active length of 600 m with 100 m for

near offset, were deployed to record the seismic energy. Most OBSs were equipped with a hydrophone and a geophone and acquired with a sampling rate of 5 ms. OBSs 03, 08, 12, 14 and 17 only have a hydrophone and acquired with a sampling rate of 20 ms. In this study, we used mostly the data from the hydrophones because they show the best quality data. The useful bandwidth for wide-angle reflection and refraction analysis was found to be 3 – 16 Hz.

The OBS sat on the seafloor between 3800 m and 5000 m water depths. During deploy OBSs drifted in the water column and the final OBSs positions at the seafloor were calculated. Each OBS position was relocated using the direct water arrival, considering a constant sound speed in the water of 1.51 km/s. The displacement of the new location when compared with the nearest shot position was less than 500 m for eleven OBS's; between 500 m to 1000 m for six OBS's; and 1100 m of displacement for one OBS.

4.4. Seismic reflection interpretation

Seismic line w51 (Figure 4.2 and Figure 4.3) was shot perpendicular to the GF and at a low angle to the crests of oceanic rotated blocks, thus the oceanic structure perpendicular to accretion is not well imaged. Nevertheless, the line cuts across various structural blocks imaging sub-basins and structural highs of the Abyssal Plains both north and south of the GF, allowing for the characterization of different structural domains.

4.4.1. Seismic units

The character of the reflections allowed the interpretation of two unconformities below seafloor, H1 and H2 that separate three seismic units, U1, U2 and U3 (Figure 4.3, Figure 4.4,Figure 4.5,Figure 4.6 and Figure 4.7).

The internal reflections of U1 show good lateral continuity, alternation of high and low amplitude reflections and parallel configuration consistent with oceanic sediments that were deposited in confined bathymetric lows or basins. Thickness of U1 varies from nil to a maximum of approximately 0.8 sec TWT, which would correspond to a maximum thickness of 800 m if an average acoustic velocity of 2 km/s is assumed. The U1 basal sediments lie on top of H1 either parallel to it onlapping on top of an erosion unconformity, or on top of tilted layers or abut directly against fault scarps.

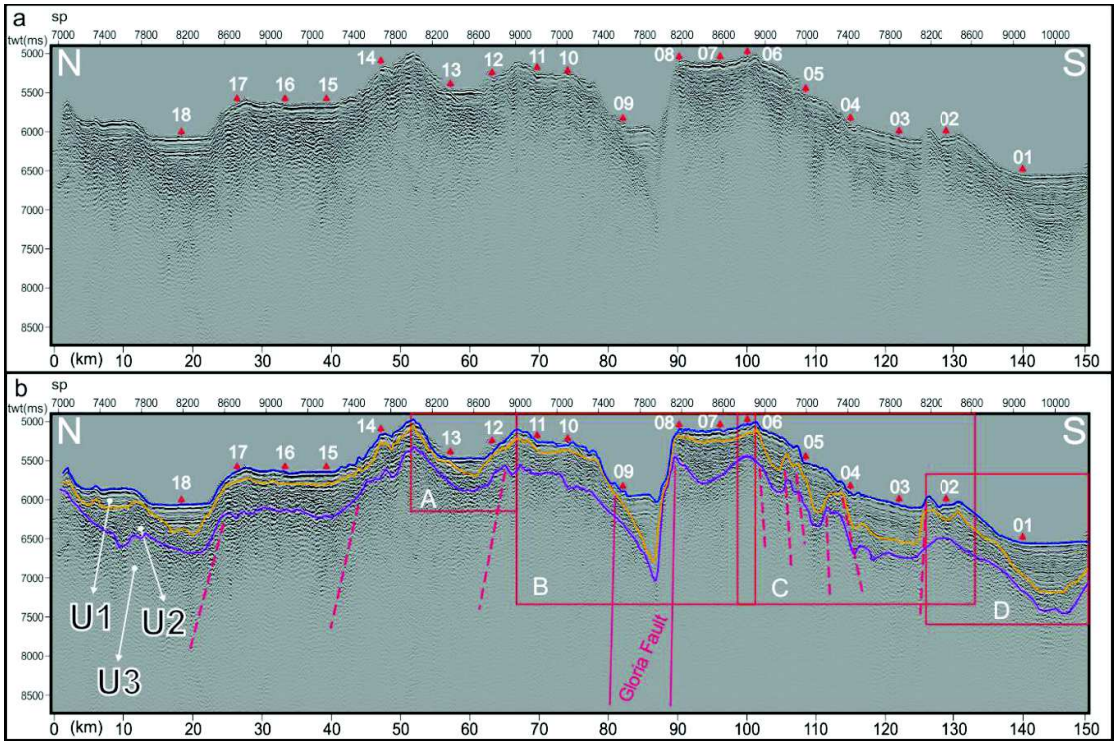

Figure 4.3: Plot of the MCS profile w51: a) raw data with OBS numbers (white numbers) and OBS position (red triangles); b) with seismic interpretation: blue line corresponds to sea bottom; yellow line corresponds to horizon H1; purple line corresponds to horizon H2; U1 corresponds to seismic unit 1; U2 corresponds to seismic unit 2; U3 corresponds to seismic unit 3 (see text for horizons and seismic units description); sp–Shotpoint; twt–Two-way-Travel Time; red lines identify the GF zone and red dashed lines schematically identify fault zones; red boxes from A to D correspond to detail figures shown below.

The second unit, U2, is limited by discontinuities H1 (top) and H2 (base). It presents internal reflections with high amplitude, poor lateral continuity and a general chaotic internal configuration although, in some places, it is possible to define some sub-parallel internal configuration (Figure 4.4, Figure 4.5,Figure 4.6 and Figure 4.7). U3 is generally acoustically transparent with some planar discontinuous reflections.

The thickness of U1 is smaller on the north flank of the GF where we observe values between 100 ms to 350 ms. The thickness of U1 in the south flank of the GF varies from 125 ms to 650 ms. Inside the GF M79 basin (Figure 4.2Figure 4.5) U1 reaches its highest thickness of 800 ms. The thickness of U2 varies from 250 ms to 500 ms. Consequently, the total maximum thickness of U1+U2 is about 1 sec (TWT) inside the GF M79 basin. On the north side U1+U2 thickness varies from 400 ms to 750 ms and on the south side of GF the thickness varies from 650 ms to 800 ms.

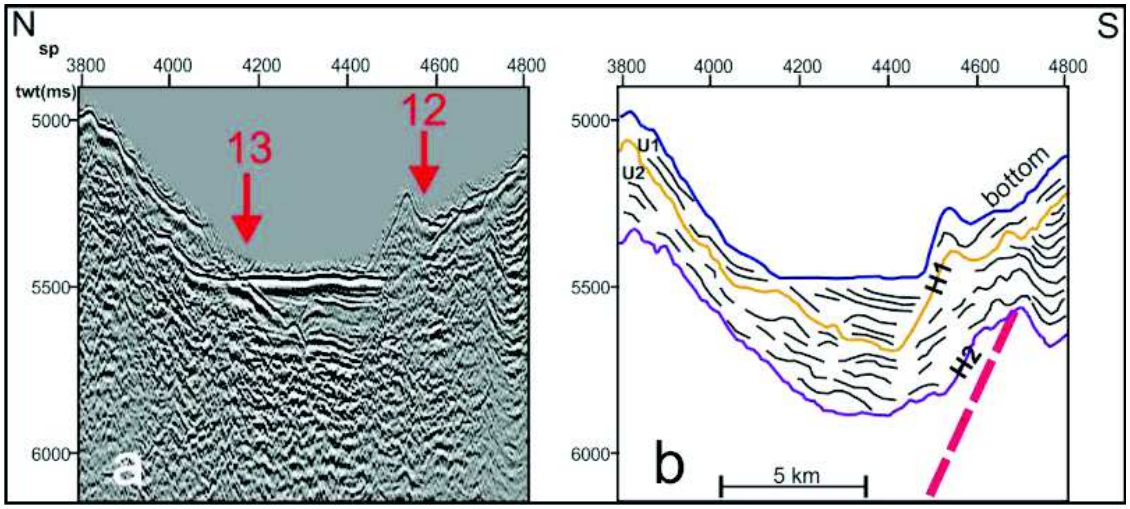

Figure 4.4: Detail of the MCS profile w51 (a) with seismic interpretation (b): blue line: sea bottom; yellow line: horizon H1; purple line: horizon H2; U1: seismic unit 1; U2: seismic unit 2; red numbers and arrows: OBS positions; red dashed lines: fault zones; sp – Shotpoint; twt – Two-way-Travel Time. For location see red box A on Figure 4.3. Note at sp 4200 – 4300 that U1 reflections are cut by the seafloor reflection.

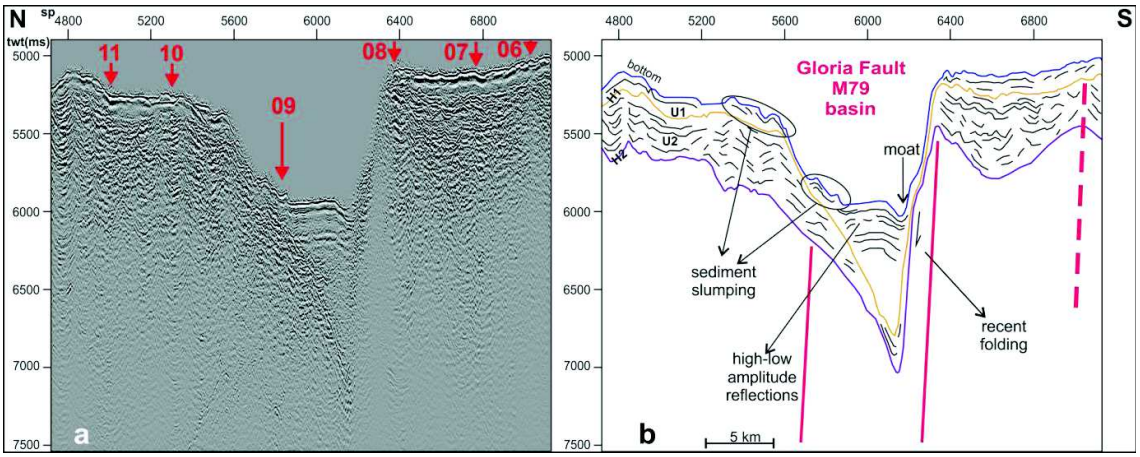

Figure 4.5: Detail of the MCS profile w51 (a) with seismic interpretation (b) of the GF basin; blue line: sea bottom; yellow line: horizon H1; purple line: horizon H2; U1: seismic unit 1; U2: seismic unit 2; sp – Shotpoint; twt – Two-way-Travel Time; red numbers and arrows: OBS position; red lines: the GF zone and red dashed lines: schematically fault zones. For location see red box B on Figure 4.3.

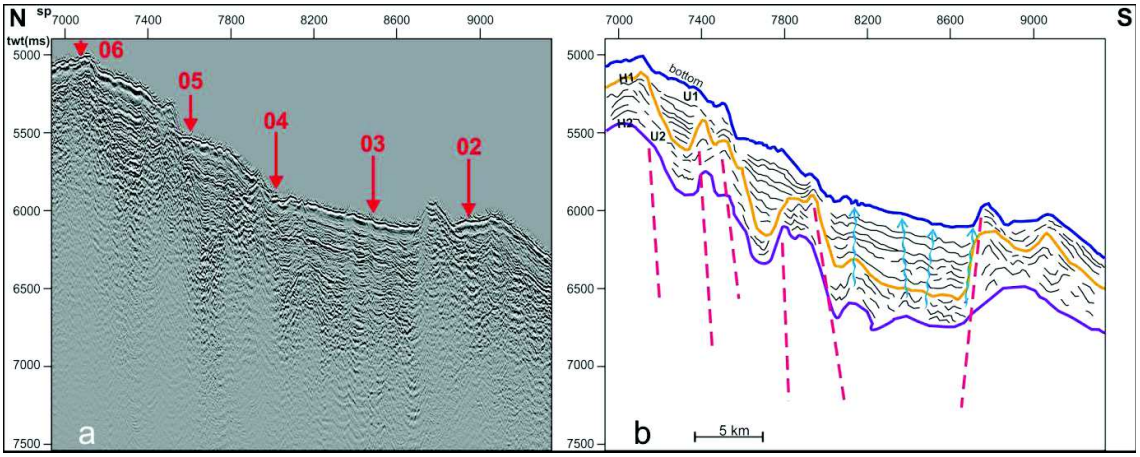

Figure 4.6: Detail of w51 MCS profile (a) with the interpretation (b) of the south segment (between OBS 02 and 06): blue line: sea bottom; yellow line: horizon H1; purple line: horizon H2; U1: seismic unit 1; U2: seismic unit 2; red numbers and arrows: OBS position; red dashed lines: schematically fault zones; sp – Shot point; twt – Two-way-Travel Time. For location see red box C on Figure 4.3. Note existence of high frequency folding and detachments probably associated with downslope creeping of sediments around sp 7800. Blue arrows indicate fluid escape structures.

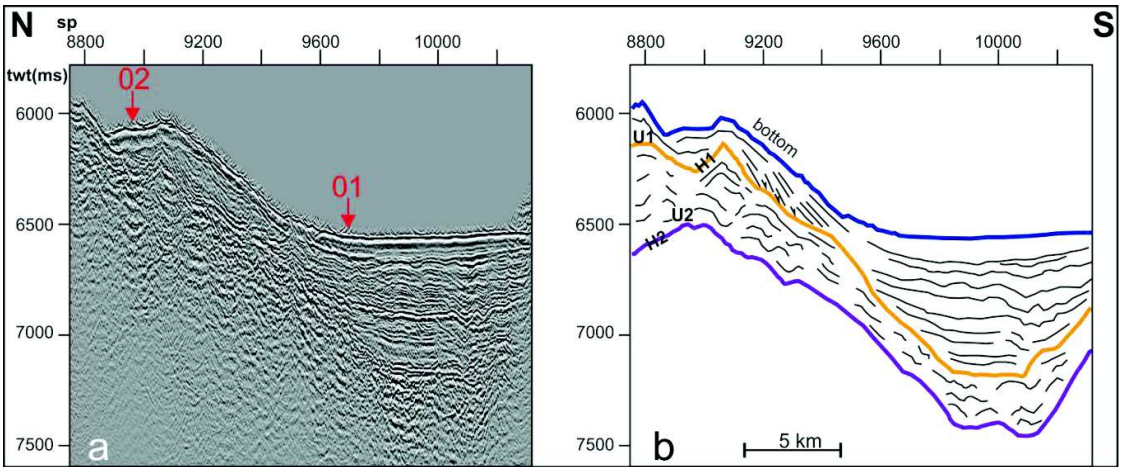

Figure 4.7: Detail of the w51 MCS profile (a) with the interpretation (b) of the south segment (between OBS 01 and 02): blue line: sea bottom; yellow line: horizon H1; purple line: horizon H2; U1: seismic unit 1; U2: seismic unit 2; red numbers and arrows: OBS position; sp – Shot point; twt – Two-way-Travel Time. For location see red box D on Figure 4.3. Note downlap and onlap geometries of U1 on top of U2 at sp 9200 and 9600, respectively; disturbed sediments probably associated with slumping or landslides at sp 10200.

4.4.2. Geological interpretation

The geometry, lateral continuity and amplitudes of the internal reflections allow the following suggestions for the nature of the three seismic units. For U1 we assume that is made of pelagic sediments deposited in confined bathymetric lows or basins interbedded with gravity

driven deposition, corresponding respectively to well defined horizons and transparent facies. The more discontinuous geometric characteristics of U2 internal reflections and the fact that U2 lies between U1 and U3, is compatible with an interpretation as a volcanic or volcanic-sedimentary complex. The lack of stratigraphic reflectors in U3 suggests a composition of magmatic crustal material.

The sediments in the north flank of the GF show little to no tectonic deformation. The top sediments are generally parallel to the seafloor with exception of the sub-basin located between OBS 12 and 13, (Figure 4.4), where a neat truncation of horizons is clearly cut by the seafloor reflection. The wedge-like structure of the sedimentary infill of this sub-basin suggests tilting towards the south, which together with the lack of sub-surface reflections suggests extensional reactivation of a normal fault.

On the northern flank of the GF M79 basin sediment slumping is clearly seen as well as recent folding against the south flank (Figure 4.5). South of the GF there are four sub-basins containing thick series of U1 sediments, only the southernmost of which has not undergone important tilting. Sub-basins between OBS02 and 06 (Figure 4.6) show high-frequency folds possibly associated with downslope creep processes. Tilting was certainly a progressive deformation process as indicated by progressive onlaps and unconformities. Sub-basin under OBS03 also shows sediment layer disruption and geometries resembling teepee-like structures that are compatible to fluid escape structures. Between OBS 01-02 the sediments of U1 are tilted and folded with onlap and downlap geometries on top of U2; in the south basin sediments (sp 9600-10200) are disturbed, showing heterogeneous folds detaching within U1 layers, suggesting tectonic deformation associated with mass transport deposits (Figure 4.7).

Sediment thickness shows good correlation with seafloor depth, the deepest basins present larger sediment thickness (Figure 4.3). The north flank of the GF shows little block tilting and minor tectonic deformation. Inspection of the regional bathymetry (Figure 4.2) shows that sub-division into sub-basins appears to be controlled by the oceanic crests of rotated blocks, probably inhibiting turbidites to be evenly distributed. It is possible that an important part of the sub-basins infill result from local mass transported deposits, possibly associated with earthquakes.

The largest sediment thickness observed in the GF M79 basin (>1 sec TWT in Figure 4.5) is consistent with subsidence with respect to the basin faulted flanks and sediment export from the northern block. The semi-circular scar in the southern flank suggests slide events. Although acoustic coherent reflections are scarce within this basin the inter-digitations of high

and low amplitude reflections suggest debris flow deposition. The high amplitude reflections at the seafloor and the moat at the foot of the southern scarp (Figure 4.5) suggest hard ground formation that can be associated with coarser sediment concentration at the base of a submarine episodic waterfall as also reported at depths of 4 km in the Horseshoe valley off southwest Iberia and Gibraltar Straits (Duarte *et al.*, 2010).

4.5. Seismic velocity structure

Processing of the data recorded by the OBSs was made following the methodology and modelling strategies discussed in (Zelt & Ellis, 1988, Zelt, 1999, Zelt, 1994, Zelt & Smith, 1992). A detailed description of the method can be found in (Afilhado, 2006).

The travel-times of refraction and wide-angle reflection seismic phases recorded by the OBSs were modelled using the xrayinvr code by Zelt & Smith (1992). The sediments layer picked from the seismic reflection profile (L1) were used as a starting point for the model. The two-way travel time (TWT) of the base of U2 was depth converted using a Vp of 2 km/s. Vp and thickness of L1 were adjusted by trial and error to improve the fit of the underlying layers and finally, L1 was reconverted into TWT in order to be compared to the seismic stratigraphic interpretation.

The velocities and thicknesses of the "Mean Oceanic Crustal Structure" defined by White *et al.* (1992) for Layer 2, Layer 3 and Lithospheric Mantle were used as initial values of the model. During the processing of the data these values were adjusted to fit with the picked arrival times.

The model was constructed in a top-to-down strategy, layer by layer. The initial model was obtained by forward trial-and-error method, adjusting the velocities and thickness of each layer to reach a reasonable fit of observed arrival times, followed by iterative dumped least square inversion on layer's velocities and depths. For the sediments we used both OBS arrival times and two-way travel-time from MCS record. The basement layers were modelled from the arrival times of refracted and reflected phases identified in the OBS record. Finally, a trial-and-error approach was applied to better adjust the velocity gradients in each layer and velocity contrasts across layers. For this we computed synthetic record sections and compared them with the observed record sections. A final ray tracing (forward) and dumped least

squares (inversion) provides the arrival time fit (TRMS) for all phases and model quality indicators.

P-waves and S-waves (converted to P-waves at the water-sediment interface) were recorded by the OBSs. Analyses of the data revealed six different phases (four from refracted waves and two from reflected waves) for compressional and shear waves (Figure 4.8) and allowed producing a final velocity model with five layers. Velocity gradients and phase identification in the velocity model were constrained by synthetic seismograms (Figure 4.8b and Figure 4.8f).

The Poisson's ratio was calculated from P and S wave models and used for discussing the crust and upper lithospheric mantle compositional models.

Phase Identification:

P2 & S2 – Phase refracted in layer 2

P3 & S3– Phase refracted in layer 3

P4P & S4S – Phase reflected from the top of layer 4

P4 & S4 – Phase refracted in layer 4

P5P & S5S – Phase reflected from the top of layer 5

P5 & S5 – Phase refracted in layer 5

Inspection of the error analysis statistics based on the number of observations (NPTS), the root-mean-square misfit between calculated and observed travel times (TRMS) and the normalized chi-squared (χ^2) together with a good coverage of ray-path support the quality of the model. The TRMS is the square root of the mean of the squares of the individual travel time residuals (difference between predicted and observed arrival times); as such, a value of zero is desirable but, unlikely to be achieved. The chi-squared is a measure of the fit between the picked data points and the predicted arrival times from the velocity model; a value of 1 is desirable and values close to 1 are considered adequate (Zelt, 1999). The values for the χ^2 parameter and the TRMS misfit for the modelled picks in individual phases and for all phases on each of P and S velocity models are listed in Table 4-1 and Table 4-2, respectively.

The final values for P and S-wave velocity models were TRMS=0.089 s and χ^2=0.786 for P-wave model and TRMS=0.123 s and χ^2=1.516 for S-wave model.

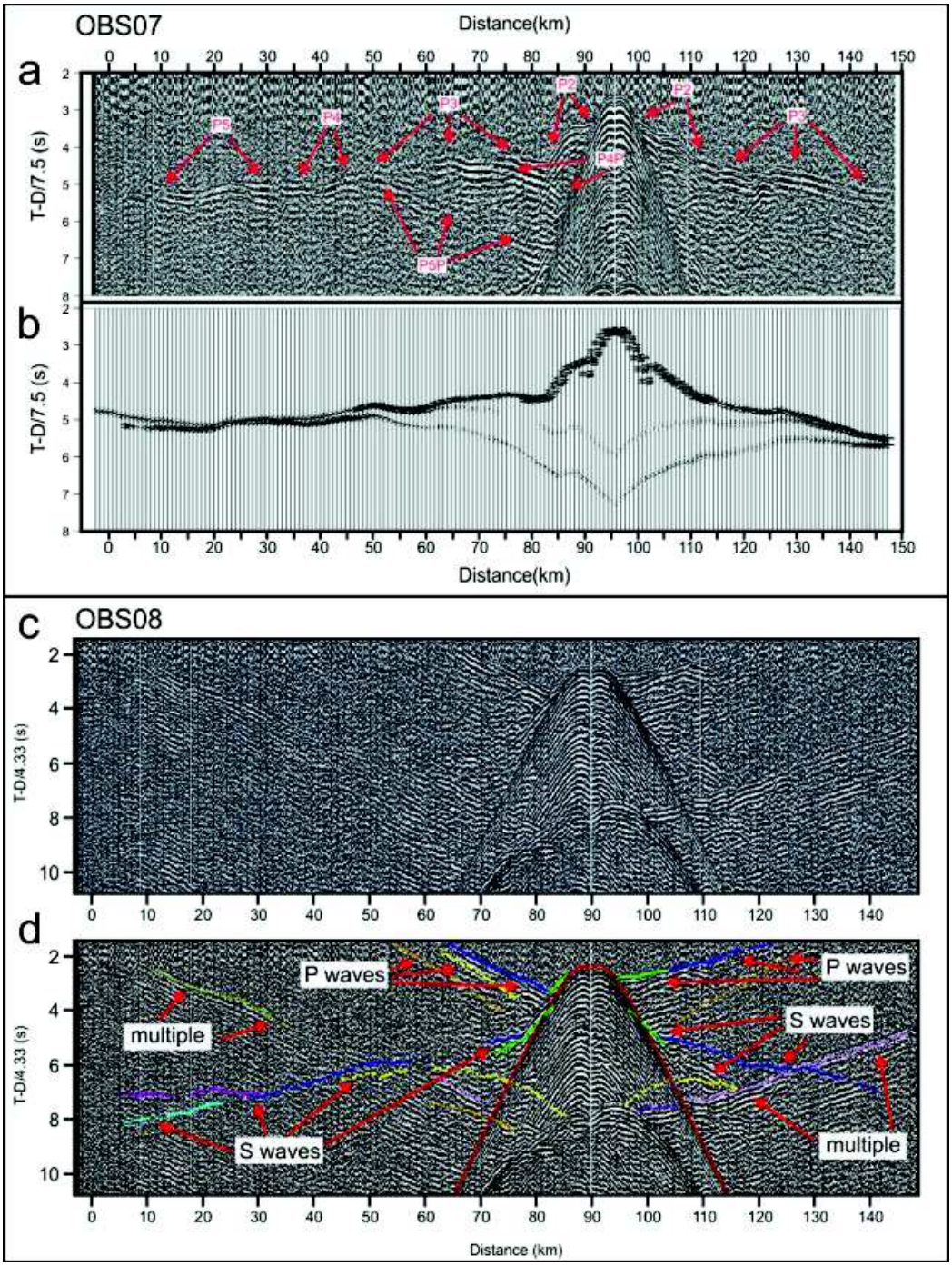

Figure 4.8: Phase identification. Energy arrivals and phase identification for P-wave in OBS07 (a) and OBS03 (e); synthetic seismogram for OBS07 (b) and OBS03 (f); energy arrivals in OBS08 (c) and OBS17 (g); phase identification for P and S-waves in OBS08 (d) and OBS17 (h): green for P2 and S2, dark blue for P3 and S3, light blue for S4, dark pink for S5, yellow for P4P and S4S, orange for P5P S5S, other colours for multiple. Reduction velocity for a), b), e) and f) is 7.5 km/s and for c), d), g) and h) is 4.33 km/s.

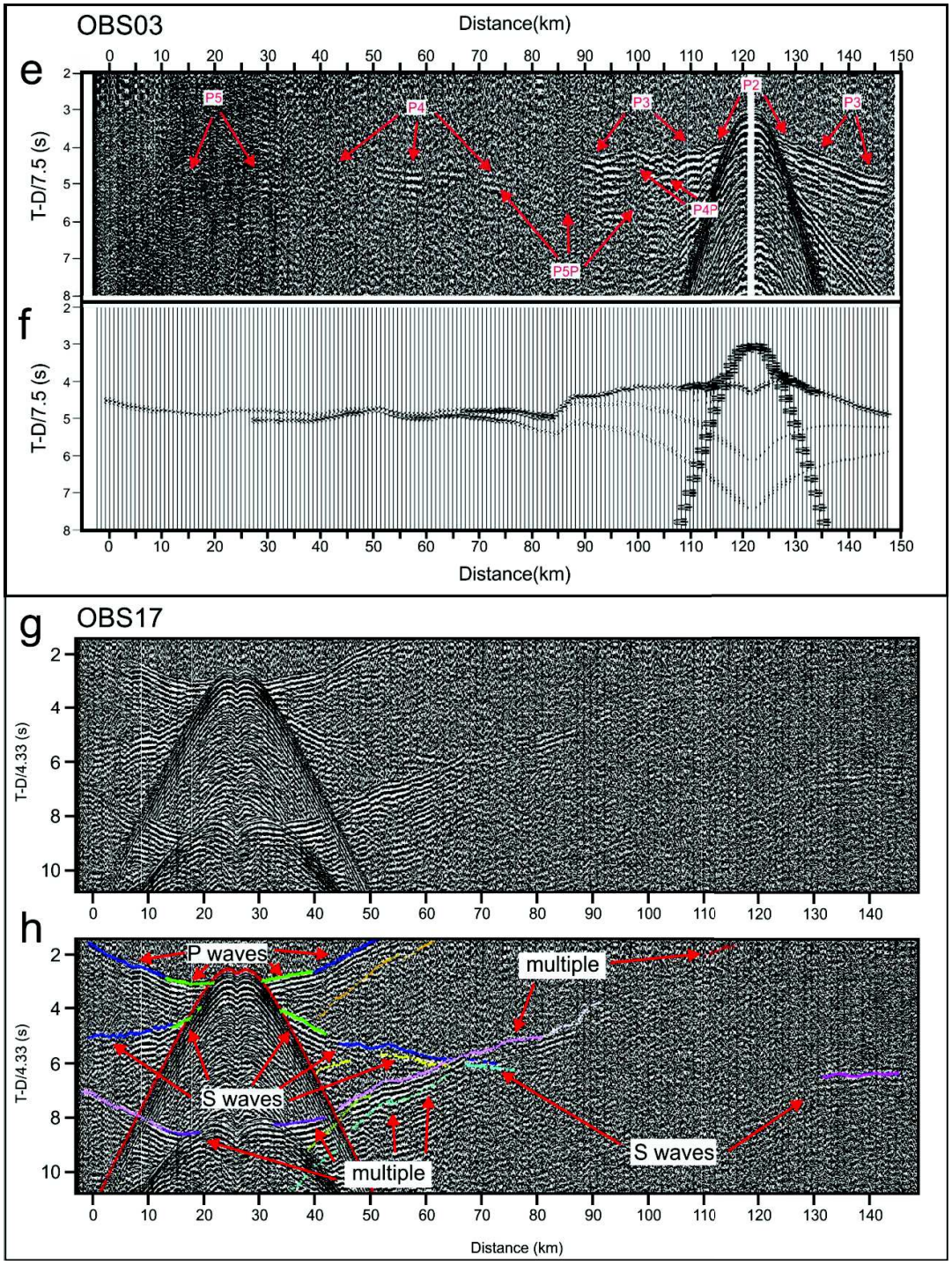

Figure 4.8: (continuation).

Table 4-1: χ 2, TRMS and pick uncertainty values for P velocity model.

Phase	npts	Pick Uncertainty(s)	Trms(s)	χ^2
P2	2466	0.050	0.076	0.575
P3	5583	0.075	0.078	0.610
P4P	1482	0.150	0.067	0.452
P4	1052	0.100	0.091	0.835
P5P	456	0.150	0.141	1.985
P5	1214	0.125	0.139	1.946
All Phases	12253		0.089	0.786

Table 4-2: χ 2, TRMS and pick uncertainty values for S velocity model.

Phase	NPTS	Pick Uncertainty(s)	TRMS(s)	χ^2
S2	1407	0.075	0.111	1.232
S3	3196	0.075	0.118	1.385
S4S	798	0.150	0.119	1.422
S4	758	0.100	0.158	2.489
S5S	1539	0.150	0.125	1.562
S5	642	0.125	0.129	1.668
All Phases	8340		0.123	0.786

A plot of the ray density (Figure 4.9) was performed together with an overview through the number of picks and picks hit by rays to reveal the quality of the model. The ray density plot in the P-wave model shows a good coverage especially between offsets 30 to 120 km. Ray density in the S-wave model shows good coverage mostly in the three top layers. The total number of picks was 12652 and 8496 for P and S models, respectively. The percentage of

picks struck by rays based on the number of observations (NPTS) was 96.8% in the P-wave model and 98% in the S-wave model.

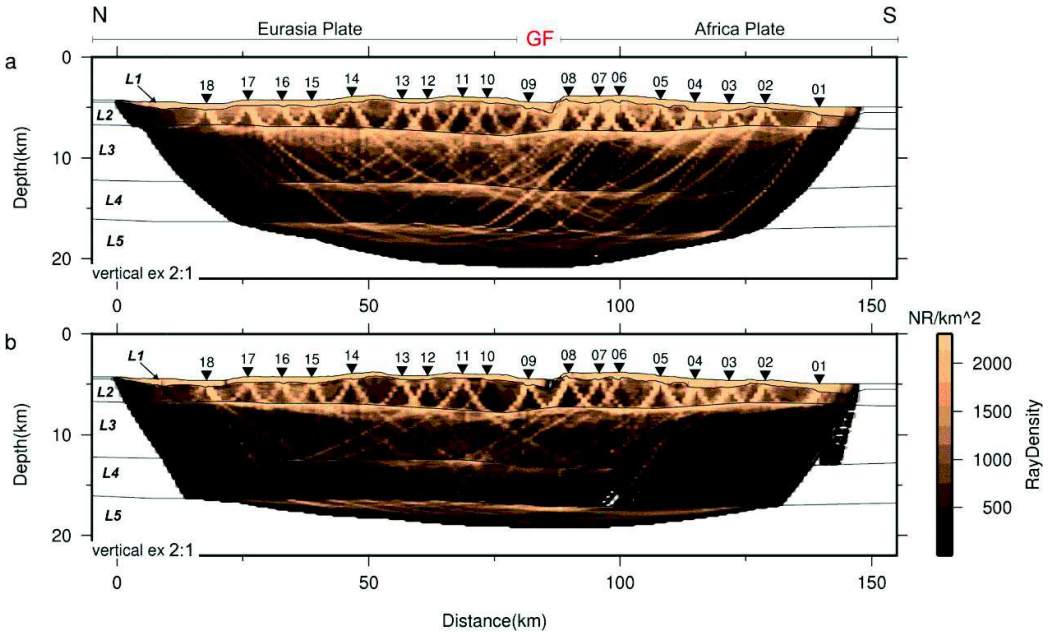

Figure 4.9: Ray density of P and S-wave models. The qualitative representation of the models resolution expressed by the number of rays (NR) per square kilometre: a) P-waves; b) S-waves. GF – Gloria Fault. L1 to L5 – modelled layers.

Pick uncertainty was empirically estimated, considering signal-to-noise ratio and lateral coherency of each phase (Table 4-1 and Table 4-2). Although our principal interest is to estimate the velocity uncertainty, our approach was to estimate simultaneously velocity and depth uncertainty, since keeping depths unchanged biases the estimate of velocity uncertainty. Here uncertainty is taken as an absolute error bound, defined by the maximum allowable fluctuation of velocities and depths that provides a fit to the data that is similar or better than our velocity model does. The absolute error bounds for P-wave and S-wave velocity were estimated by the Monte Carlo approach proposed by Loureiro *et al.* (2016). The thresholds of score, number of rays, χ^2 and Trms were set to a maximum fit quality degradation of 1.1%. We performed a final check of the results using a 95% confidence level Fisher Test on the random models, excluding those that were not able to trace more than 99% of the rays.

There is a trade-off between the velocity/depth band width and the generated number of thresholds conforming models. Therefore increasing unnecessarily the bandwidth implies a useless increase of computing time consumption and shortening it too much implies biased results, towards underestimation of error. To avoid both effects a reasonable definition of the

random model universe for P-wave is required. We set it by trial and error comprising runs with about 2000 models each. These *a priori* uncertainty bounds of velocity and depth were set to 0.2 km/s and 0.6 km for L3, L4 and 0.25 km/s and 0.6 km for L5. A similar procedure was applied to S-wave models, except the *a priori* depth bounds were set equal to the depth error previously obtained for P-wave. These *a priori* uncertainty bounds of velocity were set to 0.12 km/s for layer L3 and 0.15 km/s for layers L4 and L5. To estimate the Poisson's ratio error bounds we applied a first order approach of error propagation to equation [$\sigma = 0.5[1 - 1/(\varphi^2 - 1)]$, where $\varphi = Vp/Vs$]. The obtained results are summarized in Figure 4.10.

Error estimation for P-wave velocities varies between ±0.1 km/s and ±0.4 km/s. For S-wave velocities the error varies between ±0.1 km/s and ±0.35 km/s. For boundary depths the error estimation is ±0.2 km to ±0.6 km. The resulting Poisson's ratio error is ±0.04 for L2, ±0.02 for L3, ±0.015 for L4 and ±0.02 for L5.

The larger errors corresponds to L2, possibly because this is the thinnest of L2 to L5 layers. More important is the fact that when considering error bounds the Vp and Vs values for L4 are still below normal oceanic mantle and Poisson's ratio are still abouve normal oceanic mantel.

4.5.1. Layers velocities and thicknesses

The final models for P-wave and S-wave velocities are shown in Figure 4.11. A description and interpretation of the 5 modelled layers is presented as follows.

Layer 1 (L1) corresponds to the sediments layer that was used to initialize the model. L1 is too thin to produce discernible individual phases (both refractions and basal reflection), so we fixed the L1/2 interface from the MCS and we modelled both layers together. According to the final models the thickest sedimentary sequences are found in the GF M79 basin and further south with 1 km of maximum sediment thickness. Elsewhere along the profile, L1 thickness varies between 500 m and 700 m. Vp varies from 1.8 km/s to 3.4 km/s and Vs varies from 1.0 km/s to 1.9 km/s, at the top and at the base, respectively.

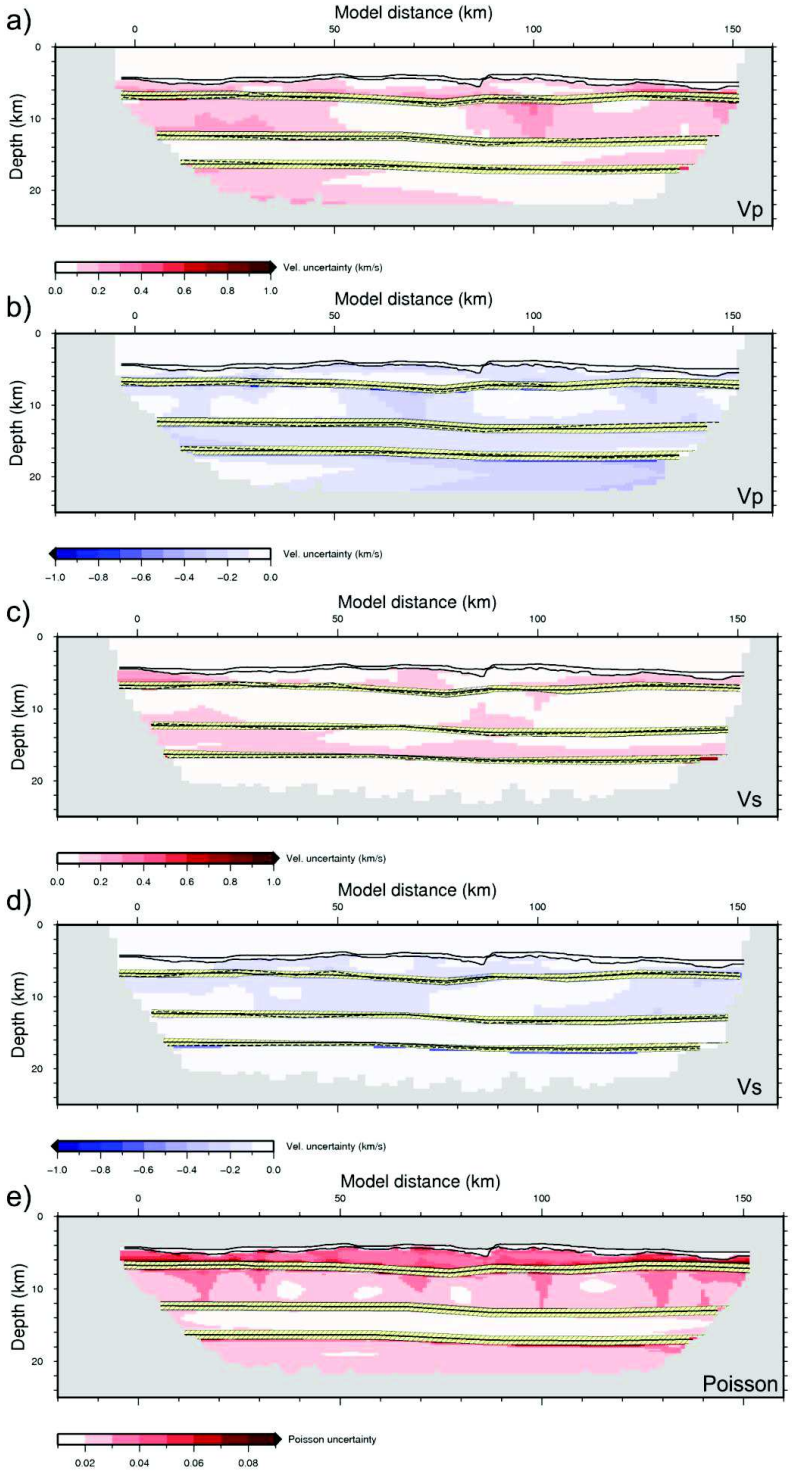

Figure 4.10: Uncertainty for P-wave, S-wave and Poisson's ratio estimated by the Monte Carlo approach; figures a) and c) for positive uncertainty; figures b) and d) for negative uncertainty for P and S-wave velocities respectively; figure e) for Poisson's ratio uncertainty.

Layer 2 (L2) was constrained by phase P2 and S2 representing respectively the P and S refracted waves in it. First arrivals from these waves are clearly identified in all OBS and allowed to characterize L2 thicknesses by varying between 1 km and 3.2 km. The highest thicknesses occur near the GF and decreases towards both ends of the profile. The Vp range is in between 4.5 km/s - 4.7 km/s at the top and 5.6 km/s - 5.8 km/s at the base and Vs ranges between 2.4 km/s - 2.6 km/s at the top and 3.2 km/s - 3.35 km/s at the base.

Layer 3 (L3) was constrained by the diving waves inside it, phases P3 and S3. The refracted waves representing P3 and S3 were well identified in all OBS. L3 shows a mean thickness between 5 km and 5.5 km north of the GF and 6 to 6.4 km south of the GF. These values show that L3 is 20% thicker on the south side of the GF, i.e. in the Africa plate with respect to the Eurasia plate. The Vp ranges between 6.2 km/s and 6.35 km/s at the top and between 6.9 km/s and 7 km/s at the base. For Vs, it ranges between 3.5 km/s and 3.6 km/s at the top and between 3.65 km/s and 3.75 km/s at the base. A small variation on the Vp gradient is observed in the north side, close to the GF. The values of Vs in L3 show that the gradient diminishes from offset 90 km both northwards and southwards until offsets 35 km and 130 km, respectively, increasing again towards both ends of profile.

Layer 4 (L4) was constrained by phases P4 and S4 representing refracted waves inside it and by phase P4P and S4S representing reflected waves on the top of L4. Although the number of the turning way rays in L4 is less than in the remaining layers (as can be seen by the ray density in Figure 4.9) it was possible to identify phase P4 first arrivals in all OBS. S4 was identified in fifteen OBSs by secondary arrivals. P4P and S4S were recognized by secondary arrivals. Thickness, velocities and gradients for both Vp and Vs are constant in this layer. L4 shows a constant thickness of 4 km, a top Vp of 7.1 km/s, a base Vp of 7.4 km/s, a top Vs of 3.75 km/s and a base Vs of 3.9 km/s.

The deepest penetrating arrivals correspond to Phases P5 and S5, which together with the reflected waves with phases P5P and S5S allowed the delimitation of Layer 5 (L5). The energy arrivals for P5 and S5 are weak but it can be identified in seventeen OBSs and in fifteen OBSs respectively. P5P and S5S were the phases with less energy and were identified from secondary waves arrivals. Nevertheless, P5P was identified by fourteen OBSs and S5S was identified by eleven OBSs. L5 was characterized with a top Vp of 7.8 km/s and a top Vs of 4.5 km/s, which correspond to lithospheric uppermost mantle velocities.

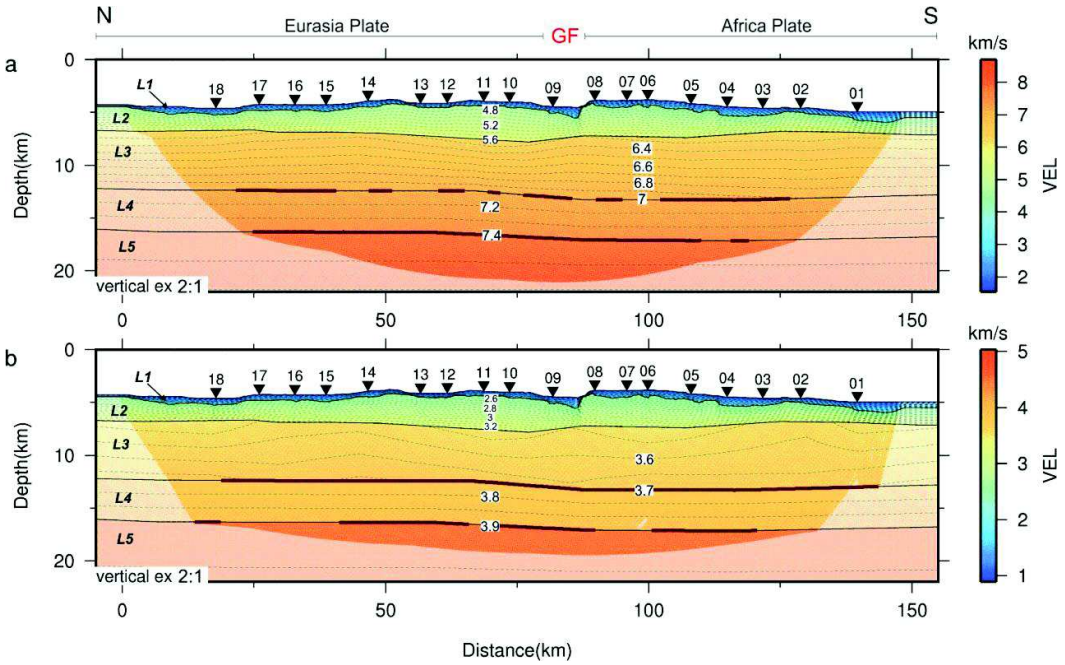

Figure 4.11: Final velocity models: a) Vp model; b) Vs model. GF – Gloria Fault; L1 to L5 – modelled layers. Dark red lines show where the reflected waves are. Contours are spaced 0.1 km/s for the Vp model and 0.05 km/s for the Vs model.

4.5.2. Poisson's ratio

In addition to the Vp velocity structure, the Poisson's ratio (σ) is an important parameter to help constraining the nature of the crust and lithospheric mantle. The Poisson's ratio is computed from the Vp and Vs velocity models by the expression: $\sigma = 0.5[1-1/(\varphi^2 - 1)]$, where $\varphi = Vp/Vs$.

The Poisson's ratio values extracted from the present model allowed for discriminating top and base of L2 and L3 values only. L2: 0.29 to 0.24, L3: 0.27 to 0.3, top and base of the layers, respectively. For L4 and L5 constant values of 0.31 and 0.25 were obtained, respectively. The distribution of the Poisson's ratio in the model is shown in Figure 4.12. There is a sharp lateral variation of the Poisson's ratio in L2 between offsets 80 and 90 km, i.e. across the GF. South of the GF L2 Poisson's ratio varies between 0.27 and 0.26 (top and bottom of the layer) in opposition to the north side of the GF where values vary between 0.29 and 0.24.

The lateral variation of the Poisson's ratio in L3 across the GF is not sharp; it is distributed across a 10 km long segment, between offsets 80 and 95 km, approximately, with higher values on the southern flank of the GF, in the Africa plate. The largest lateral variation of

Poisson's ratio in L3 is observed between offsets 20-80 km showing two negative and positive peaks.

The lateral variations of the Poisson's ratio across the GF within L2 and L3 are consistent with the existence of a fault region until at least the base of L3 and different rheological behaviour of the Africa and Eurasia plates at the GF.

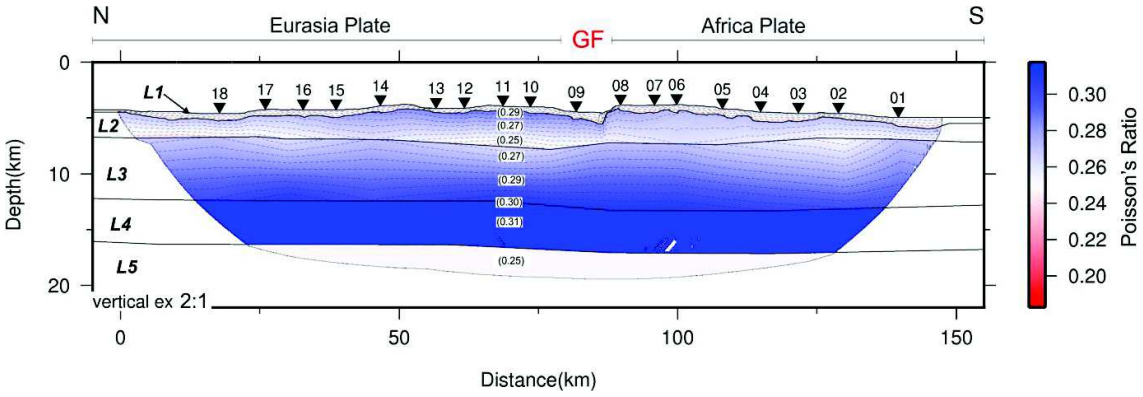

Figure 4.12: Poisson's ratio model obtained from Vp and Vs models; L1 to L5 – modelled layers; Poisson's ratio contours are spaced 0.005.

4.5.3. Gravimetric model

To help constraining the crustal structure and its nature, the Vp velocity model was converted to densities using the relation proposed by Zelt & Ellis (1988). To account for the vertical and lateral variation in Vp velocity the model is divided into blocks and the density is estimated from the average velocity inside each block (Figure 4.13a). The general density values computed from the seismic P-waves model on the GF were: between 2.53 and 2.55 g/cm^3 for L2; between 2.83-2.85 g/cm^3 for L3; 3.03 g/cm^3 for L4; 3.26 g/cm^3 for L5. The theoretical free-air gravity anomaly is then compared to a series of parallel profiles that are chosen to represent the average gravity response along the profile. We consider the central free air anomaly profile along the GF profile and eight free air anomaly profiles with an interval distance of 1, 3, 5 and 10 km to east and west of the GF profile were extracted from the WGM2012 global model (Bonvalot, 2012). To reach the best fit between observed and calculated profiles (Figure 4.13b) the density of L5 was changed to 3.28 g/cm^3 from offset 67 to 87 km and 3.3 g/cm^3 from offset 87 to 150 km. The analyses of those values are made further in text.

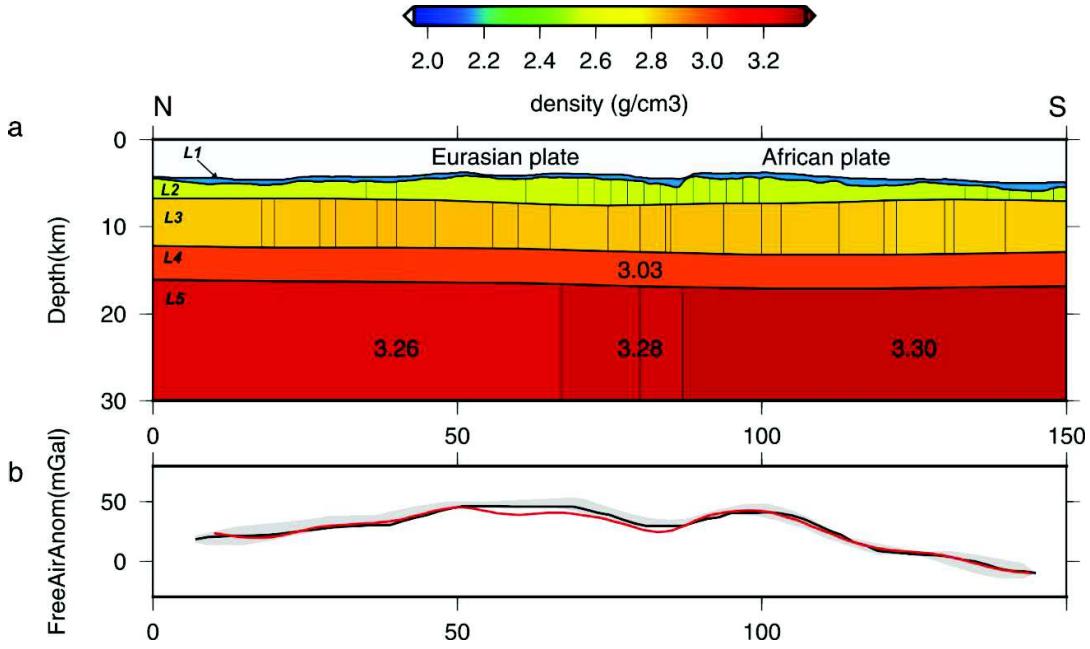

Figure 4.13: Gravimetric model and density values from Zelt software: a) modelled density values; L1 to L5 – modelled layers; b) calculated anomaly from GF model represented by red line; free-air anomaly above the GF profile represented by black line; grey shape represent the compilation of the profiles extracted with an interval distance of 1, 3, 5 and 10 km to east and west of the GF profile.

4.6. Discussion

4.6.1. Recent tectonics

As it turned out from the analysis of the MCS profile w51 (Figure 4.3) the differences in the bulk sedimentation and tectonic deformation between the north and south sides of the GF, i.e. between Eurasia and Africa plates are evident. The northern side of the GF shows evidences of minor tectonic movements whilst the southern GF side has accommodated most of the deformation associated with the GF strike-slip tectonic movement. The strike-slip tectonics is compatible with the steep fault planes observed in Figure 4.3. The Africa plate basins reveal higher sediment thickness than the basins in the Eurasia plate which can be explained by the age difference (~20 My) between the two plates.

The concentration of Neogene to recent tectonic deformation in the Africa plate suggests that this block can be softer than the northern block of the GF. Since the Africa plate is older it should also be colder and more rigid unless some thermal or metasomatic mechanism has occurred. The hotspot–like volcanism that occurred in Miocene to Present times in the MTR is restricted to the Africa plate (Geldmacher *et al.*, 2006, Merle *et al.*, 2006). Compressive tectonics of Pliocene-Quaternary age in the Madeira Abyssal Plain was reported by (Roque *et al.*, 2009), another indication of recent deformation in the oceanic crust in the Africa plate.

4.6.2. Compositional models

Analysis of Vp, Vs, Poisson's ratio and density models gives a first indication regarding the composition of the modelled layers. Considering the overall thickness values of L1 (<1 km) and the velocity values of L1 (1.8 km/s at top and 3.4 km/s at base which are too high to be accounted by sediments only (Christensen, 1978, Christensen & Salisbury, 1975)) we assume it comprises both pelagic sediments and basaltic flows, possibly a volcanic sedimentary complex. This is in good agreement with the interpretation of the MCS profile where we observed that the top unit U1 corresponds to sediments (continuous well layered reflections) and U2 shows acoustic character in accordance with basaltic flows or a volcanic-sedimentary complex (discontinuous reflections).

Thickness and velocities of L2 (1 to 3.2 km and 4.5 km/s - 4.7 km/s at the top and 5.6 km/s - 5.8 km/s at the base) are both within the values observed for basaltic composition normally referred as oceanic crust layer 2. The density and the Poisson's ratio values obtained in the model are within the range of values compiled by Christensen (1996) for oceanic crust layer 2 (Figure 4.14) except for a narrow low Poisson's ratio band at the base of L2. Inspection of Figure 4.12 shows a low Poisson's ratio (0.24) band at the base of L2 where normally a value of 0.28 is expect as described by Purdy (1983). This could be explained by the existence of thick cracks in the interface between upper and lower young oceanic crust which is responsible for a low Poisson's ratio (0.24), as suggested by Shaw (1994).

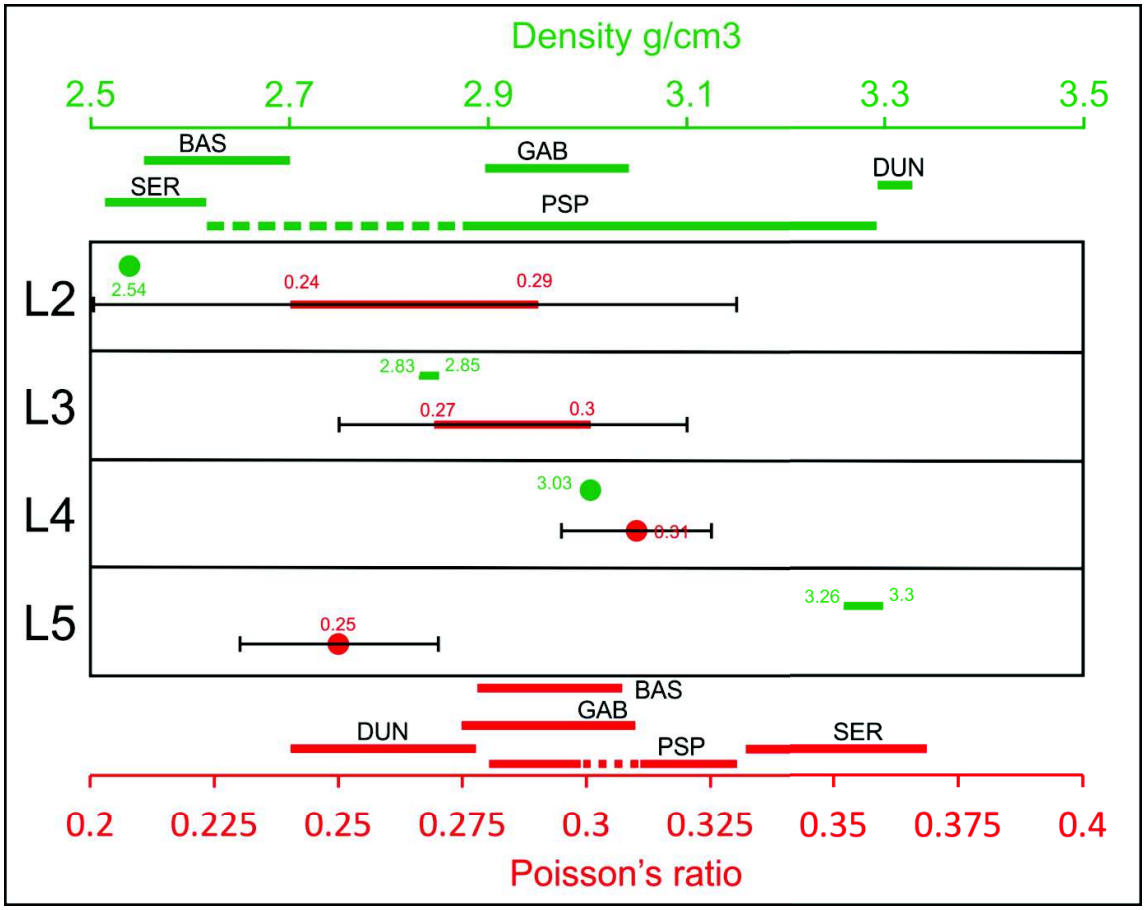

Figure 4.14: Comparison between the obtained density and the Poisson's ratios values in the various layers of the GF model and common oceanic rock values: BAS-Basalt; GAB-Gabbro; DUN-Dunite; SER-Serpentinite; PSP-Partial Serpentinized Peridotite. In green the density values and in red the Poisson's ratio (error bars in dark) values obtained for L2 through L5. Rock values ranges taken from the compilation of Christensen (1996). Dashed green and red PSP line reports to values taken from measurements made by Christensen (1978) in ophiolites. Values are for 200ºC temperature and 200 MPa pressure.

The thickness and Vs values obtained for L3 (5.5 - 6 km and 3.5 - 3.75 km/s respectively) are in agreement with a gabbroic composition for the oceanic crust Layer 3 (3.4 - 6.3 km and 3.3 - 4.0 km/s respectively) (Christensen & Salisbury, 1975), whilst the Vp velocity values are slightly lower (6.2 - 7.0 km/s compared to 6.3 - 7.2 km/s). This difference is small and inside the error band yet, it may be indicative of a compositional modification. The lateral variation of the Vp and Vs velocity gradients can also indicate compositional variability (Figure 4.11).

In Figure 4.14 we see that the Poisson's ratio for L3 is within the values for gabbro composition contrarily to the density value (2.83 to 2.85 g/cm^3) that is lower than what is expected for gabbro, which may be also indicative of compositional modification. These

deviations could result from partial hydration within L3. Alternatively, it should be noted that the presence of olivine cumulates would shift both density and Poisson's ratio values on an opposite direction.

L4 shows velocity values that can be found in rocks at the base of the lower crust and also at the top hydrated lithospheric mantle, according to (Christensen, 2004, Christensen, 1996).

The density value for L4 matches with the gabbro range values from Christensen (1996) but the Poisson's ratio allow suggesting a gabbroic composition or partially serpentinized upper lithospheric mantle (Figure 4.14). It is known from the ophiolite studies (Christensen & Salisbury, 1975, Dilek, 2003) that cumulate gabbros can occur in the lower part of L3 resulting in compressional waves velocities of 7.0 to 7.4 km/s. It supports the idea of enrichment in olivine in the lower crust as a result of underplating, as discussed in Walther (2003). On the other hand, partial (~50%) serpentinized peridotite formed as a result of hydration of the upper lithospheric mantle can also show Poisson's ratio, compressional and shear wave velocities as the ones found in L4 (Carlson & Miller, 2003, Christensen, 2004, Miller & Christensen, 1997).

L5 values (velocity, density and Poisson's ratio) point to normal upper mantle values. The difference in density between the Eurasia (3.26 to 3.28 g/cm^3) and Africa (3.3 g/cm^3) upper mantle results from the adjustment done to the density values in order to obtain a good fit in the gravity model (Figure 4.13). This difference in density can be explained by the difference in age between the two plates, i.e. a higher density for the oldest Africa plate (80 My) and a lower density for the younger Eurasia plate (60 My). Alternatively, this density difference can arise from different lithospheric mantle compositions of the two plates.

4.6.3. Comparison with other models

In order to cover all different domains across the GF study area, eight velocity profiles were extracted at offsets 20, 40, 60, 70, 80, 86, 100 and 120 km (Figure 4.15). Only the non-sedimentary section is considered in the following discussion. All these profiles show a similar pattern of velocity distribution in depth. Between profiles each layer shows similar velocity gradient and velocity jump at its top and base. If layer 5 represents the non-altered upper mantle, then the overall magmatic crust has an average thickness of 12 km, which clearly exceeds in 5 km what is expected for oceanic crust formed at intermediate spreading

velocities (Bown & White, 1994). It is clear that the difference lies in the seismic layer L4. In order to facilitate the interpretation of the Vp velocity models obtained for the GF profile, we make a comparison with other models obtained in the Atlantic for normal oceanic crust (NOC), fracture zones and oceanic crust affected by a plume as given by White *et al.* (1992) (Figure 4.16). In addition we consider also for comparison the velocity profiles from the Josephine seamount by Peirce & Barton (1991), approximately 700 km to the east of the study area (see Figure 4.1 for location).

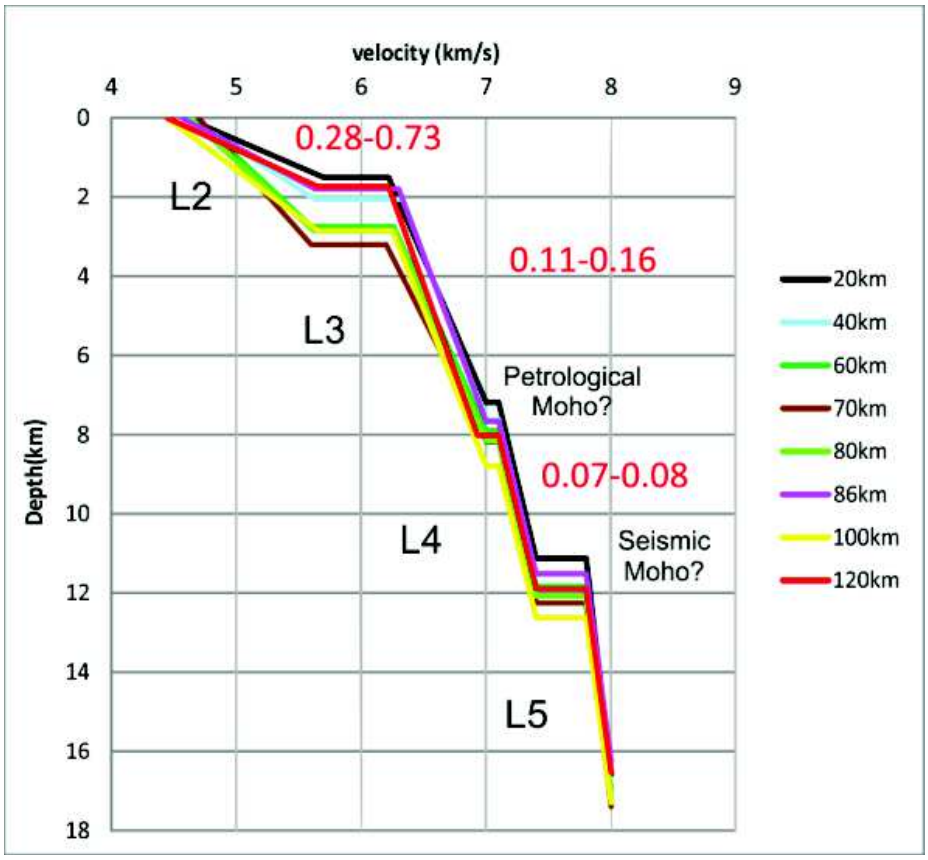

Figure 4.15: Velocity profiles along the model taken at offsets shown at the right side of the figure. Red values show gradient interval for L2, L3 and L4 (km/s/km).

The analysis of the profiles in Figure 4.15 raises two questions considering what has been discussed, where is the petrological Moho and what is the nature of L4?

The oceanic lithosphere of the study area encompasses a fracture zone that re-works an old scar of a transform fault and some similarity with the profiles from other fracture zones in the world was expected. However, when comparing velocity-thickness profiles of the GF oceanic

lithosphere with other from fracture zones worldwide (sea compilation in White *et al.* (1984)), we conclude that the study area does not match the thickness values normally observed in these tectonic environments (Figure 4.16b). The thickness of the crust in these environments is in general between 2 and 5 km, which is less than the thickness of L2 and L3 of the GF model where a range of values between 7 and 9 km (with an average of 7.5 km) is observed.

This discrepancy can probably result from the fact that most of the examples in White *et al.* (1984) are from transform faults that lie close to oceanic ridges. In these areas the oceanic crust formation is dominated by two main processes (White *et al.*, 1984): i) interaction of the cold lithosphere with the spreading centre that leads to the accretion of a thin igneous section; ii) the amount of magma available to feed a spreading ridge segment is not enough to feed the transform segments as well, thus generating a lateral reduction in magma supply. These processes imply the existence of an abnormally thin crust in the order of 3 to 5 km. This is not what we observe in the profiles from the GF area, where the lithosphere is much thicker and older, of Lower Paleogene and Upper Cretaceous in the Eurasia and Africa plates, respectively (see Figure 4.1).

When compared with the profiles for the NOC it is clear that the GF profiles do not match with them (Figure 4.16a). The NOC layer 3 thickness is similar to GF L3, although the velocities of the latter are systematically slightly lower. This could argue for a slight amount of hydration of L3 gabbros possibly through partial serpentinization (olivine hydration).

Comparison of NOC's lithospheric mantle with L4 and L5 shows that L4 has considerable lesser velocities with respect to NOC's mantle, while L5 has velocities similar to NOC's mantle. If we consider that L3 and L4 correspond to lower crust (layers 3A and 3B) this would mean that the GF lower crust is 8 km, i.e. abnormally thick when compared with NOC's (~5 km, Figure 4.16a).

This would suggest an over-thickening of the GF lower crust similar to what has been observed in oceanic crust affected by a plume (Figure 4.16c), such as the crust formed in hotspots or Large Igneous Provinces is thicker than the NOC (Korenaga *et al.*, 2002).

However, a plume-like setting is not observed in the GF area unlike in the Azores plateau or MTR, which leaves L4 to be classified as possible altered upper mantle. However, it is worthwhile noting that a compilation by Walther (2003) reports values for layer 3B with 7 km/s top and 7.4 km/s base velocities, which are in the range of the velocities obtained in layer 4 of our model.

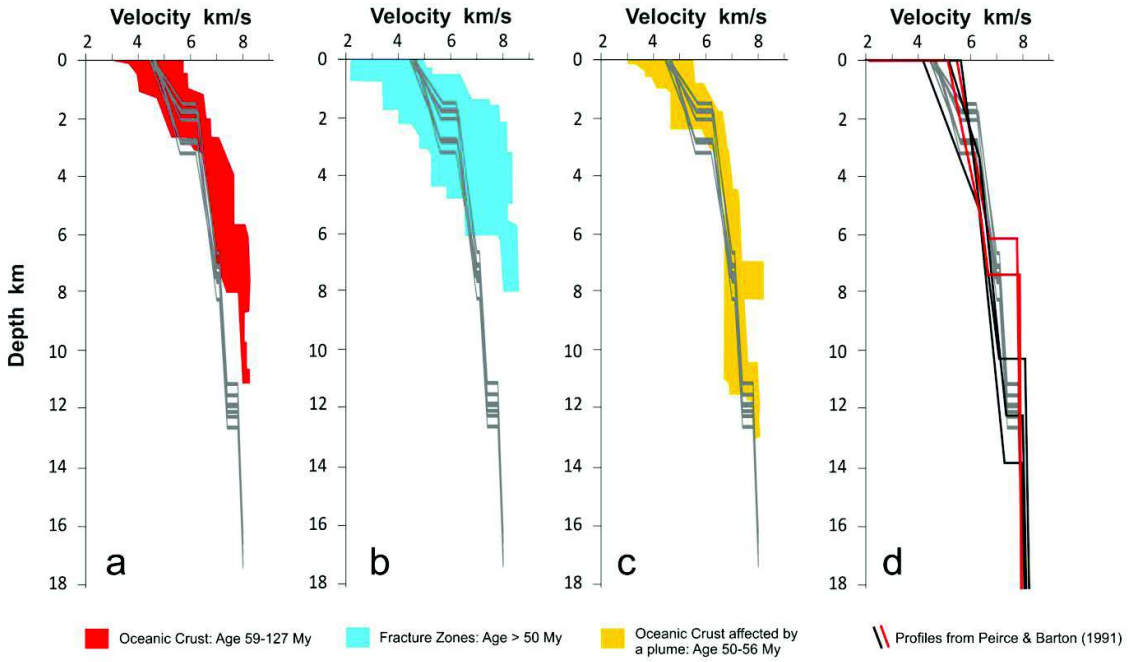

Figure 4.16: Comparison between velocity profiles from the GF model (grey profiles) and a compilation made by White *et al.* (1992) from different oceanic environments; a) for typical oceanic crust (red area); b) oceanic crust in fracture zones (blue area); c) for oceanic crust affected by a plume (yellow area) and d) a comparison of the velocity profiles from GF (grey profiles) and Josephine seamount profiles (black profiles from thickened oceanic crust and red profiles from typical oceanic crust) from Peirce & Barton (1991).

Similar evidences are shown in the velocity profiles (black profiles in Figure 4.16d) across the Josephine seamount (see Figure 4.1 for location, Peirce & Barton (1991)) where the velocity and thickness of the crust are similar to GF L2+L3+L4 values. According to these authors there is an enrichment of the lower crust that causes an increase of the layer thickness possibly by intrusion of igneous material to its base when the lithosphere was at or near the mid-ocean ridge. However, the MTR has a very different geological setting with respect to the GF. The MTR is a 1100 km long ridge striking parallel to oceanic magnetic anomalies and contains various volcanic edifices with ages spanning from approximately 110 My to Quaternary (Geldmacher *et al.*, 2006, Merle *et al.*, 2006). The MTR has been interpreted as a structure formed at the Mid-Atlantic Ridge during a period of enhanced volcanism. Later, in Neogene times, the MTR has interacted with hot spot activity (Geldmacher *et al.*, 2006).

It is recognized by some authors (Francis, 1981, Horen *et al.*, 1996, Lowell & Rona, 2002, Guillot *et al.*, 2015) that hydrothermal circulation in slow spreading ridges penetrates in the upper mantle providing the conditions for partial serpentinization of the peridotite mantle rocks. This process can penetrate deeper within fracture zones and can be active for tens of

millions years as showed by Potts *et al.* (1986) in their study of the Tydeman fracture zone (see Figure 4.1 for location) where hydrothermal circulation has persisted for at least 70 My. It has also been shown that fluid flow at Late Jurassic oceanic crust occurs along the transcurrent Africa-Eurasia plate boundary at longitude ~9ºW (Hensen *et al.*, 2015).

The Gloria Fault area investigated here formed as a transform fault during the opening of the Atlantic Ocean and developed as a fracture zone. In present day behaves as an active dextral strike-slip fault that defines the transform plate boundary between Africa and Eurasia. Instrumental seismicity with M>7 to M8.4 events is a strong evidence for large rupture along the GF that could enhance the conditions to produce long lived hydrothermal circulation contributing to the formation of a layer with serpentinized peridotite.

However, the values of Vp, Vs and Poisson's ratio in L4 of GF model do not point to a total serpentinite composition. The combination of Poisson's ratio and density values does not unequivocally point towards partial serpentinization, only. These values are also compatible with gabbro composition, suggesting that gabbro intrusives can occur within the peridotite material.

A comparison of the Vp, thickness and velocity gradient of L4 with a compilation of intermediate bodies between lower crust and upper mantle from Watremez *et al.* (2011) shows that L4 does not match either with serpentinized upper-mantle or with a Mafic Body. While the thickness and gradient of L4 are in agreement with the values for serpentinized upper-mantle the Vp values are consistent with a presence of a Mafic Body.

These observations from the GF study area suggest that the nature of L4 may be not uniform. L4 can be constituted by a miscellaneous of lithologies, such as serpentinite, gabbro and peridotite. The relation Vp/Vs ratio versus percentage of serpentinization proposed by Christensen (2004) indicates that a 40% to 60% of serpentinization of the upper mantle can be assigned to the L4 nature and is compatible with a density value of 3.03 g/cm^3.

The Southern Troodos Transform Fault zone, which can be considered a natural analog for the GF region displays a complex geologic composition, not only in what regards tectonics but also in what respects the lithotypes and their distribution in the field. Actually, peridotites, serpentinites intruded by gabbro outcrop near this transform fault (Gass *et al.*, 1994).

The lithological complexity of Layer 4 could be explained as:

i) a result of underplating caused by a mantle plume at the triple junction at a (~60 My ago) causing thickening and enrichment (probably in olivine) at the base of the lower crust (similar

to what has been observed at large igneous provinces by Korenaga *et al.* (2002) and/or an extra hydrothermal circulation that generated partial serpentinization of the upper lithospheric mantle or;

ii) mantle hydration resulting from deep water circulation into a heavily fractured lithosphere associated with the Africa-Eurasia plate boundary fracture zone, a process similar to what occurs at the mid-ocean ridges as reported by Grevemeyer *et al.* (1998) and Bartetzko (2005).

We favour the second hypothesis due to the i) obvious morphologic, geologic and seismicity evidences that indicate that the GF is liable to have been accumulating fracturing from upper mantle to the surface, probably creating pathways for fluid migration and pumping mechanisms and ii) lack of morphologic evidences associated to plume activity.

4.7. Conclusions

The following direct conclusions result from the above presented results and discussion:

i) Tectonic deformation as revealed by multichannel seismic reflection is asymmetrically distributed as it concentrates on the southern flank of the GF, i.e. the Africa plate. This is consistent with different rheology of the two plates as shown by the lateral variation of the Poisson's ratio in L2 and L3.

ii) The crust and uppermost lithospheric mantle of the studied segment of the GF is subdivided into 5 layers, from top to bottom, L1: sediment and volcanoclastic layers; L2: upper crust; L3: lower crust. L4: partially hydrated mantle or olivine enriched lower crust. L5: uppermost lithospheric mantle; L2+L3+L4 have total thickness of 12 km, which is above average by 7 km.

iii) L4 probably constitutes a complex layer consisting of partially hydrated mantle intruded by gabbro being an analogue of the onshore exposed oceanic mantle fracture zones such as the Southern Troodos Transform Fault Zone.

It is further concluded that the velocity/compositional model of the Gloria Fault upper lithosphere does not fit either normal oceanic lithosphere nor fracture zones older than 50 My (cf. Figure 4.16).

Mantle hydration within L4 results from important and deep secondary porosity (fracturing) allowing mantle hydration from 8 km into the mantle associated with unusual high magnitude

seismicity. This is in line with the findings of deep sea water convection in Jurassic age oceanic lithosphere further west (Hensen *et al.*, 2015).

Since serpentinized mantle is considerable weaker than ordinary mantle this mechanism along a trans-oceanic fracture zone bears important implications on the propagation of tectonic deformation into the deep oceanic domains. Authors have argued on the possibility of driving subduction initiation into Atlantic-type oceans along fracture zones (Mueller & Phillips, 1991, Duarte *et al.*, 2013).

5. CHAPTER 5 – CRUSTAL STRUCTURE AND TECTONICS ACROSS THE SÃO MIGUEL ISLAND

Preliminary list of authors: L. Batista; C. Hübscher; P. Terrinha; L. Matias; A. Afilhado

(This chapter is present in a paper format since it is being prepared to be submitted to an international science journal)

Abstract

The Azores islands and plateau have been mostly studied from the kinematic, neotectonic, vulcanological and geochemical points of view. This study aims at complementing the many previous ones adding knowledge to the crustal structure. This is achieved by acquisition, processing and interpreting a seismic refraction profile across the São Miguel Island.

The 160 km long seismic refraction profile shows that São Miguel island edifice is made up of 5 crustal layers, including a 1500 m thick sedimentary basin and a Moho discontinuity at a depth 15 km underneath the island and at 10 km in the distal parts. The crustal region, under the volcanic edifice, shows a complex pattern of velocities distribution and a lens-shaped layer with 2.5 km of maximum thickness and velocities less than 7.6 km/s that accounts for the existence of different crustal material that results from magmatic underplating.

1. Introduction and goal

The Azores Plateau (AzP) is a bathymetric high of volcanic origin defined by the 2000 m isobath, straddling across the Azores Triple Junction (ATJ), Mid-Atlantic Ridge (MAR) in the North Atlantic (~38ºN) and the Eurasia, Africa and North America lithospheric plates. It is limited by the East Azores Fracture Zone (EAFZ) to the south and the Terceira Rift (TR) to the north. The AzP extends westwards across the MAR into the North America plate where two of the nine islands are located (Figure 5.1). The islands in the Eurasia plate are located along volcanic ridges controlled by tectonic grabens (Figure 5.1). São Miguel is one of the nine islands and is located in the Eastern part of the TR.

Authors (Grevemeyer, 1999, Gente *et al.*, 2003, Beier *et al.*, 2006) agree that the elevation of the AzP results from over thickened crust that resulted from enhanced magmatic accretion. However, the tectonic invoked mechanisms are various, i) active oceanic rifting controlling magma ascent, ii) hot spot driven magmatic ascent or iii) the interplay of these two mechanisms.

Historical and Holocene volcanism, together with active seismicity and GPS measurements attest for the intense tectonic and magmatic activity of both the AzP and ATJ. The São Miguel island was developed during the last 1Myr inside the active Terceira Rift (Sibrant *et al.*, 2015). It shows historical volcanism (Figure 5.2), a diffuse seismicity cluster (Figure 5.4) located in its central part and widespread mass transport processes off the southern part of the island (Weiß *et al.*, 2015).

The crustal structure of the AzP has been investigated based on gravimetric modelling and 1D rheological modelling from seismicity data. These methods do not allow for the rigorous definition of the crustal structure along transects cutting across the main tectonic fabrics of the AzP, such as the tectonically and magmatically active Terceira Rift.

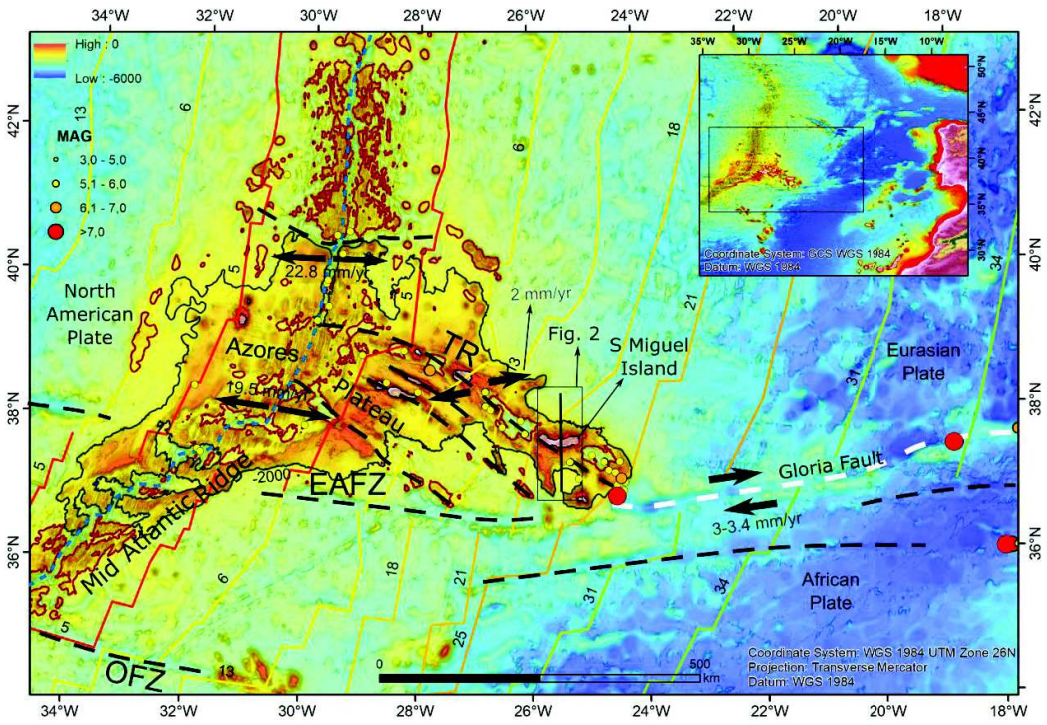

Figure 5.1: General map with the study area identified by the black rectangle and the seismic data acquisition by the black lines over São Miguel Island. Isochrones from Müller *et al.* (2008). Bathymetry from the EMODnet project (www.emodnet-bathymetry.eu); Red contours for the -2000 m isobaths; Grey contour for the -2000m isobaths bounding the AzP; TR- Terceira Rift; EAFZ- East Azores Fracture Zone; GF- Gloria Fault; OFZ- Oceanographer Fracture Zone; MAR and TR relative plate motion from DeMets *et al.* (2010), Gloria Fault slip rate inferred by Neres *et al.* (2016).

The main goal of this work is to contribute to better understanding the crustal structure across the Terceira Rift that is the most recent magmatic accretion structure of the AzP and the most active, from both tectonic and seismicity point of views. This study produces the first model of the crustal structure across the São Miguel Island based on an active seismic experiment using air guns shooting as energy source and 18 Ocean Bottom Stations distributed along two profiles, north and south of the São Miguel Island, with a total length of 160 km. Complementary information from multichannel seismic reflection profiles cast new light on near shore mass transport processes on both north and south coasts of the island. By doing this we also aim to contribute to better understand of the tectono-magmatic mechanisms that lie at the origin of the AzP, the source of the seismicity cluster of São Miguel Island and show the impact of the latter on the triggering of mass transport processes.

5.2. Geological setting

Inspection of the ages of the magnetic anomalies show that the age of the oceanic crust that comprehends the AzP to the east of the MAR (Chron 21, 45.9 - 45.1 Ma) are considerably older than the age of the Azores Islands (6 My for the oldest island) (Figure 5.1).The first reference for the initiation of the Azores triple point was first proposed by Krause & Watkins (1970) that proposed the age of 45 Ma. Later, Luis *et al.* (1994) refer a northward migration for the triple junction between 10 to 3.85 Ma and that the AzP behaved as an independent block during this time. The same authors argue that since 2.45 Ma the AzP moved together with the Eurasia plate.

Lourenço *et al.* (1998) concluded that the AzP is tectonically controlled by NW-SE trending lineation (N120º and N150º) expressed by elongated islands and/or submarine seamounts. The NE of this combination is the Terceira Rift that comprises the Graciosa, Terceira and São Miguel islands. The authors also suggest that the AzP is acting simultaneously as oblique ultra-slow spreading centre and as a transfer zone that accommodates differential shear movement between Eurasia and Africa plates. Global Kinematic models imply for the motion in the Azores boundary a right lateral transtensional regime along the Eurasia-Africa boundary with rates of 2 to 4 mm/y (Figure 5.1) (Miranda *et al.*, 2015 and references inner, DeMets *et al.*, 2010, Luis *et al.*, 1994).

The shape of the western part of the São Miguel Island follows the NW-SE trend of the TR. The central and east part is parallel to the E-W direction (Figure 5.2). The neotectonic faulting is compatible with NE-SW main extension in a dextral larger scale transtensional shear zone, the TR (Figure 5.2B). The oldest part of the island is located in the east (Volcanic zone 6 in Figure 5.3) with a volcanism age between 850 and 750 ka (Sibrant *et al.*, 2015). The most recent volcanic activity was at the western border of the island (volcanic zone 1 in Figure 5.3).The main volcanic rocks are of basaltic and trachytic compositions. Seismicity is in general of low magnitude (< M4) and shallow depth (< 15m km, Figure 5.4 and Figure 5.5) and the most recent seismic events occurred in the south central area of the island (in Gaspar *et al.*, 2015).

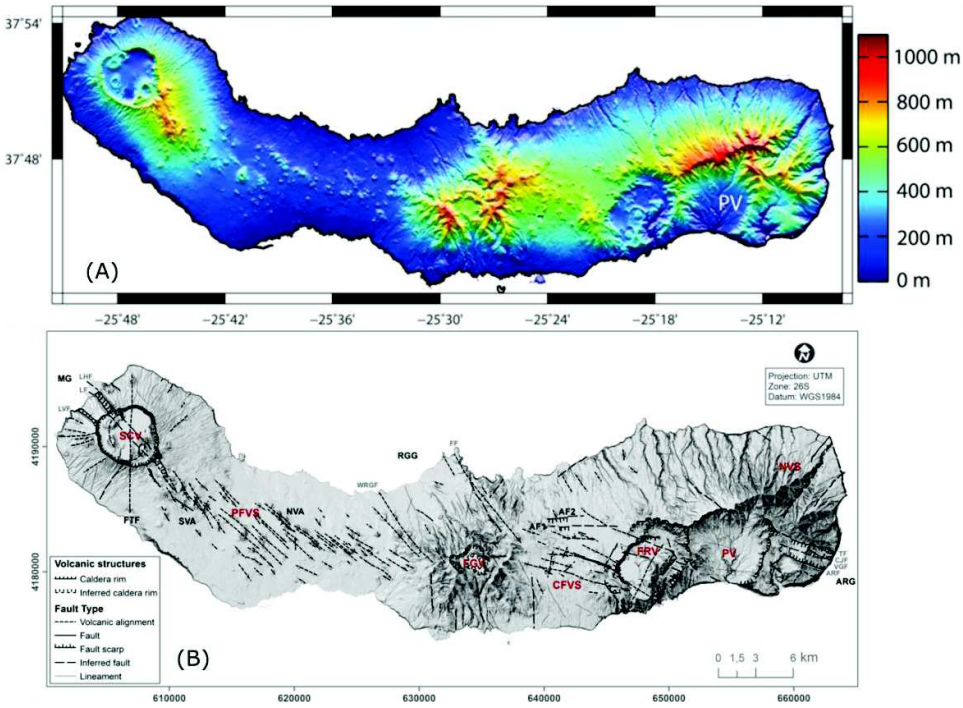

Figure 5.2: São Miguel Island. A) Topographic map tacked from Miranda *et al.* (2015). B) Neotectonic map tacked from Madeira *et al.* (2015); MG, Mosteiros Graben; LVF, Lomba do Vasco Fault; LF, Lombinha Fault; LHF, Lomba dos Homens Fault; FTF, Feteiras Fault; SVA, South Volcanic Alignment; NVA, North Volcanic Alignment; RGG, Ribeira Grande Graben; WRGF, West Ribeira Grande Fault; FF, Falca Fault; AF1, Altiprado Fault 1; AF2, Altiprado Fault 2; ARG, Água Retorta Graben; ARF, Água Retorta Fault; VGF, Vale Grande Fault; CJF, Cú de Judas Fault; TF, Tronqueira Fault; SCV, Sete Cidades Volcano; PFVS, Picos Fissural Volcanic System; FGV, Fogo Volcano; CFVS, Congro Fissural Volcanic System; FRV, Furnas Volcano; PV, Povoação Volcano; NVS, Nordeste Volcanic System.

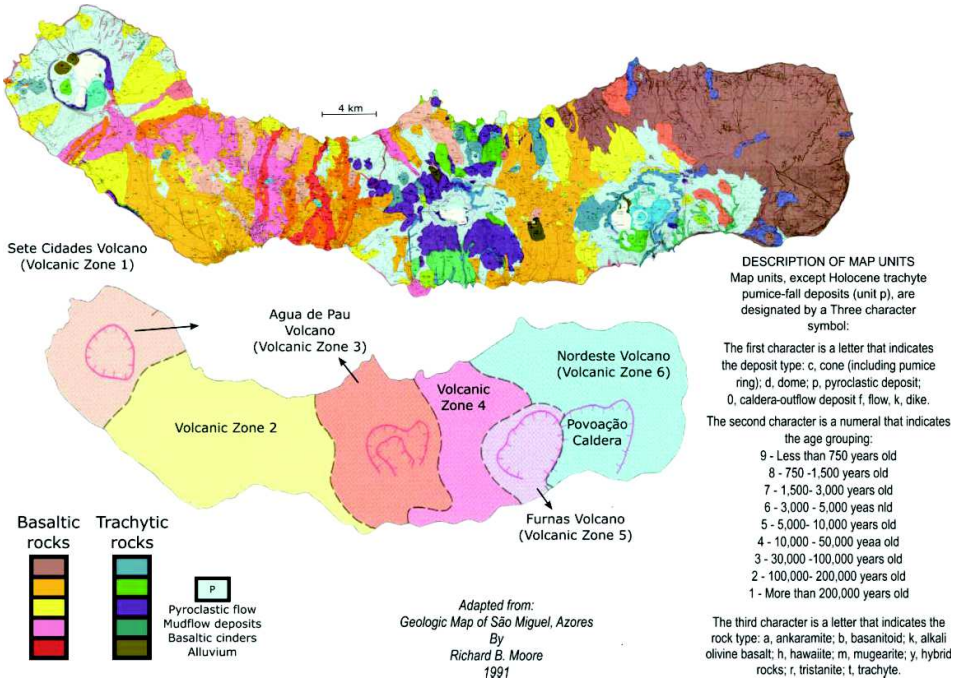

Figure 5.3: Geologic Map of São Miguel adapted from Moore (1991).

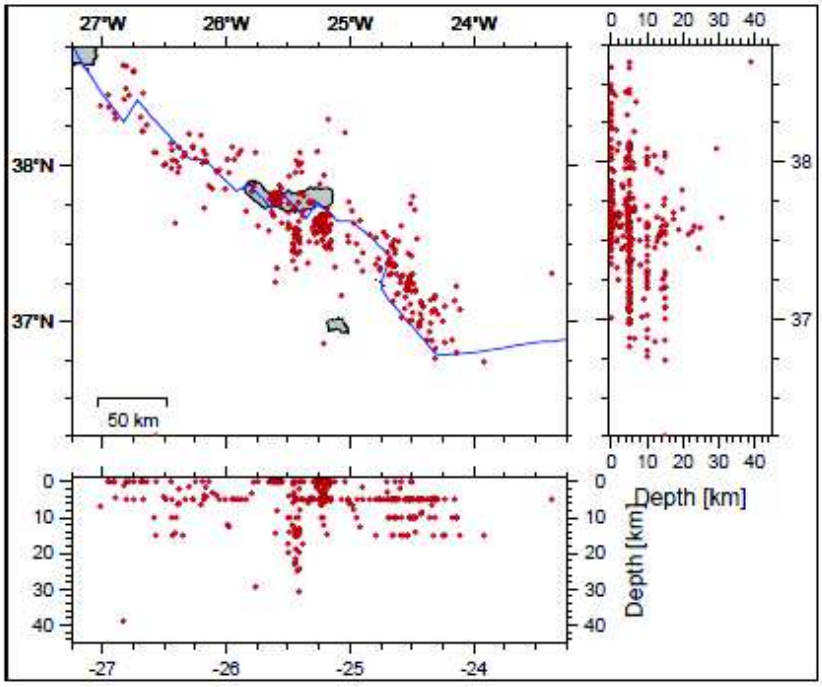

Figure 5.4: Seismicity around São Miguel Island from April to August 2009 with magnitude greater than 0.9 from Golebiowski (2012).

5.3. Data

A north-south wide-angle refraction data profile across the São Miguel island was acquired during the METEOR cruise M79-Leg2 (Hübscher, 2013). Eight OBS's on the north side of the island, ten on the south side and nine land stations performed a 160 km seismic refraction profile (Figure 5.5). Two 32 l BOLT air guns with 120 bar shooting air pressure were used as energy source for this OBS experiment. The OBS separation was approximately 8 km. More details on the wide-angle refraction seismic survey can be found in Hübscher (2013)

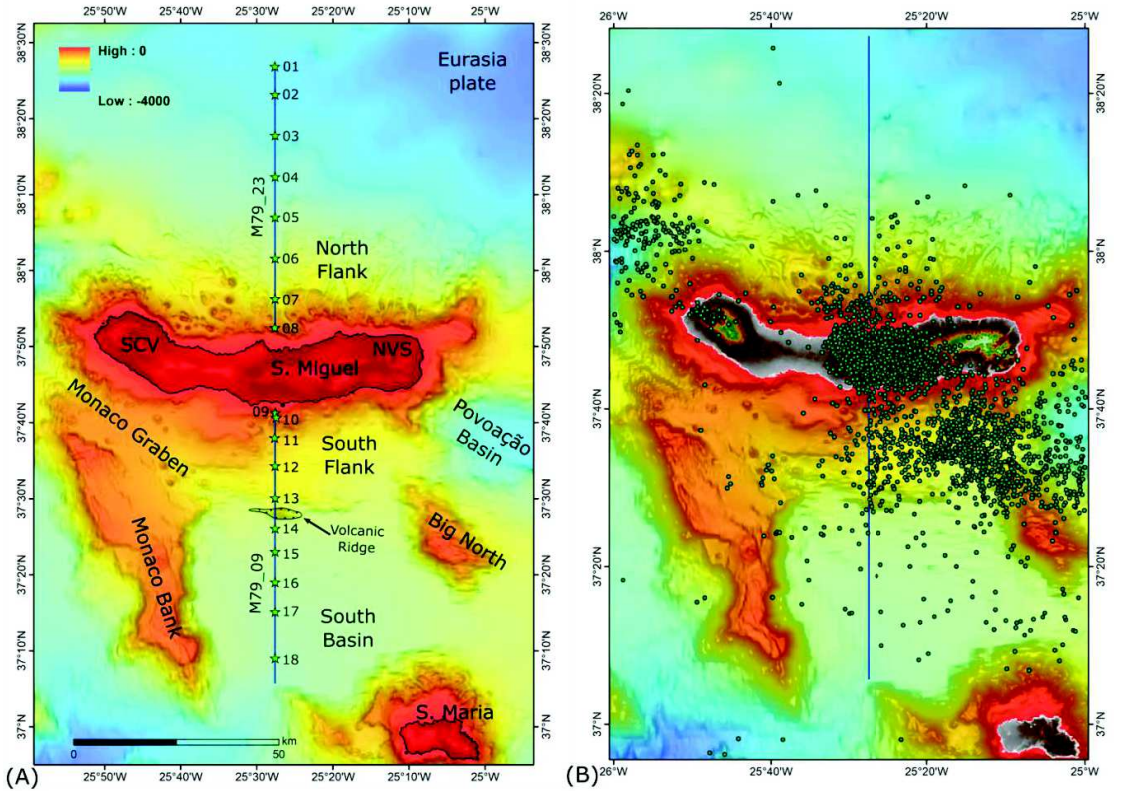

Figure 5.5: A) Reflection and Refraction seismic profile with OBS position and morpho-structures more relevant. SCV: Sete Cidades volcano; NVS: Nordeste volcanic Complex. B) Seismicity in São Miguel island and bounded area; Events are from IPMA database and occurred from 2000 to 2017 M>0.5.

To complement the wide-angle refraction data two Multichannel Seismic (MCS) profiles were acquired north and south of São Miguel Island (M79_23 and M79_09 respectively) shot on the top of the refraction line (Figure 5.5). The seismic signals were generated by an array of two GI-Guns with a generator volume of 45 in^3 and an injector volume of 105 in^3 each. For data recording a 600 m long asymmetric digital streamer was used, containing 144 channels with an average increment of 4.2 m. Shots were released every 25 m at a speed of 5 kn (Weiss et al 2015).

Bouguer anomaly data extracted from the World Gravity Map (Bonvalot, 2012) were used to compare with the results obtains from our velocity model.

5.4. Results

5.4.1. Seismic reflection

The seismo-stratigraphic interpretation of the MCS profile M79_09 (Figure 5.6 and Figure 5.7) and profile M79_23 (Figure 5.8) allowed to identify three seismic units lying on top of the acoustic basement (unit U1) U2, U3 and U4 from base to top, respectively.

Table 5-1: Seismic units interpreted from the MCS profiles

Seismic unit (U)		Seismic facies	Observations
U4	U4b	high amplitude with good lateral continuity	well layered sediments. Presence of MTD's
	U4a	high amplitude with good lateral continuity	well layered sediments
U3		high amplitude parallel reflections with good lateral continuity	several mass transport deposits (MTDs) with different magnitude
U2	U2b	regular high amplitude reflections and better lateral continuity	normal faults and a sequence of well-defined rotated blocks is visible
	U2a	alternates high and low amplitude reflections with short lateral continuity and mainly interrupt by transparent areas	normal faults and a sequence of well-defined rotated blocks is visible
U1		discontinuous low amplitude reflections sometimes with transparent areas	normal faults and a sequence of well-defined rotated blocks is visible

The MCS profile M79_09A (Figure 5.6A) represents the south side of profile M79_09. It shows a conspicuous peak interpreted as a volcanic ridge (VR in Figure 5.5 and Figure 5.6) that separates two distinct areas with different tectonic styles. To the north of the volcanic ridge the stratigraphic units U1 and U2 are cut by normal faults and a sequence of well-defined rotated blocks is visible. South of the volcanic ridge the rotated blocks tectonics is less evident, particularly in the U2 unit. In the sedimentary basin south of the ridge the seismic reflections are well defined and allowed a good interpretation of the stratigraphic units. At the base, we recognize U1 that is limited at the top by horizon h1. This unit consists of discontinuous low amplitude reflections sometimes with transparent areas, i.e. areas with no reflections. Seismic unit U1 is covered by unit U2 limited at the bottom by horizon h1 and

at the top by horizon h3. U2 can be subdivided in two units: U2a and U2b separated by an erosive discontinuity h2. U2a alternates high and low amplitude reflections with short lateral continuity and mainly interrupt by transparent areas. U2b shows more high amplitude reflections and better lateral continuity. These units are followed by unit U3 which is limited by horizon h3 at the base and by horizon h4 at the top. H3 is strongly deformed by vertical offset of blocks separated by the volcanic ridge and is slightly erosive, mainly at the foot of the escarpment defined by the volcanic ridge where MTD accumulated. Between the volcanic ridge and the island h3 has been deformed into half-grabens prior to formation of h4. H4 is mainly an aggradation surface to the south of the volcanic ridge and a progradational basal surface between the volcanic ridge and the island. U3 shows a package of high amplitude parallel reflections with good lateral continuity. Close to the volcanic ridge it is possible to identify several mass transport deposits (MTDs) with different magnitude within U3. Above seismic unit U3 and below the seafloor a package of parallel reflections with good lateral continuity and high amplitudes was identified as unit U4. It is possible to sub-divide this unit into two sub-units of well layered sediments separated by a main discontinuity h5, respectively U4a and U4b. Reflections in these units are in general of high amplitude and with good lateral continuity. Seismic unit U4b also contains MTDs (Figure 5.6B and Figure 5.7B).

The area between São Miguel Island and the VR display the same seismic units; however, clear evidence of tectonic extensional events affecting unit U2 and U3 is visible. The clear unconformity h4, separating seismic units U3 and U4 sets an emplacement relative age of the VR, i.e. post-U3 and pre-U4.

In the southernmost part of the seismic reflection profile in Figure 5.7, shortening and warping of U1, U2, U3 and U4a on the north flank of a volcanic ridge off west Santa Maria Island are clear. This deformation allows establishing a post-U4a pre-U4b age for the emplacement or tectonic reactivation of a volcanic ridge off west Sta. Maria Island, the oldest of the Azores archipelago.

On the north side of São Miguel island, the seismic interpretation of MCS line M79_23 (Figure 5.8) shows a thinner sediment cover above the horizon h4 and it is hard to identify units U4a and U4b. A landslide body with more than 20 km of length is recorded in this profile. Horizon h4 is the decollement base for this mass transport movement.

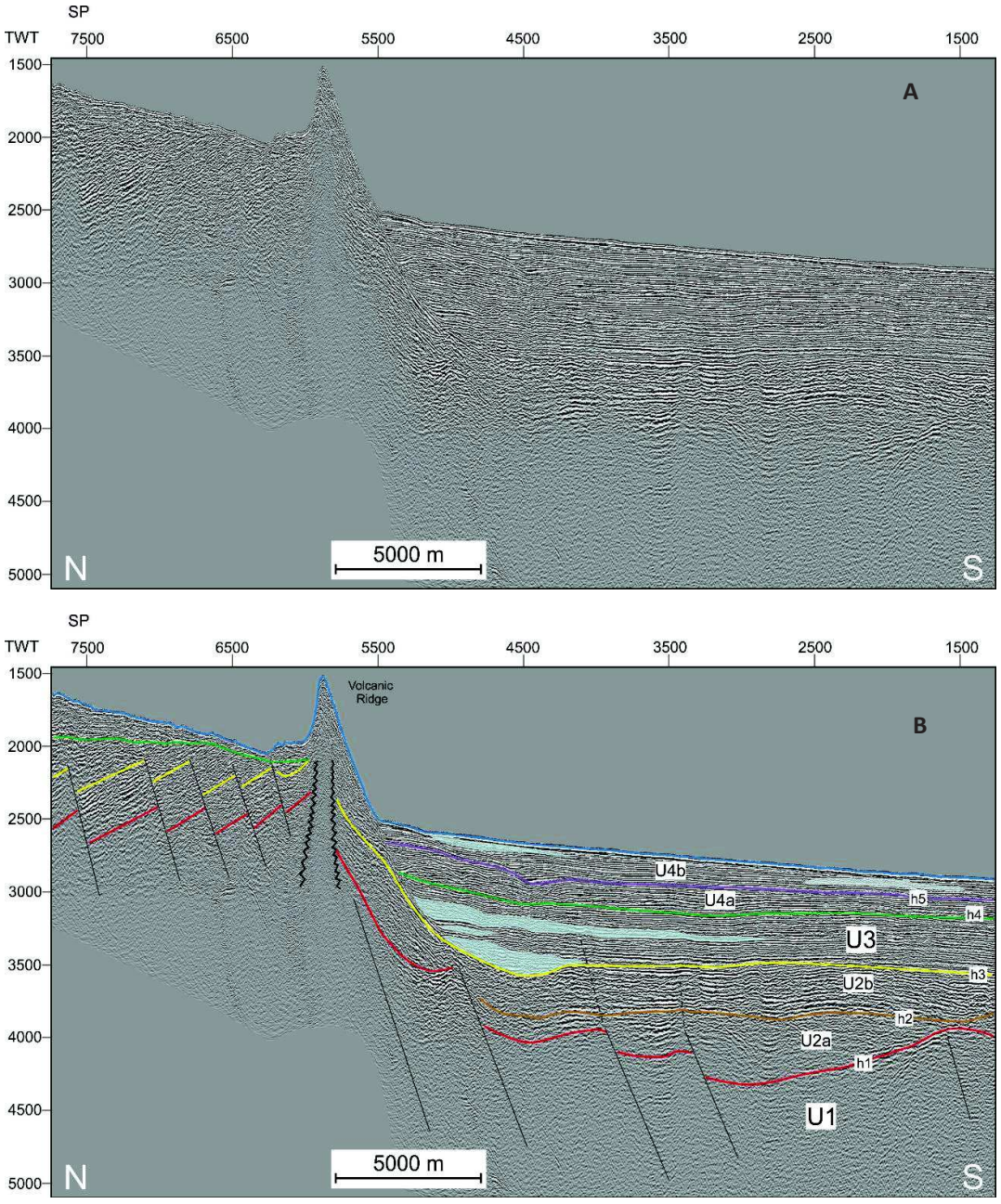

Figure 5.6: A) section of the MCS M79_09A line. B) Seismic interpretation. Blue line marks the seafloor. Transparent blue areas identifying MTD.

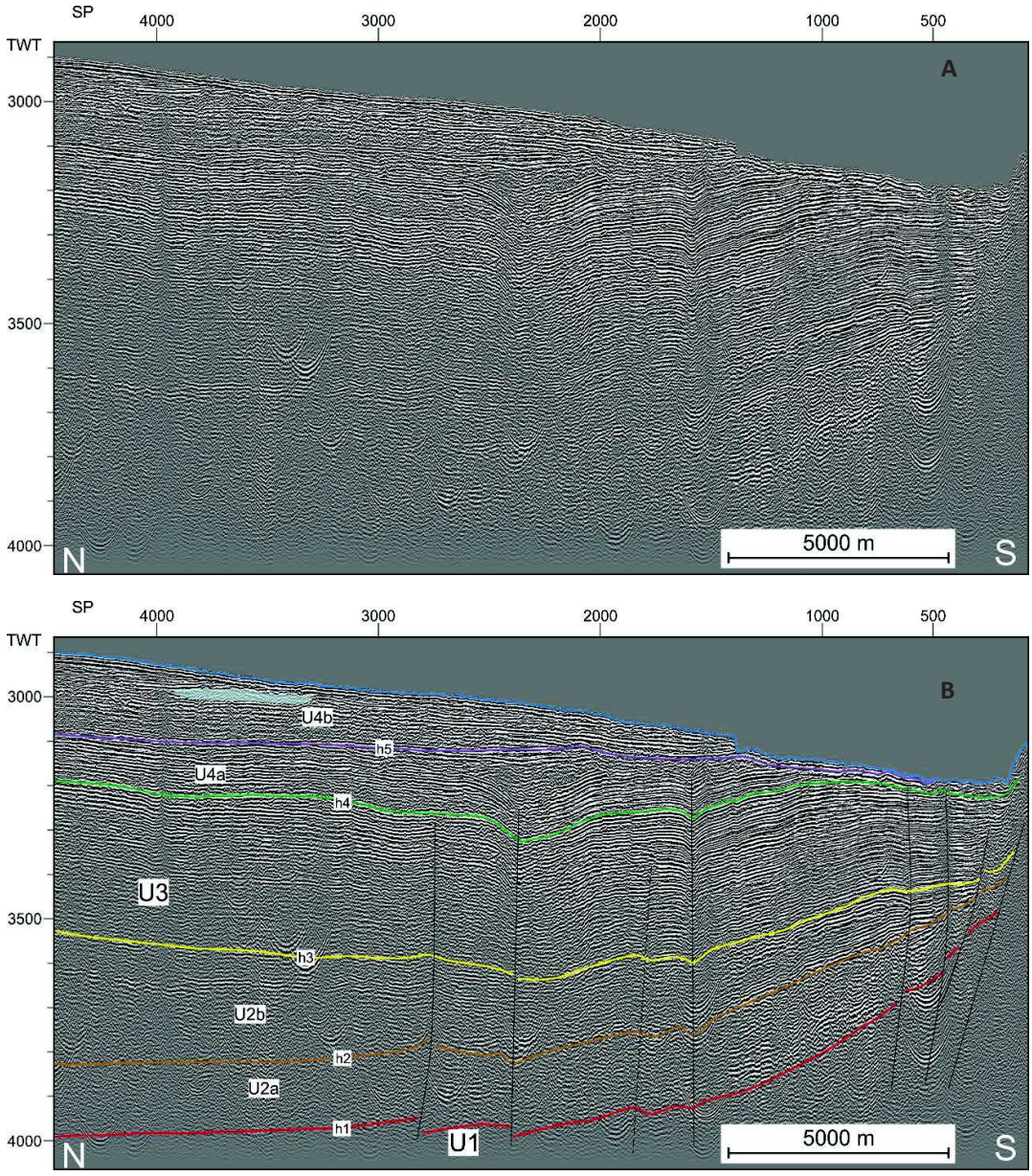

Figure 5.7: A) section of the MCS M79_09B line. B) Seismic interpretation. Blue line marks the seafloor. Transparent blue area identifies MTD.

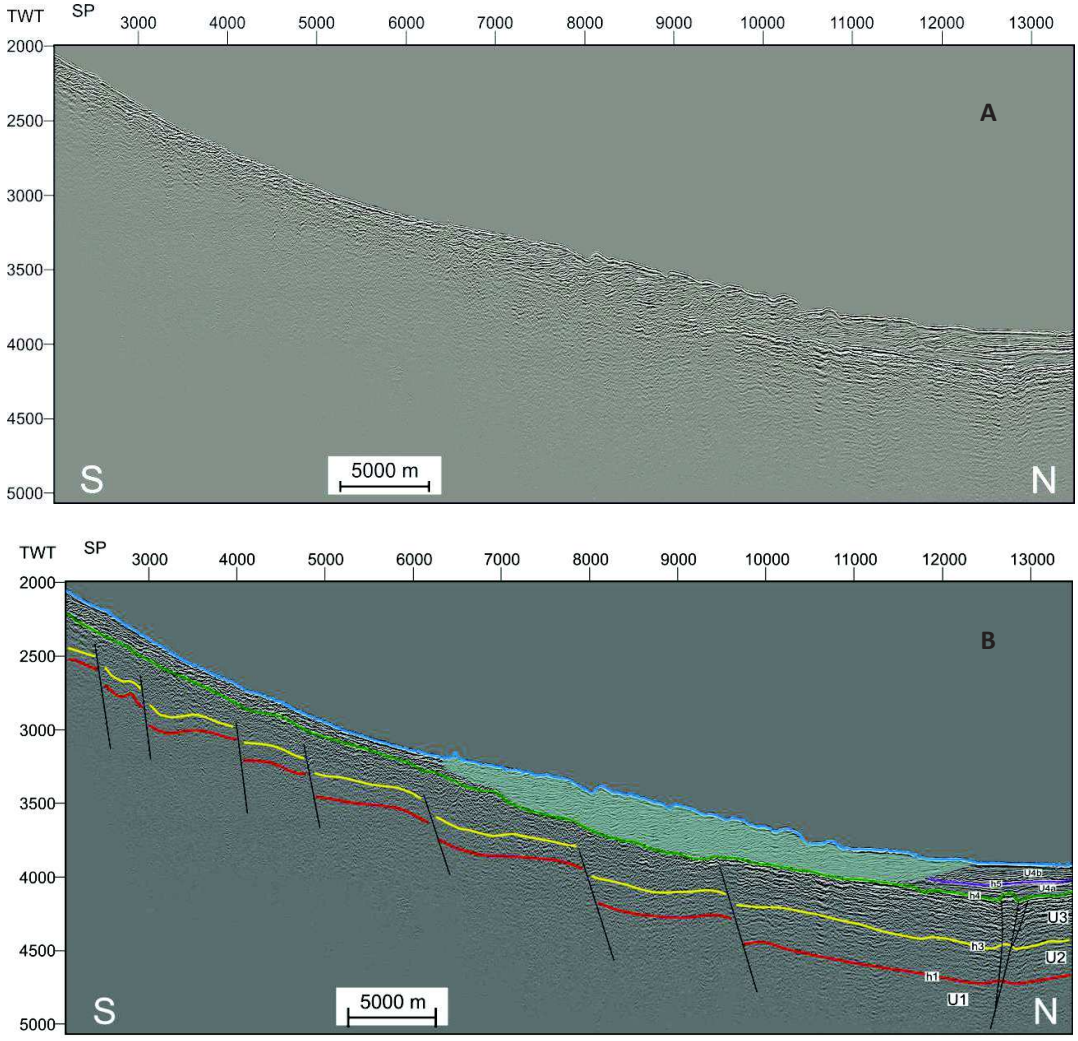

Figure 5.8: A) section of the MCS M79_23 line. B) Seismic interpretation. Blue line marks the seafloor. Transparent blue area identifies MTD.

5.4.2. Refraction data

To process the OBS recorded data we used the general methodology and modelling strategies discussed in (Zelt & Ellis (1988); Zelt (1999); Zelt & Forsyth (1994); Zelt & Smith (1992)). A compilation of the method is described in Afilhado (2006).

The refraction and wide-angle reflection data recorded by the OBSs were used to derive a P wave velocity model. We followed a top down modelling approach, starting with the sediments layer, then the crust, and finally the mantle. The initial model was constructed using sediments thickness from the multichannel seismic reflection data (Figure 5.6, Figure

5.7 and Figure 5.8). P wave velocities for equivalent volcano-sediments off the Canary islands were used as reported in Schmincke & Sumita (1998). In this work volcanoclastic sediments have a maximum age of 15 Ma at 700 m depth below. If we take the age of the oldest Azores Island (6 Ma) as the beginning of the volcanic activity in the AzP we have similar thickness, age of the sediments layer. Initial P wave crustal velocities values were based on the work of Matias *et al.* (2007), who presented a velocity model for the oceanic crust in the Faial Island shown in Figure 5.9.

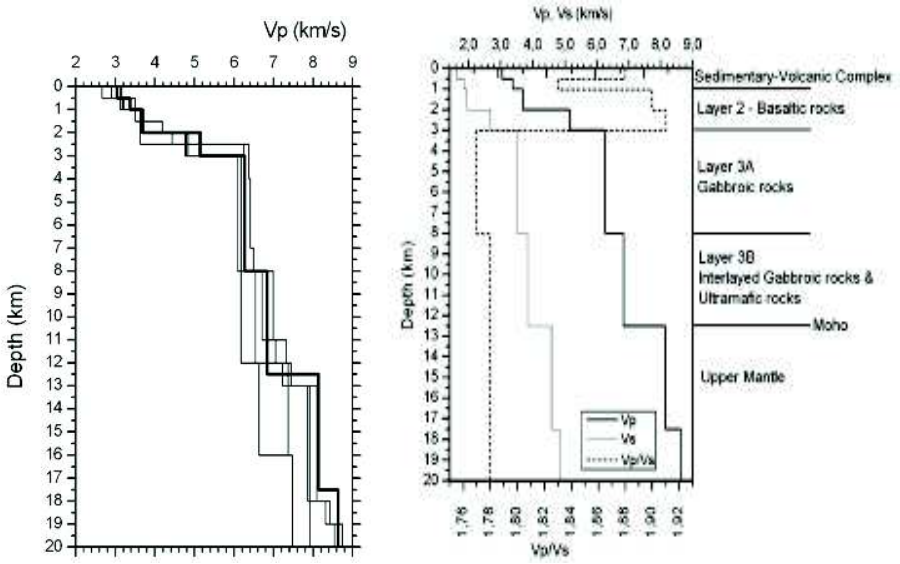

Figure 5.9: P-wave velocity model in Faial Island taken from the work of Matias (2007). A) Some of the models derived from the final stages of the inversion process with the best model in highlight. B) Vp and Vs models with the petrological interpretation.

OBS data were filtered between 3 and 15 Hz for phase interpretation and travel-time picking. OBS ray pathways identified from the data were used to derive a P wave velocity model based on the following phases: sub-basement crustal refractions (Pg), sub-basement crustal reflections (PgP), Moho wide-angle reflections (PmP), and sub-Moho refractions (Pn). Examples of OBS sections records and corresponding arrival-time energy picks are shown in Figure 5.10. There are no shots between 70 and 90 km offset which correspond to the subaerial area of the São Miguel Island. P waves traveling under the island was registered as shown in OBS07 and OBS13 (Figure 5.10).

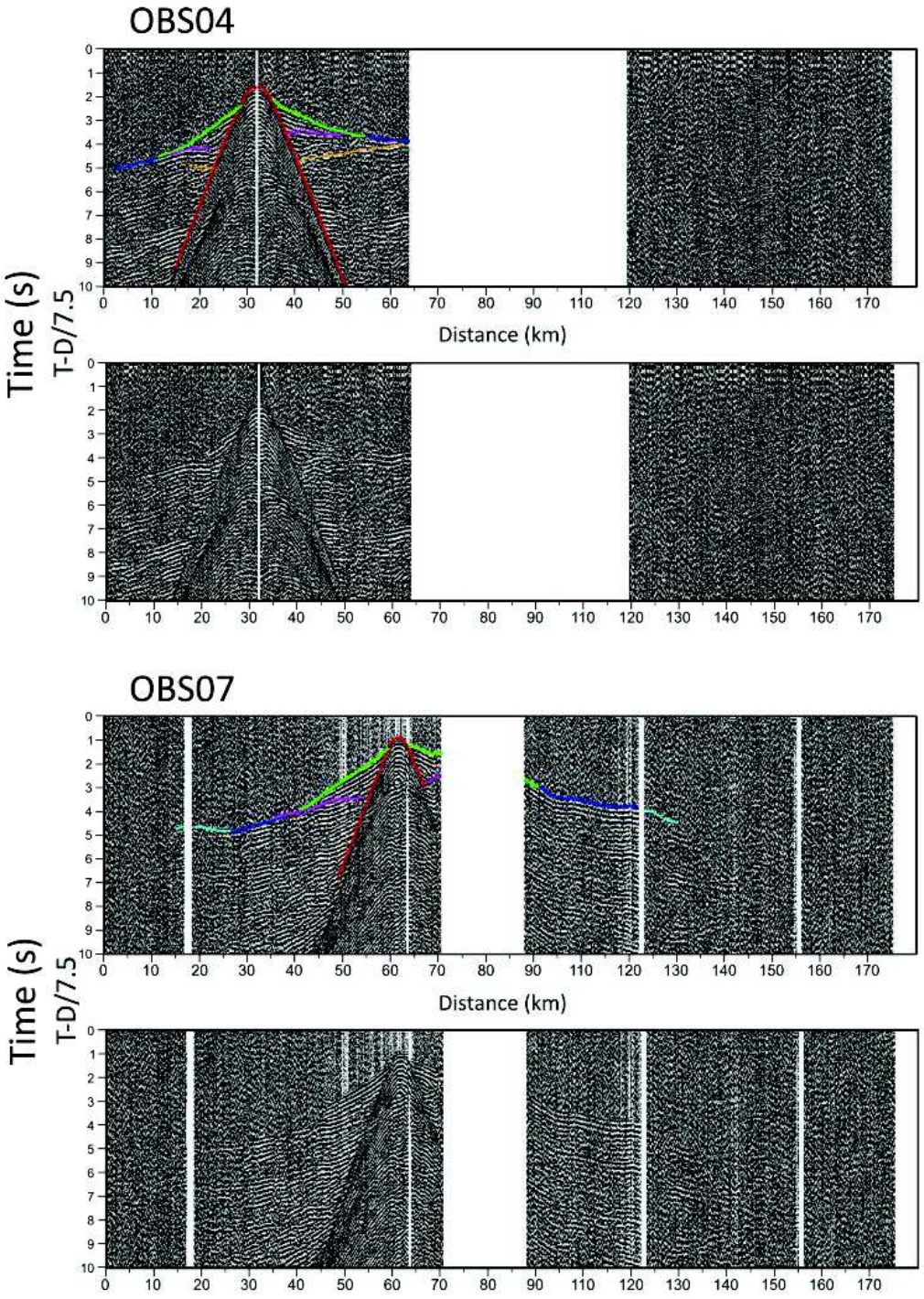

Figure 5.10: Plot of the seismic sections raw data and picks interpretation for OBS's 04, 07, 13 and 15. Colours of the picks correspond to: Red picks correspond to the energy arrivals from direct wave; Green picks correspond to Pg2 arrivals; Dark Blue picks correspond to Pg3 arrivals; Light Blue corresponds to Pn arrivals; Pink picks correspond to PgP2 arrivals; Orange picks correspond to PmP arrivals.

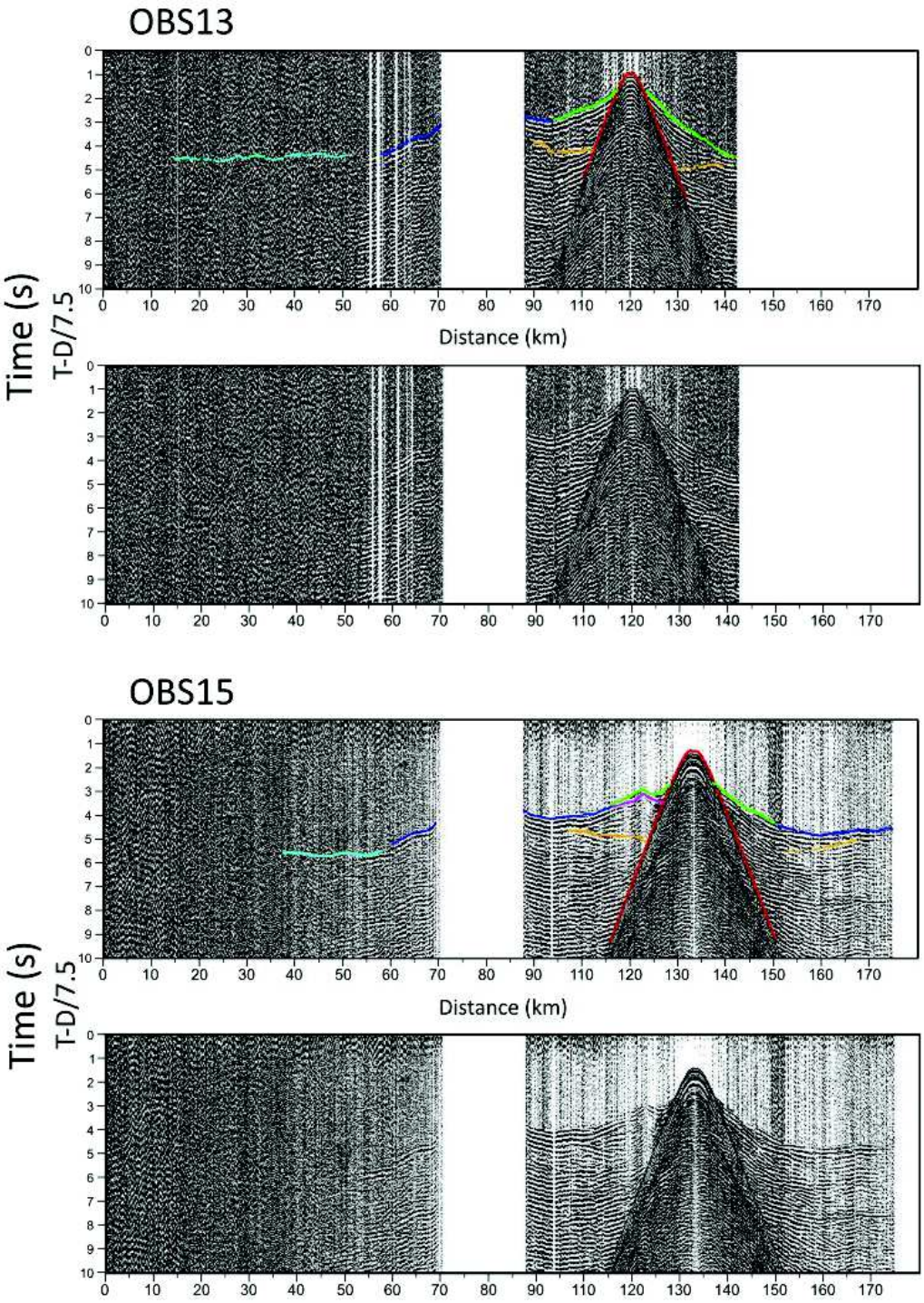

Figure 5.10: continuation

The energy refracted in layers 2 and 3 (Pg2 and Pg3 respectively) was clear identified in all 18 OBS. Energy refracted in layer 4 (Pg4) was picked by two OBS, only. Layer 4 was identified by the reflections picked on the base of layer 3 and 4 (PgP3 and PmP). Energy that

was refracted in layer 5 (Pn) was identified in 12 OBS and allowed to constrain the interface between layer 5 and the two immediately above, layer 4 and layer 3 (Figure 5.11).

Details of the error analysis statistics based on the number of observations (NPTS), the root-mean-square misfit between calculated and observed travel times (TRMS) and the normalized chi-squared (χ^2) are given in Table 5-2. Pick uncertainty was empirically calculated considering signal-to-noise ratio and lateral coherence of each phase (Table 5-2)

Table 5-2: χ^2, TRMS and pick uncertainty for P wave velocity model.

Phase	npts	Pick Uncertainty (s)	Trms (s)	χ^2
Pg1	3823	0.075	0.092	1.500
PgP1	570	0.125	0.124	0.988
Pg2	3042	0.100	0.136	1.854
PmP	649	0.125	0.123	0.976
Pg3	65	0.125	0.057	0.214
PgP3	602	0.125	0.110	0.773
Pn	1228	0.125	0.128	1.051
All Phases	9979		0.116	1.437

A plot of the ray density (Figure 5.11) was produced together with an overview through the number of picks and picks hit by rays to reveal the quality of the model. The ray density plot for the P-wave shows a good coverage with more rates for layer 2 and 3.

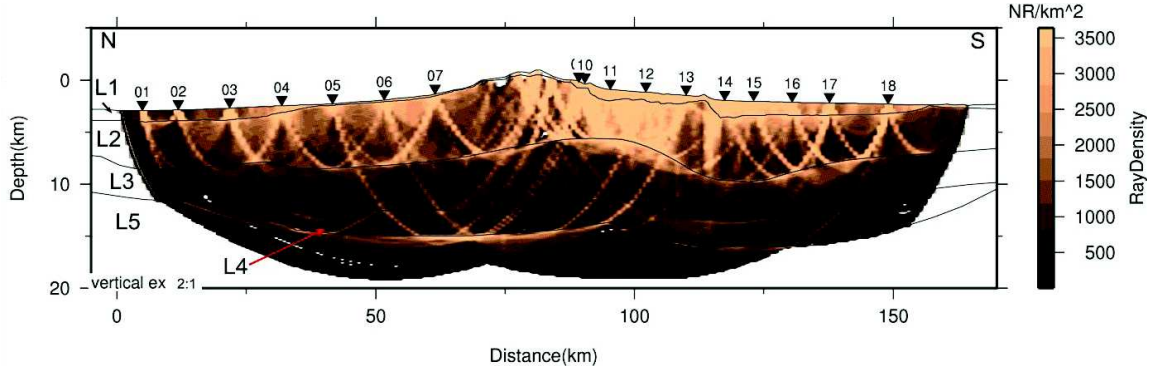

Figure 5.11: Ray density plot from the P wave model.

Interpreted phases allowed constructing a 5 layer model presented in Figure 5.12. Layer L1 presents a top velocity between 1.9 and 2.5 km/s and a base velocity between 2.6 and 3.3 km/s and a thickness variation from 150 m to 1500 m. Layer L1 corresponds to stratified layers from seafloor to the basement that in this context corresponds mostly to volcanoclastic sediments and eventually, lava flows.

Layer L2 presents a top velocity between 2.6 and 3.6 km/s, a base velocity between 5.5 and 5.8 km/s and a thickness variation from 3 km to 6 km. Layer L2 corresponds to the upper crust. Note that it thickens below the volcanic edifice that makes up the São Miguel Island. Velocities of this layer fit well with a basalt composition.

Layer L3 presents a top velocity between 5.8 and 5.9 km/s and a base velocity between 6.6 and 6.8 km/s with a mean thickness that varies from 3 km to 6 km. It corresponds to gabbro composition of the lower crust that mimics the geometry of L2.

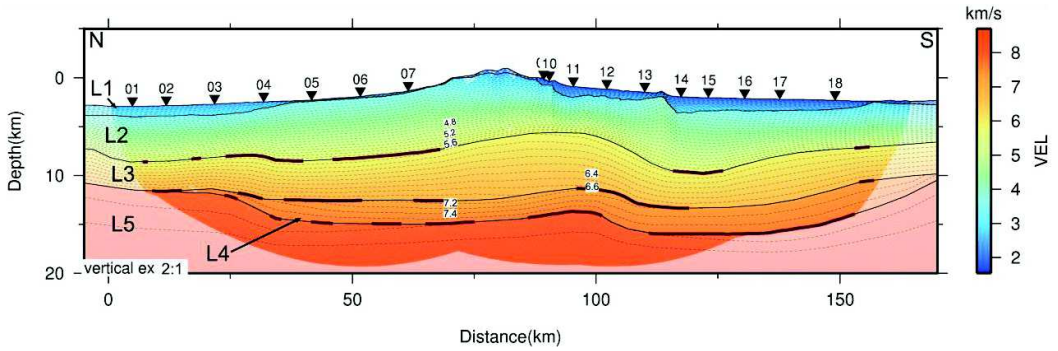

Figure 5.12: Plot of the final P-wave velocity model. L1 to L5 – modelled layers. Dark red lines show where the reflected waves are. Contours are spaced 0.1 km/s.

Layer L4 presents a top velocity between 7.1 and 7.3 km/s and a base velocity of 7.6 km/s with a mean thickness of 2.5 km. Layer L4 is bound by two discontinuities that mimic the geometry of base of L3 and L2/L3 boundary. However, L4 pinches out towards the farther realms of the island. L4 velocity curves, between 7.3 and 7.6 km/s, are truncated by the base of L3 discontinuity, allowing for discriminating the L4 domain. The obtained velocities are compatible with olivine-enriched gabbro composition. The pinch out at south has more confidence than the pinch out in the north of profile because of data limitation.

Layer L5 has velocities larger than 7.8 km/s, i.e. they are compatible with mantle velocities allowing defining the position of the Moho discontinuity at the top of L5. These layer velocities indicate typical peridotite composition.

1D velocity each 20 km of spacing are shown in Figure 5.13. It is clear in all profiles the sudden velocity increase that allowed creating a layered model for the region. Below the São Miguel island on the 80 km offset (Figure 5.13), the crustal thickness is largest (15 km). Layer 2 increase thicknesses toward the island and is thicker than layer 3 except in offset 100 km where layer 3 is thicker than layer 2. Layer 4 shows similar thickness for all offsets. In offset 80 km layer 3 shows minor velocity than the other offsets.

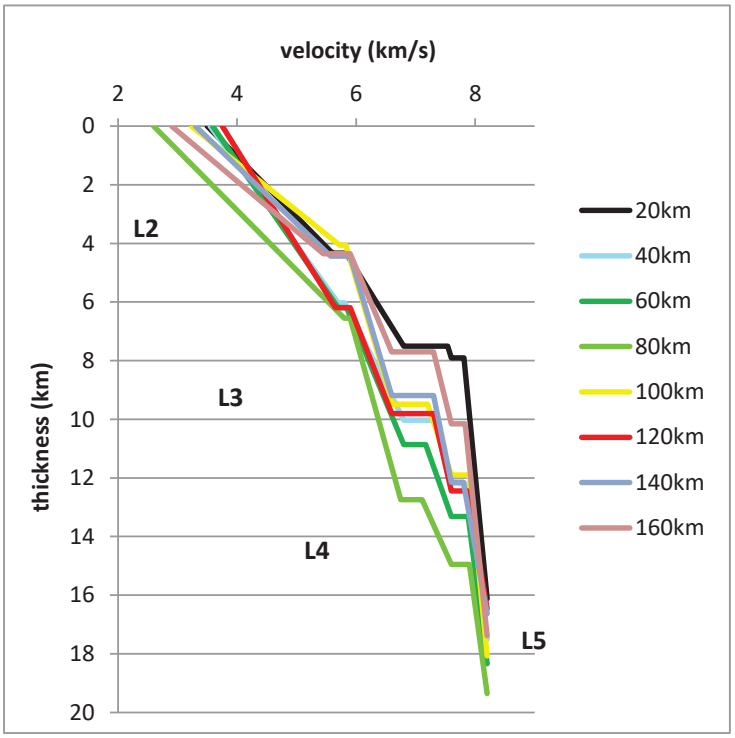

Figure 5.13: Plot of 1D P-velocity profiles extracted from the model offsets distance every 20 km. L2 to 5 corresponds to layer 2 to layer 5 respectively.

5.4.3. Gravimetric data

Bouguer gravimetric anomaly data profile was calculated from the P wave velocity model and compared with a compilation of seven profiles from world Bouguer anomaly database (Bonvalot, 2012). Six profiles were located 3, 5, 10 km east and west from refraction profile and one on the top of the refraction profile (Figure 5.14). Analysis of the figure shows a good fit for the submerged crust and the values for the island are between expected for the Bouguer anomaly.

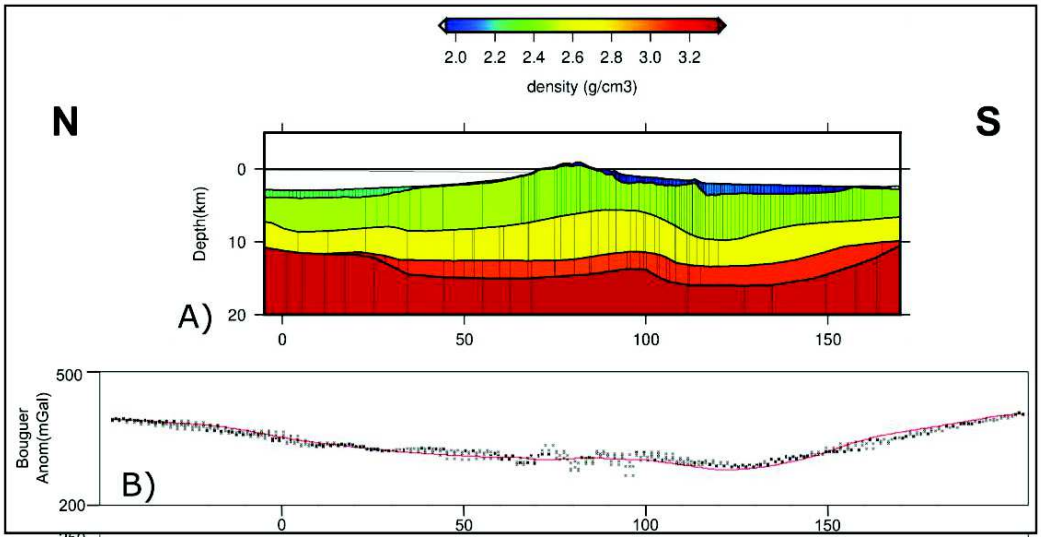

Figure 5.14: a) Density values calculated from P wave model velocities. b) Plot of the bouguer anomaly profiles; red line: profile resulted from data; black plus profiles: resulting from the compilation of the bouguer profiles extract from world data base (Bonvalot, 2012).

Density values for the 5 modelled layers were calculated with the ZELT software and the results are the following: L2 from 2.42 to 2.50 g/cm^3; L3 from 2.74 to 2.76 g/cm^3; L4 from 3.06 to 3.1 g/cm^3 and L5 from 3.3 to 3.31 g/cm^3. Densities for L2 and L3 can suggest for upper and lower crust basalt and gabbro compositions, respectively. For L5 densities are consistent with peridotite composition. L4 densities together with the P wave velocities point to the existence of a stratified body that can consist either of the crustal or mantle materials (see discussion).

5.5. Discussion

The velocity model presented in Figure 5.12 shows three striking novelties: i) the existence of a lensoid shaped layer L4 between mantle and lower crust, ii) the tectonic asymmetric geometry of the crust and lithospheric mantle and seismicity distribution with respect to the island axis and iii) a 40 km long half-graben and stepped geometry constraining the deposition of the volcanoclastic sequence south of the island.

L4 displays mantle-like densities and low P wave velocities in the range of lower crustal materials. Considering velocities and density it is here suggested that L4 corresponds to a high density cumulate gabbroic body as these can have densities as high as 3.1 g/cm^3 (Christensen, 1978). The lens-like geometry that resulted from this 2D study suggests is compatible with an underplated layer resulting from partial melting of the underlying

lithospheric mantle. Bearing in mind that the southern limit of L4 is not well constrained, i.e. that it is possible that L4 extends further south into the Azores Plateau, we envisage that L4 is related to widespread volcanism in the plateau associated with magmatic extraction from mantle.

Alternatively, hydrated mantle could also be a solution for the constitution of this layer. The obvious means to get water down to those depths would be the volcanic edifices conduits or the main deep graben bounding faults of the Terceira Rift system. Although these tectonic-magmatic systems have not, to our knowledge, been associated with mantle hydration we cannot objectively discard this alternative.

Existence of anomalous oceanic crust, such as remnants of old subducted lithosphere or sub-lithospheric Continental Mantle (SBCM) has been discussed by some authors (e.g. Beier *et al.*, 2007). The geometry of L4, however seem too continuous with the L3, not resembling remnants of exotic recycled lithosphere. In base of the above we favour underplating of cumulate gabbro for L4. This does not mean we reject the recycled lithospheric material and uncomplete homogenization (Beier *et al.*, 2007), we can only argue that L4 is a much shallower segregation process. Layer L4 has distinct density and velocity from the ones located above and below so it is certainly made of different material that can eventually contribute to exotic isotopic signatures reported by various authors (e.g. Beier *et al.*, 2007).

The Crustal structure of the Azores plateau was recently described by (Spieker *et al.* (2018)) based on teleseismic P-wave receiver functions data. They discuss that the base for the volcanic edifice is located between 1 to 4 km depth and they found strongly evidences for magmatic underplating beneath São Miguel Island around 15 km depth presenting P wave velocities of 7.6 km/s. This postulated underplating is compatible with L4 of the model of this work. The 4 km depth is the regional base depth of the sediments layer north of São Miguel (Figure 5.12) and base of the sediments in the half graben south of São Miguel.

The fold-like geometry of L2-L5 to the south of the São Miguel island axis together with local thinning of L3 (lower crust) and development of a half-graben in L1 and top of L2 is interpreted as tectonic deformation; brittle and ductile deformation are decoupled, as shown in Figure 5.15 by the lateral offset between the half-graben fault and the Deep Ductile Deformation Zone (DDDZ in Figure 5.15). This is a tectonic-magmatic process because it is associated with crustal thickening of the São Miguel (volcanic) island build up. Uplift of the footwall of the DDDZ can be due to isostatic compensation of the São Miguel thickened crust. This processes started at least as early as the initial stretching of seismic unit U2 as seen

by the tilted half-grabens on both sides of the VR and also in the northern part of the island. During U3 tilted graben formation ceased and subsidence to the south of VR continued as shown the thick U3 south of VR and important MTD contribution (Figure 5.6). The large landslide on the northern part of the island post-dates the main volcanism may result of recent uplift and northwards tilting of the island (Figure 5.8).

We propose that the southward polarity of the DDDZ extension can be due to softer rheology of the Azores Plateau lithosphere with respect to the external plateau lithosphere to the northeast. This speculation is based on the assumption that the Azores Plateau lithosphere probably has a higher thermal gradient as well as has accumulated extensional strain, hence strain softening. This is compatible with the N-S thermal distribution across the plateau proposed by Arnould *et al.* (2019).

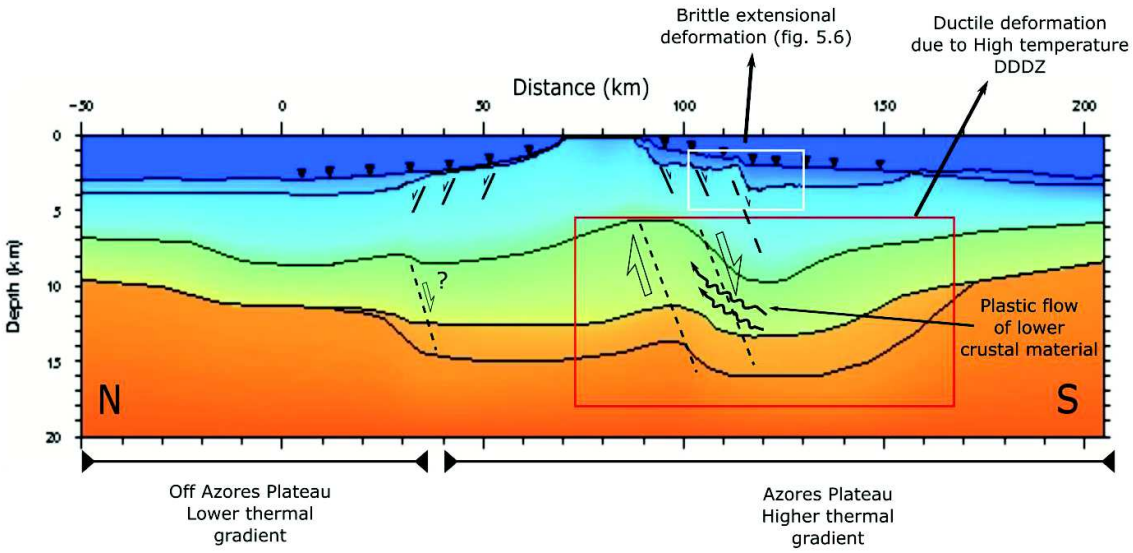

Figure 5.15: Deformation regime of the study area; DDDZ - Deep Ductile Deformation Zone.

Inspection of seismicity data of the study area, the central part of the São Miguel Island, (Figure 5.16 and Figure 5.17) can be summarized as follows: i) the main cluster lies under the São Miguel volcano and a diffuse cluster extends further south and southeast, ii) little seismicity is observed to the north of the island. This suggests that most of the seismicity has tectono-magmatic origin (under the volcano) and diffuse extensional tectonic deformation is still occurring south of the island in the VR and adjacent plateau and half-graben. It is worthwhile noting the existence of a dense seismicity cluster towards the southeast of S. Miguel offset to the south of the TR.

Altogether, the brittle deformation at the surface (VR and half-graben), the ductile deformation in depth (DDDZ of L3, L4 and L5) and the distribution of seismicity suggest that the TR south flank south of S. Miguel coincides with the Monaco graben – VR faults trace (Figure 5.18).

The few reverse fault mechanisms that occur in the eastern termination of the TR are probably associated with the clockwise rotation (west to east) of the São Miguel Island towards the Northeast graben that induces a slight restraining bend (Figure 5.17).

The constant Shmax parallel to the TR indicates that this results from ridge push. The concentration of strike-slip fault mechanism and some compressive events suggests that approximately NE-SW oriented deep shear zones are accommodating differential displacement between segments of the TR.

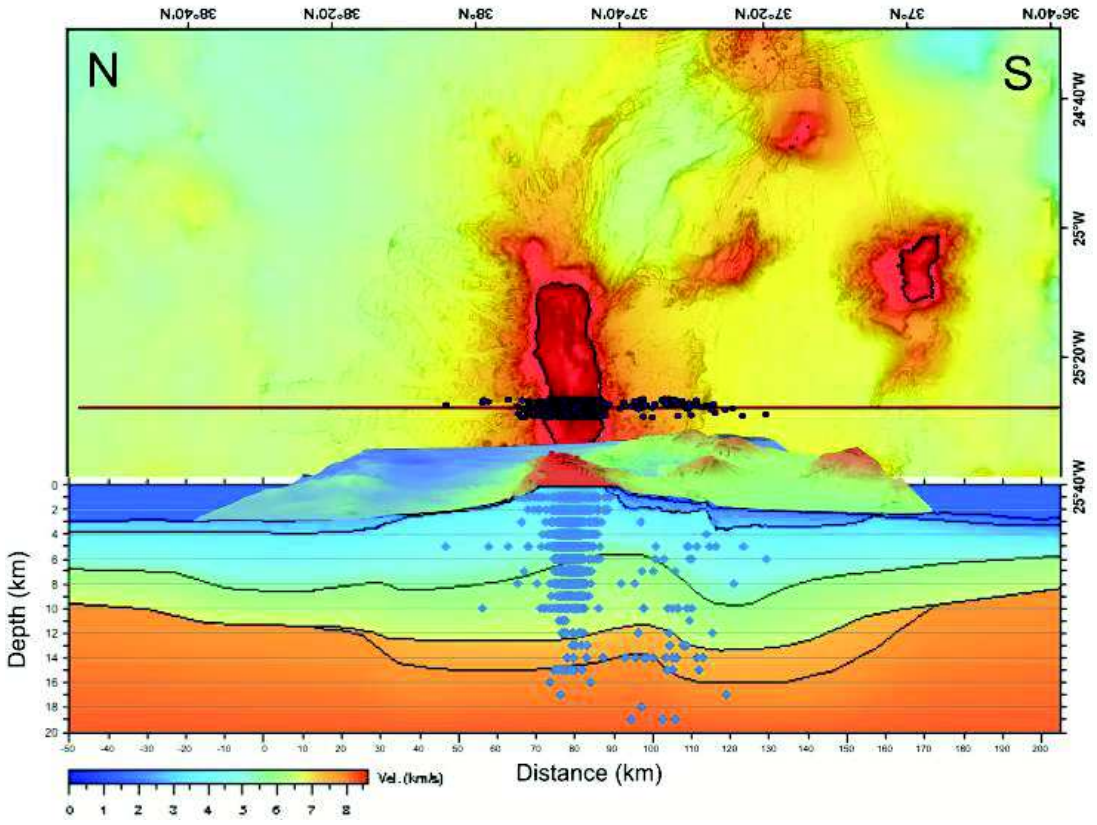

Figure 5.16: Plot of the seismicity over the São Miguel P wave velocity model. Localization distanced 2 km east-west from the model line. Events are from IPMA database and occurred between 2000 and 2017 with M>0.5.

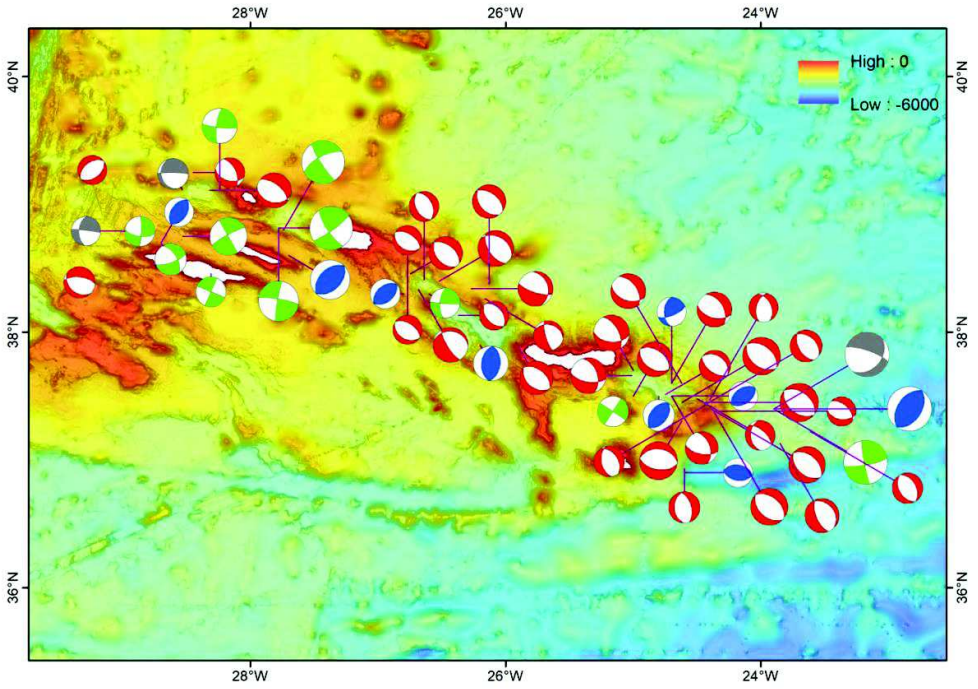

Figure 5.17: Focal mechanisms from (Custódio *et al.* (2016)) for the AzP. M>5. Red – normal solutions; Blue – invers solutions; Green – strike-slip solutions; Grey – unknown.

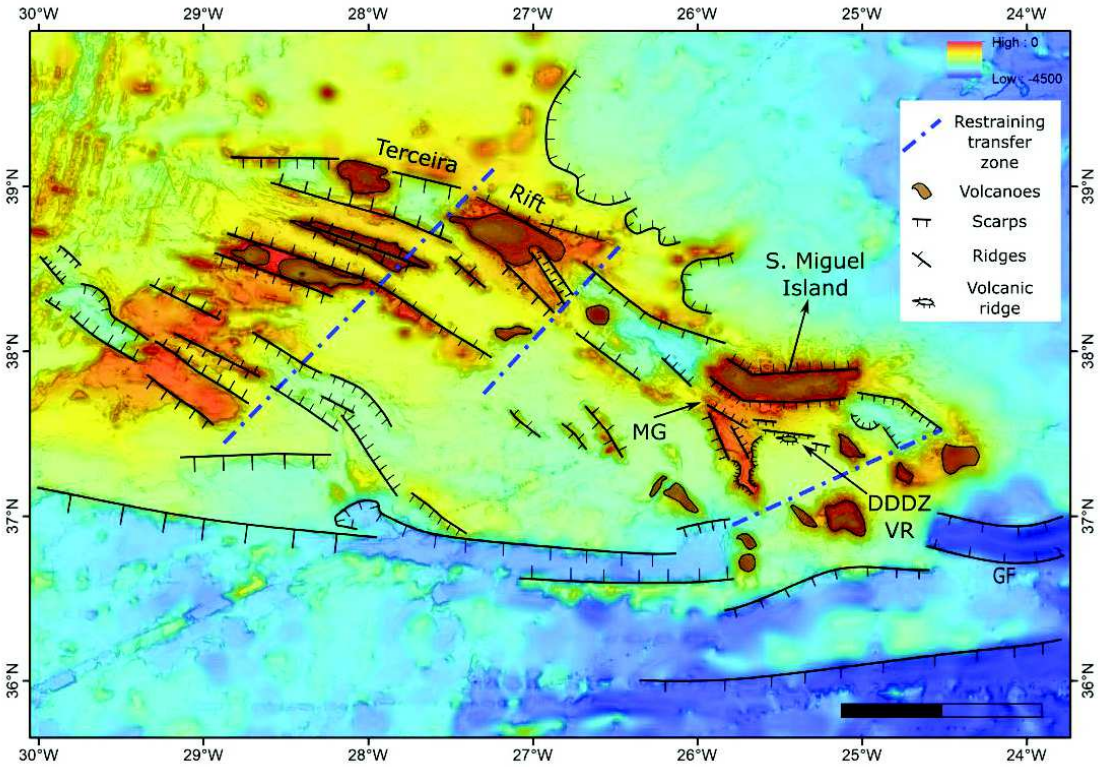

Figure 5.18: Morphologic interpretation, proposed location for the existence of deep restraining transfer zones (blue pointed lines). Also shown the location of the VR and DDDZ (Volcanic Ridge and Deep Ductile Deformation Zone) that connect laterally with the Monaco graben (MG), altogether constituting the southern limit of the Terceira Rift south of S. Miguel Island; GF-Gloria Fault.

5.6. Conclusions

Our results of the study of a seismic refraction profile across the central part of the São Miguel island show that it is made of 4 crustal layers with the Moho discontinuity at a depth of 15 km under the Fogo volcano and at 11 km in the distal offshore. The top layer (L1) includes an offshore half-graben with a maximum sediment thickness of a 2 km. A lens shaped layer (L4) was found near the Moho discontinuity, whose velocities and densities are compatible with a cumulate gabbroic composition suggesting underplating. However, a mantle hydration process cannot be excluded, assisted by ocean water percolation along the TR graben boundary faults.

Asymmetric tectonic extensional deformation accommodated by simple shear across the whole crust and top lithospheric mantle, located south of the island axis (brittle and ductile, at shallow and depth, respectively) was observed from the multichannel and refraction seismic profiles. This process caused tilting of the island to the north, possibly the cause of a recent northward directed 20 km long, 300 m thick landslide.

6. CHAPTER 6 – DISCUSSION

6.1. Crustal composition and mantle heterogeneity

This work (including Batista et al., 2017) reports two original velocity models of the upper lithosphere from two different tectonic settings, both of them within Atlantic Oceanic lithosphere. One is located at the northeast external limit of the Azores plateau, across the S. Miguel Island and Terceira Rift (TR) and another at the Gloria Fault (GF), a plate boundary fracture zone between Africa and Eurasia lithospheric plates. Both refraction profiles image below the seismic Moho discontinuity in their central parts at depths below 20 km (bsl). Discussion of results was done in the respective chapters.

Both refraction profiles show the existence of a layer L4 that is a novelty in this part of the Atlantic Ocean. Layer L4 across the GF is 4 km thick and can be followed for at least 120 km (Figure 4.11). Two possibilities for the origin of the anomalous L4 layer across the GF were posed. One was underplating caused by a mantle plume ~60 My ago and the second was mantle hydration. Batista *et al.* (2017) favored the second option.

An important discussion about the structure of the S. Miguel Island and AzP was about its origin. Now, this work comes up with a layered model in which L4 is news. Inspection of the refraction profile shows that L4 lies between normal lower crust and mantle, is ~2 km thick and can be recognized laterally for 150 km at least. However, lack of refraction data to the south of S. Miguel does not allow pin-pointing the pinch out of L4, i.e. it can continue underlying the Azores plateau.

This has two important outcomes, as follows:

i) Inspection of the bathymetry data in Batista *et al.* (2017) do not show evidences of existence of volcanic (or sob-volcanic) edifices associated with the GF; faulting sub-parallel to the GF is important as shown by existence of various deep basins along the fault and on their flanks. In addition, L4 seems to extend without thick-ness variation from end to end of the profile. So we stick to favoring the option of mantle hydration through deep fractures some of which evidenced in the shallow seismic reflection profile of Batista *et al.* (2017).

ii) Crustal overthickening in the Azores plateau is achieved through two processes, firstly, by underplating of lower crustal affinity material, and secondly by adding thick amounts of lava flows to the seafloor surface within the Azores plateau area.

6.2. Tectonic deformation and plate boundary

Present day tectonic activity along the GF is demonstrated by seismicity ((Buforn *et al.*, 1988, Johnston, 1996) and by deformation of upper crust and recent sediments in Batista *et al.* (2017). Active tectonic deformation along the TR is clear and also undisputed based on seismicity, plate kinematics, and GPS velocities (e.g. Bezzeghoud *et al.*, 2014, Borges *et al.*, 2007, Fernandes *et al.*, 2004, Fontiela *et al.*, 2014, Miranda *et al.*, 2015, Miranda *et al.*, 2014).

In Figure 6.1 we show two seismicity maps, one for crustal hypocentres and another for mantle hypocentres (Figure 6.1 A and B). Seismicity in the mantle in the south of S. Miguel Island is scarce, which is compatible with the ductile/plastic deformation interpreted in Figure 5.15. Further southeast a mantle cluster of earthquakes with extensional focal mechanisms with extension direction ~90º suggests a brittle connection between the GF and the TR (Figure 6.1 C).

On the basis of exposed above we propose that the TR is a transtensional leaky plate boundary that connects the GF fracture Zone plate boundary (actually, a transform fault at the eastern TR tip). Due to high heat flow and temperature, tectonic deformation at the mantle level is ductile, mainly accommodated by plastic flow, thus yielding little seismicity. The leaky character is given by interruption of the TR graben segments by volcanic edifices. Towards the northwest, i.e. towards the MAR, the TR ends at the present-day triple junction area (Miranda *et al.*, 2014). The TR is possibly a tectonic structure that results from a still not well understood mantle plume-GF-MAR interaction. In this area (Azores plateau) the NW-SE Shmax associated with the GF transpression is interrupted by a magmatic ascent process that allows for NE-SW increase of extensional strain.

We speculate that the northeastwards migration of the Princess Alice rift to the TR has to do with the mantle plume northwards migration from the great Meteor region and that this process somehow displaces brittle deformation to the north within the Azores plateau and to the east along the GF (western segments became inactive).

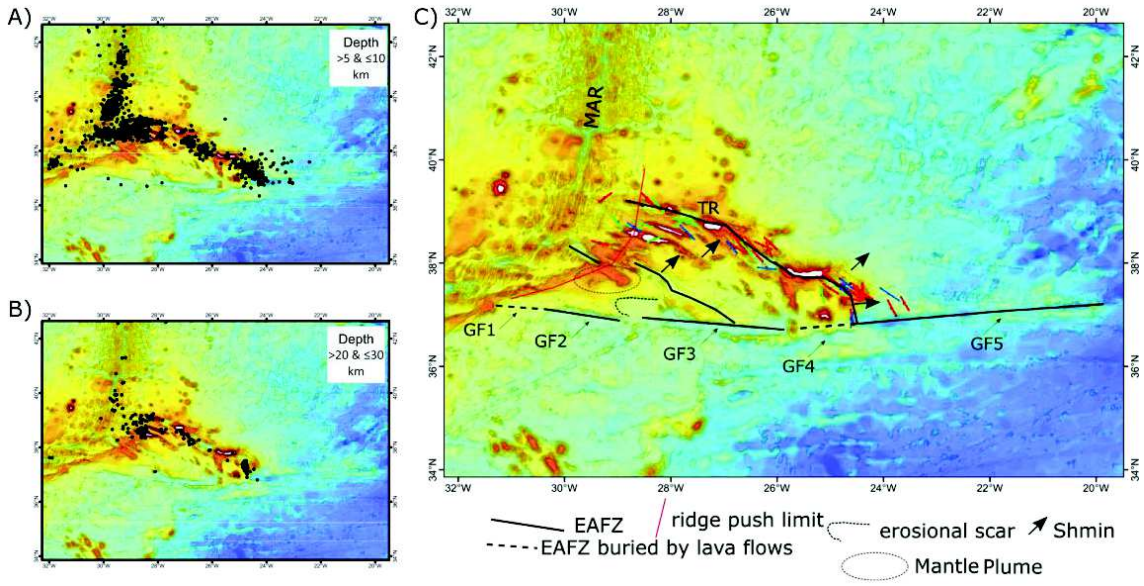

Figure 6.1: seismicity in the crust (A) and in the mantle (B). Note N-S trending cluster at the intersection of the TR with the GF with rotation of the Shmax from NW-SE to N-S. C) Schematic interpretation of the main structural features. GF , Gloria Fault; only GF5 segment is active at present and since the formation of the TR, ~3 Ma. The activity and deactivation of the GF segments has to do with NW-SE striking rifts and/or volcanic ridges.

6.3. Mass Transport Processes and fluid flow

Mass transport processes were identified on the seismic reflection profiles of both GF and TR (Figure 4.5 and Figure 5.6). In the south part of the S. Miguel Island study area the mass transport deposits are located at the foot of the Volcanic Ridge scarp pinching out towards the offshore, i.e. certainly associated with differential vertical movements of an extensional fault possibly a series of avalanches and turbidites and debris flows. In the north of the S. Miguel Island the identified MTD appears to be a large single landslide event. Although at this stage it is not possible to ascertain a cause for this event we favour the hypothesis of general or partial island uplift. This could be caused by the asymmetric development and tilting to the north of the S. Miguel Island (Figure 5.15).

In the GF region smaller scale MTDs were identified by Batista *et al.* (2017). Some of these are slumps with barely any horizontal movement (Figure 4.5 and Figure 4.7). Inspection of the high-resolution bathymetry suggests the possible existence of landslide scars and transported blocks. Deposits at the foot of the main fault scarp of the strike-slip basin were also identified (Figure 4.5). In Figure 4.6 evidences of fluid flow were pointed out disturbing the sediments. One of these, lies at the flank of a main fault and stands out as a positive sharp relief. Inspection of the multibeam bathymetry (Figure 4.2) shows various examples of sharp

peaks apparently with no connection to linear tectonic features. This could be an evidence of ascent of serpentinites or, alternatively, small volcanic plugs.

7. CHAPTER 7 – CONCLUSIONS

The following main conclusions can be withdrawn from this work:

1) The oceanic crust in both Africa and Eurasia segments of the GF seems to have similar structure and constitution despite their age difference (~20 My), ~60 Ma and ~80 Ma in the Eurasia and Africa plates, respectively;

2) The oceanic crust in the Gloria Fault crust is subdivided in typical L1, sediment and volcanoclastic layer, L2, upper crust (3 km of thickness), L3, lower crust (6 to 7 km thick), that are underlain by L4, a 4km thick layer whose Vp and Vs and Poisson's coefficient indicate a mixed nature, possibly corresponding to partially hydrated mantle intruded by gabbros, similar to what is observed at the Southern Troodos Transform Fault Zone. Altogether, the crust is about 12 km (L1+L2+L3+L4), rather thicker than the average of 7 km. The mantle underneath has typical mantle velocities.

3) The oceanic crust underneath S. Miguel Island and both sides of the TR is made of 4 crustal layers with a Moho discontinuity, under the Fogo volcano, at depth of 15 km.

4) A lens shaped layer (L4) was found near the Moho discontinuity, whose velocities and densities are compatible with a cumulate gabbroic composition suggesting underplating. However, a mantle hydration process cannot be excluded, assisted by ocean water percolation along the TR graben boundary faults.

5) Asymmetric tectonic extensional deformation accommodated by simple shear across the whole crust and top lithospheric mantle, located south of the island axis (brittle and ductile, at shallow and depth, respectively) was observed from complementary inspection of the multichannel and refraction seismic profiles.

6) This process caused tilting of the island to the north, possibly the cause of a recent northward directed 20 km long, 300 m thick landslide.

7) The extensional shear zone located to the south S. Miguel Island coincides with a cluster of seismicity corroborating active deformation; this shear zone is the eastern prolongation of the Monaco Graben and constitutes the south limit of the TR south of S. Miguel Island.

8) The composition of the oceanic crust depends on the geo-tectonic environment and this work as shown for two different locations along the Eurasia-Africa Plate Boundary.

REFERENCES

Afilhado, A., 2006. *Modelação geofísica na margem meridional de Portugal continental*, PhD Thesis, University of Lisbon, Science Faculty.

Afilhado, A., Matias, L., Shiobara, H., Hirn, A., Mendes-Victor, L. & Shimamura, H., 2008. From unthinned continent to ocean: The deep structure of the West Iberia passive continental margin at 38°N, *Tectonophysics,* 458**,** 9-50.

Argus, D.F., Gordon, R.G., DeMets, C. & Stein, S., 1989. Closure of the Africa-Eurasia-North America Plate motion circuit and tectonics of the Gloria Fault, *Journal of Geophysical Research: Solid Earth,* 94**,** 5585-5602.

Arnould, M., Ganne, J., Coltice, N. & Feng, X., 2019. Northward drift of the Azores plume in the Earth's mantle, *Nature Communications,* 10**,** 3235.

Bartetzko, A., 2005. Effect of hydrothermal ridge flank alteration on the in situ physical properties of uppermost oceanic crust, *Journal of Geophysical Research: Solid Earth,* 110**,** n/a-n/a.

Batista, L., Hübscher, C., Terrinha, P., Matias, L., Afilhado, A. & Lüdmann, T., 2017. Crustal structure of the Eurasia–Africa plate boundary across the Gloria Fault, North Atlantic Ocean, *Geophysical Journal International,* 209**,** 713-729.

Beier, C., Haase, K.M. & Hansteen, T.H., 2006. Magma Evolution of the Sete Cidades Volcano, São Miguel, Azores, *Journal of Petrology,* 47**,** 1375-1411.

Beier, C., Stracke, A. & Haase, K.M., 2007. The peculiar geochemical signatures of São Miguel (Azores) lavas: Metasomatised or recycled mantle sources?, *Earth and Planetary Science Letters,* 259**,** 186-199.

Bezzeghoud, M., Adam, C., Buforn, E., Borges, J.F. & Caldeira, B., 2014. Seismicity along the Azores-Gibraltar region and global plate kinematics, *J Seismol,* 18**,** 205-220.

Bonvalot, S., Balmino, G., Briais, A., M. Kuhn, Peyrefitte, A., Vales N., Biancale, R., Gabalda, G., Reinquin, F., Sarrailh, M., , 2012. World Gravity Map. Commission for the Geological Map of the World. *in Eds. BGI-CGMW-CNES-IRD*, Paris.

Borges, J.F., Bezzeghoud, M., Buforn, E., Pro, C. & Fitas, A., 2007. The 1980, 1997 and 1998 Azores earthquakes and some seismo-tectonic implications, *Tectonophysics,* 435**,** 37-54.

Bouysse, P., Westercamp, D. & Andreieff, P., 1990. The Lesser Antilles Island Arc, *Proc., scientific results, ODP, Leg 110, Barbados Ridge,* 110**,** 29-44.

Bown, J.W. & White, R.S., 1994. Variation with spreading rate of oceanic crustal thickness and geochemistry, *Earth and Planetary Science Letters,* 121**,** 435-449.

Buforn, E., Udías, A. & Colombás, M.A., 1988. Seismicity, source mechanisms and tectonics of the Azores-Gibraltar plate boundary, *Tectonophysics,* 152**,** 89-118.

Caldeira, B., Fontiela, J., Borges, J.F. & Bezzeghoud, M., 2017. Grandes terremotos en Azores, *Fisica de la Tierra***,** 29-45.

Carlson, R.L. & Miller, D.J., 2003. Mantle wedge water contents estimated from seismic velocities in partially serpentinized peridotites, *Geophysical Research Letters,* 30**,** 1250.

Christensen, N.I., 1978. Ophiolites, seismic velocities and oceanic crustal structure, *Tectonophysics,* 47**,** 131-157.

Christensen, N.I., 1996. Poisson's ratio and crustal seismology, *Journal of Geophysical Research: Solid Earth,* 101**,** 3139-3156.

Christensen, N.I., 2004. Serpentinites, Peridotites, and Seismology, *International Geology Review,* 46**,** 795-816.

Christensen, N.I. & Salisbury, M.H., 1975. Structure and constitution of the lower oceanic crust, *Reviews of Geophysics,* 13**,** 57-86.

Custódio, S., Dias, N.A., Carrilho, F., Góngora, E., Rio, I., Marreiros, C., Morais, I., Alves, P. & Matias, L., 2015. Earthquakes in western Iberia: improving the understanding of lithospheric deformation in a slowly deforming region, *Geophysical Journal International,* 203**,** 127-145.

Custódio, S., Lima, V., Vales, D., Cesca, S. & Carrilho, F., 2016. Imaging active faulting in a region of distributed deformation from the joint clustering of focal mechanisms and hypocentres: Application to the Azores–western Mediterranean region, *Tectonophysics,* 676**,** 70-89.

Dean, S.M., Minshull, T.A., Whitmarsh, R.B. & Louden, K.E., 2000. Deep structure of the ocean-continent transition in the southern Iberia Abyssal Plain from seismic refraction profiles: The IAM-9 transect at 40°20′N, *Journal of Geophysical Research: Solid Earth,* 105**,** 5859-5885.

DeMets, C., Gordon, R.G. & Argus, D.F., 2010. Geologically current plate motions, *Geophysical Journal International,* 181**,** 1-80.

Dilek, Y., 2003. Ophiolite concept and its evolution, *Geological Society of America Special Papers,* 373**,** 1-16.

Duarte, J.C., Rosas, F.M., Terrinha, P., Gutscher, M.-A., Malavieille, J., Silva, S. & Matias, L., 2011. Thrust–wrench interference tectonics in the Gulf of Cadiz (Africa–Iberia plate boundary in the North-East Atlantic): Insights from analog models, *Marine Geology,* 289**,** 135-149.

Duarte, J.C., Rosas, F.M., Terrinha, P., Schellart, W.P., Boutelier, D., Gutscher, M.-A. & Ribeiro, A., 2013. Are subduction zones invading the Atlantic? Evidence from the southwest Iberia margin, *Geology*.

Duarte, J.C., Terrinha, P., Rosas, F.M., Valadares, V., Pinheiro, L.M., Matias, L., Magalhães, V. & Roque, C., 2010. Crescent-shaped morphotectonic features in the Gulf of Cadiz (offshore SW Iberia), *Marine Geology,* 271**,** 236-249.

Fernandes, R.M.S., Bastos, L., Ambrosius, B.A.C., Noomen, R., Matheussen, S. & Baptista, P., 2004. Recent Geodetic Results in the Azores Triple Junction Region, *pure and applied geophysics,* 161**,** 683-699.

Fontiela, J., Bezzeghoud, M., Borges, P., Oliveira, C., Rosset, P. & Rodrigues, F.C., 2014. *AZORES SEISMOGENIC ZONES,* edn, Vol., pp. Pages.

Francis, T.J.G., 1981. Serpentinization faults and their role in the tectonics of slow spreading ridges, *Journal of Geophysical Research: Solid Earth,* 86**,** 11616-11622.

Gaspar, J.L., Queiroz, G., Ferreira, T., Medeiros, A.R., Goulart, C. & Medeiros, J., 2015. Chapter 4 Earthquakes and volcanic eruptions in the Azores region: geodynamic implications from major historical events and instrumental seismicity, *Geological Society, London, Memoirs,* 44**,** 33-49.

Gass, I.G., MacLeod, C., Murton, B., Panayiotou, A., Simonian, K., Xenophontos, C., Adamides, N., Allerton, S. & Georgiou, E., 1994. *The geology of the Southern Troodos transform fault zone,* Geological Survey Department, Ministry of Agriculture, Natural Resources and Environment.

Geldmacher, J., Hoernle, K., Bogaard, P.v.d., Duggen, S. & Werner, R., 2005. New 40Ar/39Ar age and geochemical data from seamounts in the Canary and Madeira volcanic provinces: Support for the mantle plume hypothesis, *Earth and Planetary Science Letters,* 237**,** 85-101.

Geldmacher, J., Hoernle, K., Klügel, A., Bogaard, P.v.d., Wombacher, F. & Berning, B., 2006. Origin and geochemical evolution of the Madeira-Tore Rise (eastern North Atlantic), *Journal of Geophysical Research: Solid Earth,* 111**,** B09206.

Gente, P., Dyment, J., Maia, M. & Goslin, J., 2003. Interaction between the Mid-Atlantic Ridge and the Azores hot spot during the last 85 Myr: Emplacement and rifting of the hot spot-derived plateaus, *Geochemistry, Geophysics, Geosystems,* 4**,** 8514.

Golebiowski, B., 2012. *Seismicity analysis offshore in the region of São Miguel (Azores)*, Diploma, University Hamburg.

Grevemeyer, I., 1999. Isostatic geoid anomalies over mid-plate swells in the Central North Atlantic, *Journal of Geodynamics,* 28**,** 41-50.

Grevemeyer, I., Weigel, W. & Jennrich, C., 1998. Structure and ageing of oceanic crust at 14°S on the East Pacific Rise, *Geophysical Journal International,* 135**,** 573-584.

Grimison, N.L. & Chen, W.-P., 1986. The Azores-Gibraltar Plate Boundary: Focal mechanisms, depths of earthquakes, and their tectonic implications, *Journal of Geophysical Research: Solid Earth,* 91**,** 2029-2047.

Gueydan, F. & Précigout, J., 2014. Modes of continental rifting as a function of ductile strain localization in the lithospheric mantle, *Tectonophysics,* 612–613**,** 18-25.

Guillot, S., Schwartz, S., Reynard, B., Agard, P. & Prigent, C., 2015. Tectonic significance of serpentinites, *Tectonophysics,* 646**,** 1-19.

Gutscher, M.-A., Malod, J., Rehault, J.-P., Contrucci, I., Klingelhoefer, F., Mendes-Victor, L. & Spakman, W., 2002. Evidence for active subduction beneath Gibraltar, *Geology,* 30**,** 1071-1074.

Hayward, N., Watts, A., Westbrook, G. & Collier, J., 1999. A seismic reflection and GLORIA study of compressional deformation in the Gorringe Bank region, eastern North Atlantic, *Geophysics Journal International,* 138**,** 831-850.

Hensen, C., Scholz, F., Nuzzo, M., Valadares, V., Gràcia, E., Terrinha, P., Liebetrau, V., Kaul, N., Silva, S., Martínez-Loriente, S., Bartolome, R., Piñero, E., Magalhães, V.H., Schmidt, M., Weise, S.M., Cunha, M., Hilario, A., Perea, H., Rovelli, L. & Lackschewitz, K., 2015. Strike-slip faults mediate the rise of crustal-derived fluids and mud volcanism in the deep sea, *Geology*.

Horen, H., Zamora, M. & Dubuisson, G., 1996. Seismic waves velocities and anisotropy in serpentinized peridotites from xigaze ophiolite: Abundance of serpentine in slow spreading ridge, *Geophysical Research Letters,* 23**,** 9-12.

Hübscher, C., 2013. Tragica - Cruise No. M79/2 - August 26 – September 21, 2009 - Ponta Delgada (Azores / Portugal) – Las Palmas (Canary Islands / Spain), pp. 37DFG Senatskommission für Ozeanographie.

Jiménez-Munt, I., Fernàndez, M., Torne, M. & Bird, P., 2001. The transition from linear to diffuse plate boundary in the Azores-Gibraltar region: results from a thin-sheet model, *Earth and Planetary Science Letters,* 192**,** 175-189.

Jiménez-Munt, I. & Negredo, A.M., 2003. Neotectonic modelling of the western part of the Africa-Eurasia plate boundary: from the Mid-Atlantic ridge to Algeria, *Earth and Planetary Science Letters,* 205**,** 257-271.

Johnston, A.C., 1996. Seismic moment assessment of earthquakes in stable continental regions—III. New Madrid 1811–1812, Charleston 1886 and Lisbon 1755, *Geophysical Journal International,* 126**,** 314-344.

Korenaga, J., Kelemen, P.B. & Holbrook, W.S., 2002. Methods for resolving the origin of large igneous provinces from crustal seismology, *Journal of Geophysical Research: Solid Earth,* 107**,** ECV 1-1-ECV 1-27.

Krause, D.C. & Watkins, N.D., 1970. North Atlantic Crustal Genesis in the Vicinity of the Azores, *Geophysical Journal of the Royal Astronomical Society,* 19**,** 261-283.

Loureiro, A., Afilhado, A., Matias, L., Moulin, M. & Aslanian, D., 2016. Monte Carlo approach to assess the uncertainty of wide-angle layered models: Application to the Santos Basin, Brazil, *Tectonophysics,* 683**,** 286-307.

Lourenço, N., Miranda, J.M., Luis, J.F., Ribeiro, A., Victor, L.A.M., Madeira, J. & Needham, H.D., 1998. Morpho-tectonic analysis of the Azores Volcanic Plateau from a new bathymetric compilation of the area, *Marine Geophysical Researches,* 20**,** 141-156.

Lowell, R.P. & Rona, P.A., 2002. Seafloor hydrothermal systems driven by the serpentinization of peridotite, *Geophysical Research Letters,* 29**,** 26-21-26-24.

Luis, J.F. & Miranda, J.M., 2008. Reevaluation of magnetic chrons in the North Atlantic between 35°N and 47°N: Implications for the formation of the Azores Triple Junction and associated plateau, *Journal of Geophysical Research: Solid Earth,* 113**,** B10105.

Luis, J.F., Miranda, J.M., Galdeano, A. & Patriat, P., 1998. Constraints on the structure of the Azores spreading center from gravity data, *Marine Geophysical Researches,* 20**,** 157-170.

Luis, J.F., Miranda, J.M., Galdeano, A., Patriat, P., Rossignol, J.C. & Mendes Victor, L.A., 1994. The Azores triple junction evolution since 10 Ma from an aeromagnetic survey of the Mid-Atlantic Ridge, *Earth and Planetary Science Letters,* 125**,** 439-459.

Luis, J.F. & Neves, M.C., 2006. The isostatic compensation of the Azores Plateau: A 3D admittance and coherence analysis, *Journal of Volcanology and Geothermal Research,* 156**,** 10-22.

Madeira, J., Brum da Silveira, A., Hipólito, A. & Carmo, R., 2015. Chapter 3 Active tectonics in the central and eastern Azores islands along the Eurasia–Nubia boundary: a review, *Geological Society, London, Memoirs,* 44**,** 15-32.

Martínez-Loriente, S., Sallarès, V., Gràcia, E., Bartolome, R., Dañobeitia, J.J. & Zitellini, N., 2014. Seismic and gravity constraints on the nature of the basement in the Africa-Eurasia plate boundary: New insights for the geodynamic evolution of the SW Iberian margin, *Journal of Geophysical Research: Solid Earth,* 119**,** 2013JB010476.

Matias, L., Dias, N.A., Morais, I., Vales, D., Carrilho, F., Madeira, J., Gaspar, J.L., Senos, L. & Silveira, A.B., 2007. The 9th of July 1998 Faial Island (Azores, North Atlantic) seismic sequence, *J Seismol,* 11**,** 275-298.

Matias, L.M., Cunha, T., Annunziato, A., Baptista, M.A. & Carrilho, F., 2013. Tsunamigenic earthquakes in the Gulf of Cadiz: fault model and recurrence, *Nat. Hazards Earth Syst. Sci.,* 13**,** 1-13.

McKenzie, D., 1972. Active Tectonics of the Mediterranean Region, *Geophysical Journal of the Royal Astronomical Society,* 30**,** 109-185.

Merle, R., Jourdan, F. & Girardeau, J., 2018. Geochronology of the Tore-Madeira Rise seamounts and surrounding areas: a review, *Australian Journal of Earth Sciences,* 65**,** 591-605.

Merle, R., Schärer, U., Girardeau, J. & Cornen, G., 2006. Cretaceous seamounts along the continent–ocean transition of the Iberian margin: U–Pb ages and Pb–Sr–Hf isotopes, *Geochimica et Cosmochimica Acta,* 70**,** 4950-4976.

Miller, D.J. & Christensen, N.I., 1997. Seismic velocities of lower crustal and upper mantle rocks from the slow-spreading Mid-Atlantic Ridge, south of the Kane Transform Zone (MARK). *in Karson, J.A., Cannat, M., Miller, D.J., and Elthon, D. (Eds.), Proc. ODP, Sci. Results, 153: College Station, TX (Ocean Drilling Program)*, pp. 437–454.

Miranda, J.M., Luis, J.-F., Lourenço, N. & Goslin, J., 2014. Distributed deformation close to the Azores Triple "Point", *Marine Geology,* 355**,** 27-35.

Miranda, J.M., Luis, J.F., Lourenço, N. & Fernandes, R.M.S., 2015. Chapter 2 The structure of the Azores Triple Junction: implications for São Miguel Island, *Geological Society, London, Memoirs,* 44**,** 5-13.

Moore, R.B., 1991. Geologic map of Sao Miguel, Azores. *in IMAP*.

Mueller, S. & Phillips, R.J., 1991. On The initiation of subduction, *Journal of Geophysical Research: Solid Earth,* 96**,** 651-665.

Müller, R.D., Sdrolias, M., Gaina, C. & Roest, W.R., 2008. Age, spreading rates, and spreading asymmetry of the world's ocean crust, *Geochemistry, Geophysics, Geosystems,* 9**,** Q04006.

Neres, M., Bouchez, J.L., Terrinha, P., Font, E., Moreira, M., Miranda, R., Launeau, P. & Carvallo, C., 2014. Magnetic fabric in a Cretaceous sill (Foz da Fonte, Portugal): flow model and implications for regional magmatism, *Geophysical Journal International,* 199**,** 78-101.

Neres, M., Carafa, M.M.C., Fernandes, R.M.S., Matias, L., Duarte, J.C., Barba, S. & Terrinha, P., 2016. Lithospheric deformation in the Africa-Iberia plate boundary: Improved neotectonic modeling testing a basal-driven Alboran plate, *Journal of Geophysical Research: Solid Earth,* 121**,** 6566-6596.

Omira, R., Neres, M. & Batista, L., 2019. Chapter 8 - The Gloria Transform Fault—NE Atlantic: Seismogenic and Tsunamigenic Potential. *in Transform Plate Boundaries and Fracture Zones*, pp. 157-167, ed. Duarte, J. C. Elsevier.

Omira, R., Ramalho, I., Terrinha, P., Baptista, M.A., Batista, L. & Zitellini, N., 2016. Deep-water seamounts, a potential source of tsunami generated by landslides? The Hirondelle Seamount, NE Atlantic, *Marine Geology,* 379**,** 267-280.

Palano, M., González, P.J. & Fernández, J., 2015. The Diffuse Plate boundary of Nubia and Iberia in the Western Mediterranean: Crustal deformation evidence for viscous coupling and fragmented lithosphere, *Earth and Planetary Science Letters,* 430**,** 439-447.

Peirce, C. & Barton, P.J., 1991. Crustal structure of the Madeira-Tore Rise, eastern North Atlantic—results of a DOBS wide-angle and normal incidence seismic experiment in the Josephine Seamount region, *Geophysical Journal International,* 106**,** 357-378.

Potts, C.G., Calvert, A.J. & White, R.S., 1986. Crustal structure of Atlantic Fracture Zones - III. The Tydeman fracture zone, *Geophysical Journal International,* 86**,** 909-942.

Purdy, G.M., 1975. The Eastern End of the Azores-Gibraltar Plate Boundary, *Geophysical Journal of the Royal Astronomical Society,* 43**,** 973-1000.

Purdy, G.M., 1983. The seismic structure of 140 Myr old crust in the western central Atlantic Ocean, *Geophysical Journal International,* 72**,** 115-137.

Roque, C., Simões, M., Lourenço, N. & Pinto de Abreu, M., 2009. Evidence of intraplate deformation in the West Madeira Abyssal Plain (eastern North Atlantic) from seismic reflection and multibeam swath bathymetry data, *EGU, General Assembly 2009*.

Rosas, F.M., Duarte, J.C., Neves, M.C., Terrinha, P., Silva, S., Matias, L., Gràcia, E. & Bartolome, R., 2012. Thrust–wrench interference between major active faults in the Gulf of Cadiz (Africa–Eurasia plate boundary, offshore SW Iberia): Tectonic implications from coupled analog and numerical modeling, *Tectonophysics,* 548–549**,** 1-21.

Rosenbaum, G., Lister, G.S. & Duboz, C., 2002. Relative motions of Africa, Iberia and Europe during Alpine orogeny, *Tectonophysics,* 359**,** 117-129.

Sallarès, V., Gailler, A., Gutscher, M.-A., Graindorge, D., Bartolomé, R., Gràcia, E., Díaz, J., Dañobeitia, J.J. & Zitellini, N., 2011. Seismic evidence for the presence of Jurassic oceanic crust in the central Gulf of Cadiz (SW Iberian margin), *Earth and Planetary Science Letters,* 311**,** 112-123.

Sallarès, V., Martínez-Loriente, S., Prada, M., Gràcia, E., Ranero, C., Gutscher, M.-A., Bartolome, R., Gailler, A., Dañobeitia, J.J. & Zitellini, N., 2013. Seismic evidence of exhumed mantle rock basement at the Gorringe Bank and the adjacent Horseshoe and Tagus abyssal plains (SW Iberia), *Earth and Planetary Science Letters,* 365**,** 120-131.

Sartori, R., Torelli, L., Zitellini, N., Peis, D. & Lodolo, E., 1994. Eastern Segment of the Azores-Gibraltar Line (Central-Eastern Atlantic) - an Oceanic Plate Boundary with Diffuse Compressional Deformation, *Geology,* 22**,** 555-558.

Schettino, A. & Turco, E., 2009. Breakup of Pangaea and plate kinematics of the central Atlantic and Atlas regions, *Geophysical Journal International,* 178**,** 1078-1097.

Schmincke, H. & Sumita, M., 1998. *Volcanic evolution of Gran Canaria reconstructed from apron sediments: synthesis of VICAP Project Drilling,* edn, Vol. 157, pp. Pages.

Serpelloni, E., Vannucci, G., Pondrelli, S., Argnani, A., Casula, G., Anzidei, M., Baldi, P. & Gasperini, P., 2007. Kinematics of the Western Africa-Eurasia plate boundary from focal mechanisms and GPS data, *Geophysical Journal International,* 169**,** 1180-1200.

Shaw, P.R., 1994. Age variations of oceanic crust Poisson's ratio: Inversion and a porosity evolution model, *Journal of Geophysical Research: Solid Earth,* 99**,** 3057-3066.

Sibrant, A.L.R., Hildenbrand, A., Marques, F.O., Weiss, B., Boulesteix, T., Hübscher, C., Lüdmann, T., Costa, A.C.G. & Catalão, J.C., 2015. Morpho-structural evolution of a volcanic island developed inside an active oceanic rift: S. Miguel Island (Terceira Rift, Azores), *Journal of Volcanology and Geothermal Research,* 301**,** 90-106.

Silveira, G., Stutzmann, E., Davaille, A., Montagner, J.-P., Mendes-Victor, L. & Sebai, A., 2006. Azores hotspot signature in the upper mantle, *Journal of Volcanology and Geothermal Research,* 156**,** 23-34.

Silveira, G., Vinnik, L., Stutzmann, E., Farra, V., Kiselev, S. & Morais, I., 2010. Stratification of the Earth beneath the Azores from P and S receiver functions, *Earth and Planetary Science Letters,* 299**,** 91-103.

Spieker, K., Rondenay, S., Ramalho, R., Thomas, C. & Helffrich, G., 2018. Constraints on the structure of the crust and lithosphere beneath the Azores Islands from teleseismic receiver functions, *Geophysical Journal International,* 213**,** 824-835.

Srivastava, S.P., Roest, W.R., Kovacs, L.C., Oakey, G., Lévesque, S., Verhoef, J. & Macnab, R., 1990. Motion of Iberia since the Late Jurassic: Results from detailed aeromagnetic measurements in the Newfoundland Basin, *Tectonophysics,* 184**,** 229-260.

Stich, D., Martín, R. & Morales, J., 2010. Moment tensor inversion for Iberia-Maghreb earthquakes 2005-2008, *Tectonophysics,* 483**,** 390-398.

Terrinha, P., Kullberg JC, Neres M, Alves T, Ramos A, Ribeiro C, Mata J, Pinheiro L, Afilhado A, Matias L, Luís J, JA, M. & O., F., 2019. Ch 6. Rifting of the Southwest and West Iberia Continental Margins, ch 6. *in The Geology of Iberia: A Geodynamic Approach*, pp. pp. 251-284, eds. Quesada, C. & Oliveira, J. T. Springer International Publishing, Switzerland AG.

Terrinha, P., Matias, L., Vicente, J., Duarte, J., Luís, J., Pinheiro, L., Lourenço, N., Diez, S., Rosas, F., Magalhães, V., Valadares, V., Zitellini, N., Roque, C. & Víctor, L.M., 2009. Morphotectonics and strain partitioning at the Iberia-Africa plate boundary from multibeam and seismic reflection data, *Marine Geology,* 267**,** 156-174.

Terrinha, P., Pueyo, E.L., Aranguren, A., Kullberg, J.C., Kullberg, M.C., Casas-Sainz, A. & Azevedo, M.d.R., 2018. Gravimetric and magnetic fabric study of the Sintra Igneous complex: laccolith-plug emplacement in the Western Iberian passive margin, *International Journal of Earth Sciences,* 107**,** 1807-1833.

Torsvik, T.H., Van der Voo, R., Preeden, U., Mac Niocaill, C., Steinberger, B., Doubrovine, P.V., van Hinsbergen, D.J.J., Domeier, M., Gaina, C., Tohver, E., Meert, J.G., McCausland, P.J.A. & Cocks, L.R.M., 2012. Phanerozoic polar wander, palaeogeography and dynamics, *Earth-Science Reviews,* 114**,** 325-368.

Udías, A., Arroyo, A.L. & Mezcua, J., 1976. Seismotectonic of the Azores-Alboran region, *Tectonophysics,* 31**,** 259-289.

Verzhbitskii, E., Kononov, M., Byakov, A. & Grinberg, O., 2010. Specific features of the genesis of the Azores-Gibraltar fault zone (North Atlantic), *Izvestiya Physics of the Solid Earth,* 46**,** 872-882.

Walther, C.H.E., 2003. The crustal structure of the Cocos ridge off Costa Rica, *Journal of Geophysical Research: Solid Earth,* 108**,** 2136.

Watremez, L., Leroy, S., Rouzo, S., d'Acremont, E., Unternehr, P., Ebinger, C., Lucazeau, F. & Al-Lazki, A., 2011. The crustal structure of the north-eastern Gulf of Aden continental margin: insights from wide-angle seismic data, *Geophysical Journal International,* 184**,** 575-594.

Weiß, B.J., Hübscher, C. & Lüdmann, T., 2015. The tectonic evolution of the southeastern Terceira Rift/São Miguel region (Azores), *Tectonophysics,* 654**,** 75-95.

White, R.S., Detrick, R.S., Sinha, M.C. & Cormier, M.H., 1984. Anomalous seismic crustal structure of oceanic fracture zones, *Geophysical Journal International,* 79**,** 779-798.

White, R.S., McKenzie, D. & O'Nions, R.K., 1992. Oceanic crustal thickness from seismic measurements and rare earth element inversions, *Journal of Geophysical Research: Solid Earth,* 97**,** 19683-19715.

Wilson, M., 1992. Magmatism and continental rifting during the opening of the South Atlantic Ocean: a consequence of Lower Cretaceous super-plume activity?, *Geological Society, London, Special Publications,* 68**,** 241-255.

Zelt, C. & Ellis, R., 1988. Practical and efficient ray tracing in two-dimensional media for rapid traveltime and amplitude forward modeling, *Canadian Journal of Exploration Geophysics,* 24**,** 16-31.

Zelt, C.A., 1994. 3-D velocity structure from simultaneous traveltime inversion of in-line seismic data along intersecting profiles, *Geophysical Journal International,* 118**,** 795-801.

Zelt, C.A., 1999. Modelling strategies and model assessment for wide-angle seismic traveltime data, *Geophysical Journal International,* 139**,** 183-204.

Zelt, C.A. & Forsyth, D.A., 1994. Modeling wide-angle seismic data for crustal structure: Southeastern Grenville Province, *Journal of Geophysical Research: Solid Earth,* 99**,** 11687-11704.

Zelt, C.A. & Smith, R.B., 1992. Seismic traveltime inversion for 2-D crustal velocity structure, *Geophysical Journal International,* 108**,** 16-34.

Zitellini, N., Gracia, E., Matias, L., Terrinha, P., Abreu, M.A., DeAlteriis, G., Henriet, J.P., Danobeitia, J.J., Masson, D.G., Mulder, T., Ramella, R., Somoza, L. & Diez, S., 2009. The quest for the Africa-Eurasia plate boundary west of the Strait of Gibraltar, *Earth and Planetary Science Letters,* 280**,** 13-50.

ANNEXES

Annexe 1: Seismic sections from all OBS with Vp waves arrival and interpretation from S.Miguel area. Reduction velocity is 7.5 km/s.

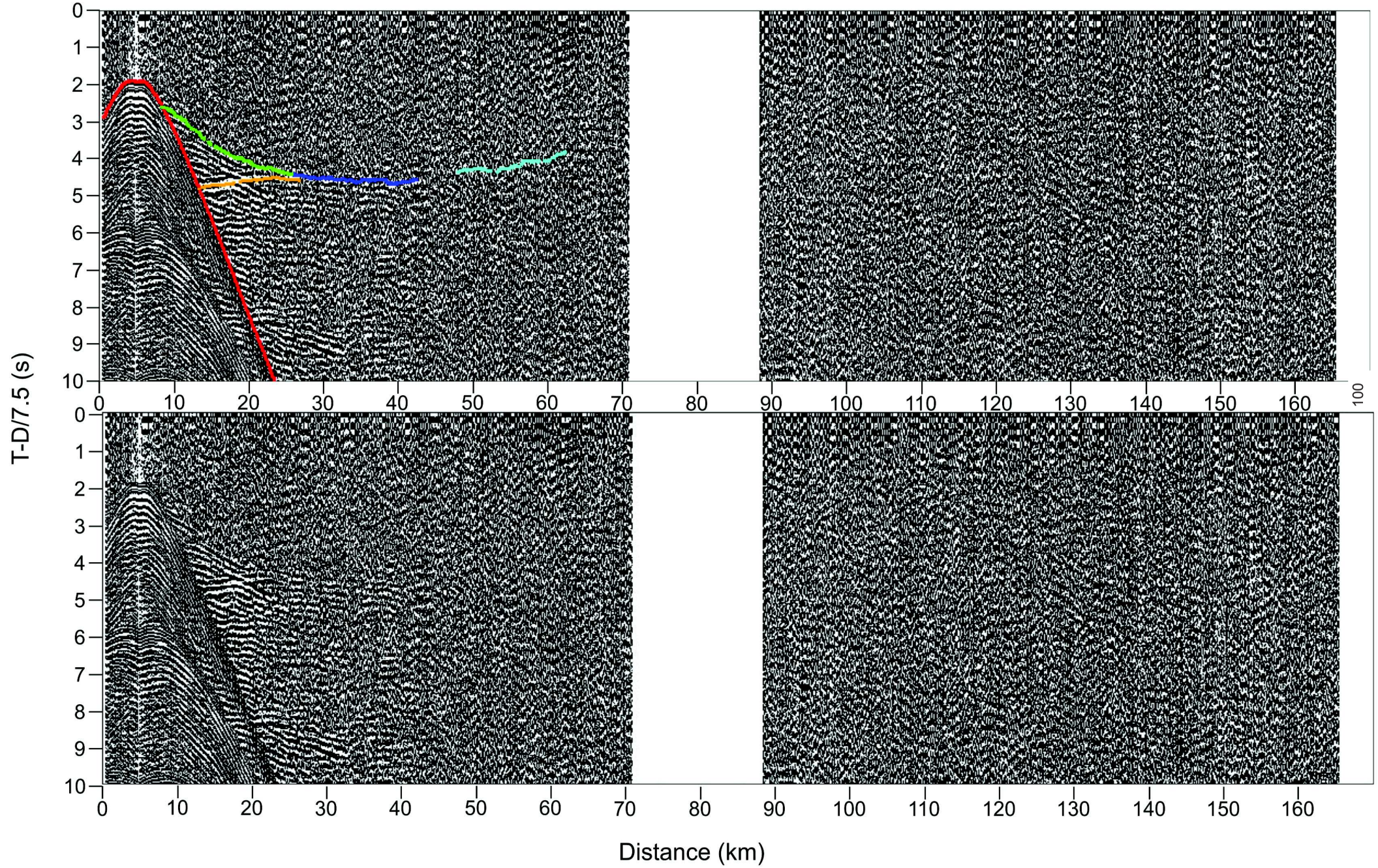
OBS01
T-D/7.5 (s)
0
1
2
3
4
5
6
7
8
9
10
0
10
20
30
40
50
60
70
80
90
100
110
120
130
140
150
160
100
Distance (km)

OBS02

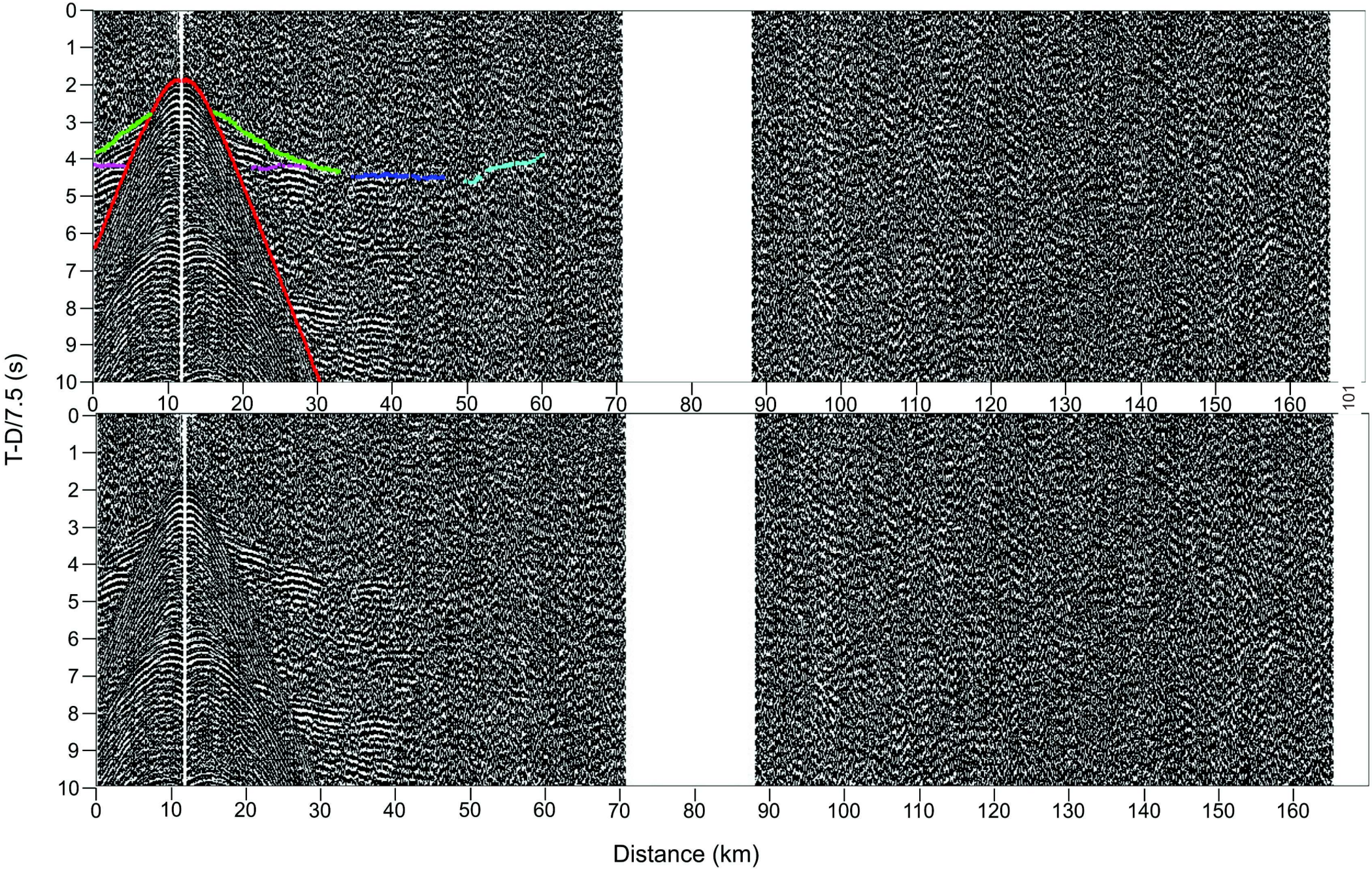
T-D/7.5 (s)
0
1
2
3
4
5
6
7
8
9
10
0
10
20
30
40
50
60
70
80
90
100
110
120
130
140
150
160
101
Distance (km)

OBS03

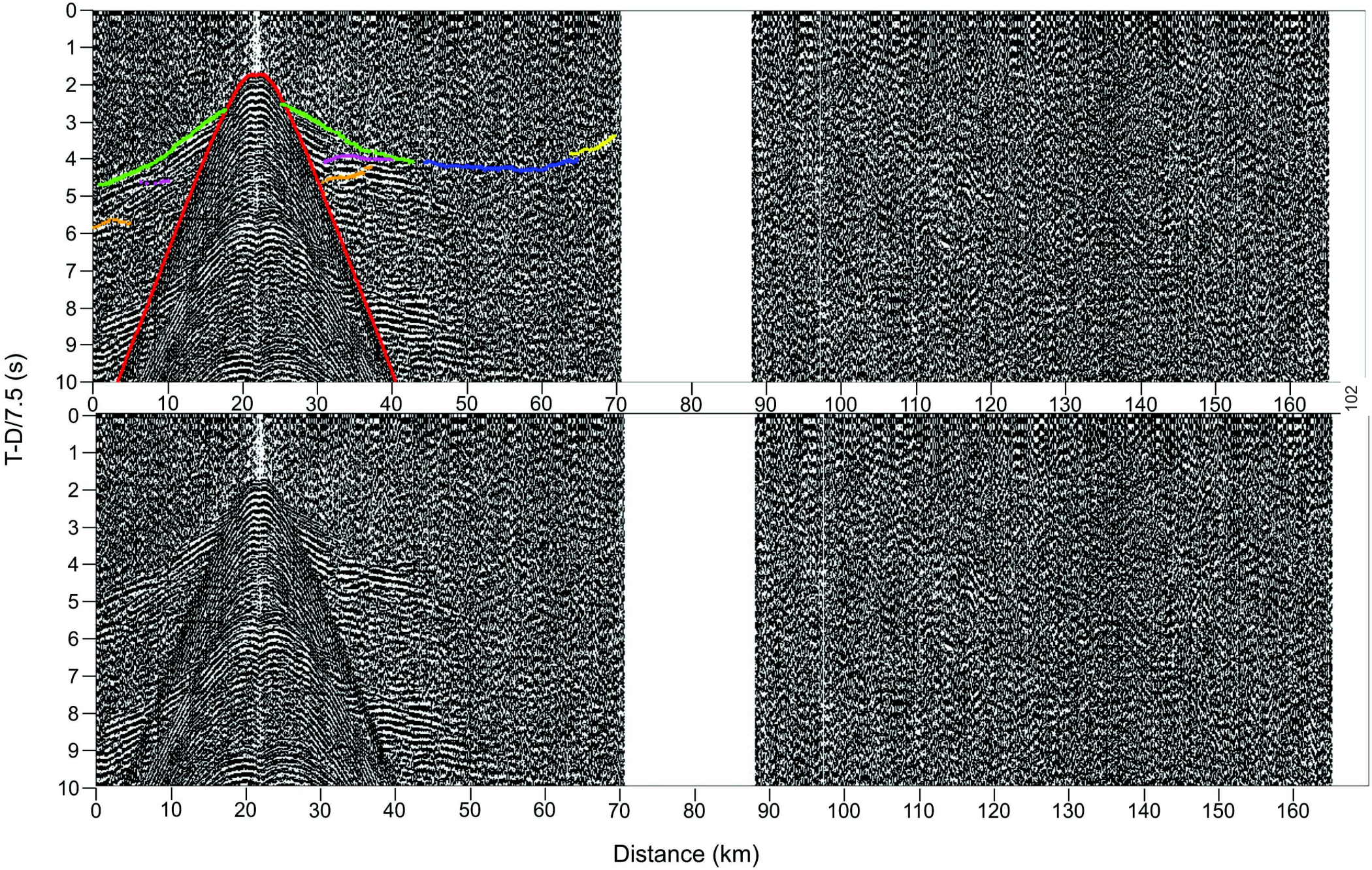
T-D/7.5 (s)
0
1
2
3
4
5
6
7
8
9
10
0
10
20
30
40
50
60
70
80
90
100
110
120
130
140
150
160
102
Distance (km)

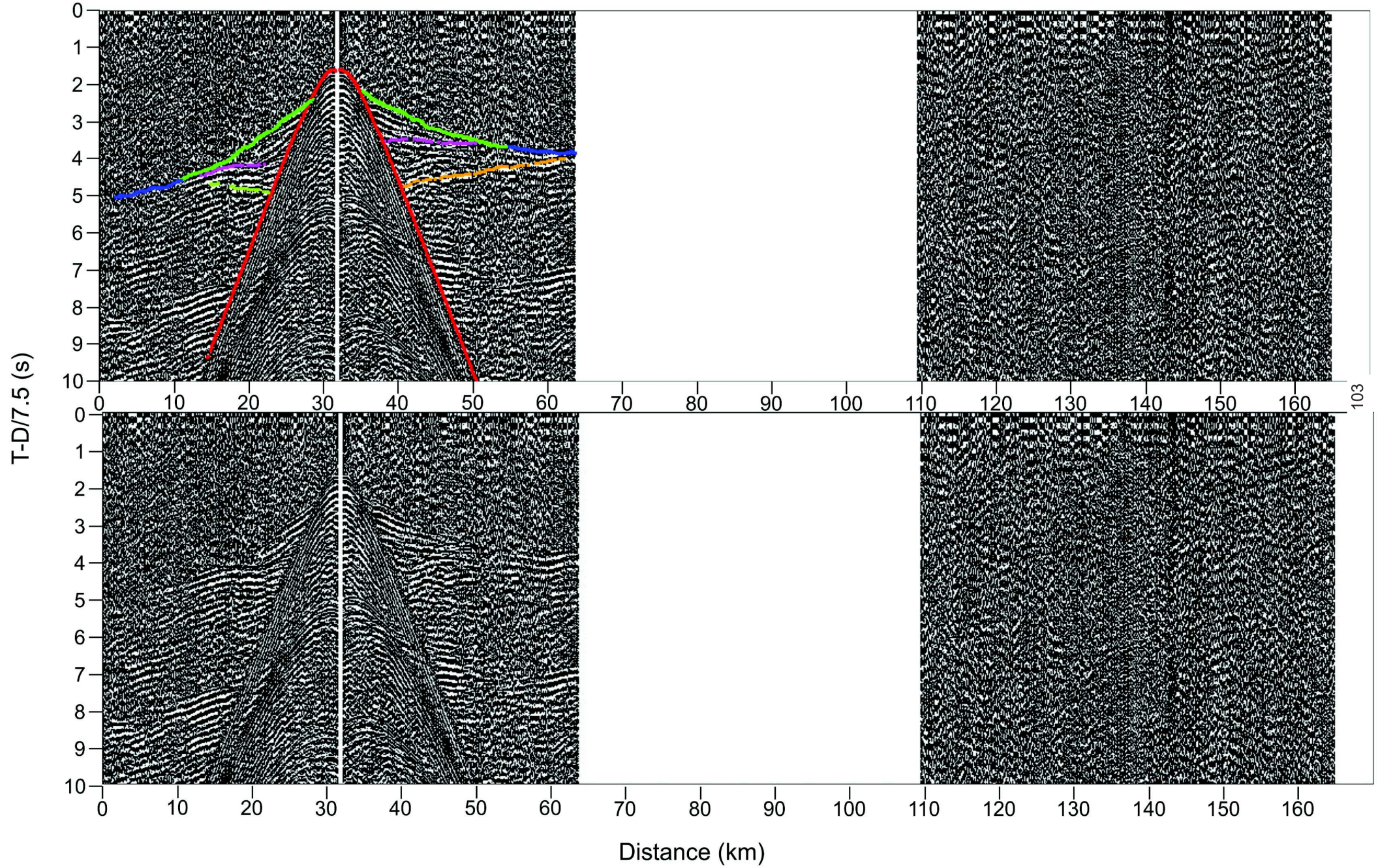
OBS04
T-D/7.5 (s)
0
1
2
3
4
5
6
7
8
9
10
0
10
20
30
40
50
60
70
80
90
100
110
120
130
140
150
160
103
Distance (km)

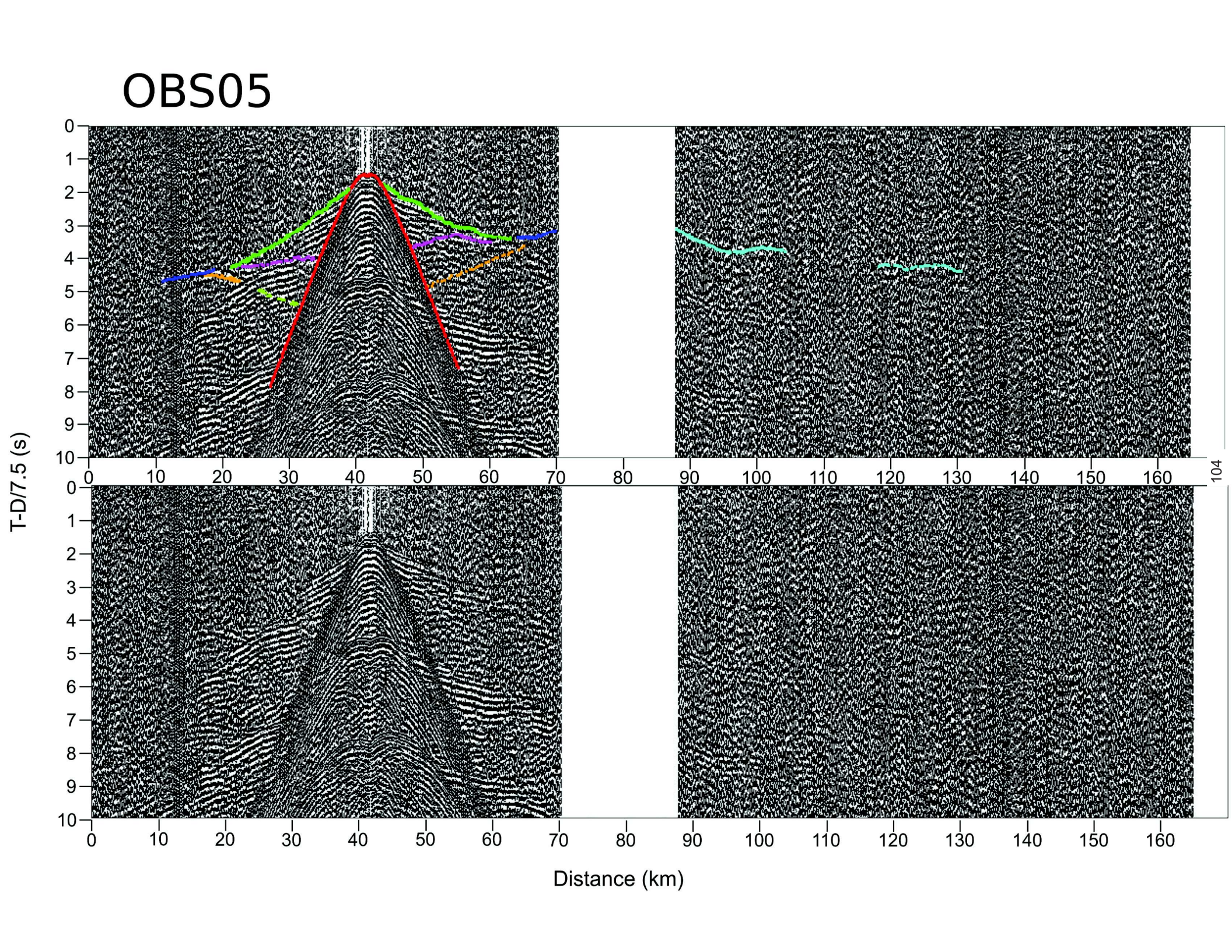
OBS05
T-D/7.5 (s)
Distance (km)
0
1
2
3
4
5
6
7
8
9
10
0
10
20
30
40
50
60
70
80
90
100
110
120
130
140
150
160
104

OBS06

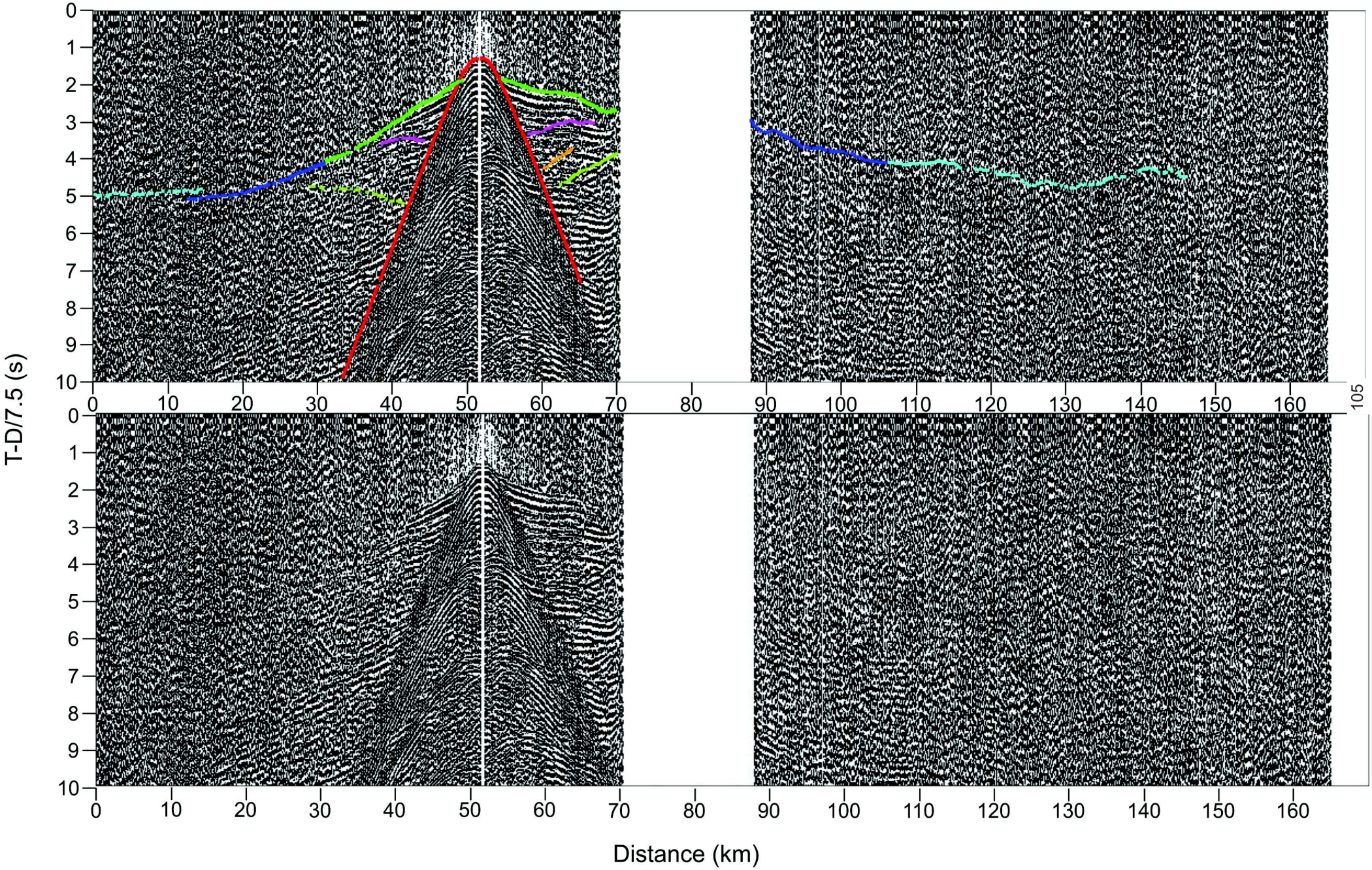
T-D/7.5 (s)
0
1
2
3
4
5
6
7
8
9
10
0
10
20
30
40
50
60
70
80
90
100
110
120
130
140
150
160
105
Distance (km)

OBS07

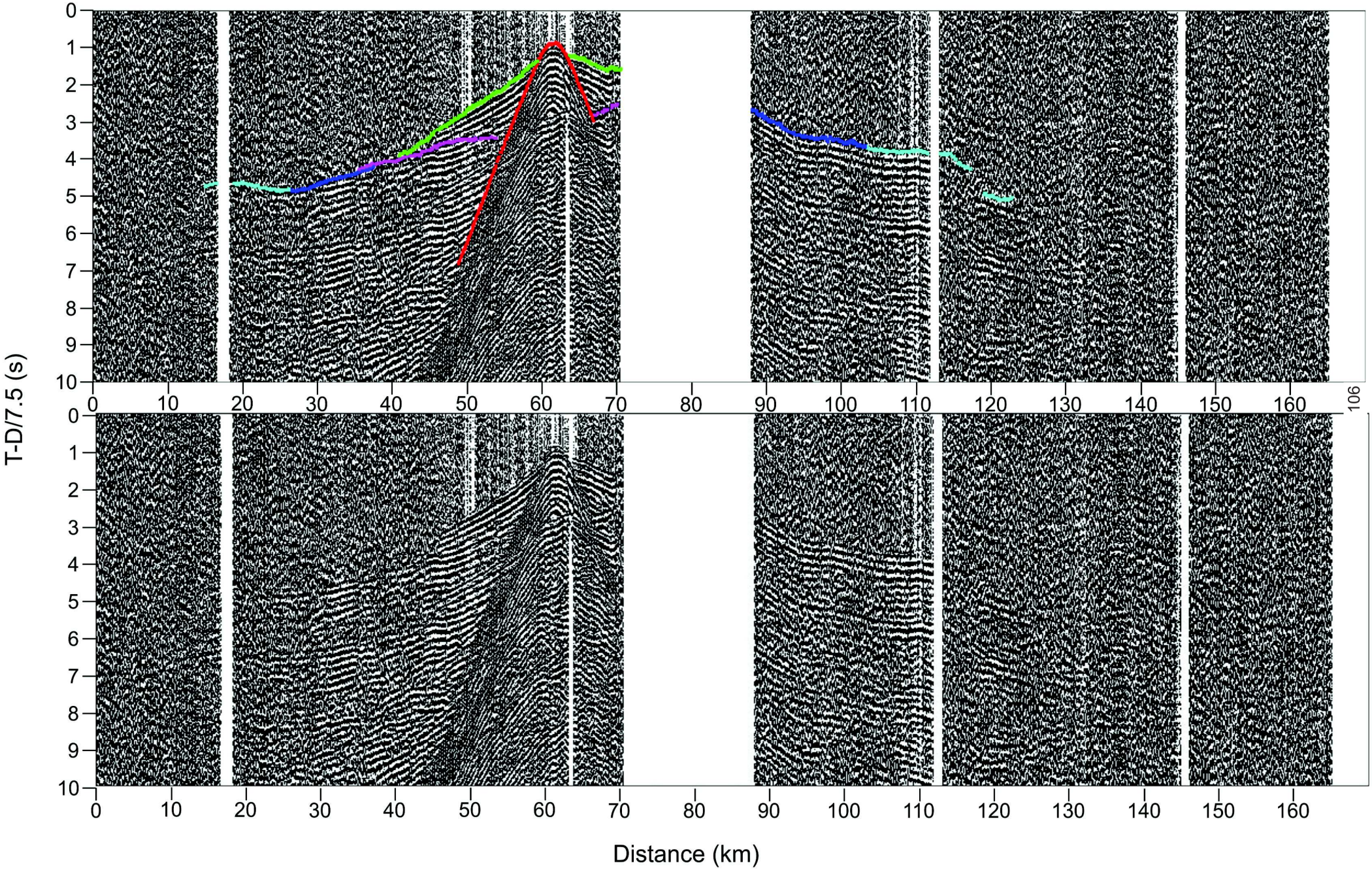
T-D/7.5 (s)
0
1
2
3
4
5
6
7
8
9
10
0
10
20
30
40
50
60
70
80
90
100
110
120
130
140
150
160
106
Distance (km)

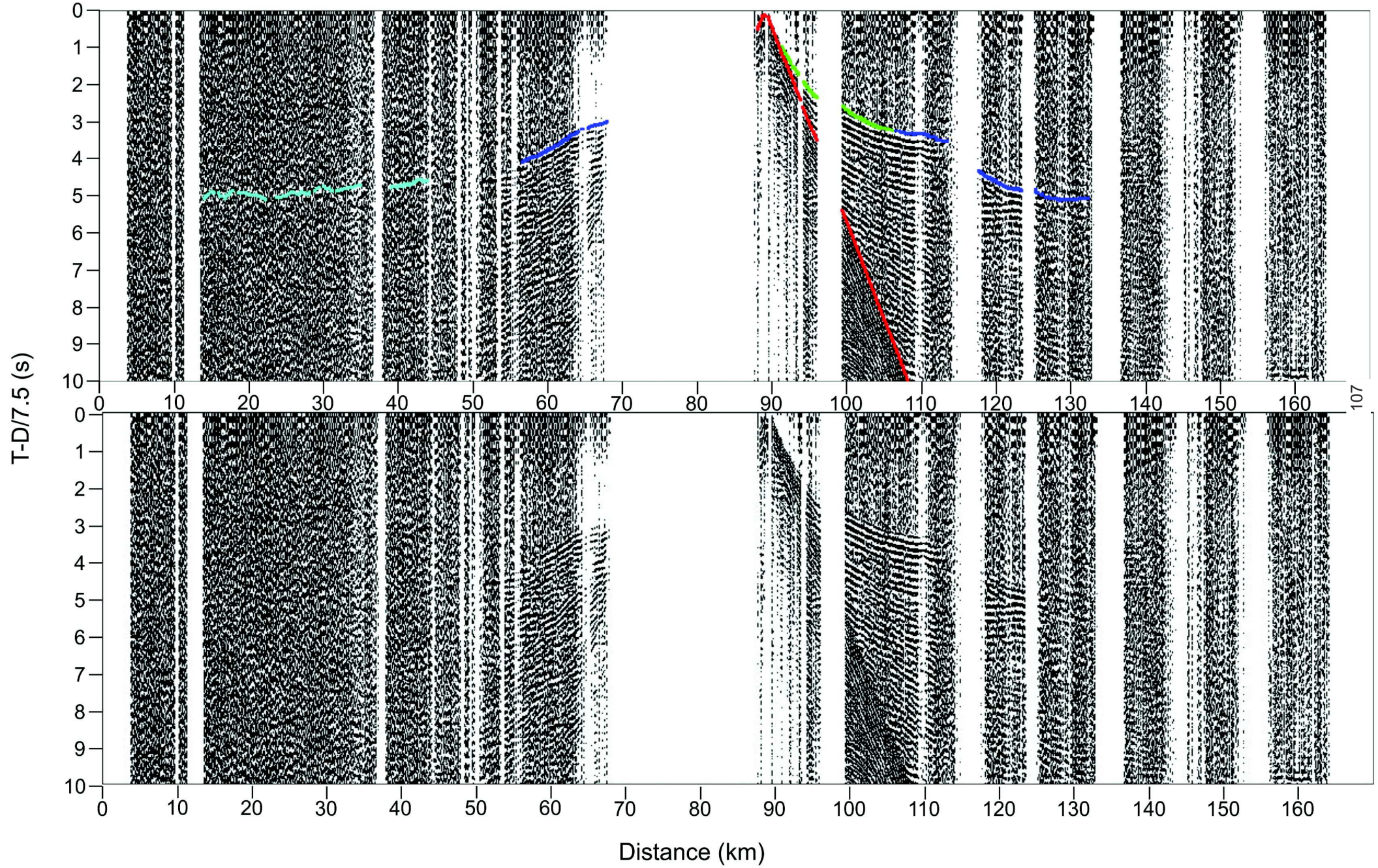
OBS09
T-D/7.5 (s)
0
1
2
3
4
5
6
7
8
9
10
0
10
20
30
40
50
60
70
80
90
100
110
120
130
140
150
160
107
Distance (km)

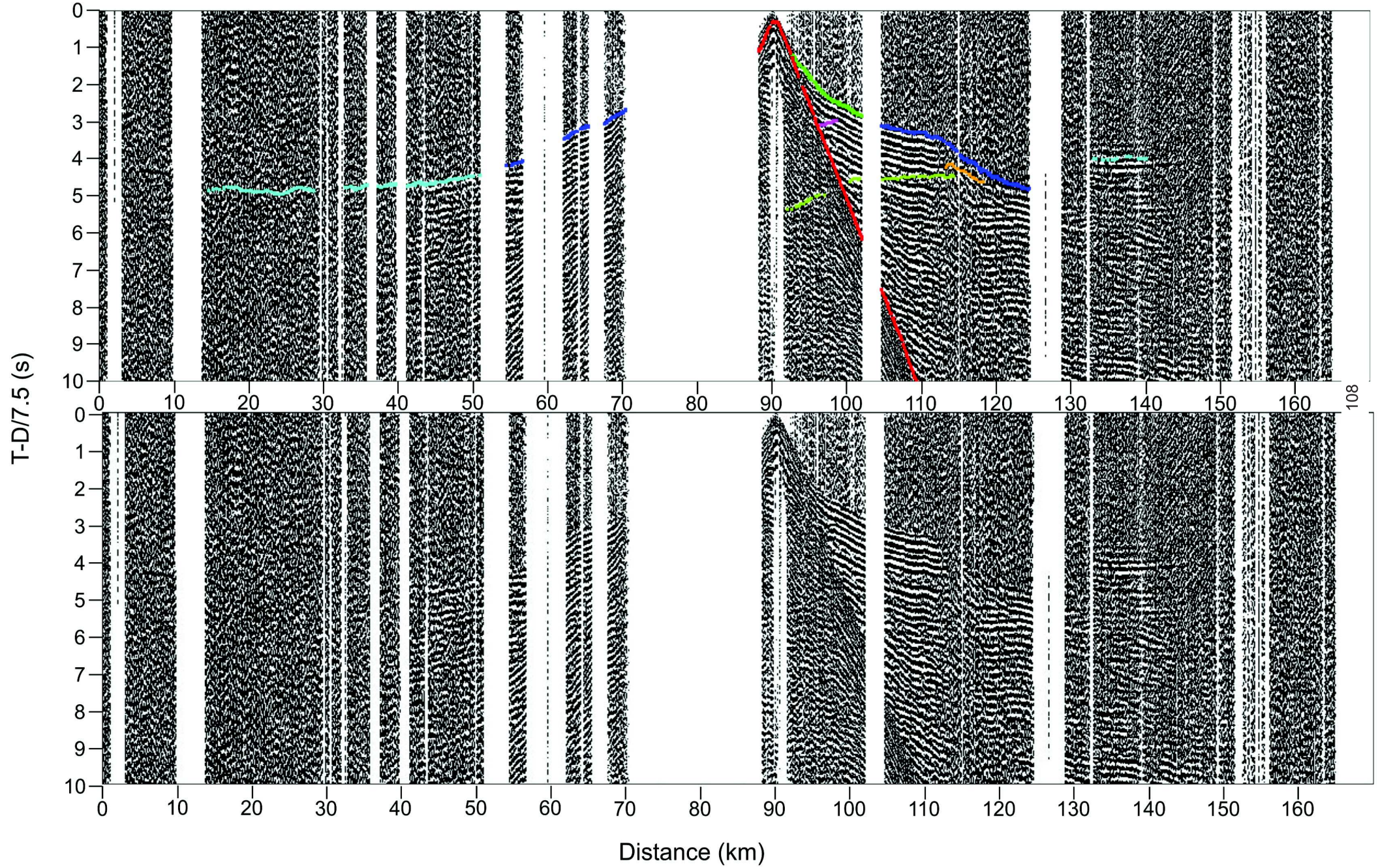
OBS10
T-D/7.5 (s)
0
1
2
3
4
5
6
7
8
9
10
0
10
20
30
40
50
60
70
80
90
100
110
120
130
140
150
160
108
Distance (km)

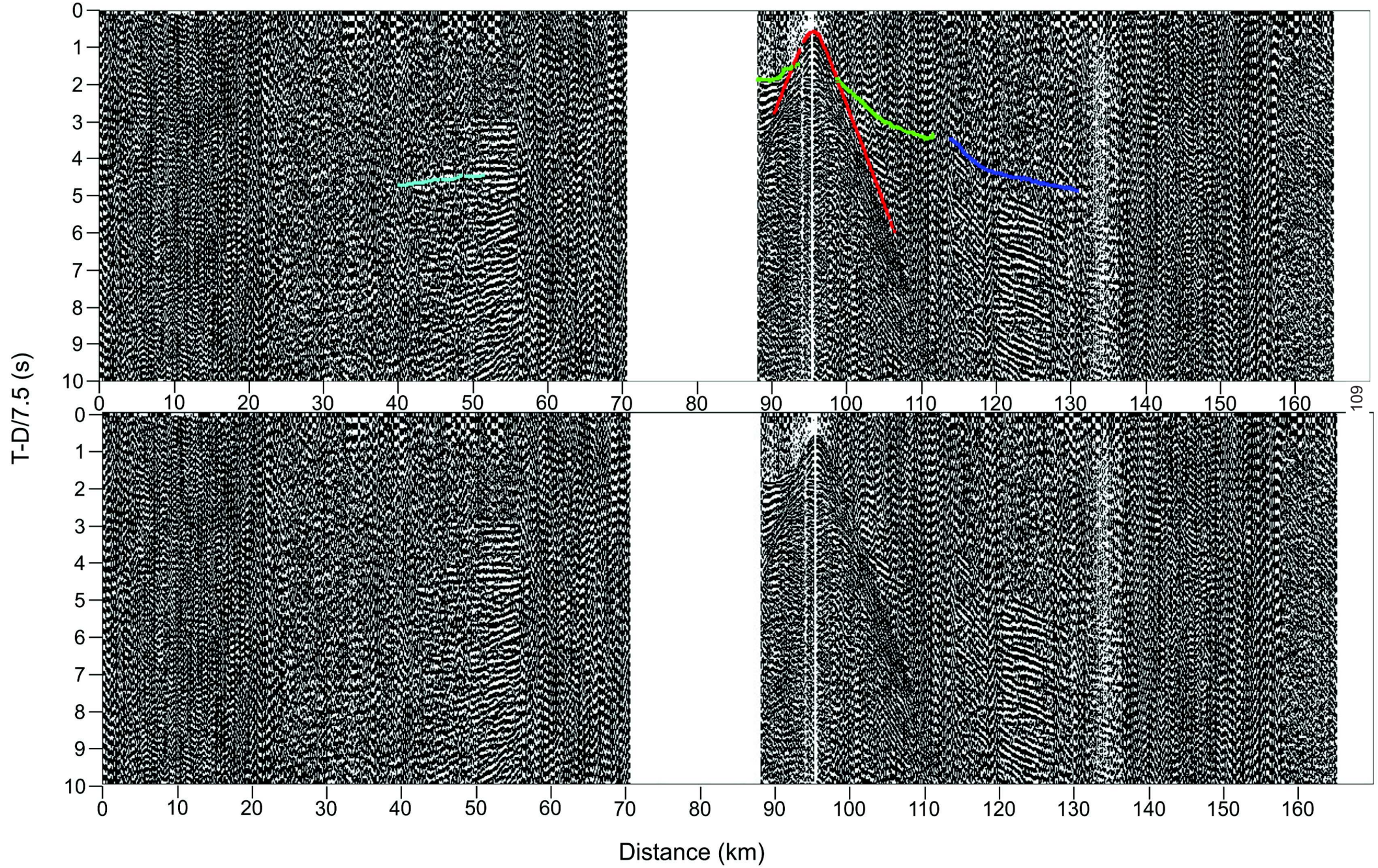
OBS11
T-D/7.5 (s)
0
1
2
3
4
5
6
7
8
9
10
0
10
20
30
40
50
60
70
80
90
100
110
120
130
140
150
160
109
Distance (km)

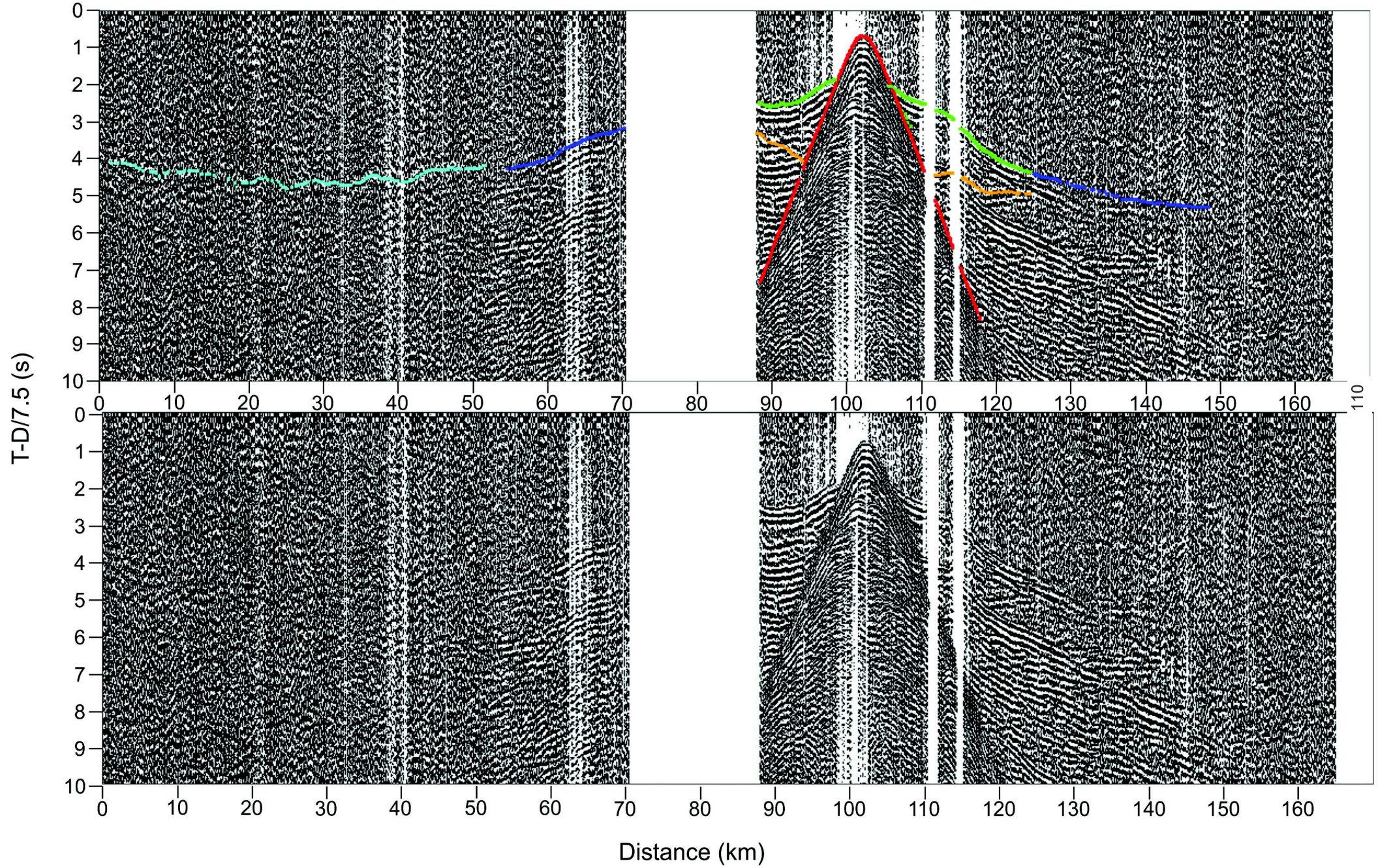
OBS12
T-D/7.5 (s)
0
1
2
3
4
5
6
7
8
9
10
0
10
20
30
40
50
60
70
80
90
100
110
120
130
140
150
160
110
Distance (km)

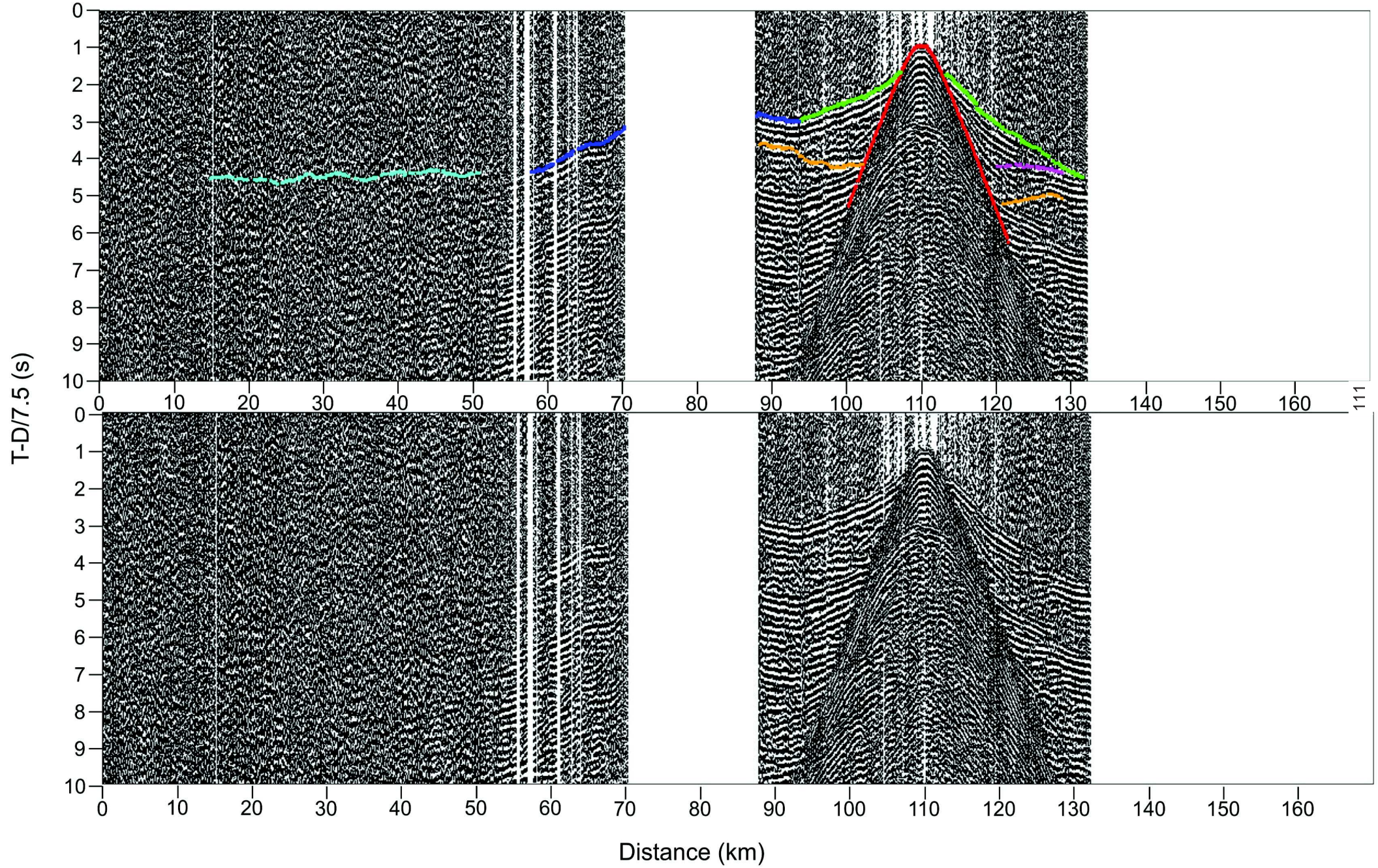
OBS13
T-D/7.5 (s)
0
1
2
3
4
5
6
7
8
9
10
0
10
20
30
40
50
60
70
80
90
100
110
120
130
140
150
160
111
Distance (km)

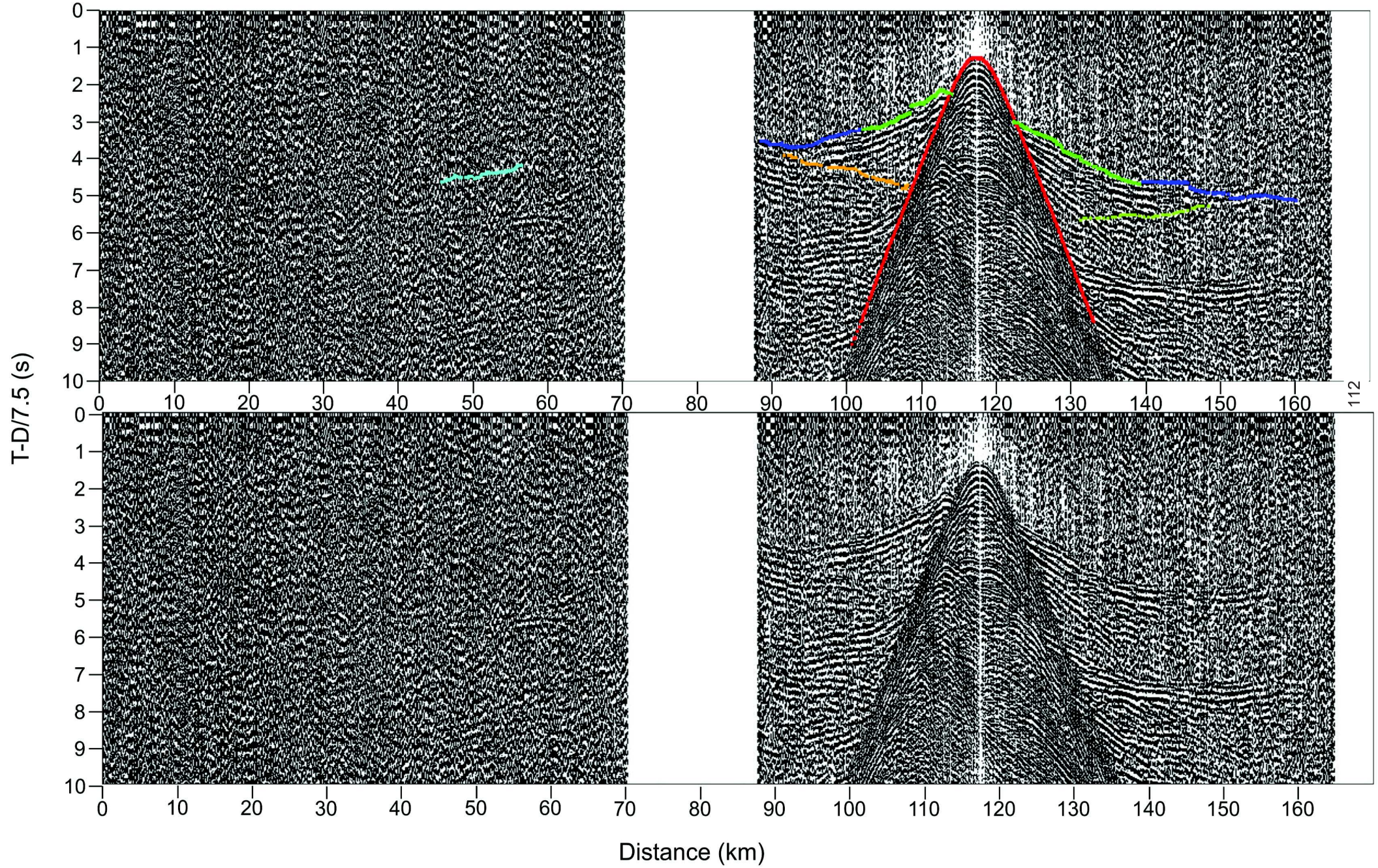
OBS14
T-D/7.5 (s)
0
1
2
3
4
5
6
7
8
9
10
0
10
20
30
40
50
60
70
80
90
100
110
120
130
140
150
160
112
Distance (km)

OBS15

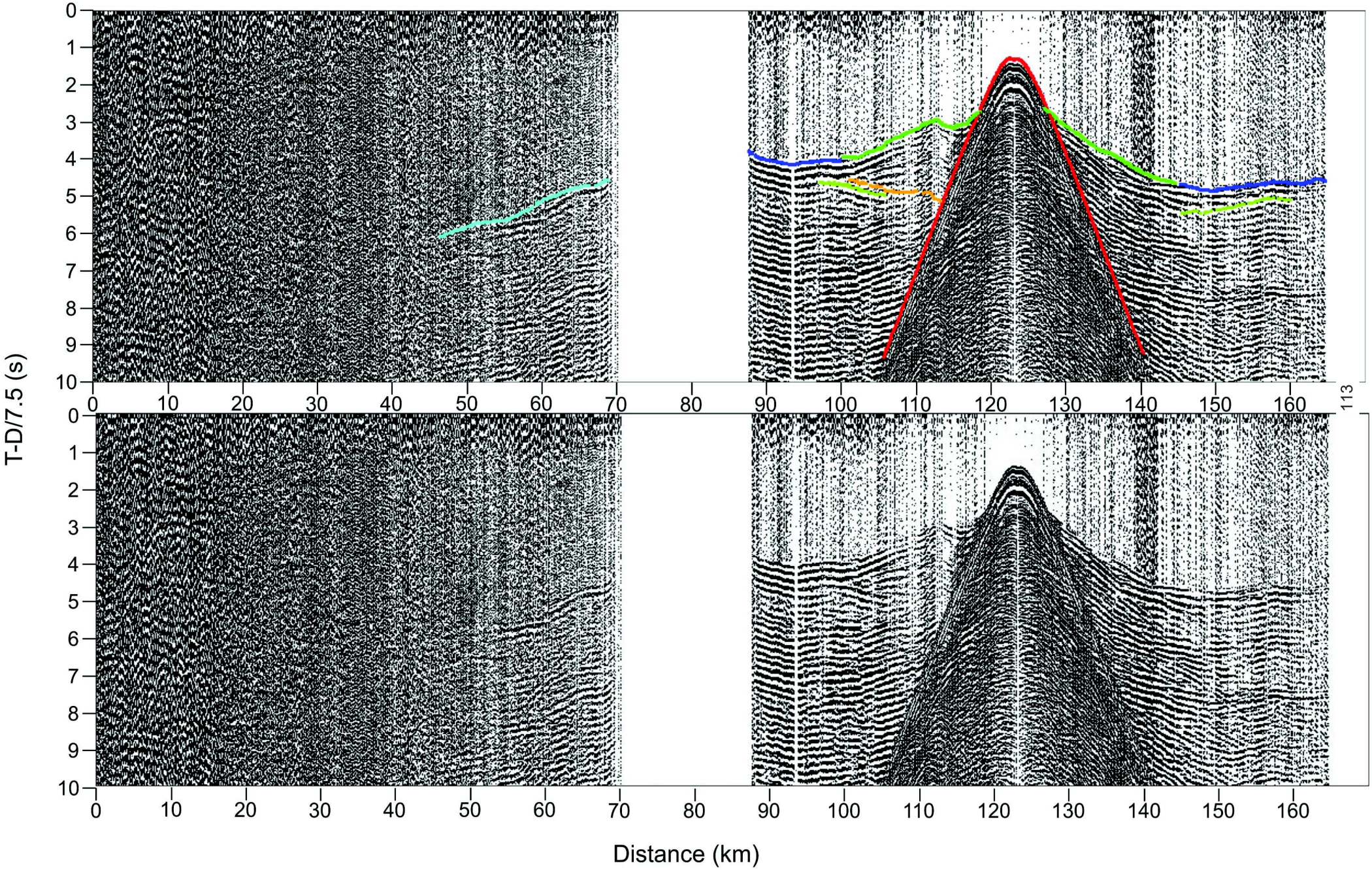
T-D/7.5 (s)
0
1
2
3
4
5
6
7
8
9
10
0
10
20
30
40
50
60
70
80
90
100
110
120
130
140
150
160
113
Distance (km)

OBS16

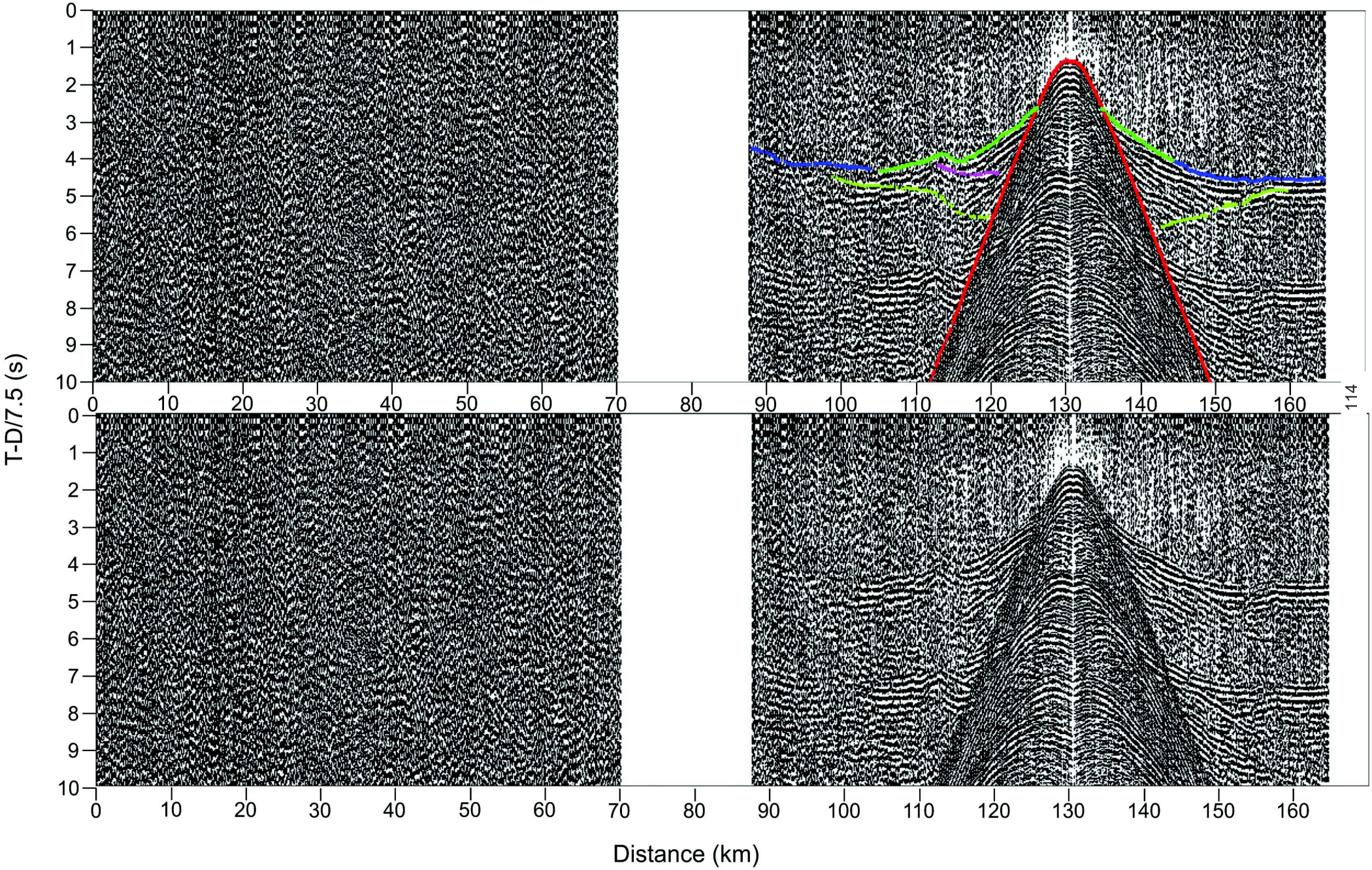
T-D/7.5 (s)
0
1
2
3
4
5
6
7
8
9
10
0
10
20
30
40
50
60
70
80
90
100
110
120
130
140
150
160
114
Distance (km)

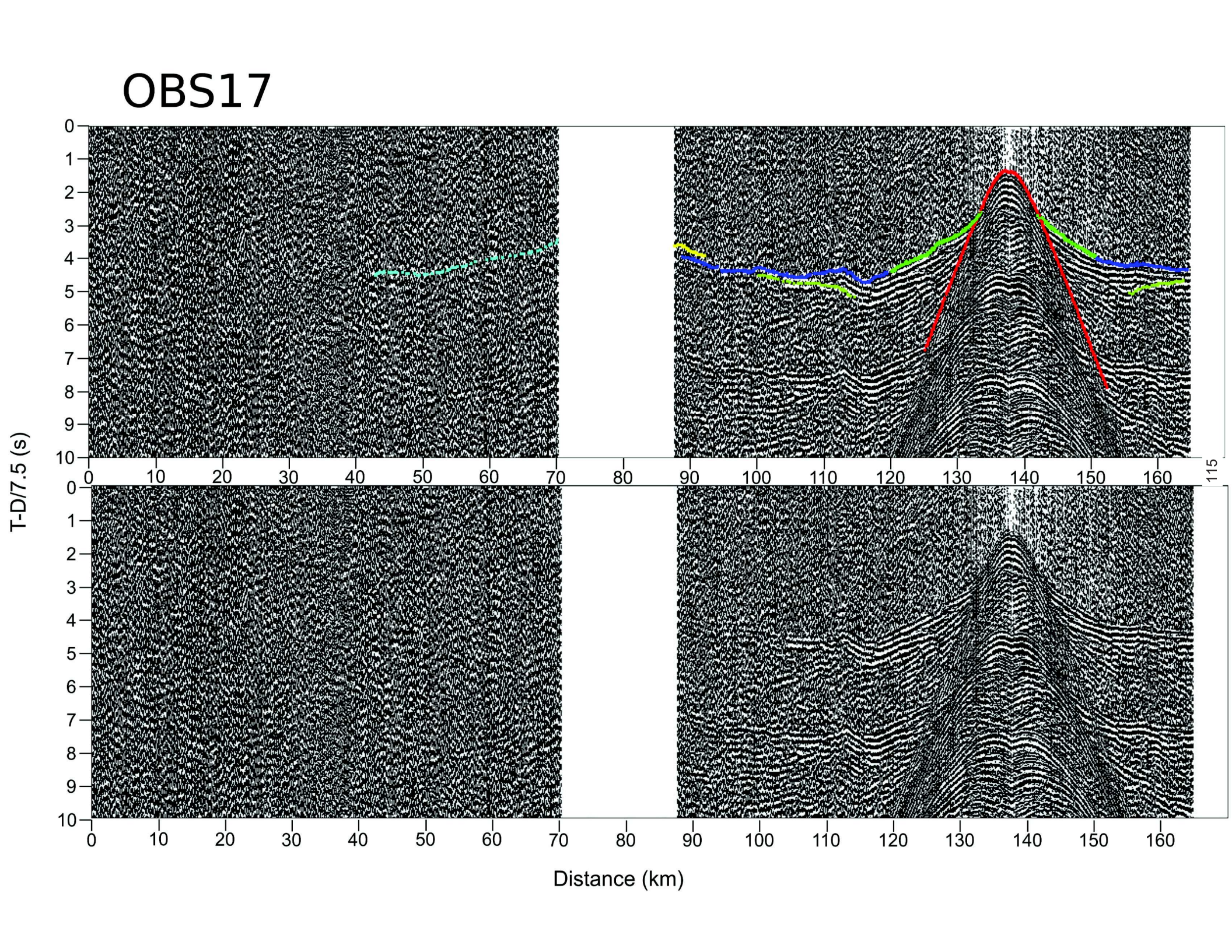
OBS17
T-D/7.5 (s)
0
1
2
3
4
5
6
7
8
9
10
0
10
20
30
40
50
60
70
80
90
100
110
120
130
140
150
160
115
Distance (km)

OBS18

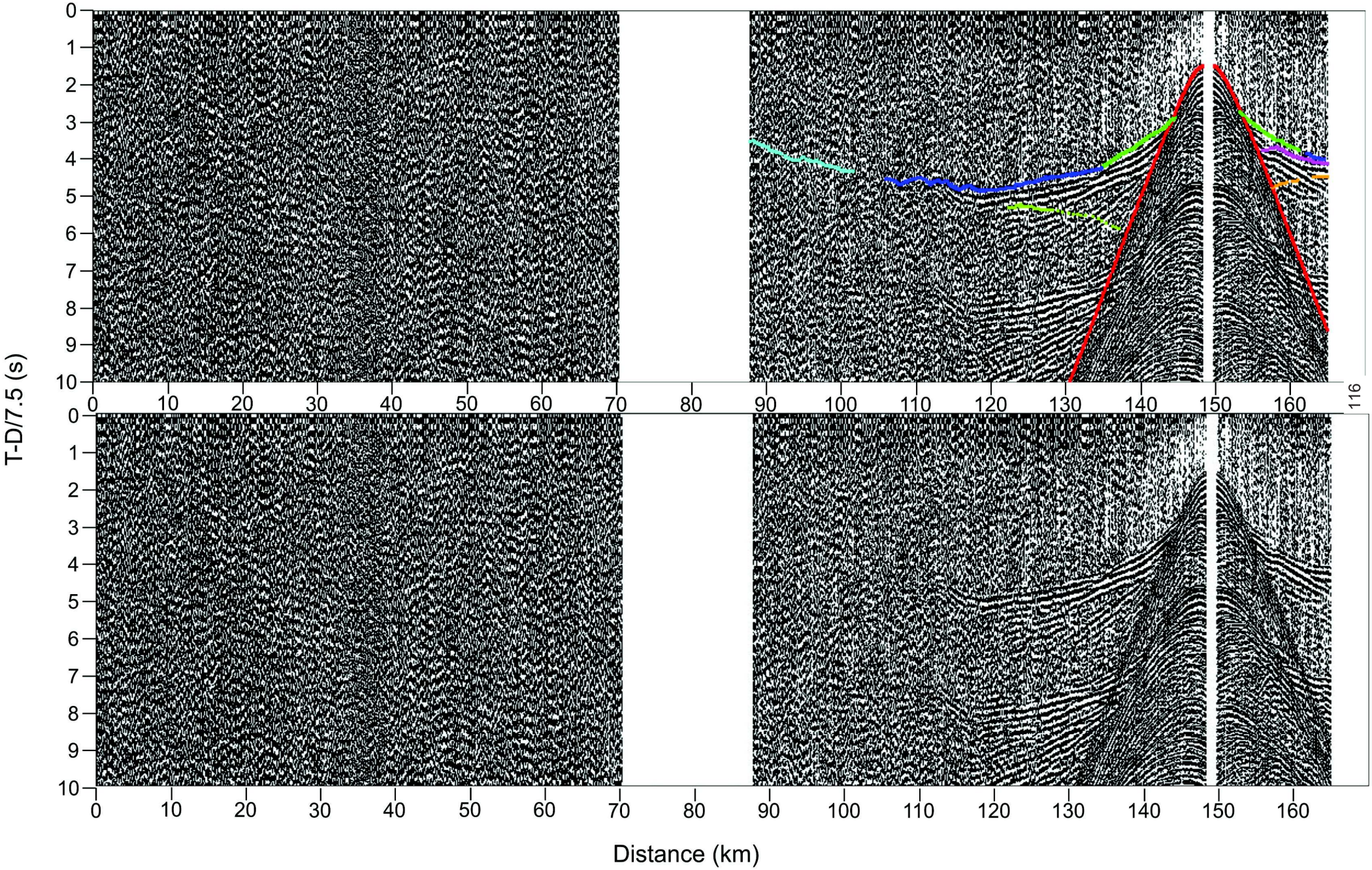
T-D/7.5 (s)
0
1
2
3
4
5
6
7
8
9
10
0
10
20
30
40
50
60
70
80
90
100
110
120
130
140
150
160
116
Distance (km)

Annexe 2: Seismic sections from all OBS with Vp waves arrival and interpretation from Gloria Fault area. Reduction velocity is 7.5 km/s.

OBS01

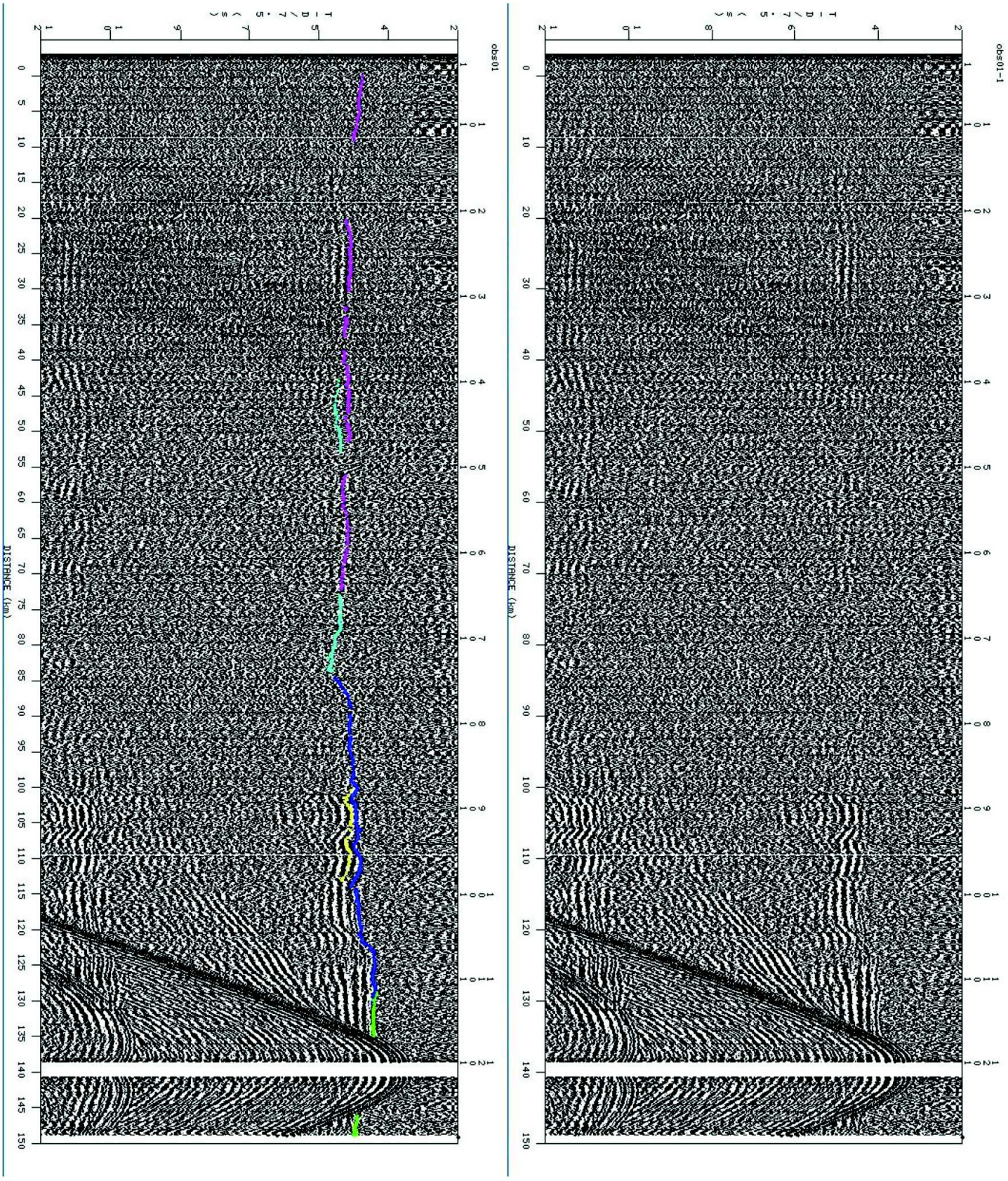

OBS02

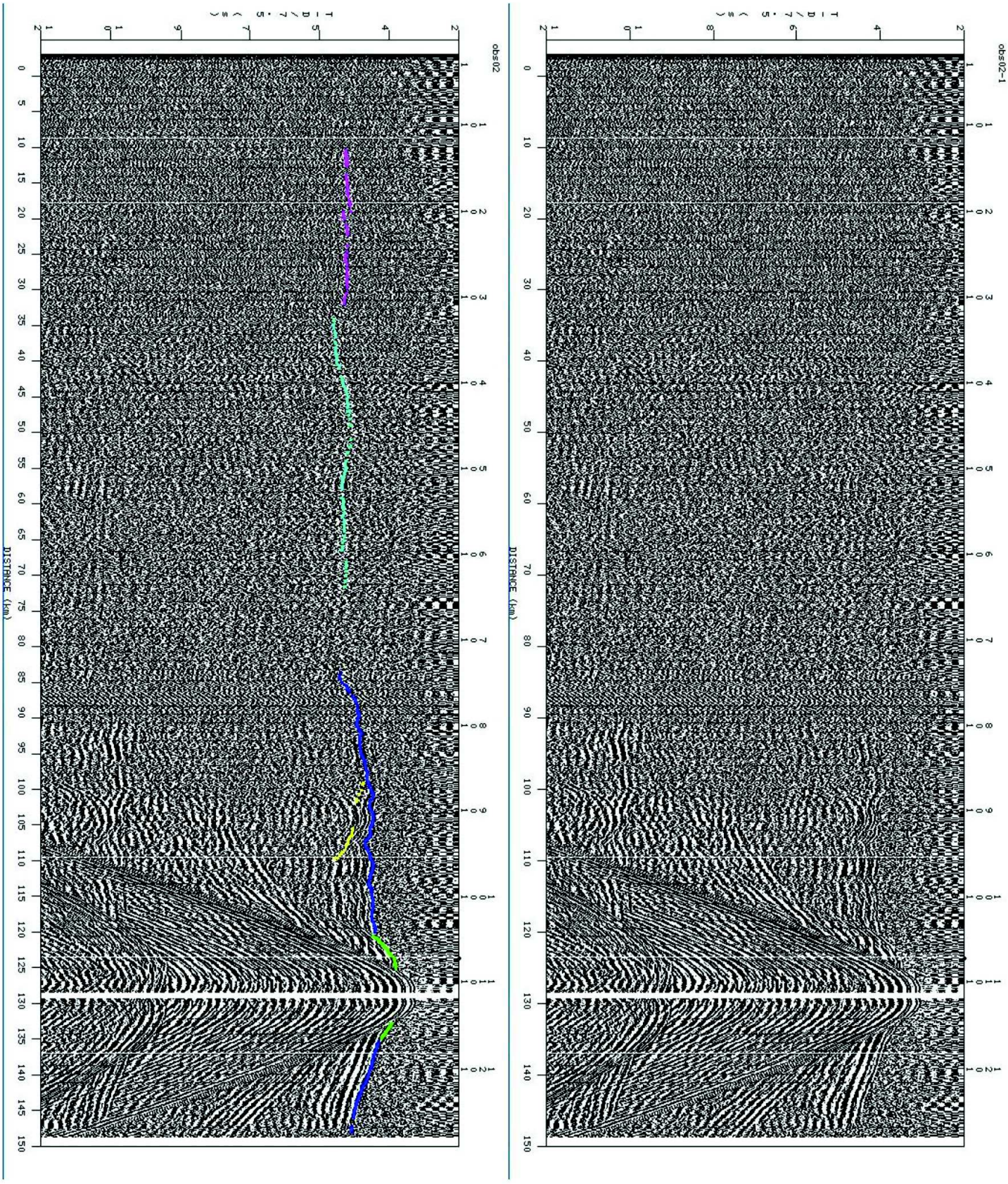

OBS03

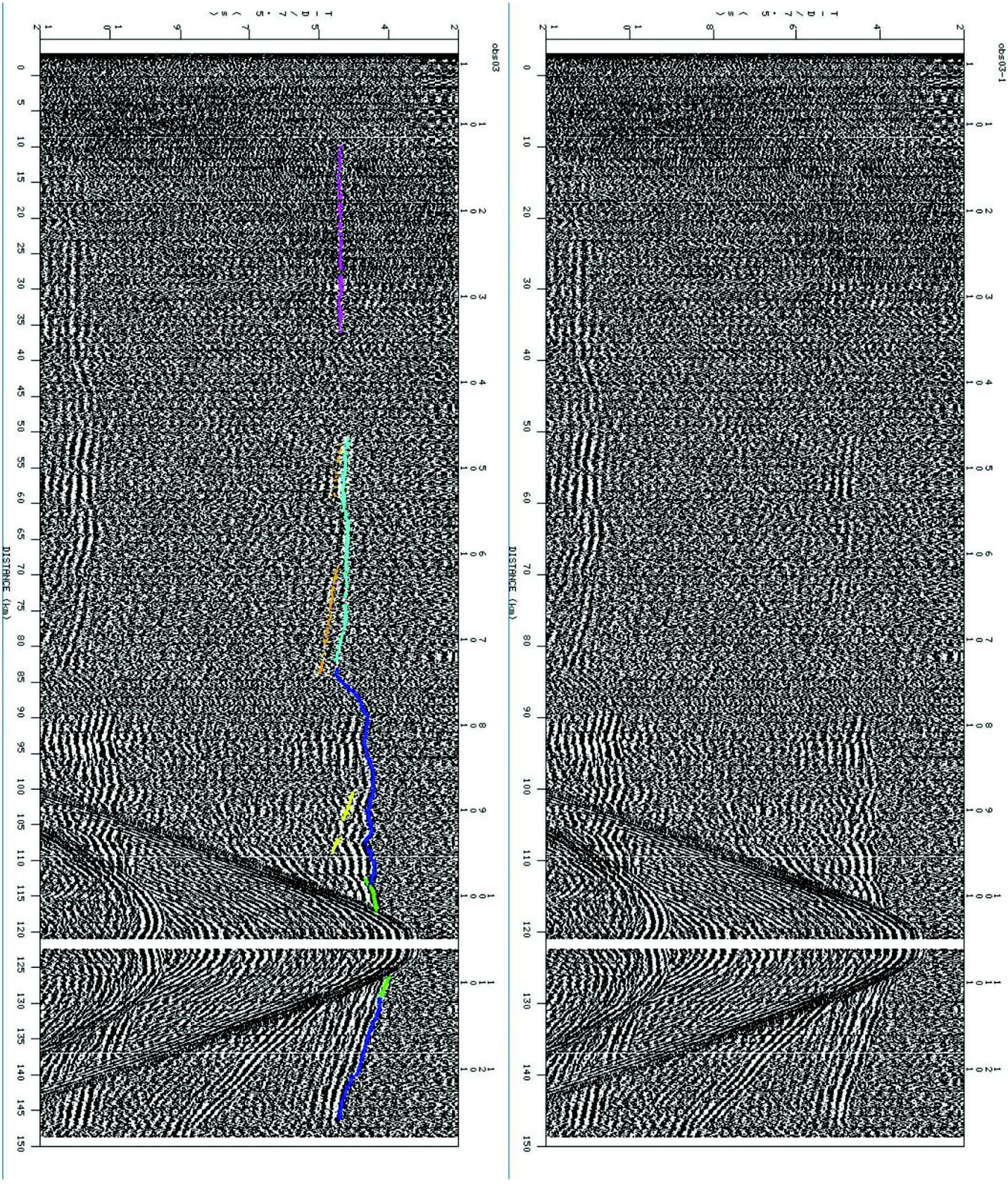

OBS04

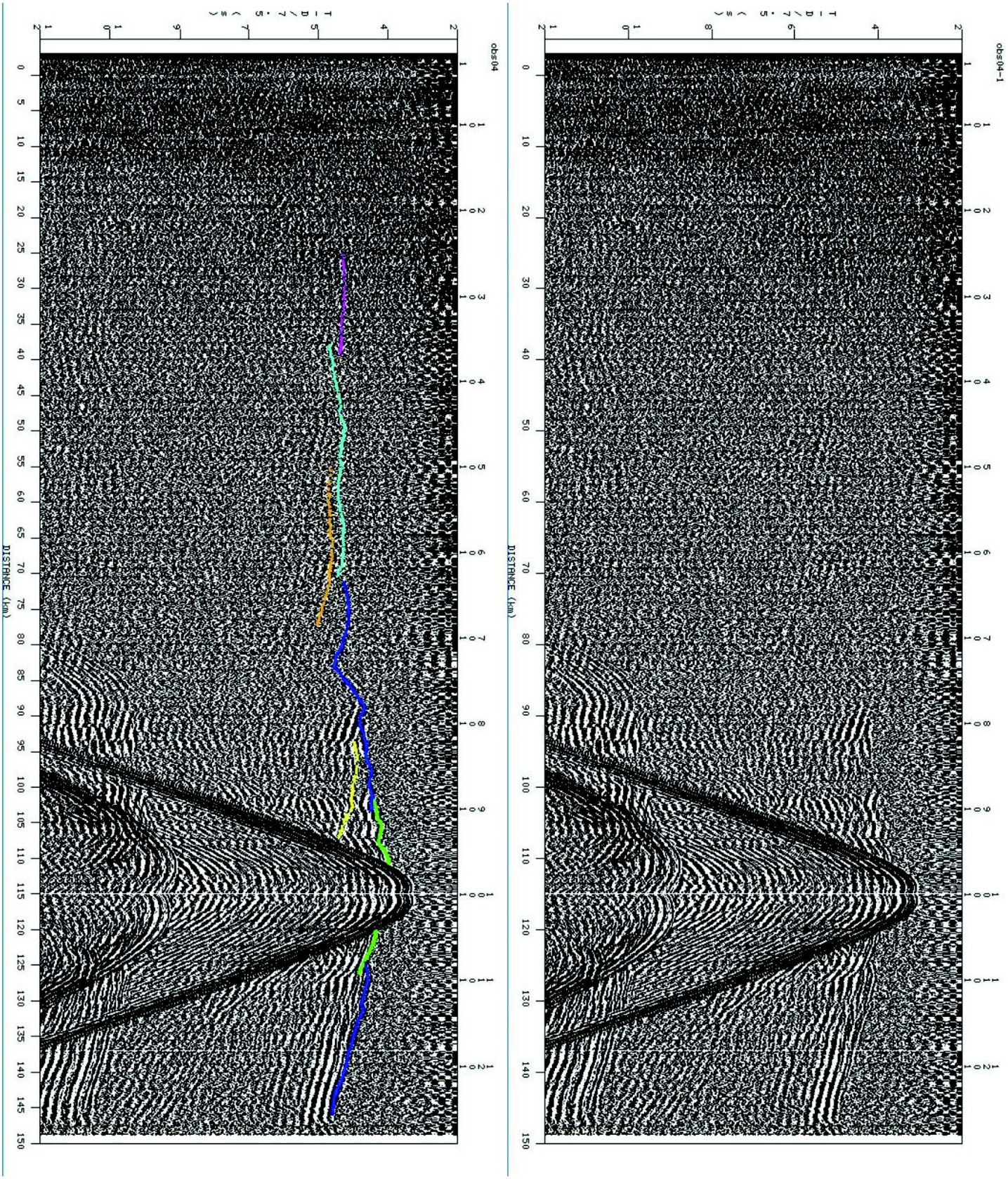

OBS05

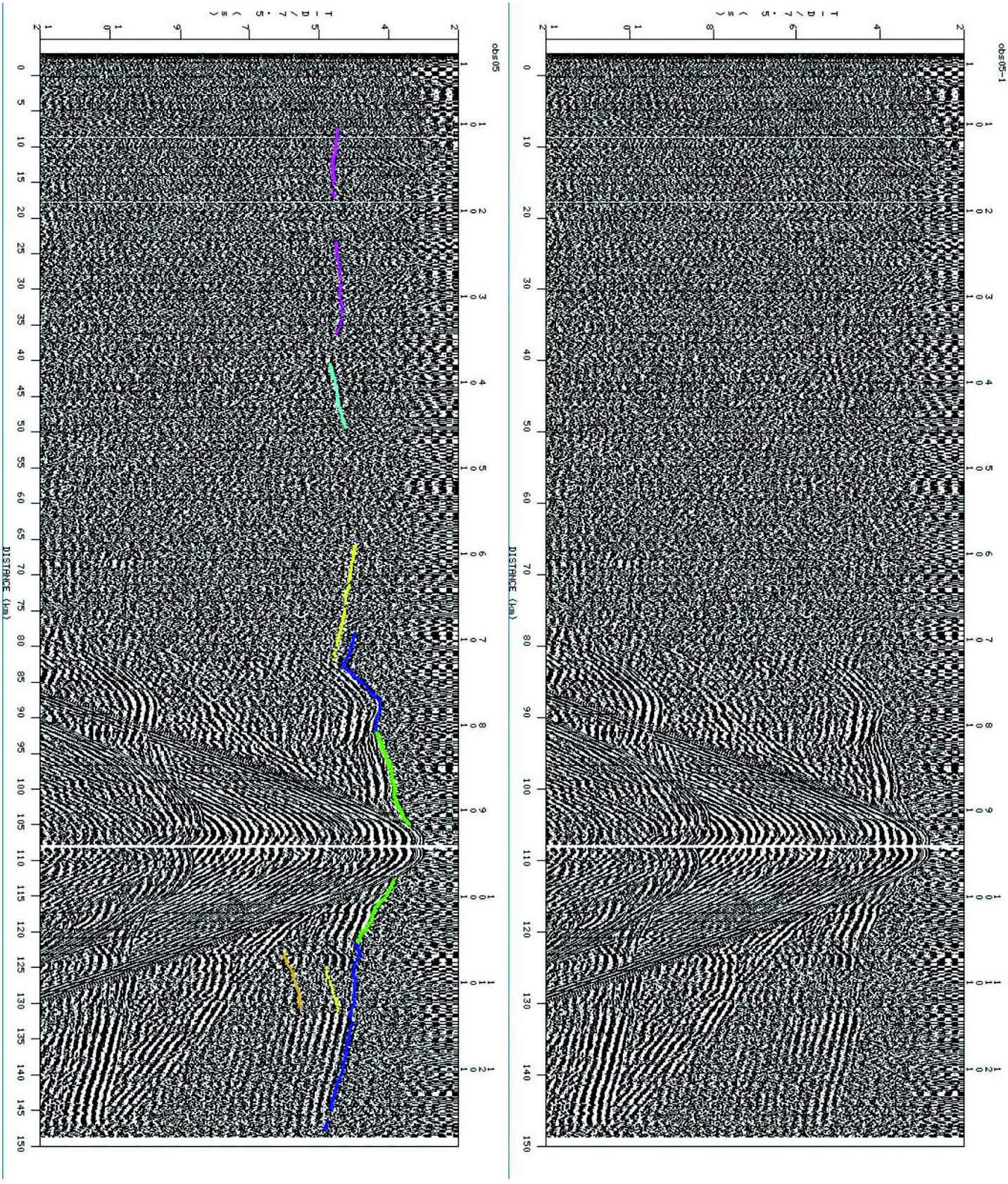

OBS06

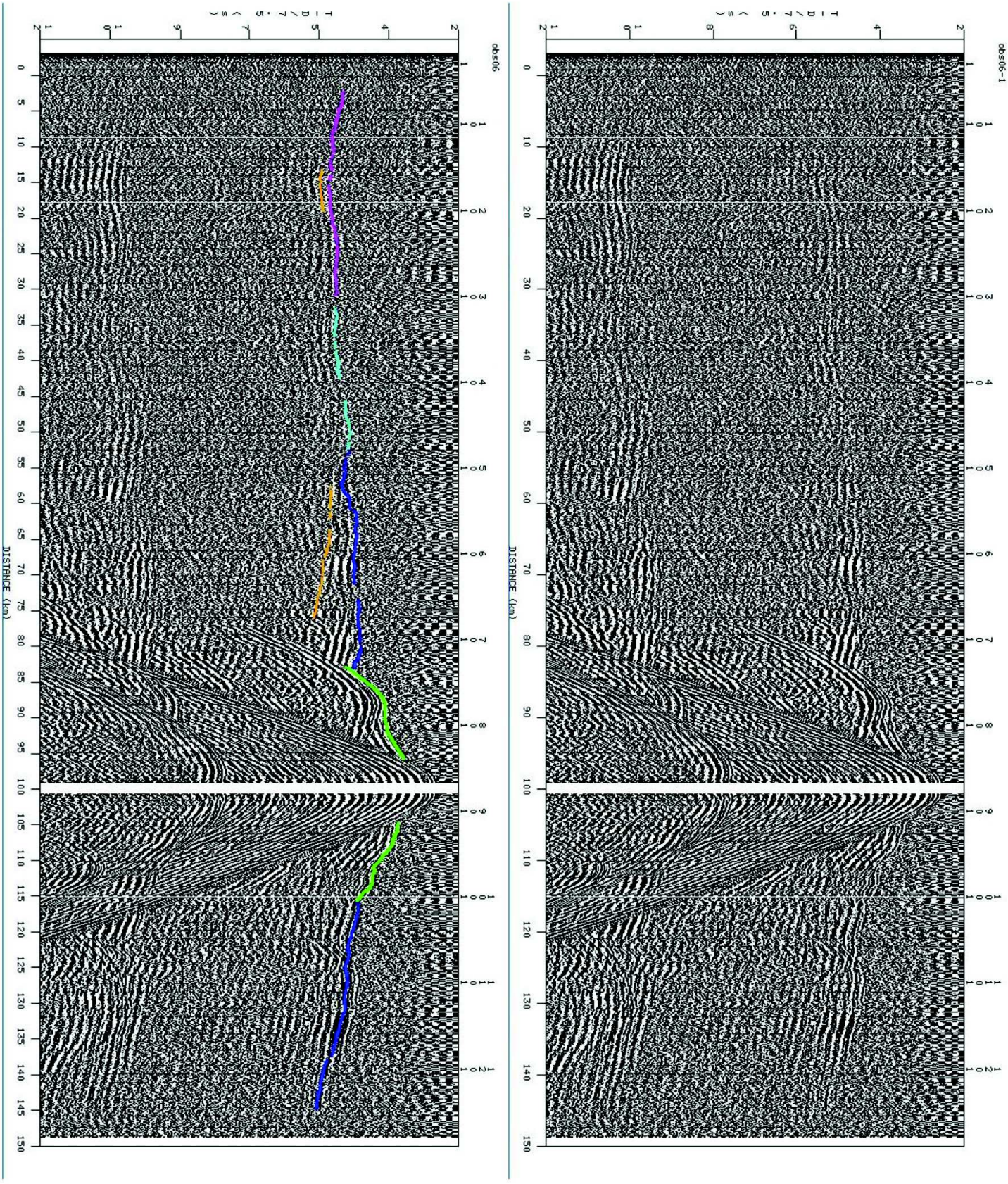

OBS07

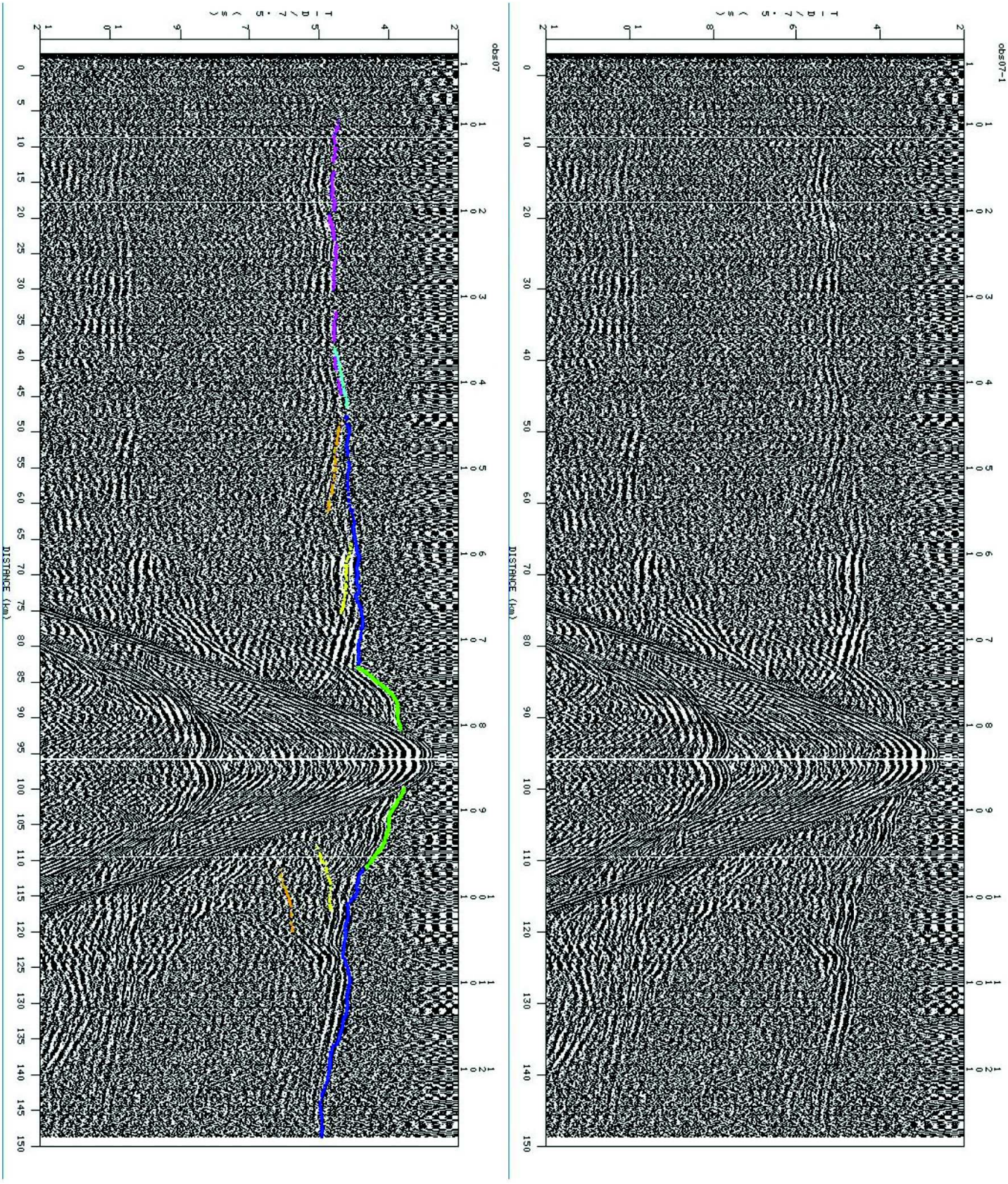

OBS08

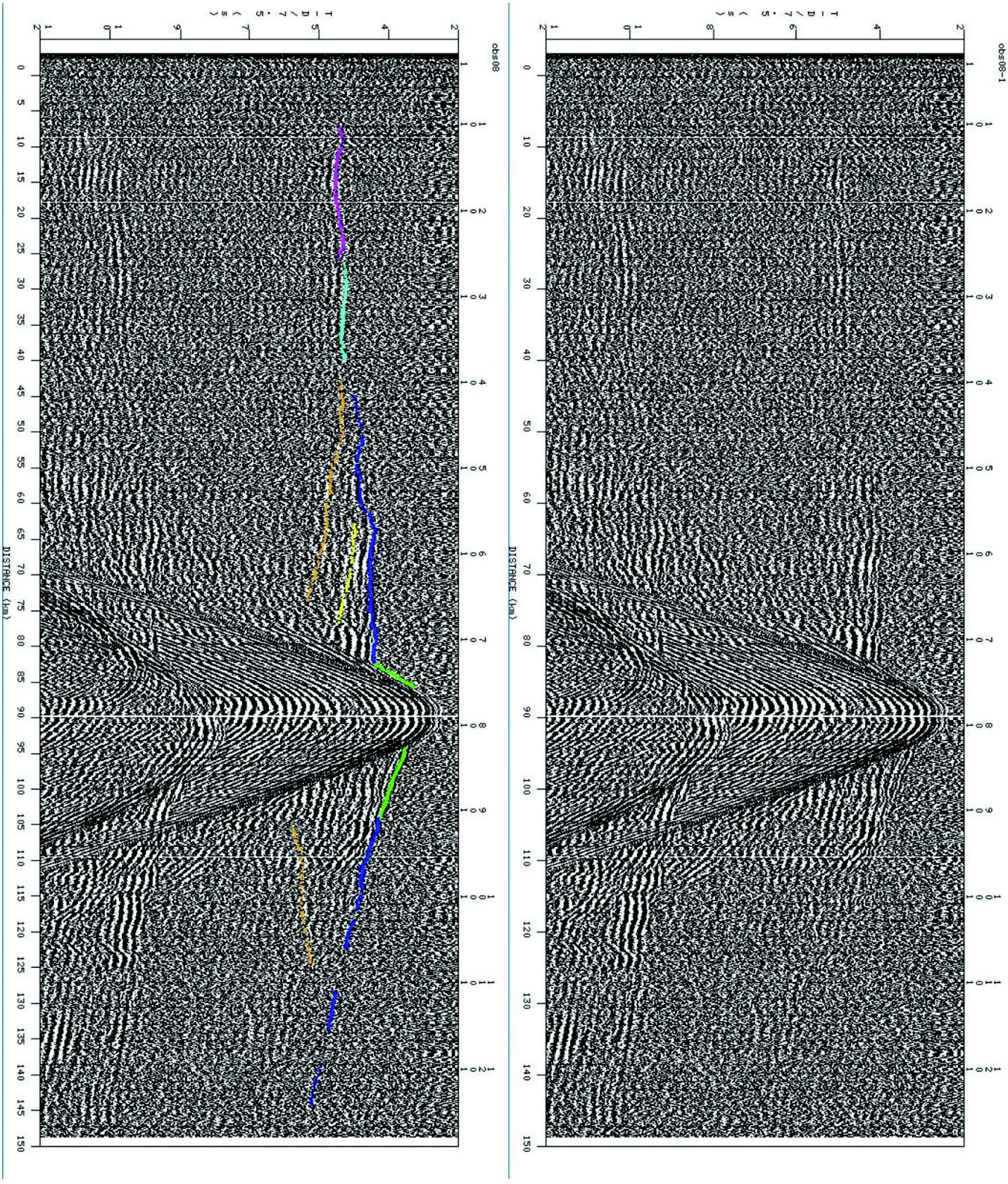

OBS09

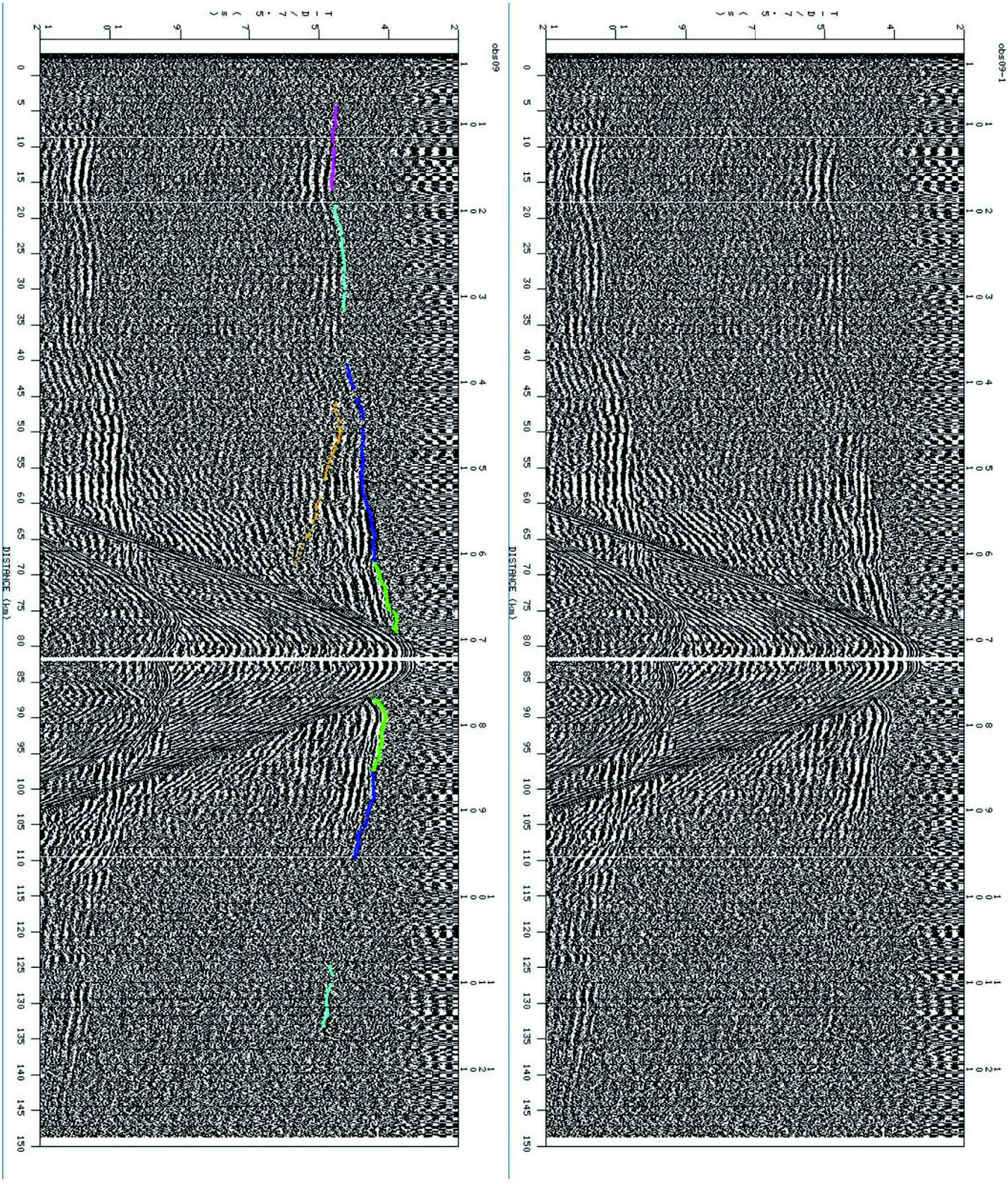

OBS10

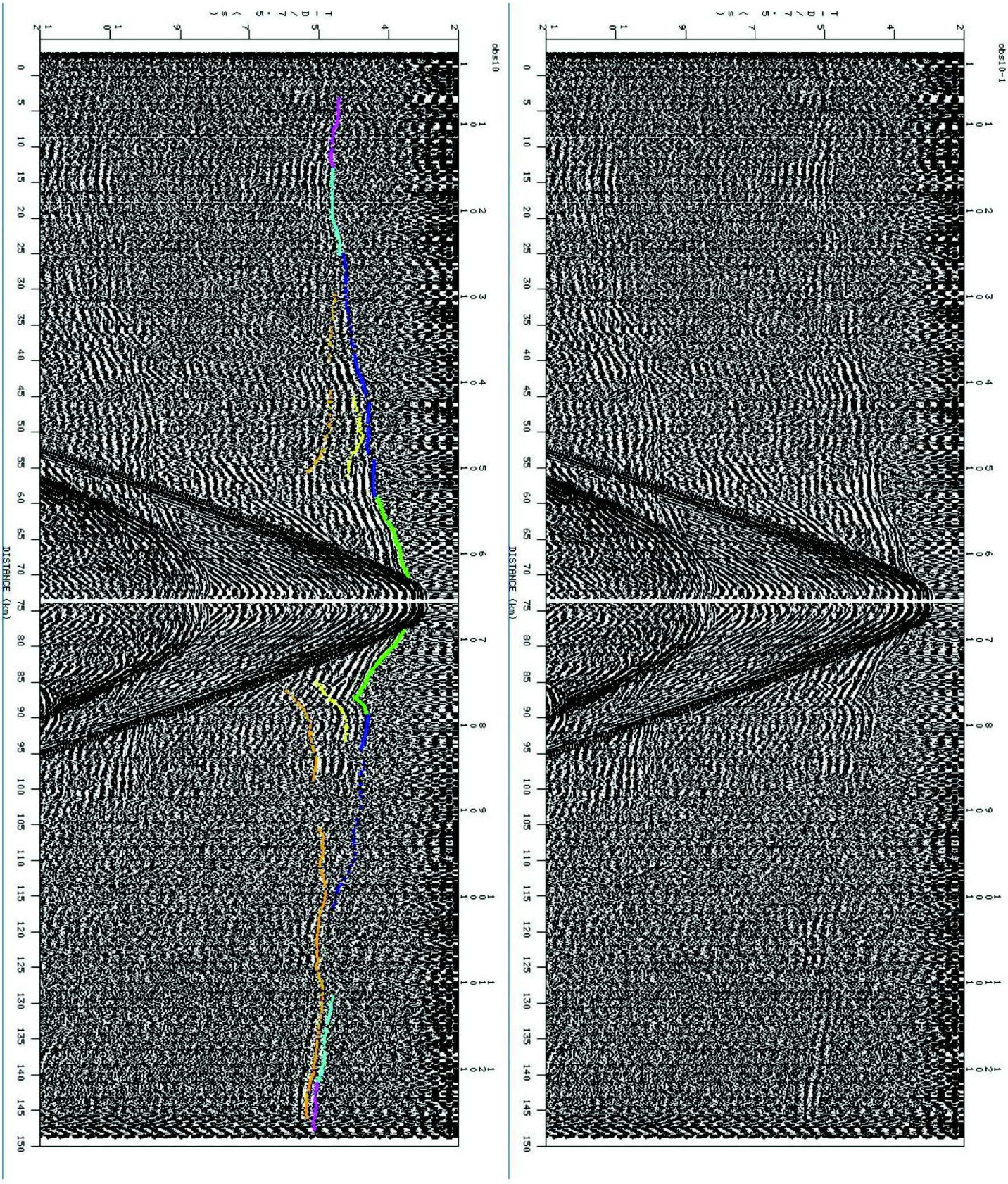

OBS11

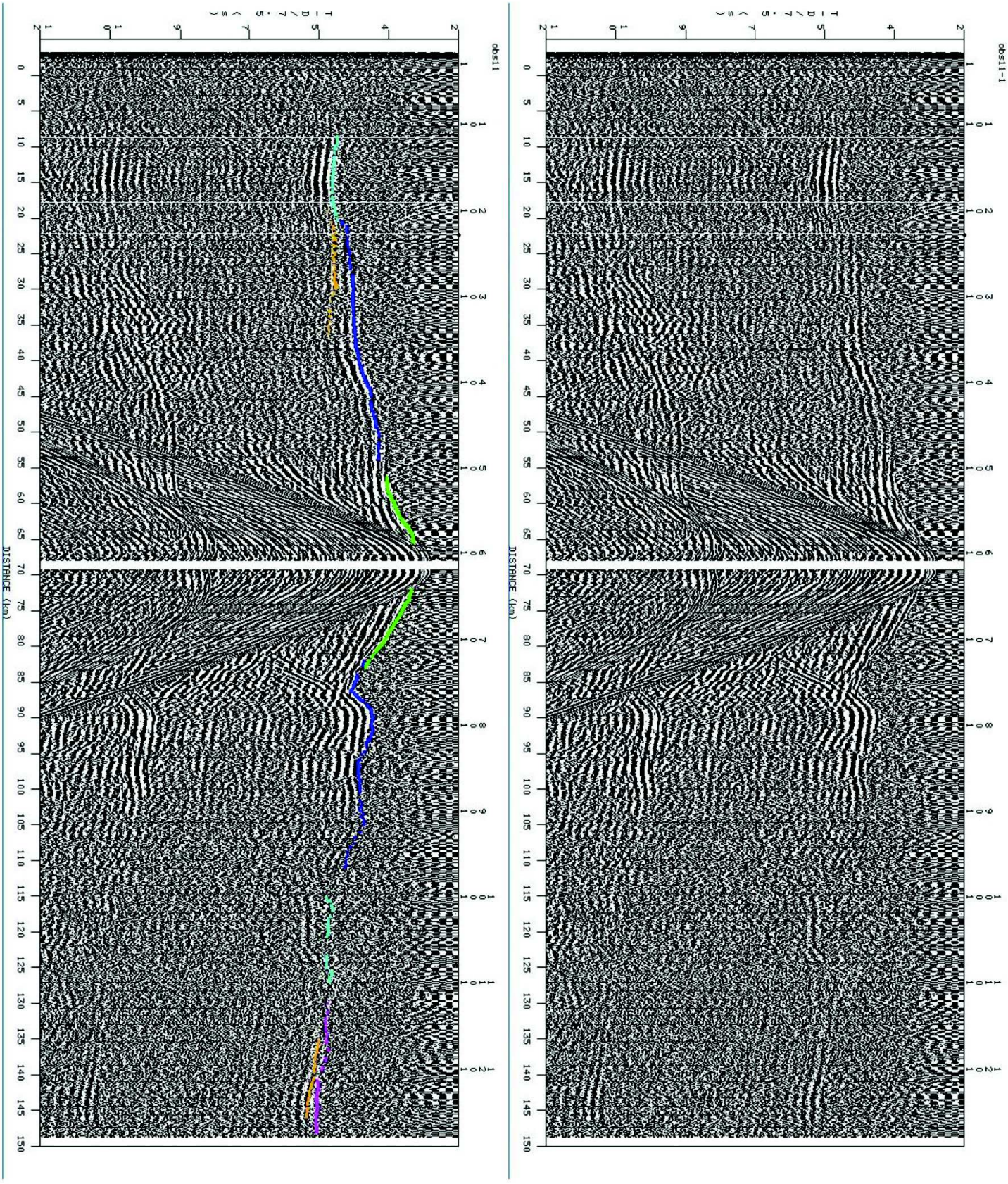

OBS12

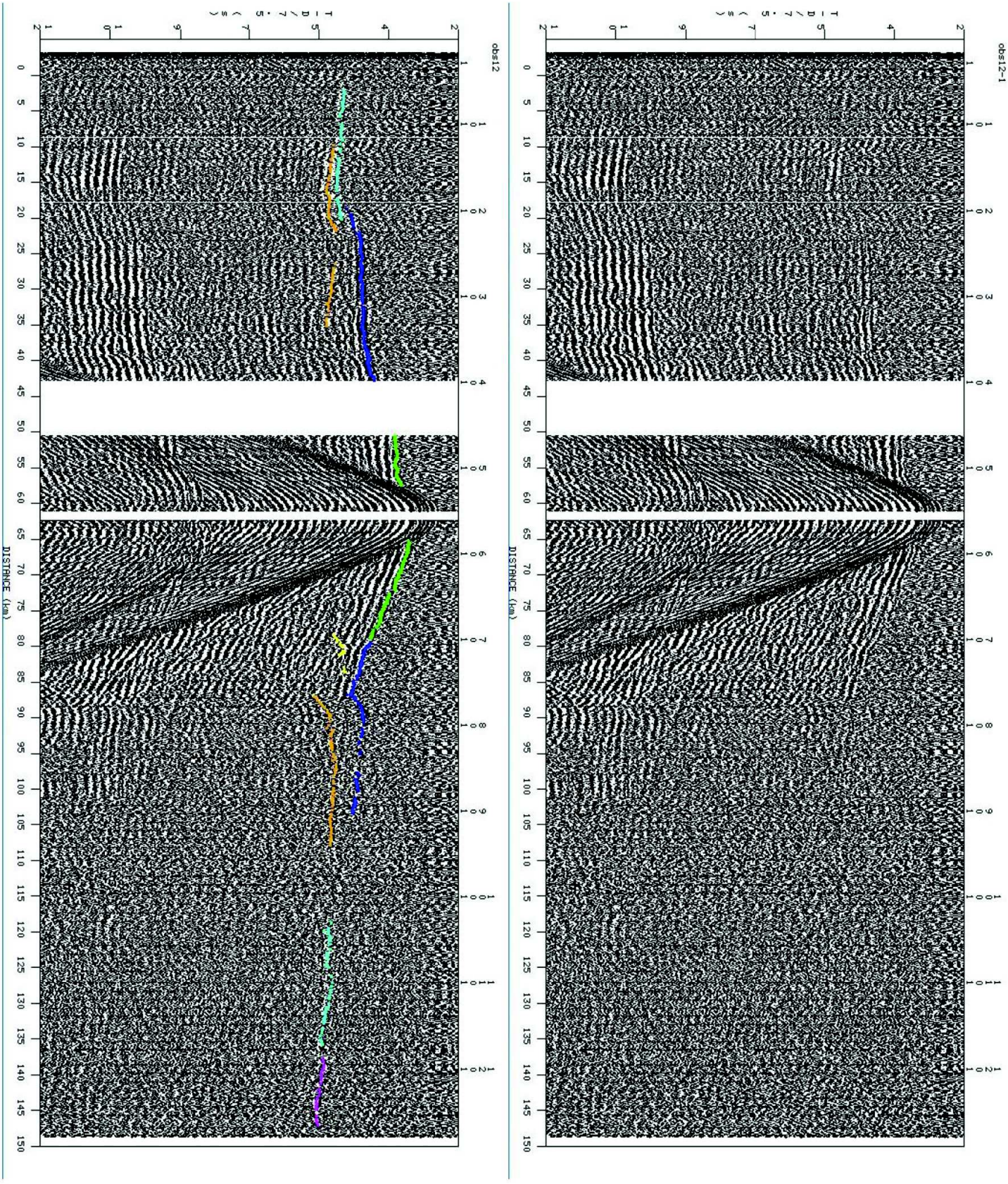

OBS13

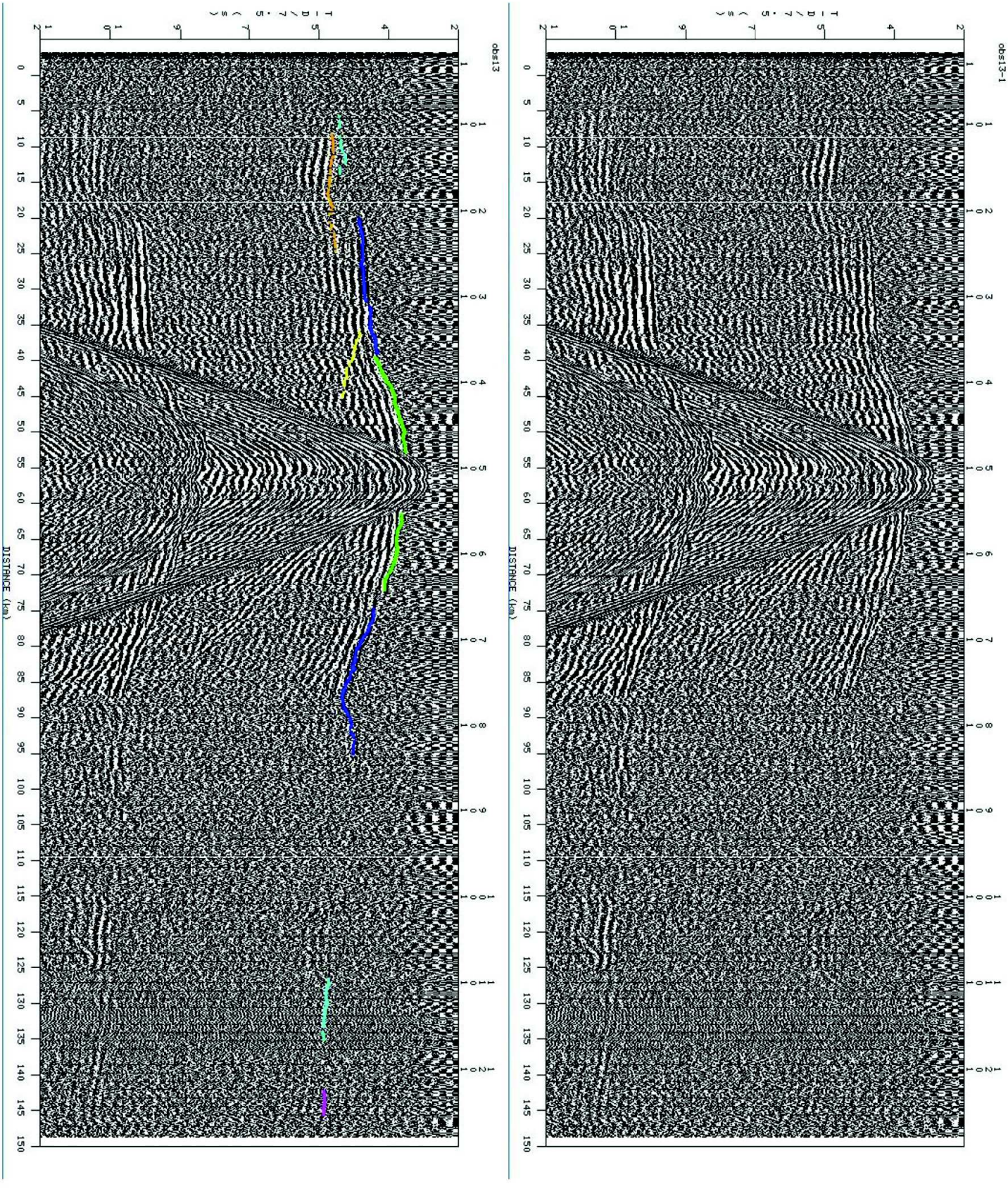

OBS14

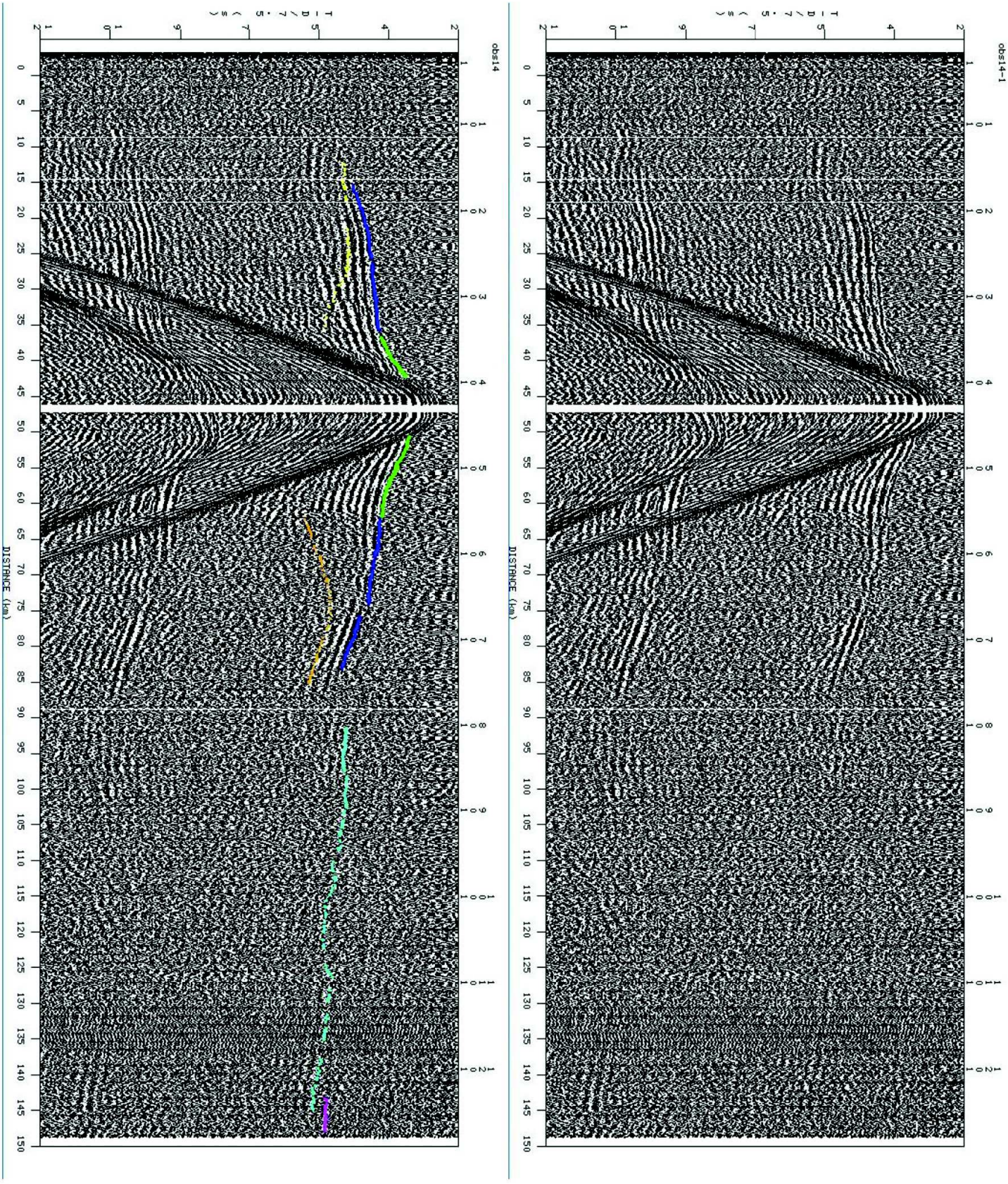

OBS15

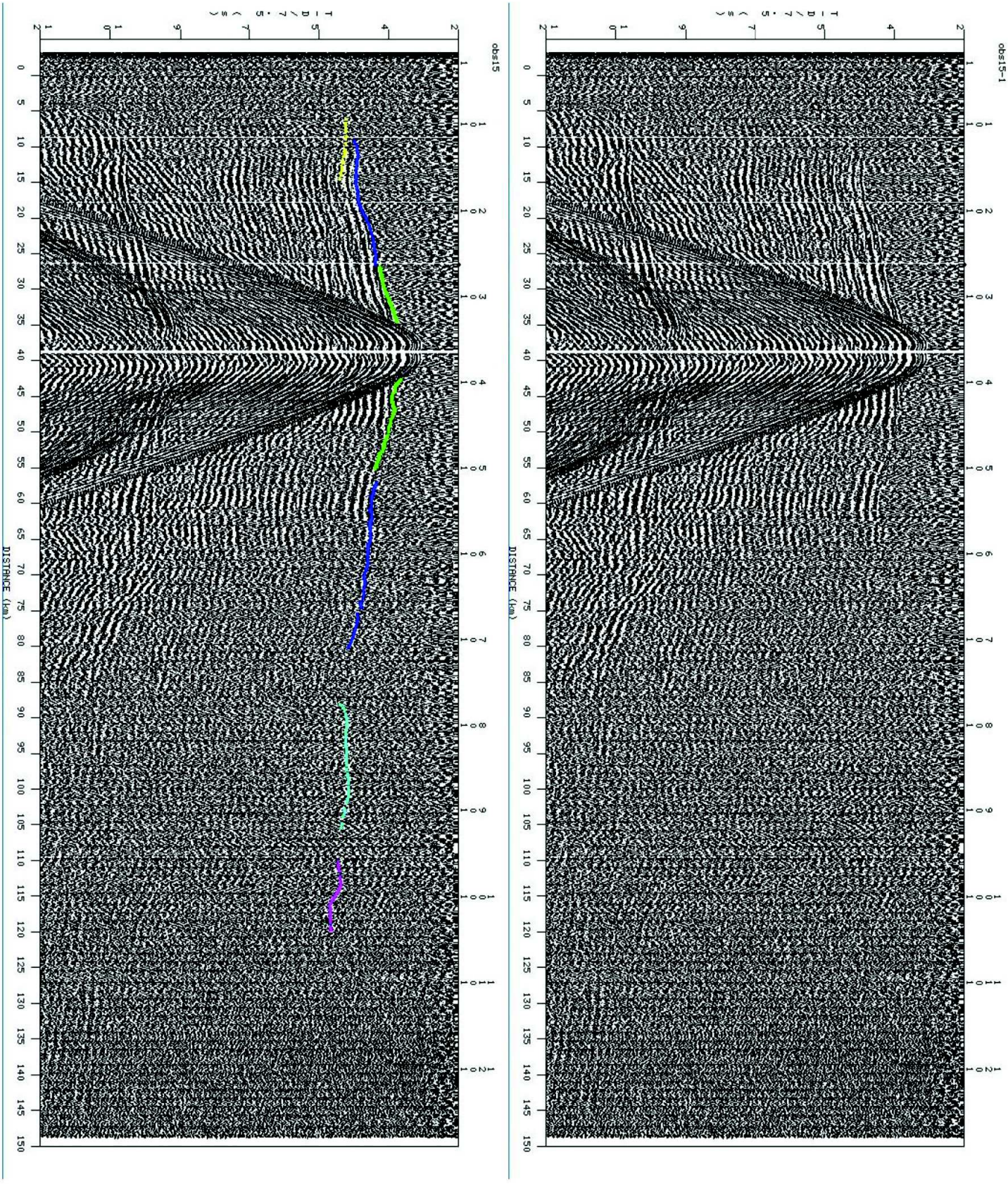

OBS16

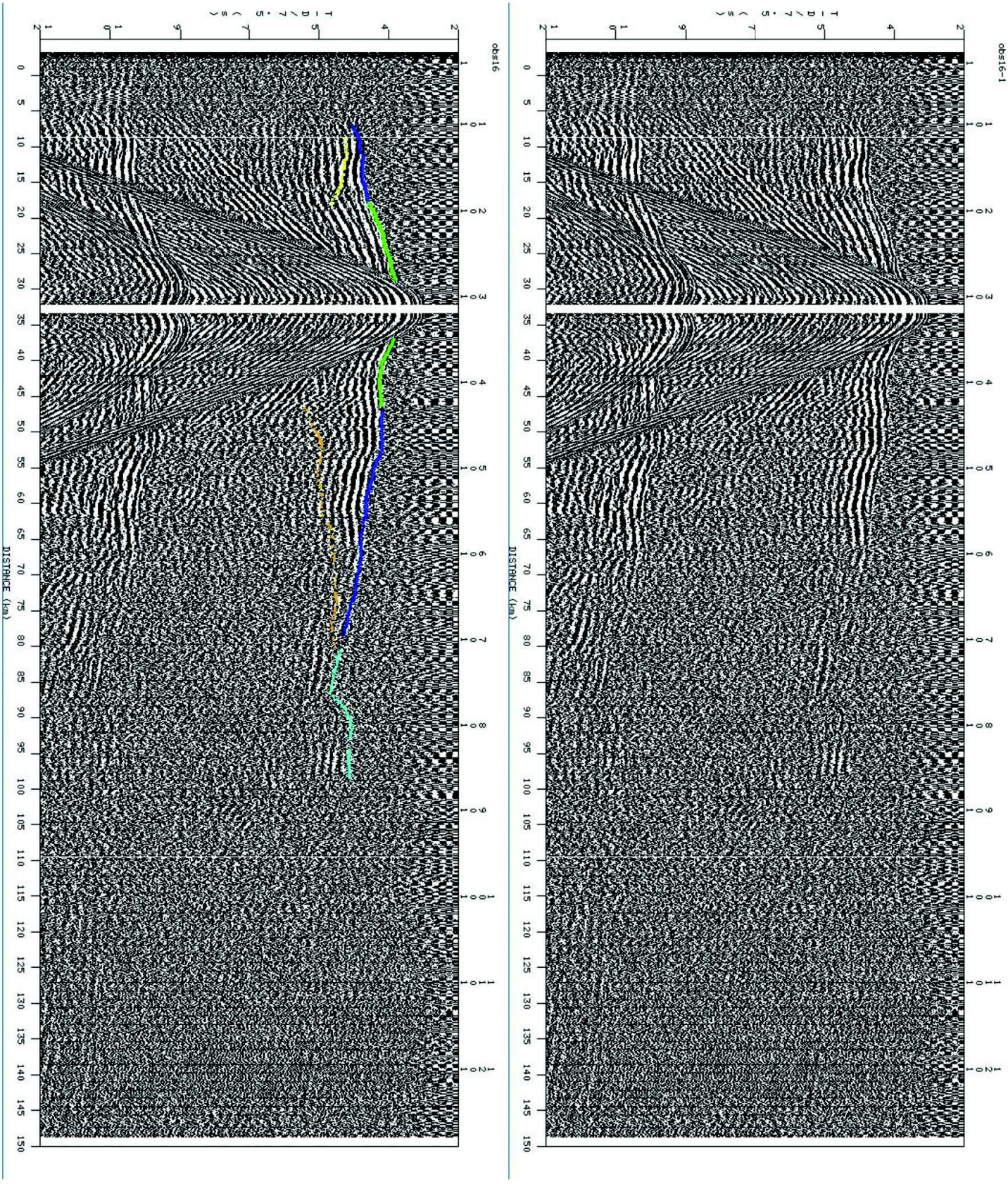

OBS17

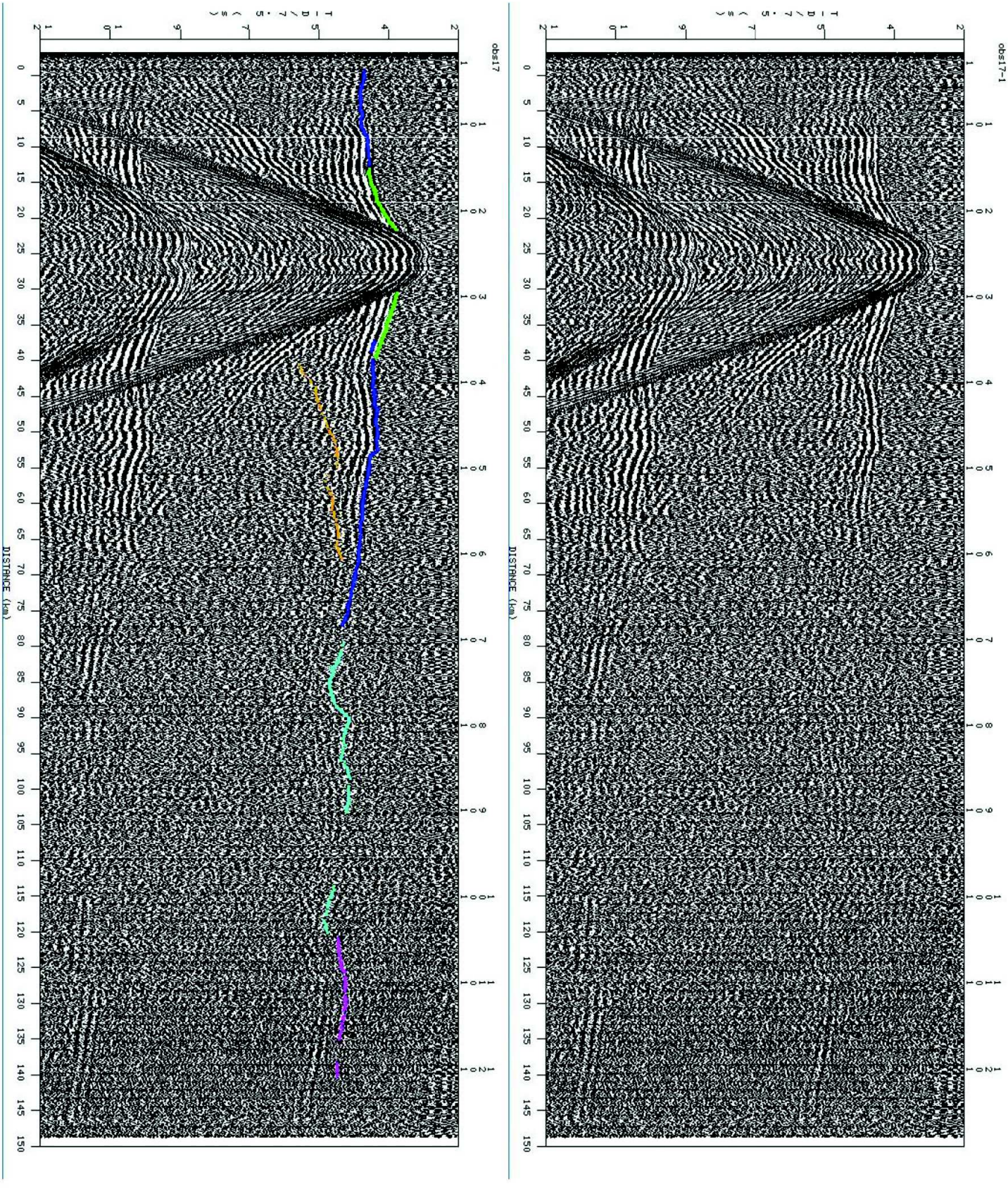

OBS18

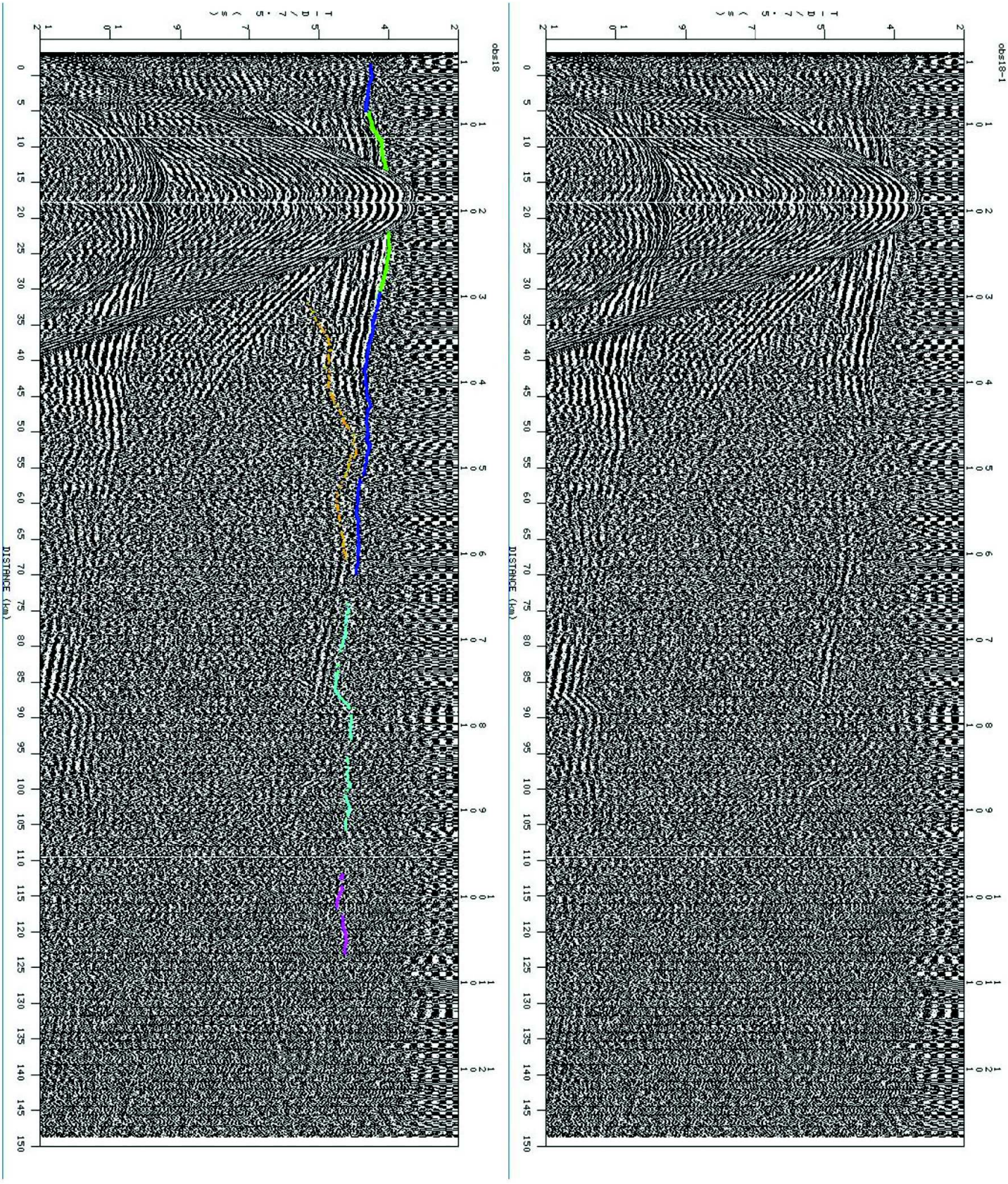

Annexe 3: Seismic sections from all OBS with Vs waves arrival and interpretation from Gloria Fault area. Reduction velocity is 7.5 km/s.

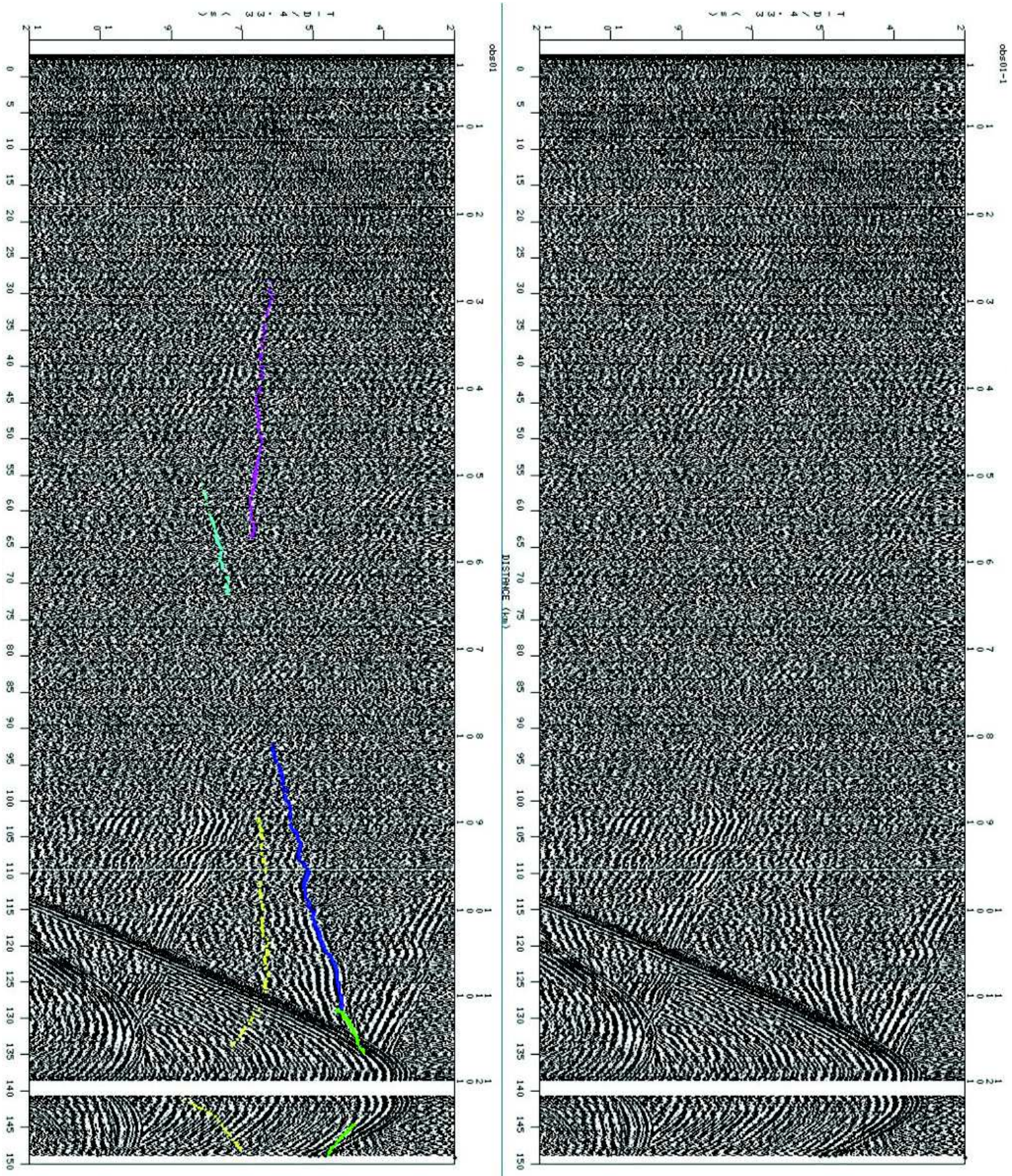
obs01-1
obs01
DISTANCE (km)

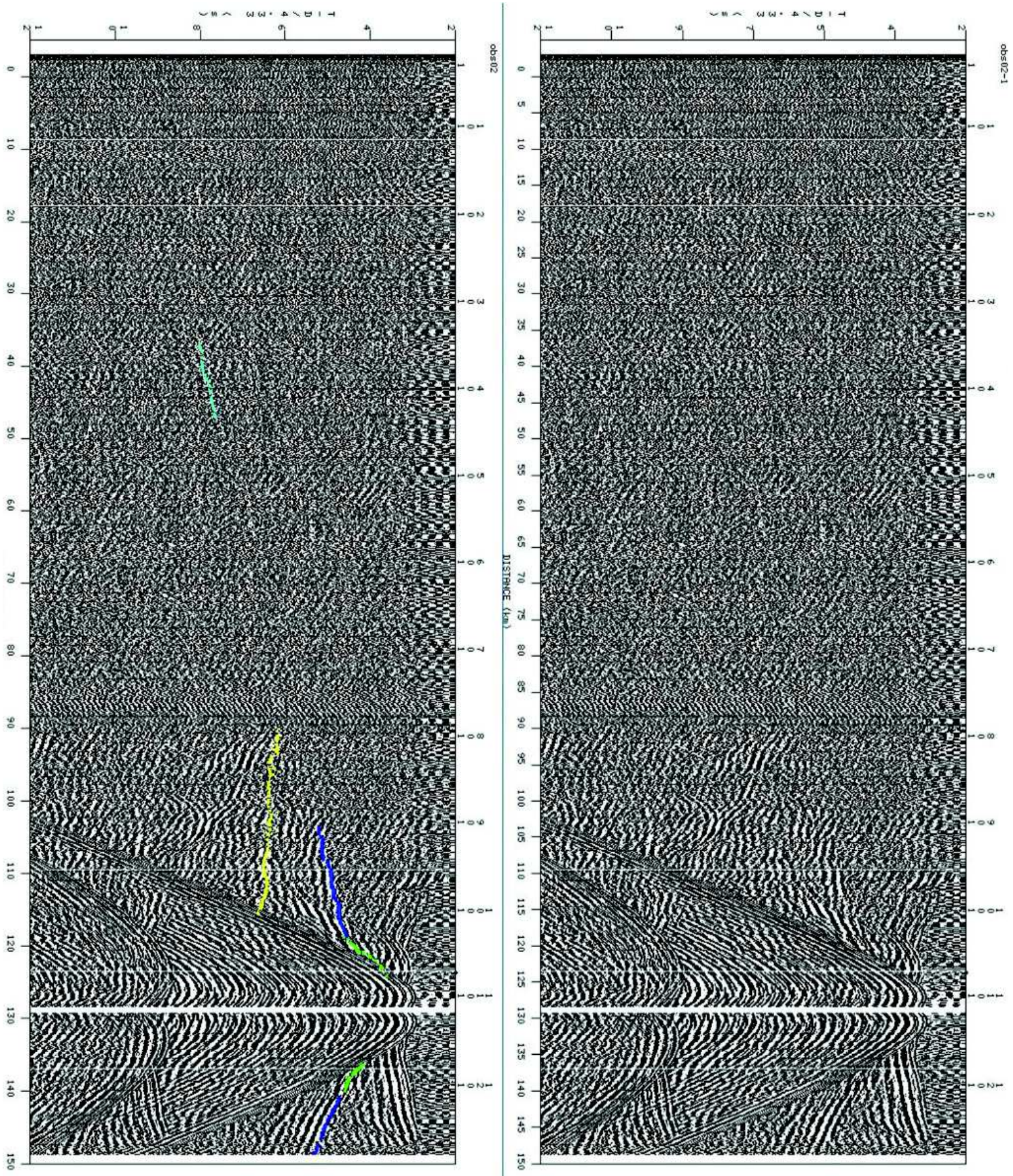
obs02-1
obs02
DISTANCE (km)

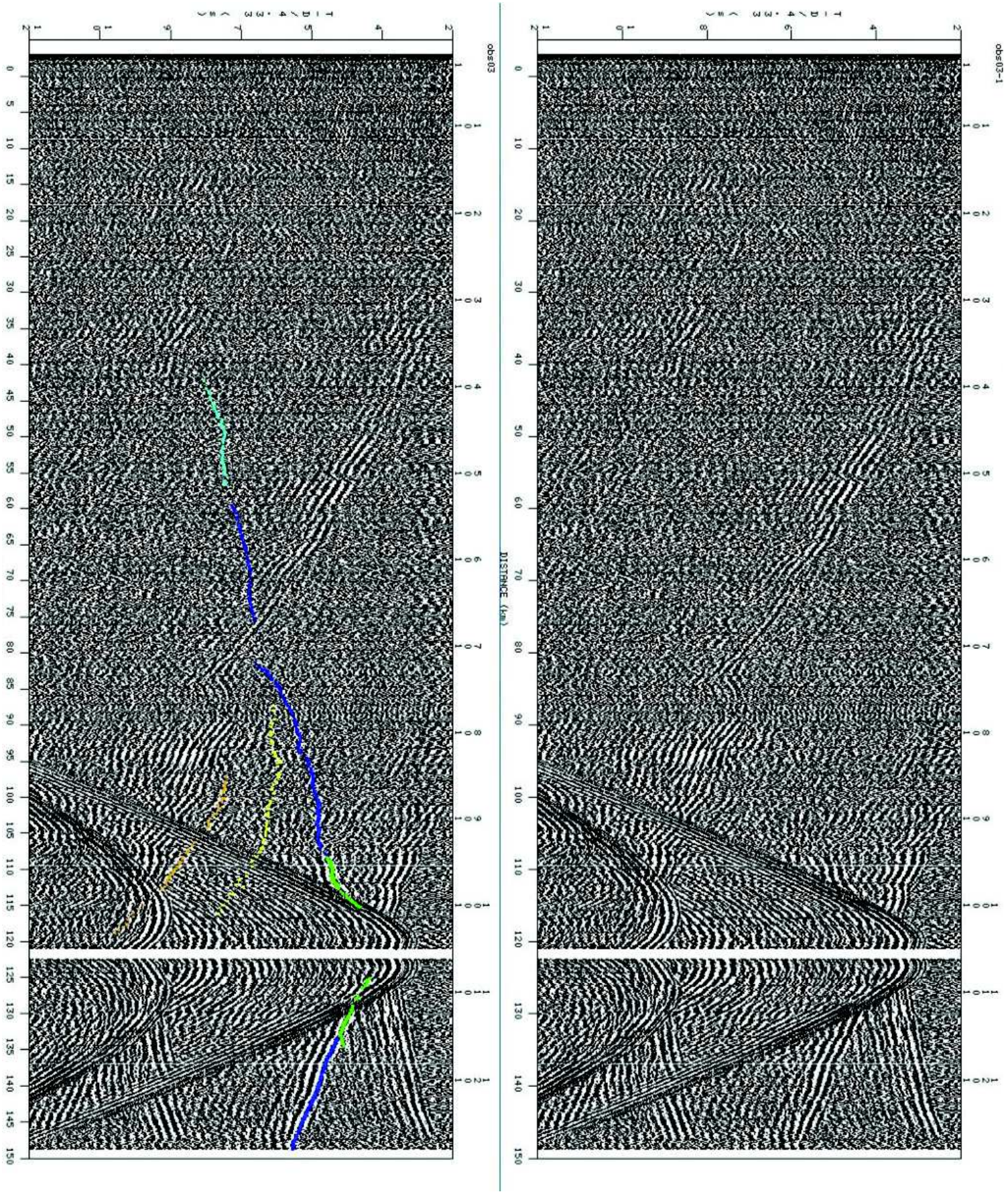
obs03-1
obs03
DISTANCE (km)

OBS04

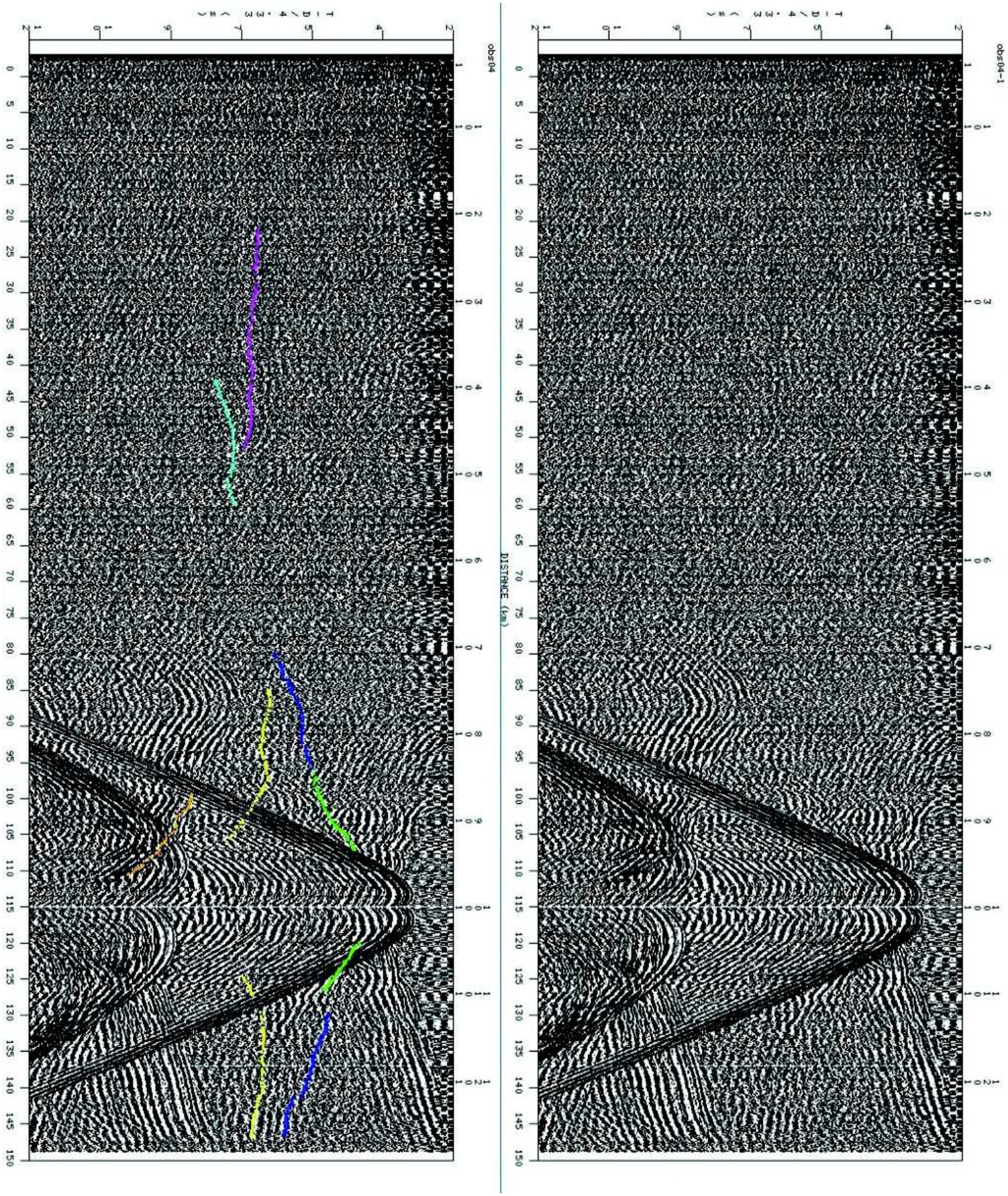

OBS05

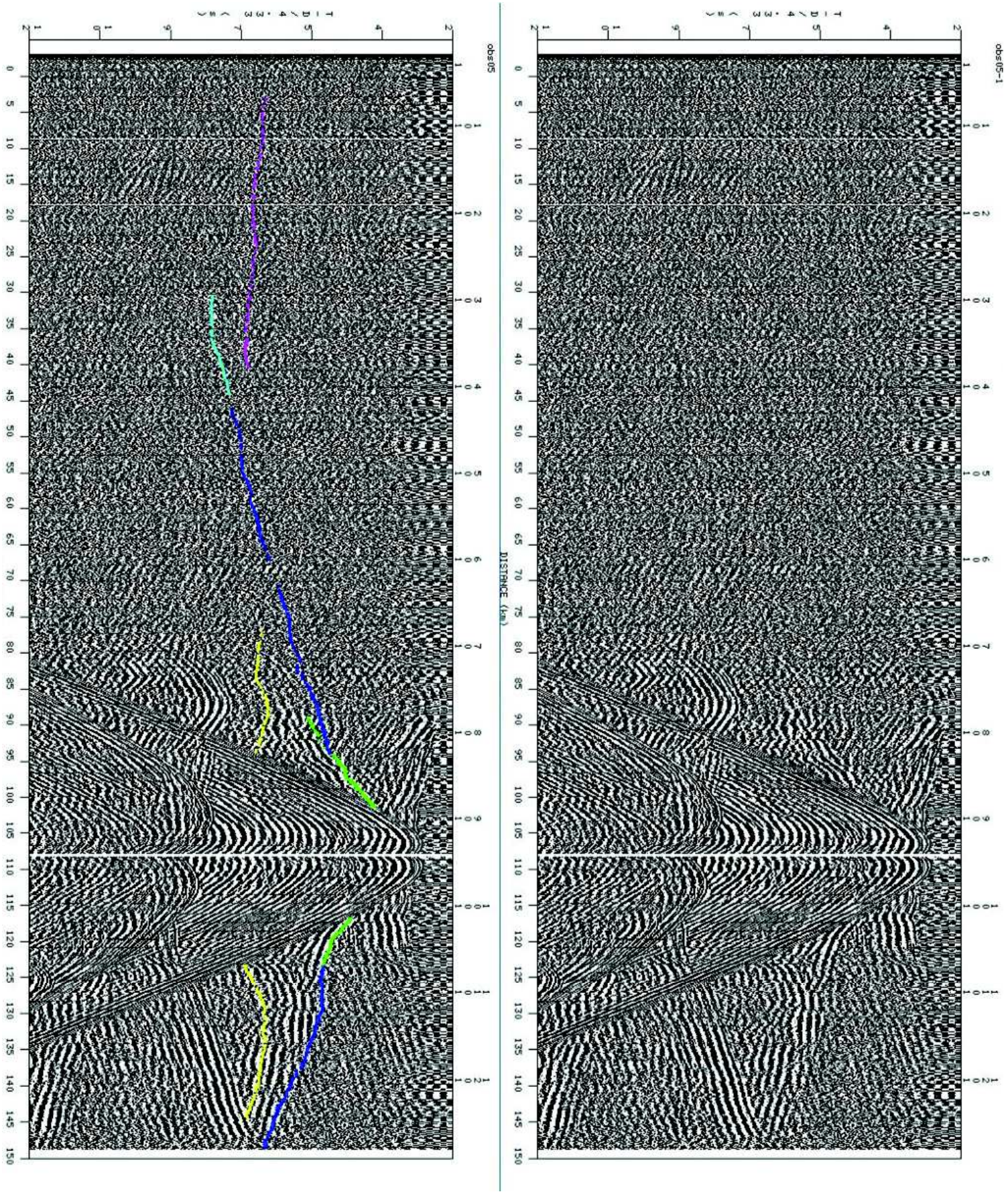

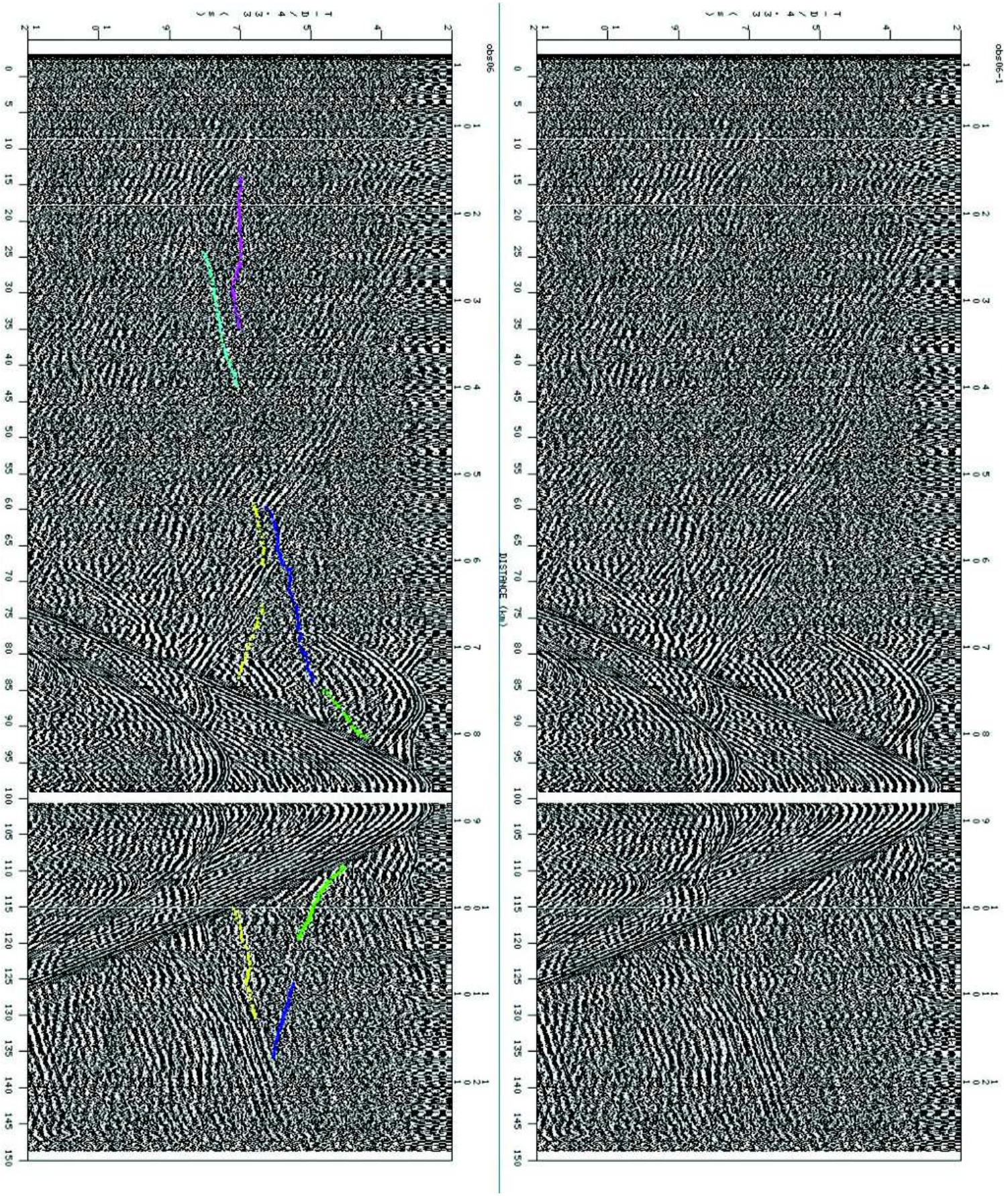
obs06-1
obs06
DISTANCE (km)

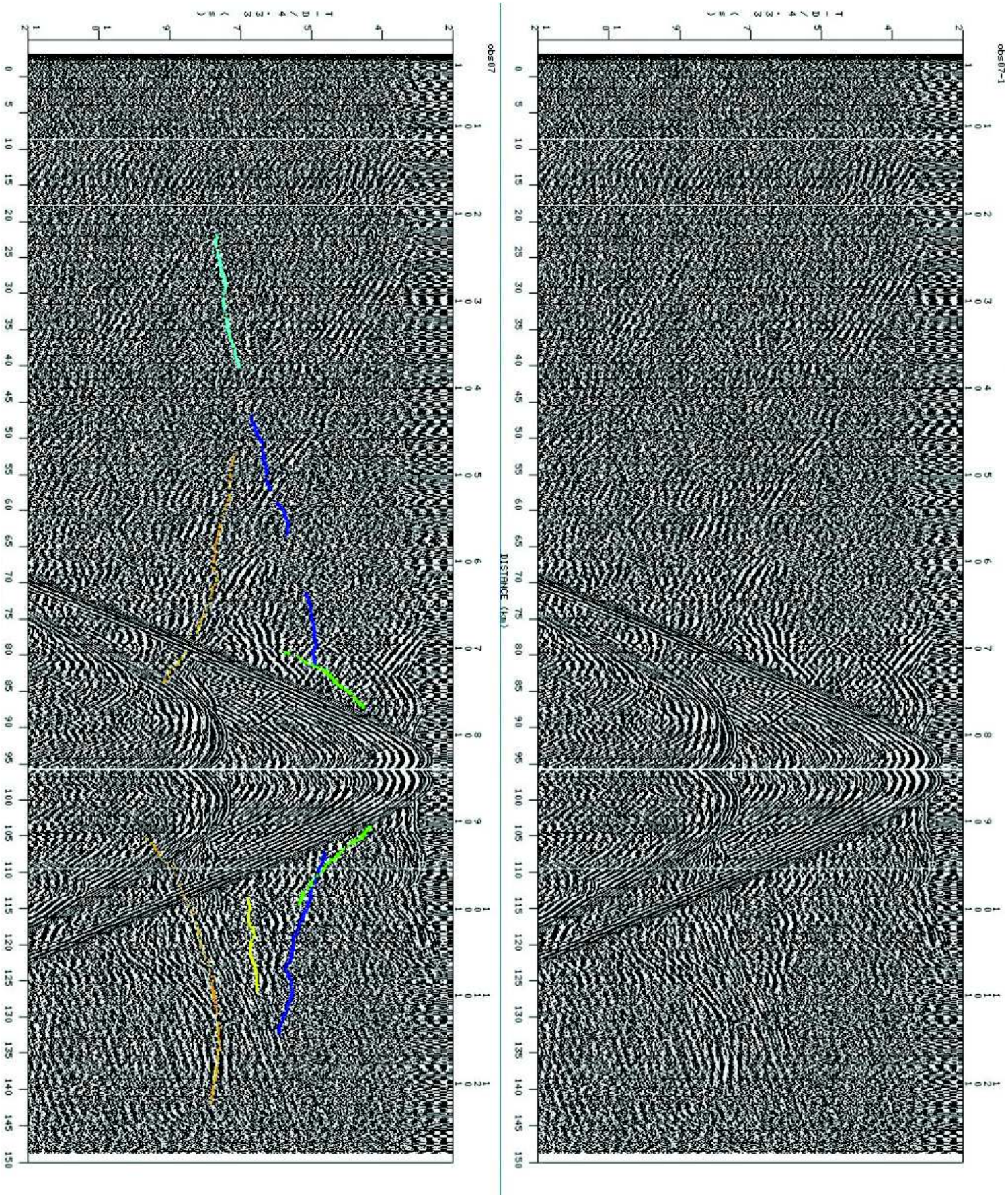
obs07-1
obs07
DISTANCE (km)

OBS08

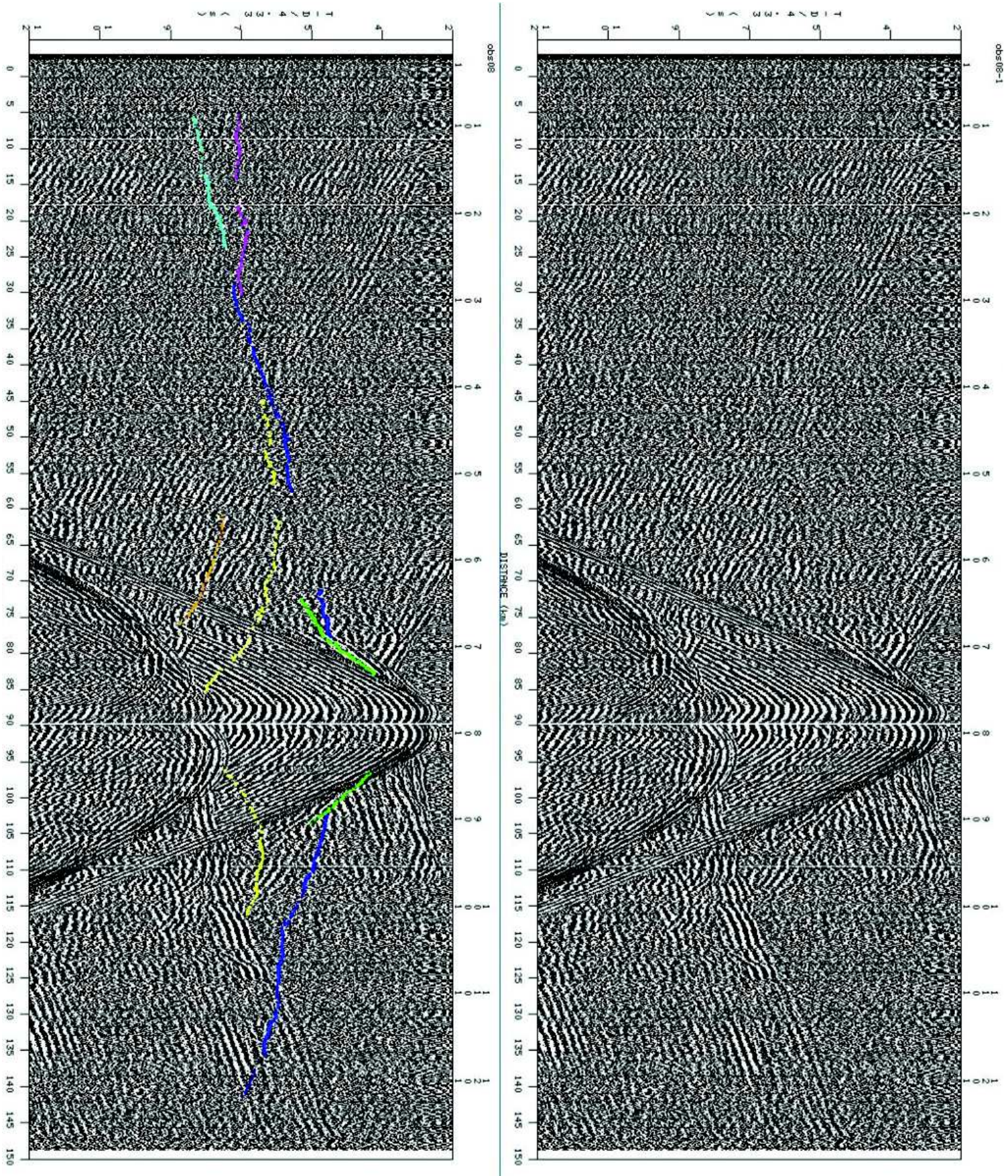

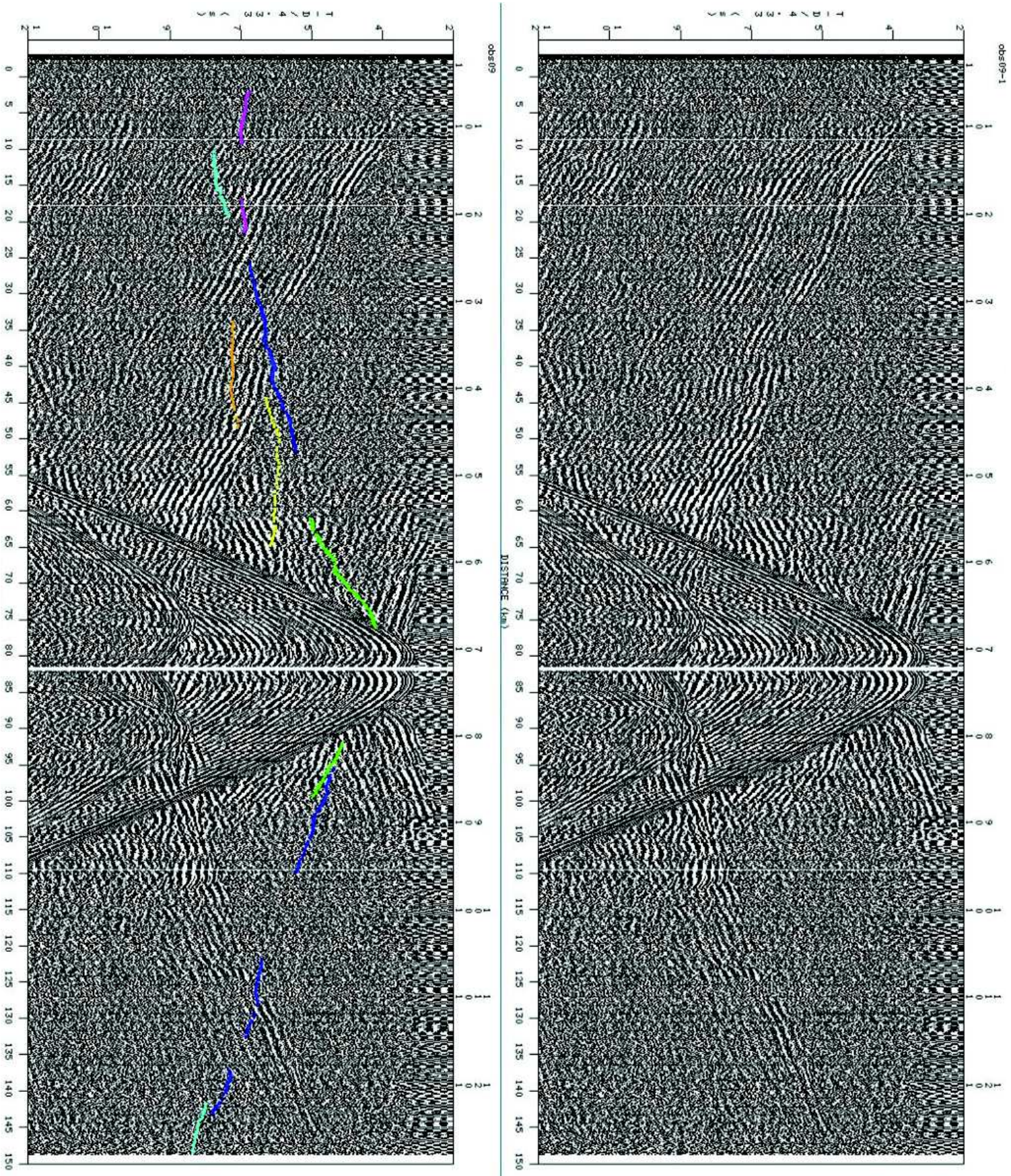
obs09-1
obs09
DISTANCE (km)

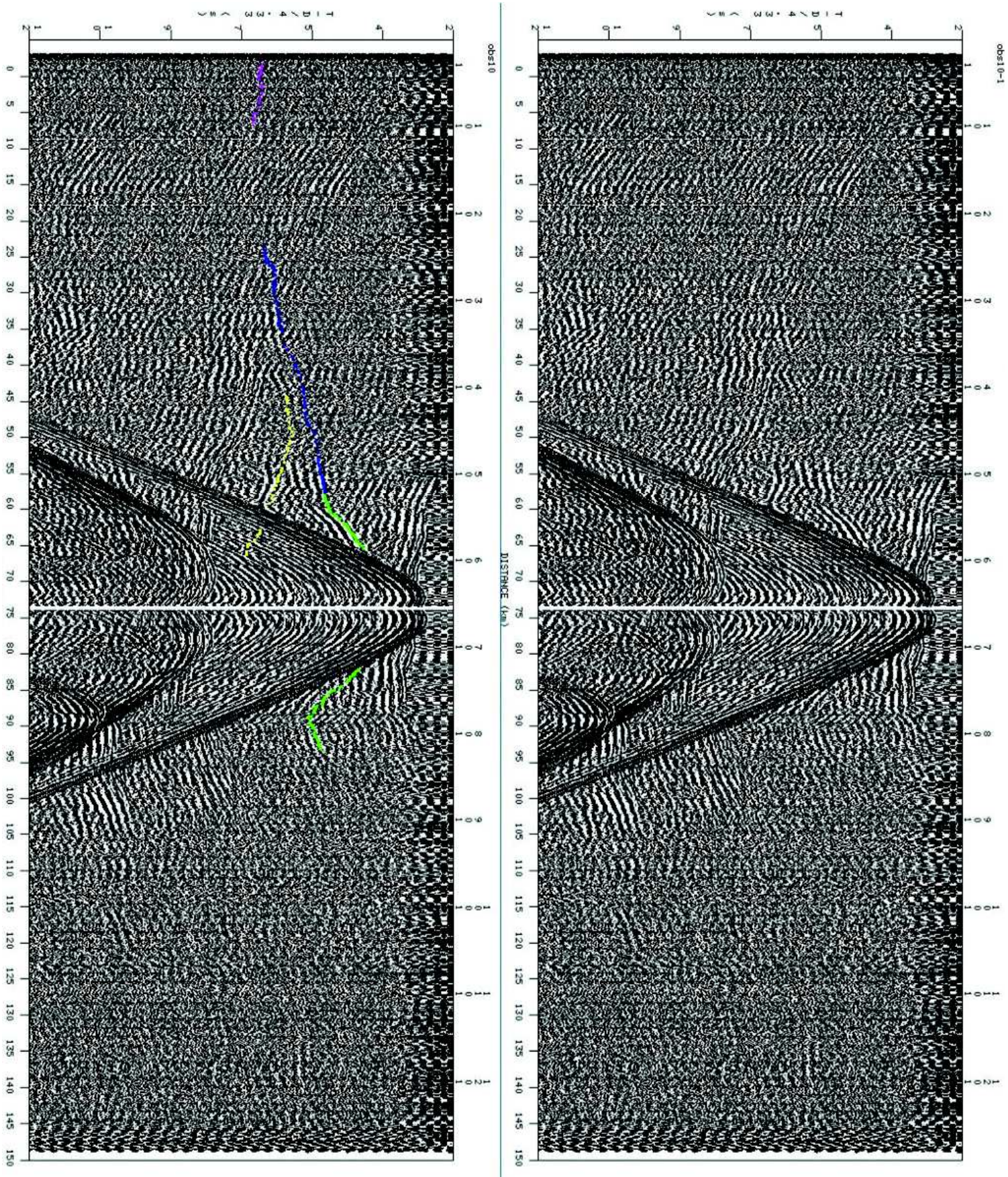
obs10-1
obs10
DISTANCE (km)

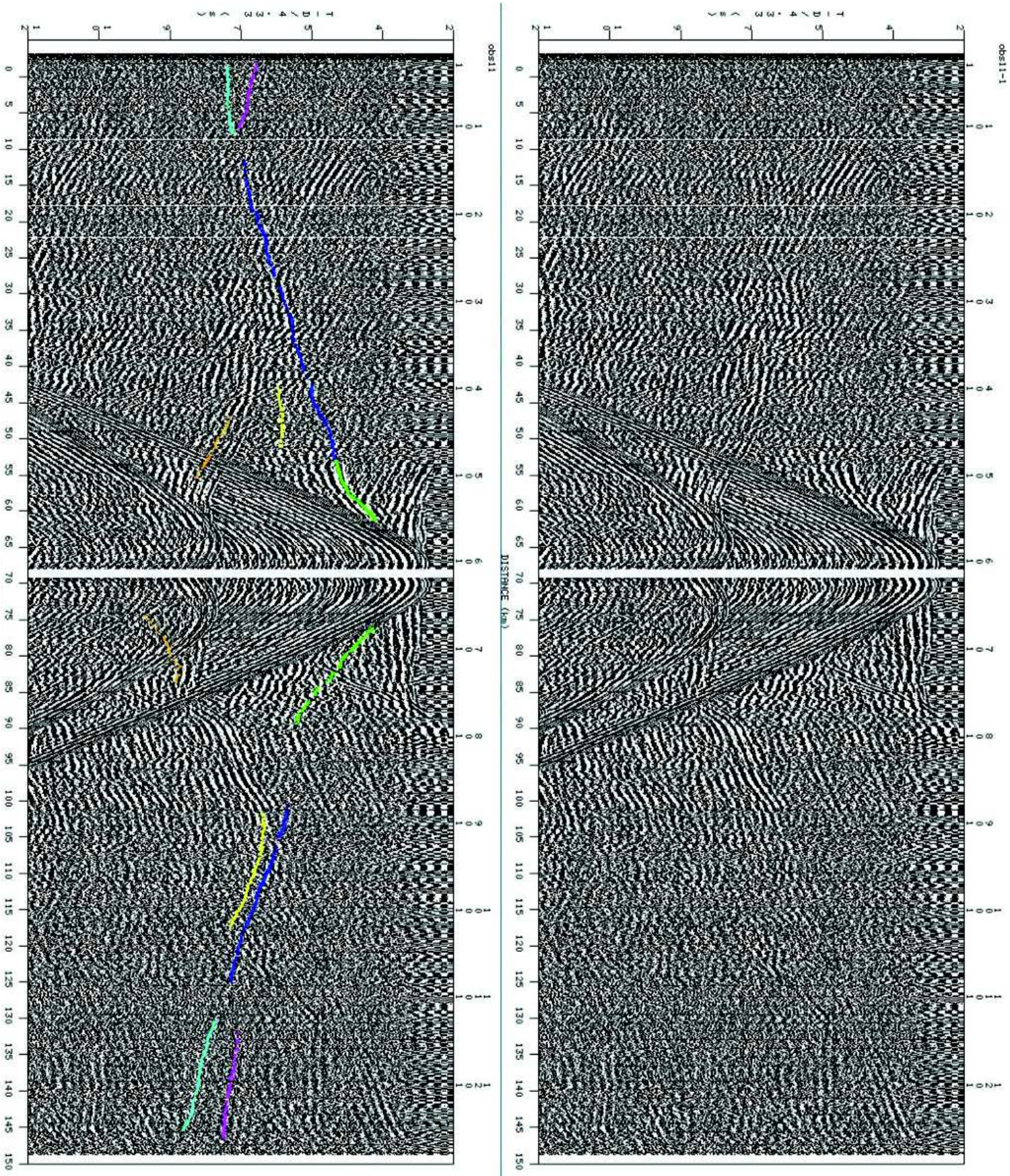
obs11-1
obs11
DISTANCE (km)

OBS12

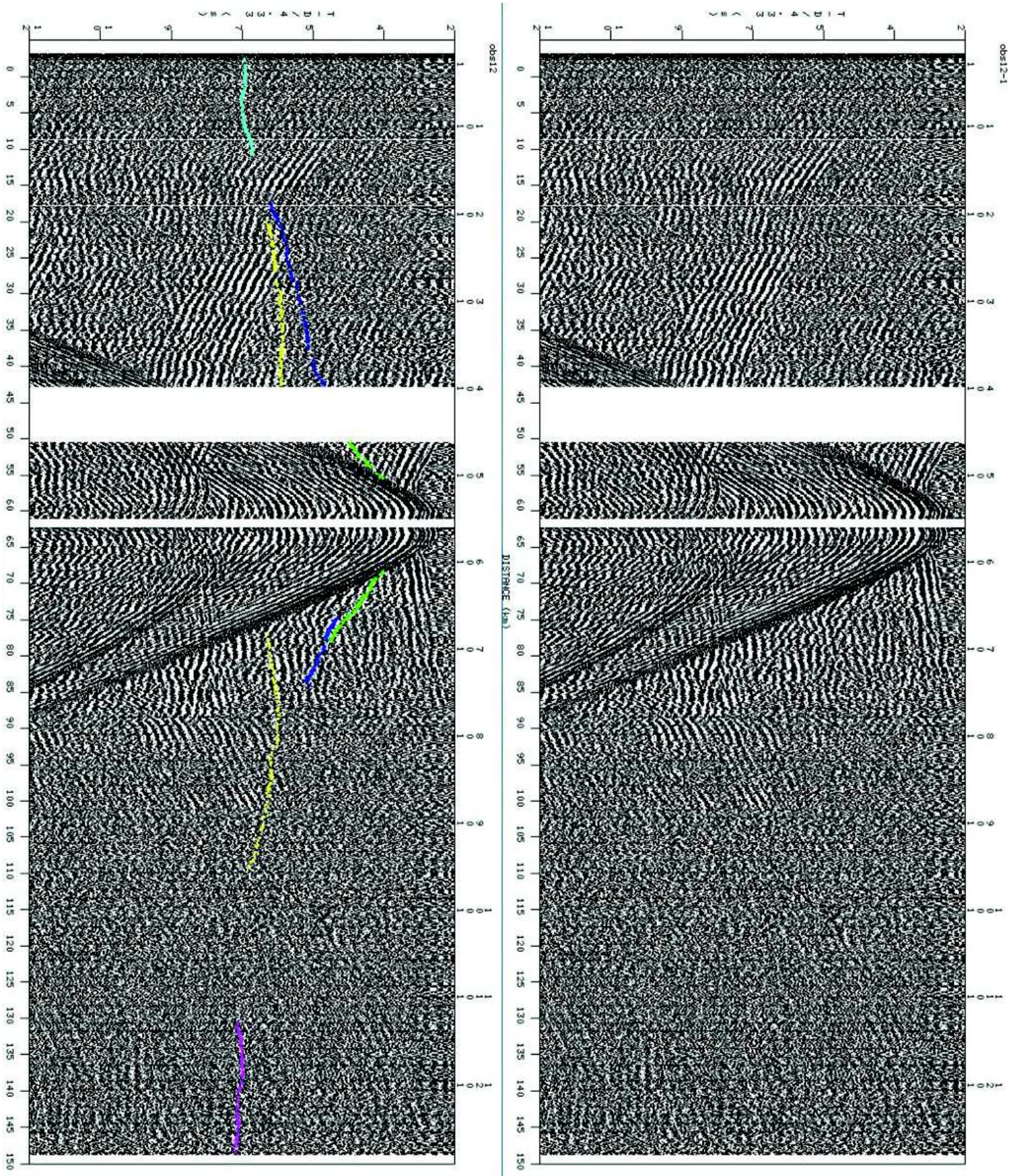

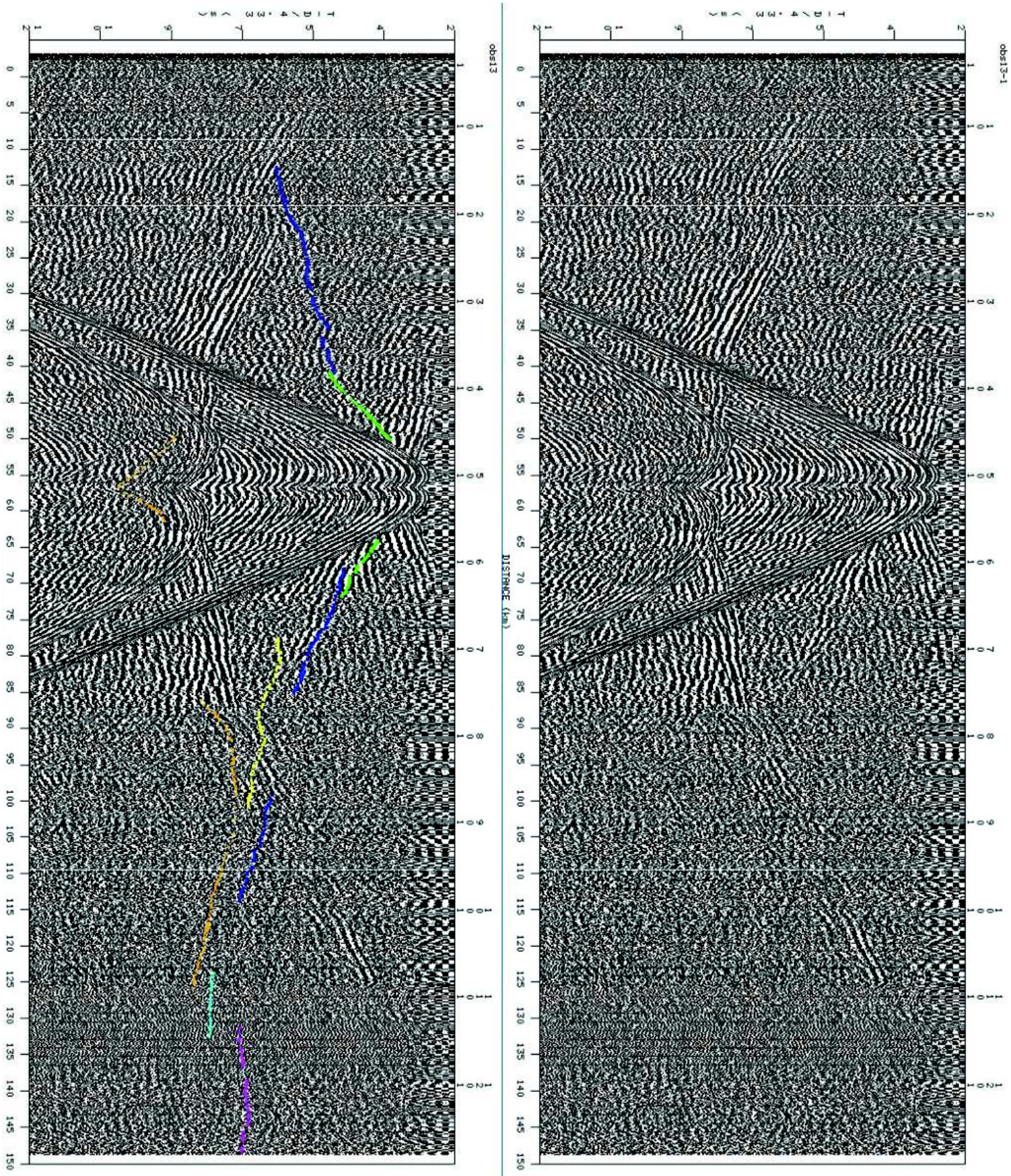
obs13-1
obs13
DISTANCE (km)

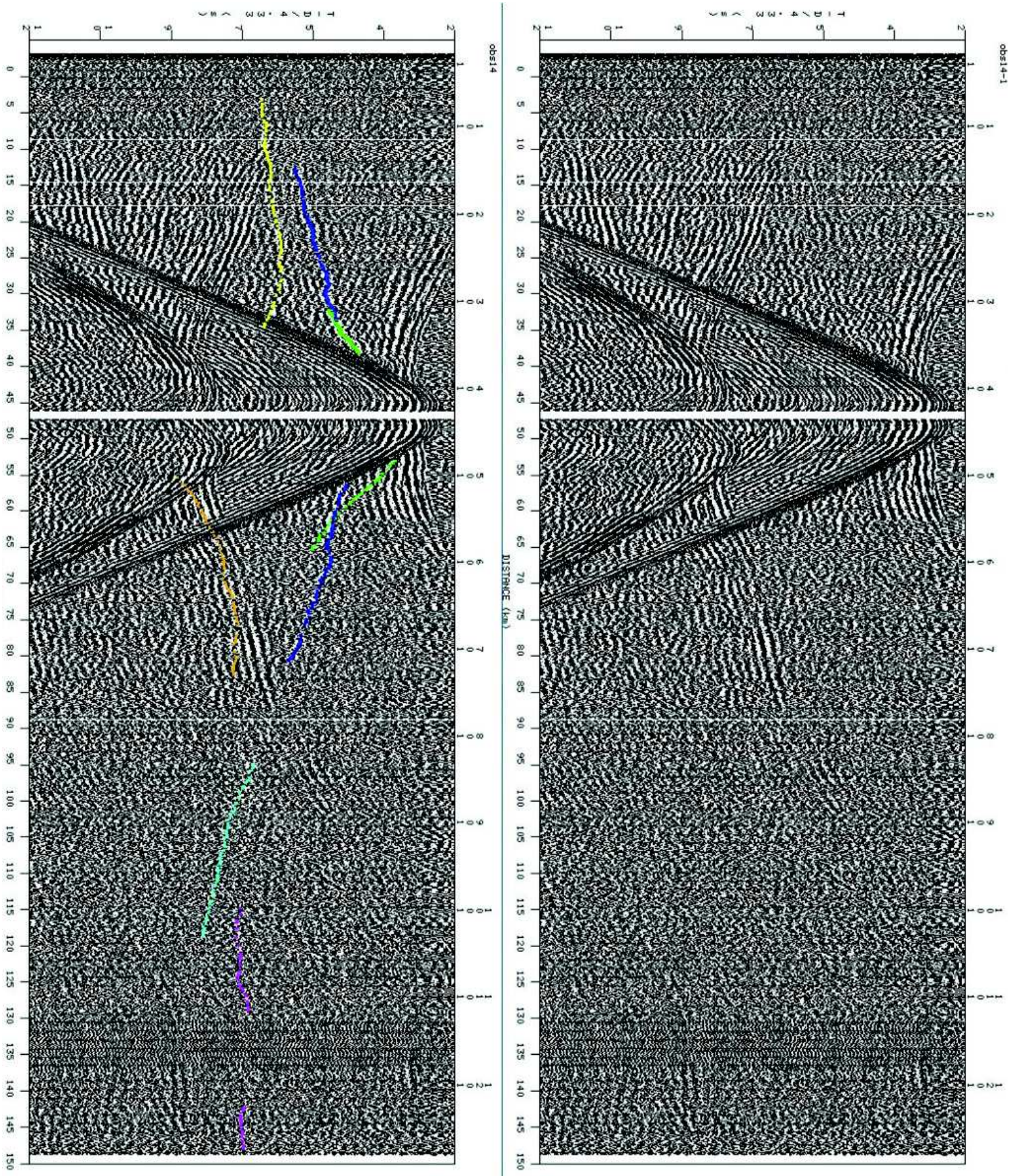
obs14-1
obs14
DISTANCE (km)

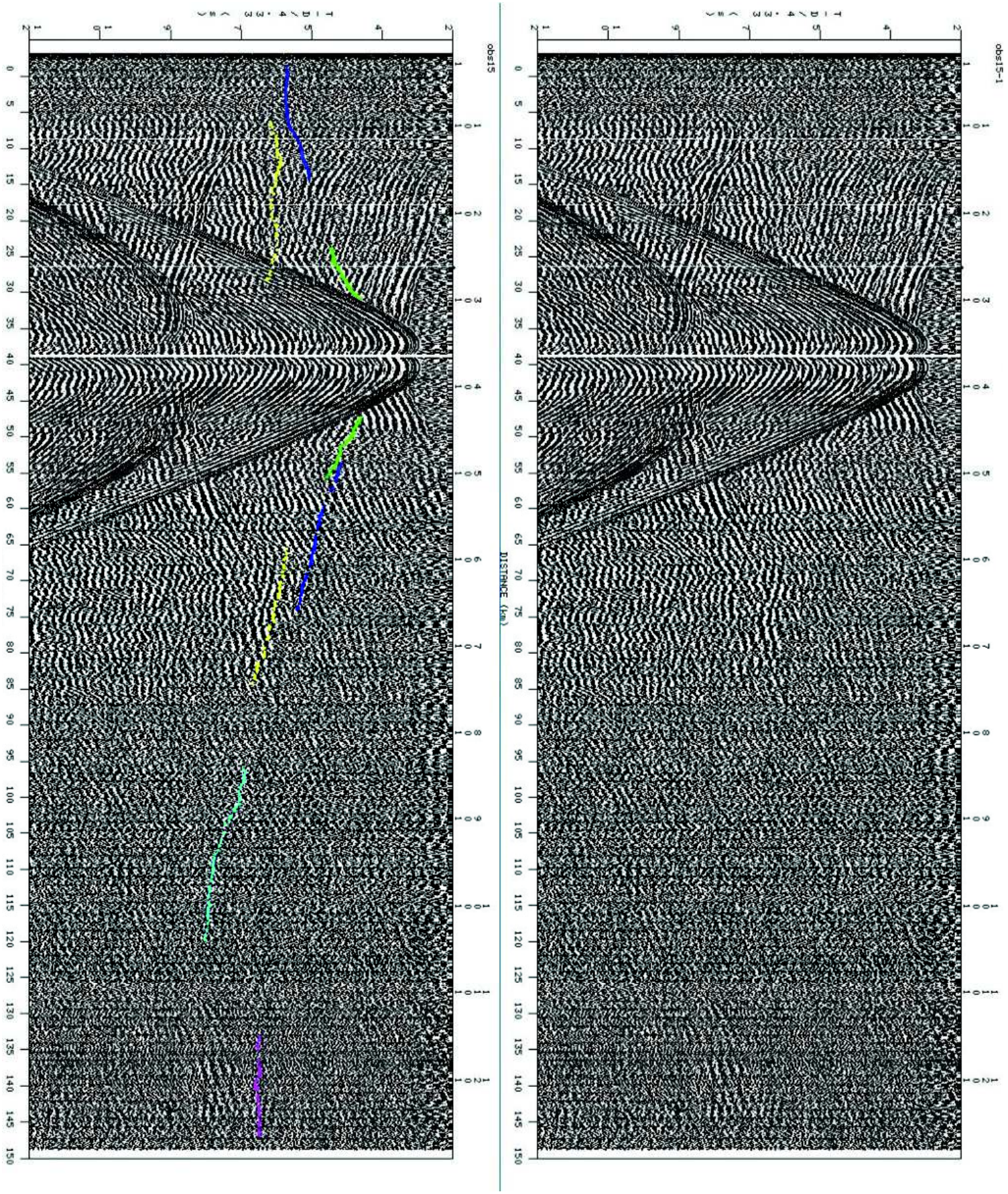
obs15
obs15-1
DISTANCE (km)

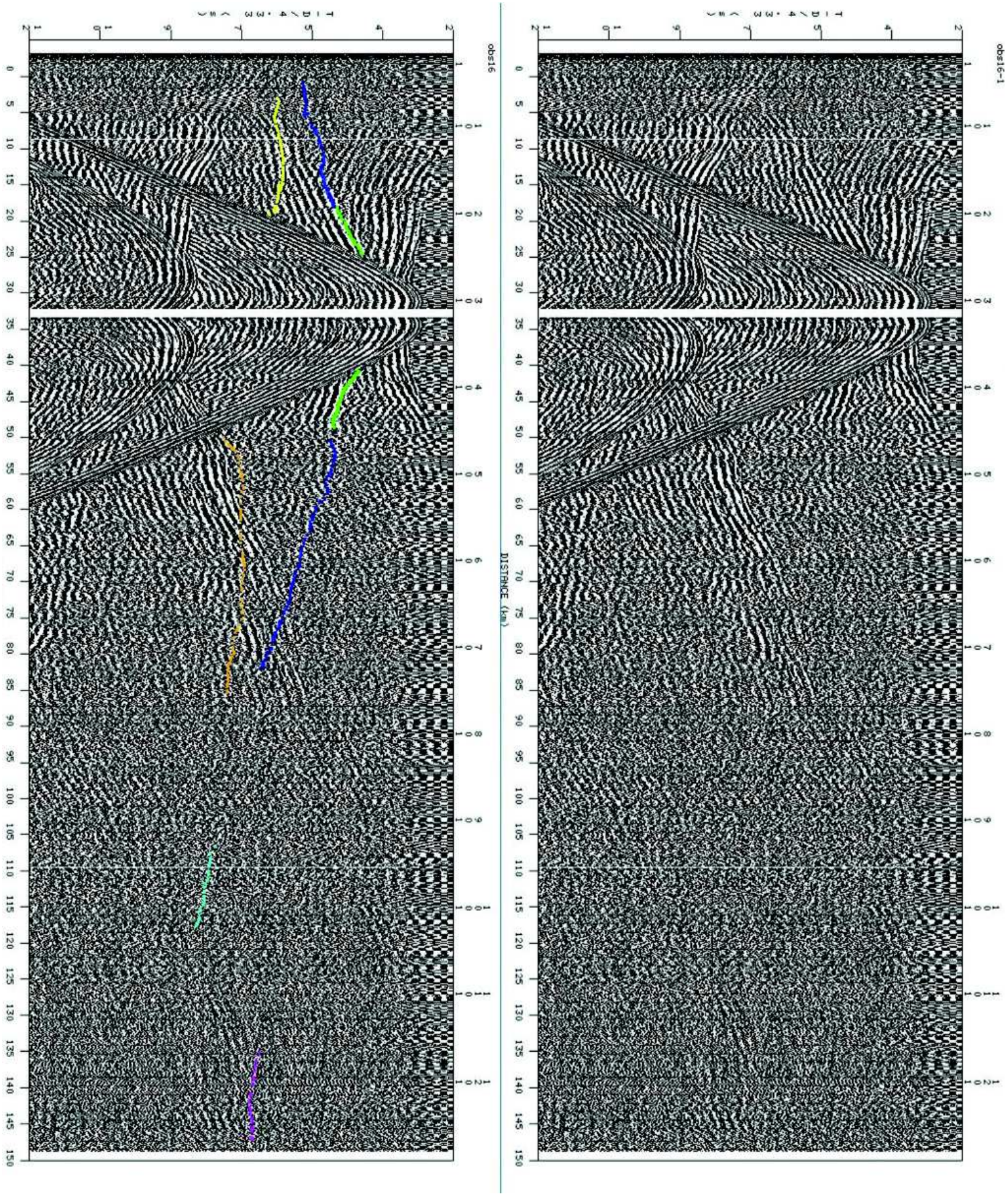
obs16-1
obs16
DISTANCE (km)

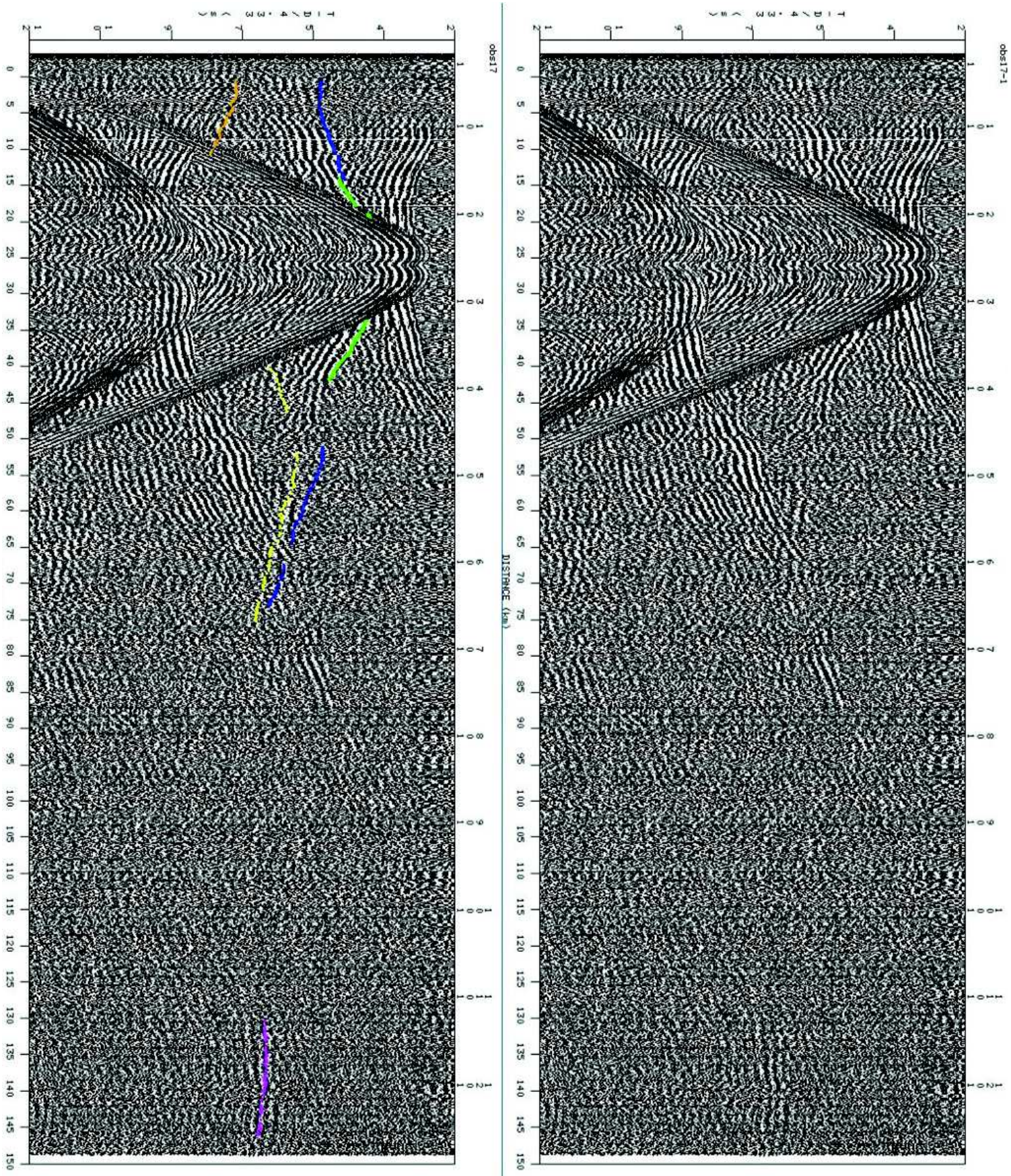
obs17-1
obs17
DISTANCE (km)

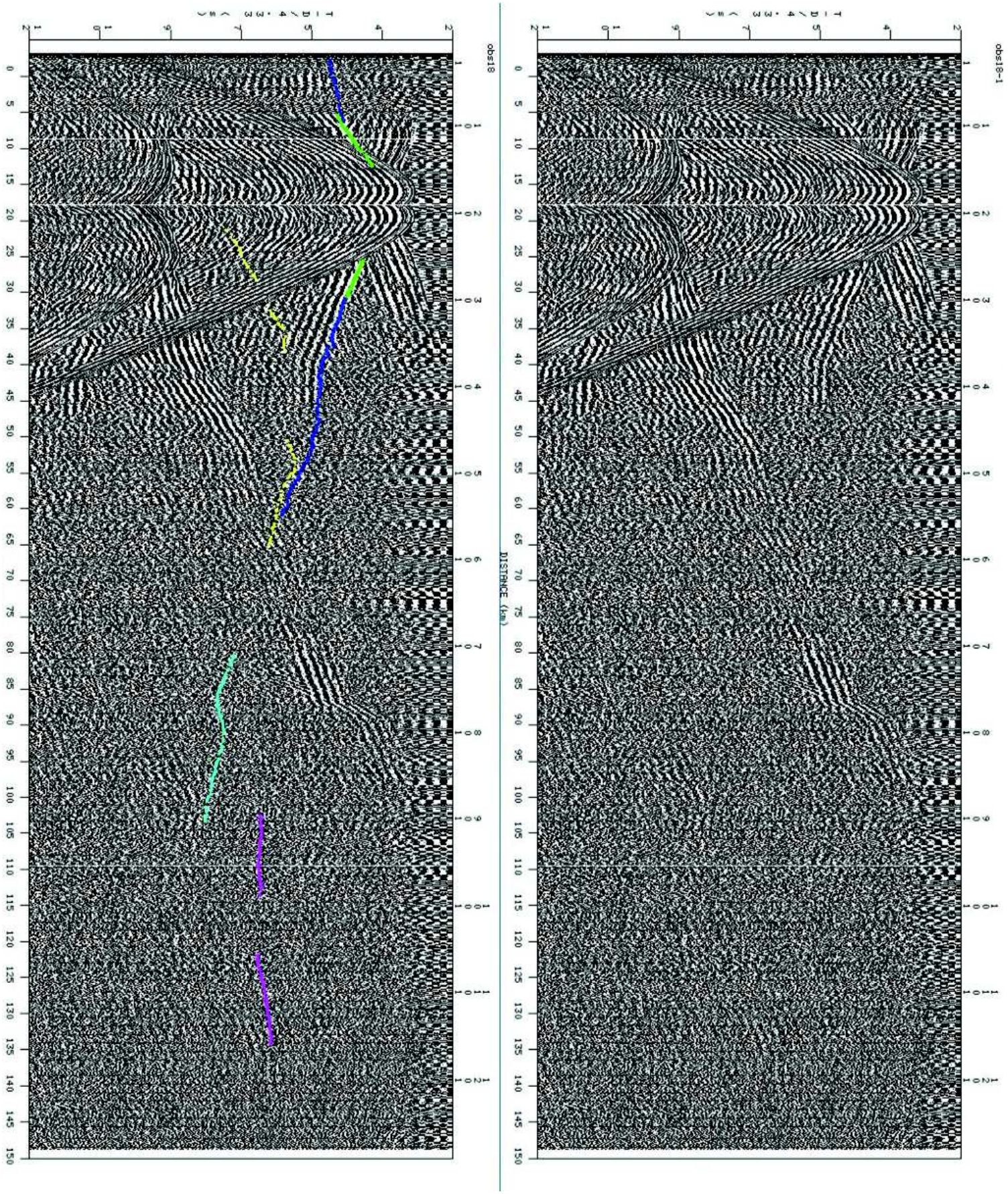
obs18
obs18-1
DISTANCE (km)

APPENDIXES

Omira, R., Ramalho, I., Terrinha, P., Baptista, M.A., Batista, L. & Zitellini, N., 2016. *Deep-water seamounts, a potential source of tsunami generated by landslides? The Hirondelle Seamount, NE Atlantic*, Marine Geology, 379, 267-280.

Omira, R., Neres, M. & Batista, L., 2019. Chapter 8 - The Gloria Transform Fault—NE Atlantic: Seismogenic and Tsunamigenic Potential. in Transform Plate Boundaries and Fracture Zones, pp. 157-167, ed. Duarte, J. C. Elsevier.

Hensen, C., Duarte, J.C., Vannucchi, P., Mazzini, A., Lever, M.A., Terrinha, P., Géli, L., Henry, P., Villinger, H., Morgan, J., Schmidt, M., Gutscher, M.-A., Bartolome, R., Tomonaga, Y., Polonia, A., Gràcia, E., Tinivella, U., Lupi, M., Çağatay, M.N., Elvert, M., Sakellariou, D., Matias, L., Kipfer, R., Karageorgis, A.P., Ruffine, L., Liebetrau, V., Pierre, C., Schmidt, C., Batista, L., Gasperini, L., Burwicz, E., Neres, M. & Nuzzo, M., 2019. *Marine Transform Faults and Fracture Zones: A Joint Perspective Integrating Seismicity, Fluid Flow and Life*, Frontiers in Earth Science, 7.

Marine Geology 379 (2016) 267–280

Contents lists available at ScienceDirect

Marine Geology

journal homepage: www.elsevier.com/locate/margo

Deep-water seamounts, a potential source of tsunami generated by landslides? The Hirondelle Seamount, NE Atlantic

Rachid Omira [a,b,*], Inês Ramalho [a], Pedro Terrinha [a,b], Maria Ana Baptista [b,c], Luis Batista [a,b], Nevio Zitellini [d]

[a] Instituto Português do Mar e da Atmosfera – IPMA, I.P., Rua C do Aeroporto, 1749-077 Lisbon, Portugal
[b] Instituto Dom Luiz – IDL, Faculdade de Ciências da Universidade de Lisboa, Campo Grande, Edifício C8, Piso 3, 1749-016 Lisbon, Portugal
[c] Instituto Superior de Engenharia de Lisboa – ISEL, Instituto Politécnico de Lisboa, Rua Conselheiro Emídio Navarro, 1, 1959-007 Lisbon, Portugal
[d] Istituto di Scienze Marine, CNR; 40129 Bologna, Italy

ARTICLE INFO

Article history:
Received 2 December 2015
Received in revised form 1 June 2016
Accepted 19 June 2016
Available online 20 June 2016

Keywords:
Submarine mass-failures
Deep-water seamount
Tsunamigenic potential
NE Atlantic

ABSTRACT

Submarine mass failures represent one of the most significant marine geo-hazards. Their importance as a major contributor to tsunami generation and hazard has been recognized over the last 20–30 years. This study investigates a newly mapped submarine landslide, the South Hirondelle Landslide (SHL), and its potential to generate a tsunami and to threat the surrounding coasts. The SHL is located 150 km offshore South West Iberia, along the southern flank of the Hirondelle Seamount. Here, available swath bathymetry and one multichannel seismic profile show the presence of large, geometrically well constrained, deep-water landslide deposit of about 500 km^3 and its associated scar. The failure likely occurred in one single event and according to a detailed numerical modelling of the landslide dynamics and of the resulting water propagation the mass failure generated a mega-tsunami, with significant impact along the surrounding coastal areas of Iberia and Morocco. This result strongly supports the inclusion of tsunami induced by deep-water submarine landslides in the marine geo-hazard assessment of the North East Atlantic region.

1. Introduction

Submarine mass-failures (SMFs) represent a widely recognized source of marine geo-hazards. They have the potential to generate significant morphological changes of the sea bottom and, in some cases, to damage large offshore infrastructures, particularly communication cables (Fine et al., 2005). Tsunamis generated by large SMFs are known to cause heavy coastal impact, particularly at local scales (Okal and Synolakis, 2004; Masson et al., 2006). Nevertheless, although their importance as contributors to tsunami hazard has been recognized over the last 20–30 years, they are seldom considered in the quantitative evaluation of tsunami hazard or in the design of tsunami warning strategies, mainly because they are hard to localize and monitor.

In spite of that, a number of large tsunamigenic SMFs events have been identified worldwide. The Storegga event is one of the largest prehistoric SMFs (7000 B.C.), with an estimated volume of 1700 km^3, that occurred on the continental slope west of Norway (Harbitz, 1992; Masson et al., 2006). According to both historical observations and numerical simulations (Harbitz, 1992; Bondevik et al., 2005), the Storegga slide triggered waves that flooded most of coastal areas around the Norwegian Sea and the North Sea. In 1929, the $M_w = 7.2$ Grand Banks earthquake caused the failure of ~200 km^3 of submarine sediments that travelled down slope for a distance of ~700 km from the source (Murty, 1977; Clague, 2001). The Grand Banks SMF caused a tsunami that killed at least twenty seven people in Newfoundland and one in Nova Scotia (Fine et al., 2005). A maximum run-up of 27 m was observed at Taylors Bay (Assier-Rzadkiewicz et al., 1997; Fine et al., 2005) and the waves were recorded as far as the Portuguese coasts and Azores islands (Fine et al., 2005). One of the widely studied SMF events has occurred in 1998, when a tsunami was generated following a $M_w = 6.9–7.3$ earthquake in Papua New Guinea. The first hypothesis associated the observed tsunami with the earthquake (Kawata et al., 1999; McSaveney et al., 2000). However, later studies revealed that the fault dislocation was unable to produce a wave fitting the arrival time and tsunami heights distribution observed in the near-field (Heinrich et al., 2000; Tappin et al., 2001; Imamura et al., 2001). A SMF source was then proposed and evidence was found to support this hypothesis (Heinrich et al., 2000; Imamura et al., 2001; Synolakis et al., 2002). Tappin et al. (2001) simulated the Papua New Guinea tsunami from an underwater landslide, 750 m thick, involving an approximate volume of 7 km^3 of cohesive sediments, obtaining run-up and wave heights in good agreement with the observed ones.

SMFs are almost impossible to observe and characterize, therefore, numerical modelling remains one of the key ways to understand the SMFs dynamics and to assess the associated tsunami (Harbitz et al., 2006). According to Masson et al. (2006) various mechanisms can

* Corresponding author at: Instituto Português do Mar e da Atmosfera – IPMA, I.P., Rua C do Aeroporto, 1749-077 Lisbon, Portugal.
E-mail address: omirarachid10@yahoo.fr (R. Omira).

http://dx.doi.org/10.1016/j.margeo.2016.06.010
0025-3227/

trigger submarine landslides, including: i) earthquakes, ii) sea-level rise, iii) overpressure due to rapid deposition, vi) presence of weak sediment layers, and v) oversteepened slopes.

In the NE Atlantic, less emphasis has been given so far to tsunamigenic landslide compared to the tsunamis of seismic origin, despite SMFs may occur more frequently than expected. In fact, Lo Iacono et al. (2012) have recently shown the evidences of large SMFs in the Gorringe Bank, with significant tsunami potential and impact along the surrounding coasts of the NE Atlantic region.

In this paper, we study a large SMF found in the NE Atlantic and its possible tsunamigenic potential. The study is based on an available multichannel seismic profile and multi-beam swath bathymetric data which allowed to define the geomorphologic characteristics of the landslide including the evacuation and depositional areas. The identified SMF is located in the south flank of Hirondelle Seamount, NE Atlantic, 100 km west of the Gorringe Bank (see Fig. 1 for localization). The investigation of the South Hirondelle Landslide (SHL) includes: i) localization and measure of the landslide source area and deposit, ii) landslide failure scenarios: one single event versus multiple events, and iii) modelling of the tsunami generation potential and propagation towards the target coasts. We further discuss the SHL age and its possible trigger mechanism as well as the numerical modelling limitations.

2. The Hirondelle Seamount: geological setting and landslide

2.1. Geological setting

The Hirondelle Seamount is located along the Eurasia-Africa plate boundary in the Atlantic Ocean. This plate boundary is well defined only between the Azores plateau and the Madeira-Tore Rise (MTR in Fig. 1), where the boundary is discrete and accommodated by a dextral strike-slip fracture zone, the Gloria Fault (GF in Fig. 1), along which instrumental earthquakes of M_w = 7.1–8.4 (Bird and Kagan, 2004; Buforn et al., 1988) were recorded (Fig. 1).

To the east of the MTR, the location of the plate boundary is still a subject of debates and research. The role of plate boundary has been assigned to two lithospheric tectonic structures, the subduction zone underneath the Gibraltar Arc (Gutscher et al., 2002) and the South-West Iberia Margin (SWIM in Fig. 2) dextral strike-slip faults between Europe and Africa (Zitellini et al., 2009) (Fig. 1). Besides these two lithospheric fault zones a series of thrust faults with demonstrated activity in the Quaternary have been studied by several authors and summarized in Zitellini et al. (2004) (Fig. 2). The main landslides described in southwest Iberia are associated with these thrust faults: the Marquês de Pombal (260 km^2) landslide and Gorringe landslide (380 km^2), both showing active deformation, frontal thrust fault scarps of 1.4 km and 5 km height, respectively, and clusters of seismicity (Gràcia et al., 2003; Terrinha et al., 2003; Lo Iacono et al., 2012) (Figs. 1 and 2).

The Hirondelle Seamount (Hsm) is located east of the MTR, between the Josephine Seamount (Jsm) and the Gorringe Bank (GB) (Fig. 1). The alignment of these three seamounts forms an ESE-WNW oriented continuous ridge about 300 km long and about 80 km wide, which separates the Horseshoe Abyssal Plain (HAP in Fig. 2) from the Tagus Abyssal Plain (TAP in Fig. 2) and where most of the seismicity associated to the Europe-Africa plate boundary is located. The Hsm is made up of oceanic crust of Upper Jurassic age, chron M21 after Seton et al. (2012). Southward of the Hirondelle-Gorringe seamounts are located the Coral Patch Seamount (CPsm in Fig. 2) and the Coral Patch Ridge. These seamounts separate the Seine Abyssal Plain from the Horseshoe Abyssal Plain and were affected by thrusting and folding during the Miocene (Zitellini et al., 2004). Despite recent deformation has been described based on seismic reflection data, the recorded seismicity associated is low (Martinez-Loriente et al., 2013, Fig. 2).

Although the published information on the Josephine and Hirondelle seamounts is scarce, the Gorringe Bank has been widely investigated with seismic reflection and refraction, swath bathymetry (Sartori et al., 1994; De Alteriis et al., 2003), manned dives (Girardeau et al., 1998) and by an Ocean Drilling Project drill (Ryan et al., 1973). The Gorringe Bank is a piece of exhumed lithospheric mantle carried on

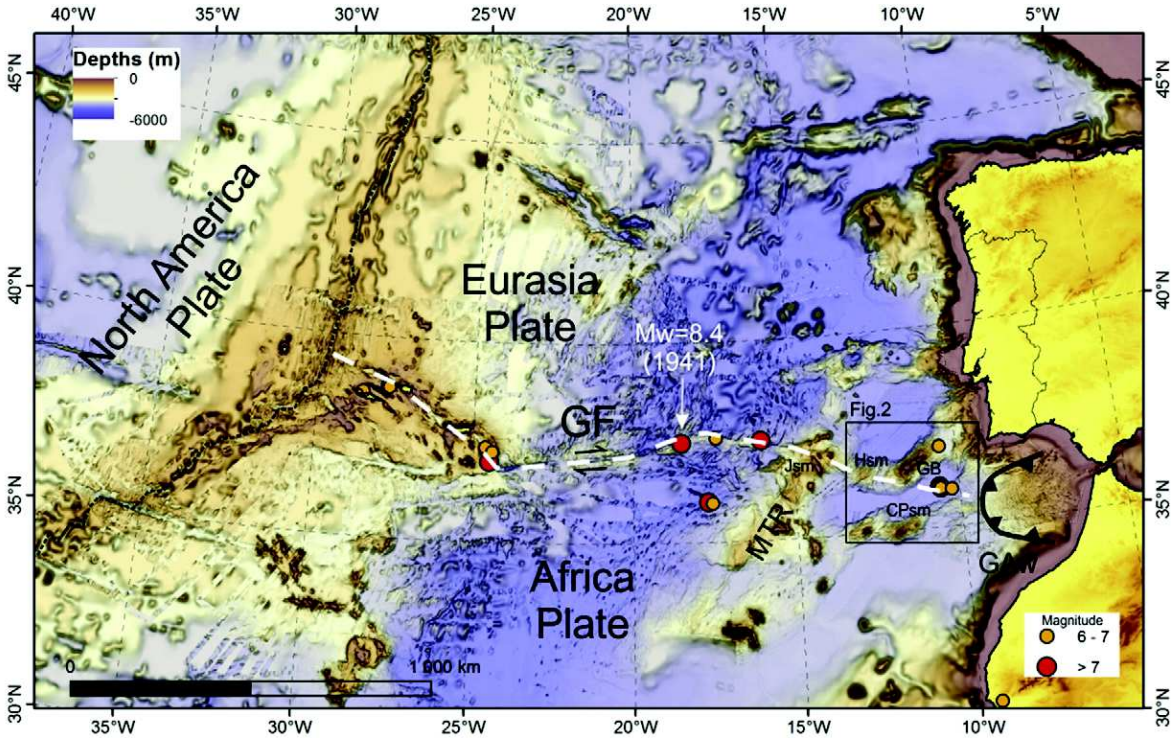

Fig. 1. Location of the study area with bathymetry of a part of the North Atlantic encompassing the study area (black square). Red and yellow circles mark the epicenters of instrumental earthquakes M > 6. MTR, Madeira-Tore Rise; GF, Gloria Fault; GAw, Gibraltar Accretionary wedge; Jsm, Josephine Seamount; Hsm, Hirondelle Seamount.

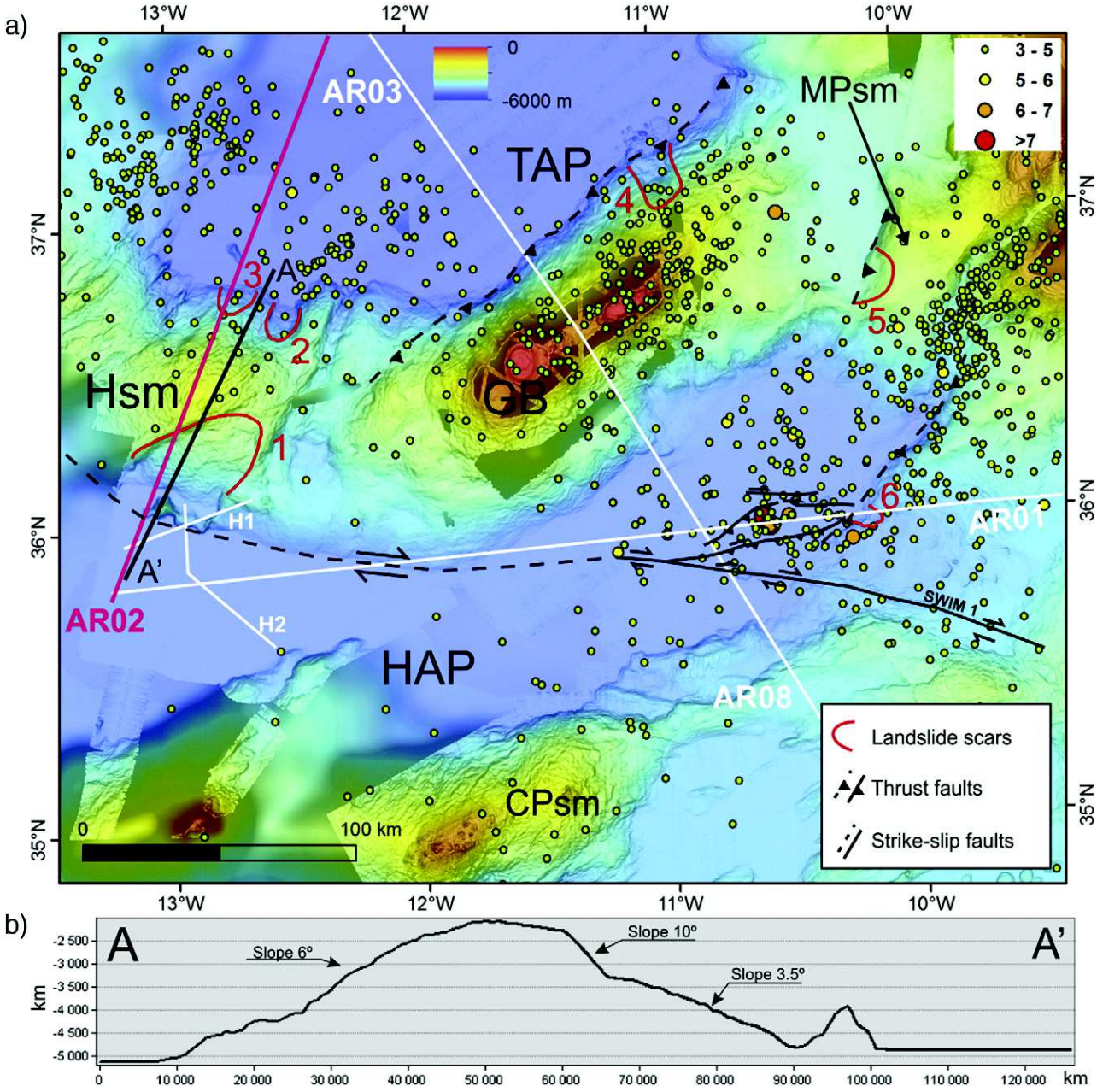

Fig. 2. Morphology and tectonics of the study area: a) Bathymetry of the Hirondelle seamount and neighbour area and main tectonic features: fault interference pattern between Horseshoe thrust and SWIM strike-slip faults. Location of landslides: 1) South Hirondelle Landslide (SHL) (this study); 2 and 3) North Hirondelle; 4) North Gorringe (Lo Iacono et al., 2012); 5) Marquês de Pombal (Gràcia et al., 2003; Terrinha et al., 2003) and 6) Horseshoe (in prep.). Seismic reflection also shown: AR02 is shown in Fig. 3; AR01 (Torelli et al., 1997), AR03 and AR08 (Sartori et al., 1994); H1 and H2 (Hayward et al., 1999). GB, Gorringe Bank; HAP, Horseshoe Abyssal Plain; Hsm, Hirondelle seamount; MPsm, Marquês de Pombal seamount; TAP, Tagus Abyssal Plain; CPsm, Coral Patch seamount; b) Bathymetric profile across the Hirondelle Seamount and South Hirondelle Landslide.

top of a north-westward directed thrust for approximately 20 km mostly during Miocene times (Hayward et al., 1999; Sartori et al., 1994; Auzende et al., 1978; Jiménez-Munt et al., 2010; Sallarès et al., 2013). The recent tectonic activity of the Josephine-Gorringe ridge is attested by instrumental seismicity whose focal mechanisms indicate a maximum horizontal stress parallel to NW-SE direction (Geissler et al., 2010).

There are various chrono-stratigraphic models used for calibrating the seismic reflection data of the HAP, all based on the DSDP sites 135 and 120 drillings on the Coral Patch Ridge and Gorringe Bank by Hayes et al. (1972) and Ryan et al. (1973) respectively, and on the ODP 339 in the Gulf of Cadiz (Hernández-Molina et al., 2014). Hayward et al. (1999) showed a MCS profile south of the Hsm producing the first stratigraphic model of the study area that consists of six seismic units on top of acoustic basement. Table 1 shows the correspondence between seismic units identified in this work and those of Hayward et al. (1999). For identifying the base of Quaternary we used the model by Roque (2007) and Roque et al. (2012). The existence of Holocene hemipelagic deposits on the seafloor of the HAP and at the foot of the Marquês de Pombal thrust was confirmed by Gràcia et al. (2010). For estimating the thickness of the slide we used the depth conversion velocities by Martinez-Loriente et al. (2013).

2.2. The Hirondelle Seamount and the South Hirondelle Landslide

The Hirondelle Seamount is a west to east trending seamount rising >2800 m above the HAP and 3000 m above the TAP. An ENE-WSW striking scarp dipping 14° SE separates an area to the northwest where a

Table 1
Correlation between stratigraphic models in the West Horseshoe Abyssal Plain.

This work	Hayward et al. (1999)
UIV- Holocene – Lower Miocene	WHI- Pleistocene-Late Oligocene
UIII- Oligocene – Early Aptian	WHII–WHIII-Early Eocene to early Aptian
UII- Early Aptian to Late Jurassic	WHIV–WHV-Early Aptian to Late Jurassic
UI- Early Aptian to Late Jurassic	WHVI- Early Aptian to Late Jurassic
Acoustic Basement- Jurassic oceanic crust	Acoustic Basement- Upper Jurassic

pervasive NE-SW trending linear fabric occurs from an area to the southeast where this fabric is absent and the seafloor morphology is smoother and wrinkled, corresponding to the South Hirondelle Landslide (SHL) (1 in Fig. 2). The structure of the Hsm, the seismic stratigraphic model and the internal geometry of the SHL are described based on the interpretation of the multichannel seismic reflection profile AR02 (Fig. 3) that cuts across the Hsm although not parallel to the main dip direction of the SHL.

This seismic profile was acquired in 1992 by the R/V OGS Explora using an array of 32 guns for a total volume of 5000 in.^{3} and a 120-channel streamer with group interval of 25 m and shot interval of 50 m. The record length was 13 s with 2×10^{-3} s sample interval. The processing was

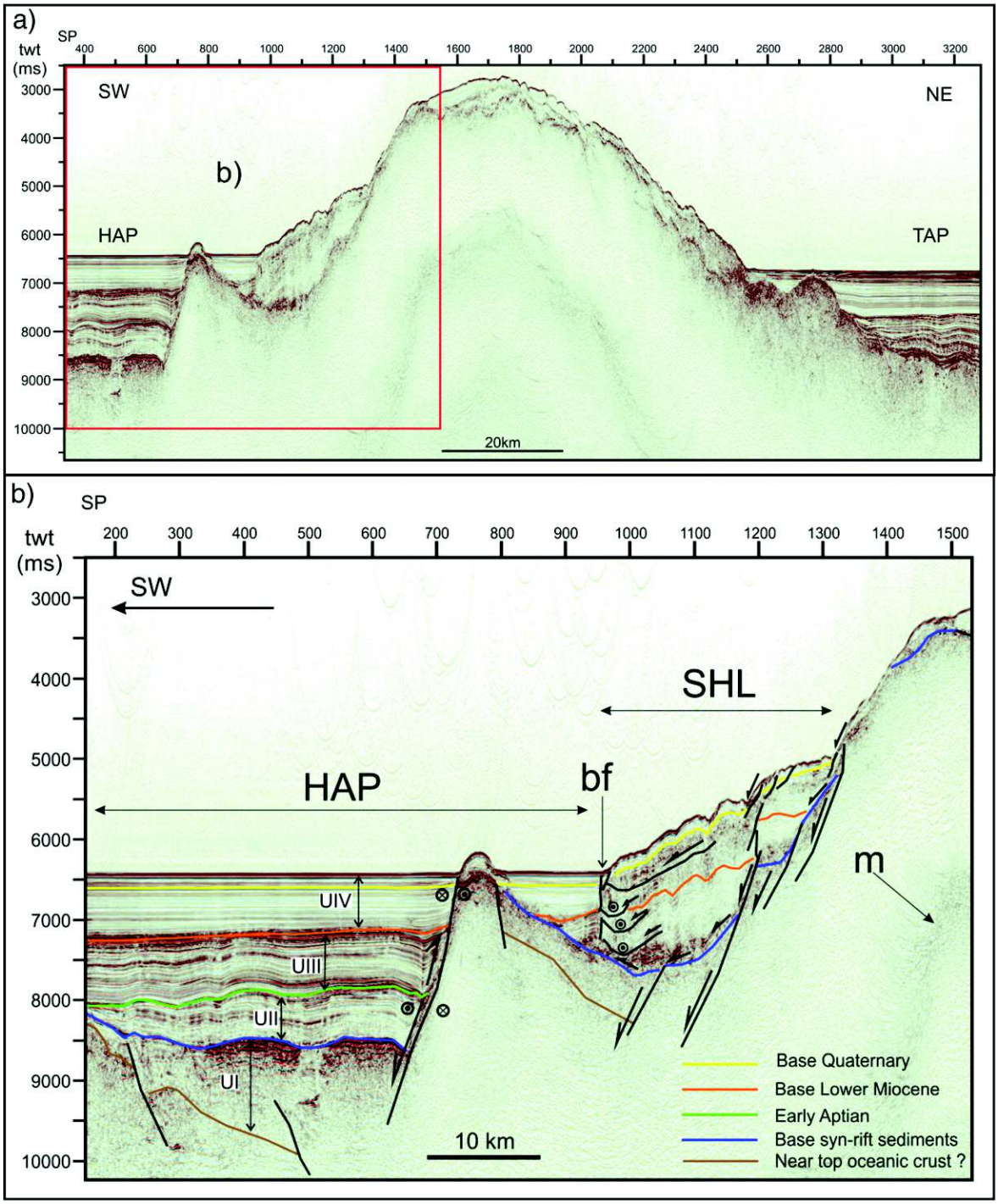

Fig. 3. Seismic reflection line AR02: a) Uninterpreted full line across the Hirondelle seamount; b) Interpretation of the southern part of AR02 across the South Hirondelle Landslide.

carried out at the Institute of Marine Science (ISMAR) of Bologna using the DISCO package of COGNISEIS Development Inc. applying a standard processing sequence. The seismic processing sequence can be summarized as follows: demultiplexing, resampling to 4×10^{-3} s, sorting, spike deconvolution, velocity analysis every 2.5 km, normal move out, muting, CDP staking, spherical divergence correction, finite-difference wave-equation migration, time-variable filtering.

The seismic reflection line AR02 images the stratigraphic record and tectonic structure across the Hsm (Fig. 3a) and part of the HAP and TAP. On the southern flank of the seamount, the internal structure of the SHL, a rotational slide, is depicted (Fig. 3b). The basal failure has a concave curvature over the whole length implying reduced down-slope displacement. Extensional deformation is accommodated down dip in the head of the landslide, as faults cutting through the whole body of the landslide or affecting its topmost layer only (Fig. 3b). Shortening is accommodated in the toe thrust part (up dip) and central part of the slide. The existence of a buttress fault (bf) against which shortening builds up may indicate that this acted as a lateral ramp to the main slide movement. Actually, the MCS AR02 profile is not parallel to the main slope dip parallel to which the slide movement could have occurred.

The maximum thickness of the deformed slide is approximately 1.6 s TWT, calculated as follows. Using the velocity model in Martinez-Loriente et al. (2013) for the equivalent layers in MCS AR02 we can assign a layer velocity of 2000 $m \cdot s^{-1}$ to UIV and a mean velocity of 2800 $m \cdot s^{-1}$ for the underlying layers. The maximum thickness of UIV (0.7 s TWT) corresponds to 700 m and the underlying package (0.9 s TWT) corresponds to 1260 m, a total thickness of 1960 m, roughly.

In the Horseshoe Abyssal Plain we identified four main seismo-stratigraphic units, UI to UIV above the acoustic basement (Fig. 3b). UI is the lowest seismic unit that displays organized stratified reflections. It lays on top of acoustic basement that should correspond to oceanic crust of Late Jurassic age, according to general agreement (Seton et al., 2012; Sallarès et al., 2013; Martinez-Loriente et al., 2013). The wedge shape of UI and UII indicates that these units were deposited during tectonic extension, i.e., intra-oceanic rifting. The lateral discontinuity of reflectors within horizons in UI suggests tectonic structuring of this block and the presence of sediments of variable composition, compatible with the presence of volcano-clastics. Above UI, reflectors are more continuous indicating that tectonic extension concentrated on the main fault during the deposition of UII. UIII also shows slightly undulated – parallel and laterally continuous reflections suggesting the presence mostly of hemipelagic sediments; the constant thickness indicates this is a post-extension sequence. Coherent folding of UI–UII–UIII indicates that tectonic shortening occurred previous to deposition of UIV, which lies on top of folded UIII displaying parallel, laterally continuous reflections. UIV is clearly a post tectonic shortening unit showing minor drag at the contact with the rotated basement block shown in Fig. 3b. We interpret the faults that appear in the uppermost part of the SHL (Fig. 3b) as gravity faults and disruptures caused by the landslide movement. While in the southernmost part of the AR02 line (Fig. 3b), the fault is deep seated and has a long lived history of rifting and inversion, previous to the deposition of UIV. Inspection of available and published seismic reflection lines in the study area (see Fig. 2a for location) shows that the top of the folded horizons of UIII are covered by sediments that are lateral equivalent of the Allochthonous unit of the Gulf of Cadiz (Medialdea et al., 2004). Accordingly, the base of the UIV is considered to be of Early Miocene age, also in agreement with Fig. 3 of Torelli et al. (1997).

Stratigraphic correlation of the seismic units of the HAP and top of the Hsm is not possible because the lack of lateral continuity of the reflectors across the landslide headscarp. However, it is straightforward that the crest of the seamount is covered by a package of condensed stratigraphic series, indicating that the Hsm was a structural high at the time of formation of the Lower Jurassic oceanic crust.

The stratigraphic correlation between the HAP and SHL was attempted and is shown in Fig. 3. Two seismic horizons (base Quaternary and UIV–UIII boundary) were correlated from the HAP across the acoustic basement peak at shot point 750. Sub-division of UIII to UI within the SHL was not possible due to the homogenization of the seismic character caused the deformation of the slid body. Nevertheless, comparison of the acoustic character at the base of the landslide suggests that the main decollement surface to the SHL is near the UI–UII boundary (Fig. 3b).

The joint interpretation of the AR02 seismic reflection profile (Fig. 3b) and swath bathymetry (Fig. 4a) allows the characterization of the SHL, as follows: i) The wrinkled surface of the slope corresponds to folded strata of a slid body; ii) The larger wave-length folds affect the UII through UIV sedimentary sequence; iii) Minor folds are observed at the top of the youngest sedimentary horizons, as well as interbedded in deeper packages, indicating existence of internal detachments that account for localized non-harmonic folding of the whole body; the detailed inspection of non-harmonic folding and internal bed cut offs allowed for interpretation of detachment faults in the slid body; iv) internal shortening of the slide terminates against a vertical buttress fault (bf in Fig. 3b); the presence of a channel shaped extensional detachment horizon suggests that the main slide direction is not parallel to the profile section, but rather probably towards the southeast, i.e., parallel to the main slope dip.

The main morphologic features of the SHL were identified in the swath bathymetry model depicted in Fig. 4a. The SHL covers a total

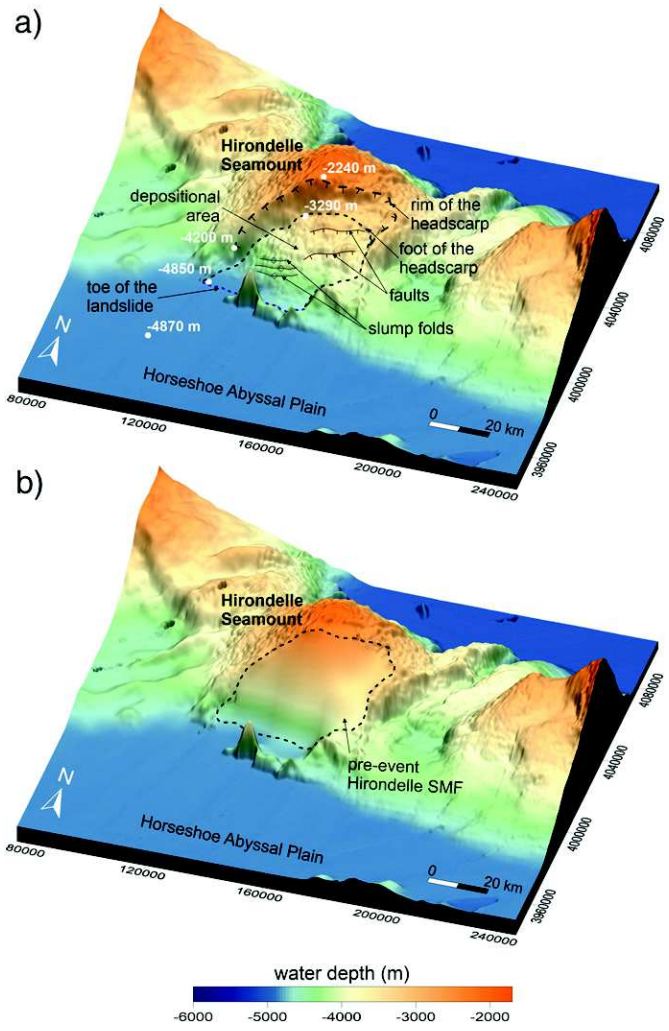

Fig. 4. Bathymetric models: a) Post-event (present day) bathymetric model including the main morphologic features of the South Hirondelle Landslide; b) Pre-event, including the reconstruction of the South Hirondelle Landslide, bathymetric model. The maps coordinates system is UTM – Zone 29 N, Datum WGS-84.

area of ~1200 km^2 comprising erosion and depositional areas. The SHL source area extends for ~80-km-long with slopes varying from ~3.5° to ~16°. The rim of the headscarp, standing in the upper limit of the source area, has a curvilinear shape with two main orientations (Fig. 4a). The western part coincides with the WSW-ENE striking oceanic rift faults, suggesting that it is controlled by an inherited tectonic fabric. The northern part of the headscarp is parallel to the Hsm crest, normal to the dip of the seamount, suggesting that this segment of the scarp has a gravity control only. The rim of the headscarp is located at depths −2240 m to −4200 m with a maximum slope of 16° SSE. The depositional area covers ~680 km^2. It is bounded at the top by the foot of the headscarp, located at −3290 m depth, and at the bottom by the foot of the landslide, located at −4850 m depth (Fig. 4a). Slopes within this area vary from ~0.2° up to ~3.5°. Comparison of the swath bathymetry (Fig. 4a) with the MCS profile (Fig. 3b) allowed the interpretation of additional SHL morphologic features, such as internal faults and slump folds as marked in Fig. 4a. At the base of the SHL the bathymetry model allowed outlining the lateral extent of the buttress fault/toe of the landslide identified in the seismic profile.

3. Tsunamigenic potential and wave propagation

3.1. Methodology and data

To assess the tsunami generation potential and wave impact posed by the failure of the SHL, we employ a numerical modelling methodology that considers a realistic pre-event bathymetry model, that uses a sensitivity analysis to constrain the material parameters of the landslide from the observed deposit, and that uses a "two-way" coupling model, taking into account the effect of the slide on the water and the effect of the wave on the slide. This later effect is more important in the case of shallow-water landslides where the generated wave can affect the landslide motion (Jiang and LeBlond, 1994). Our methodology consists of five steps that include: i) build the pre-mass failure bathymetric model, ii) run multiple times the landslide flow simulations with varied landslide body physical parameters (i.e., density, kinematic viscosity, and drag coefficient), iii) compare the simulated landslide run-out mass with the landslide deposit identified in the bathymetry and multichannel seismic profiles, iv) select the landslide physical parameters for which the simulations lead to a better representation of the observed deposit, v) run, using the selected physical parameters, the "two-way" coupling model that simulate the landslide-induced tsunami generation and propagation.

3.1.1. Pre-event bathymetric model

In order to model properly the mass-failure motion it is necessary to infer the pre-event bathymetric model, taking into account the landslide deposit and the source area. The pre-failure sea-bottom topography can be inferred by restoring in the original position the sedimentary package involved in the slide using the swath bathymetry and the multichannel seismic profile AR02. From the AR02 line we can infer the amount of shortening suffered by the individual units U1–UVI by unfolding strata showing consistent lateral continuity. This exercise will allow determining the rough amount of the horizontal mass movement and the original thickness of the landslide deposit. Once these numbers are known we can restore the position and arrangement of the sediments taking into account the conservation of the SMF volume.

Fig. 4 depicts both post-event (Fig. 4a) and the pre-event (Fig. 4b) bathymetric models. Analysis of the post-event bathymetric model results in a volume of about 500 km^3 of depositional material. In Fig. 4b we build the pre-event SHL with respect to the depositional volume and the origin area of the failure. The SMF material is distributed in order to cover the origin area of the landslide body and conserve the landslide depositional volume. In Fig. 5a, we plot profiles of the observed deposit (MCS profile AR02, in Fig. 3a) and the reconstructed SHL.

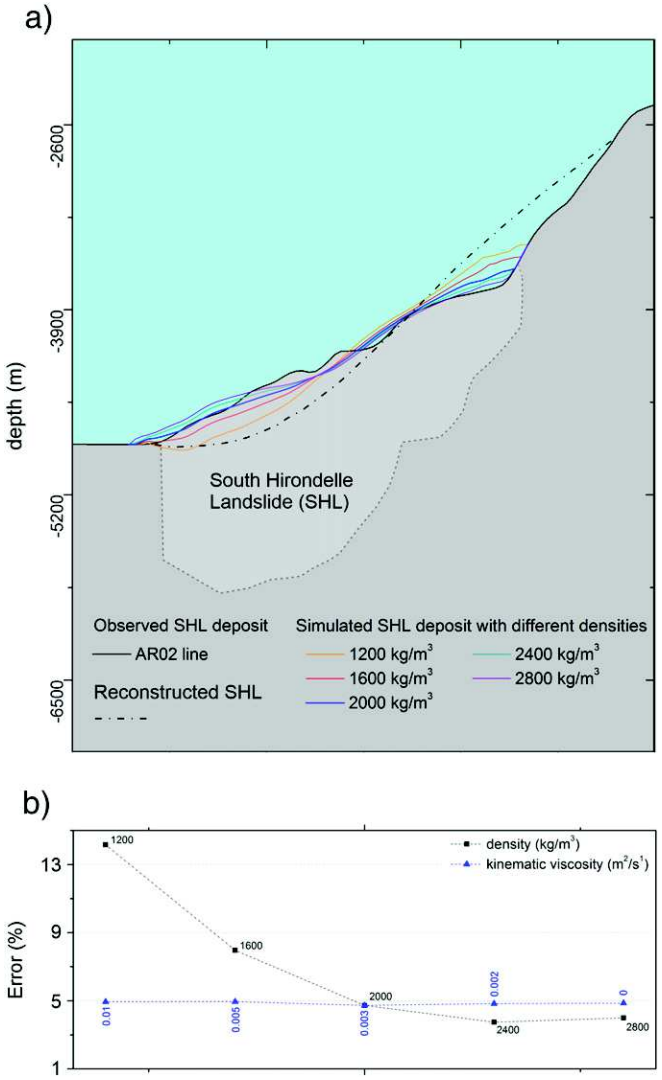

Fig. 5. Sensitivity analysis of the South Hirondelle Landslide movement to the physical material parameters: a) comparison between the observed (black profile) and the simulated deposits considering different landslide densities. Dashed black profile corresponds to the reconstructed pre-event SHL. All profiles are extracted at the same location as the MCS profile AR02 depicted in Fig. 3a; b) error associated to the misfit between the observation and the simulations: the black dashed curve indicates the error associated to the influence of the density parameter on the SHL behaviour considering fixed drag coefficient ($C_d = 0.0030$) and kinematic viscosity ($\nu = 0.01$ m$^2\cdot$s^{-1}); the blue dashed curve indicates the error associated to the influence of the drag coefficient for fixed density ($\rho_2 = 2000$ kg$\cdot$m^{-3}) and kinematic viscosity ($\nu = 0.01$ m$^2\cdot$s^{-1}).

3.1.2. Numerical modelling

To simulate both the movement of the landslide body and the wave generated by the seafloor deformation we employ a multi-layers viscous shallow-water (VSW) model (Jiang and LeBlond, 1994). The lower layer represents the landslide that is assumed to be a viscous-incompressible fluid, and characterized by sediment density, kinematic viscosity and horizontal velocity. The landslide is bounded by the upper layer consisting of seawater assumed to be inviscid and incompressible. The motion of the underwater landslide body and the generation and propagation of the subsequent tsunami are governed by Eqs. (1.1), (1.2), and (1.3) and (2.1), (2.2), and (2.3), respectively. Eqs. (1.1), (1.2), and (1.3) and Eqs. (2.1), (2.2), and (2.3), presented in Cartesian coordinates, constitute an adapted version of the VSW model of Jiang and LeBlond (1994) that includes a realistic bottom bathymetry (Thomson et al., 2001; Fine et al., 2003; Rabinovich et al.,

2003). Also, to account for the drag effects we integrate a quadratic function in the last terms of the momentum conservation equations of the landslide (Fine et al., 2005).

$$\frac{\partial D}{\partial t}+\frac{2}{3}\left[\frac{\partial (DU)}{\partial x}+\frac{\partial (DV)}{\partial y}\right]=0 \tag{1.1}$$

$$\frac{3}{2}\frac{\partial U}{\partial t}-\frac{2}{15}\frac{U}{D}\frac{\partial D}{\partial t}+\frac{8}{15}\left[\left(U\frac{\partial U}{\partial x}+V\frac{\partial U}{\partial y}\right)\right] = -\frac{g}{\rho_2}\left[(\rho_2-\rho_1)\left(\frac{\partial D}{\partial x}-\frac{\partial h_s}{\partial x}\right)+\rho_1\frac{\partial \eta}{\partial x}\right]-\frac{2\nu U}{D^2}+C_d\frac{U|U|}{D} \tag{1.2}$$

$$\frac{3}{2}\frac{\partial V}{\partial t}-\frac{2}{15}\frac{V}{D}\frac{\partial D}{\partial t}+\frac{8}{15}\left[\left(U\frac{\partial V}{\partial x}+V\frac{\partial V}{\partial y}\right)\right] = -\frac{g}{\rho_2}\left[(\rho_2-\rho_1)\left(\frac{\partial D}{\partial y}-\frac{\partial h_s}{\partial y}\right)+\rho_1\frac{\partial \eta}{\partial y}\right]-\frac{2\nu V}{D^2}+C_d\frac{V|V|}{D} \tag{1.3}$$

$$\frac{\partial (h_s+\eta-D)}{\partial t}+\frac{\partial (h_s+\eta-D)}{\partial x}+\frac{\partial (h_s+\eta-D)}{\partial y}=0 \tag{2.1}$$

$$\frac{\partial u}{\partial t}+u\frac{\partial u}{\partial x}+v\frac{\partial u}{\partial y}=-g\frac{\partial \eta}{\partial x} \tag{2.2}$$

$$\frac{\partial v}{\partial t}+u\frac{\partial v}{\partial x}+v\frac{\partial v}{\partial y}=-g\frac{\partial \eta}{\partial y} \tag{2.3}$$

where D is the thickness of the landslide; η is the ocean free surface displacement; ν is the kinematic viscosity, h_s is the static water depth; u,v,U,V are the horizontal components of the velocities in x- and y-direction of the wave and landslide, respectively; g is the gravity acceleration; C_d is the drag coefficient; and $\rho_1$and ρ_2 are the densities of the water and the landslide, respectively.

The governing equations (Eqs. (1.1), (1.2), and (1.3) and (2.1), (2.2), and (2.3)) were solved in an explicit leap-frog finite-difference scheme, with an upwind method for the advection terms. To ensure the numerical stability of the simulations a Courant-Friedrich-Levy condition as well as artificial viscosities for the landslide and the wave were considered.

We consider the pre-event bathymetric model (Fig. 4b) and we run the landslide motion code (governed by Eqs. (1.1), (1.2), and (1.3)) for different landslide "scenarios". Each scenario is characterized by specific physical material parameters (density, kinematic viscosity, and drag coefficient). Then we compare the simulated deposit with the landslide run-out mass until getting the SMF "scenario" that better fits the observed deposit. Both the density and the drag coefficient were subjected to a sensitivity analysis to evaluate their influence on the SHL movement. Fig. 5a shows a comparison between the observed (MCS profile AR02, in Fig. 3a) and the simulated deposits considering different landslide densities. The error associated to the misfit between the observation and the simulations considering different density values and drag coefficients is calculated and the results are depicted in Fig. 5b. Using these results, we selected the parameters that lead to the smaller error (~5%, see Fig. 5b), excluding the high density values ($\rho_2 > 2000$ kg·m^{-3}) assumed to be inappropriate for our case study (Hayes et al., 1972; Schmincke et al., 1995). On the other hand, the numerical tests carried out considering different kinematic viscosity values ($\nu < 1$ m^2·s^{-1}) show that there is no noticeable influence of this parameter on the SHL motion due to the large volume involved, which led us to adopt a viscosity value from the published literature on the SMFs (Fine et al., 2003; Rabinovich et al., 2003; Fine et al., 2005). Therefore, to assure a good representation of the deposited material, we assumed a landslide density of 2000 kg·m^{-3} with a kinematic viscosity of 0.01 m^2·s^{-1}, and a drag coefficient of 0.0030. Finally, for this scenario we ran the "two-way" coupling model (Eqs. (1.1), (1.2), (1.3), (2.1), (2.2), and (2.3)) for tsunami generation and propagation.

The tsunami potential and impact posed by the occurrence of the Hirondelle SMF is assessed through modelling of the tsunami generation, propagation and coastal impact considering the SMF scenario that well reproduces the observed deposit.

3.2. Assessment of tsunami potential and coastal hazard

3.2.1. Potential of tsunami generation

The landslide-induced tsunami generation results from the deformation of the sea-bottom caused by the motion of the SHL body. Fig. 6 depicts the potential of tsunami generation following the motion of the SHL body along the slope. We plot the time evolution of both the lower layer representing the SHL thickness during its motion and the upper layer of the subsequent sea free-surface perturbation. The snapshots are presented from the initiation of the failure ($t = 0$ s) until that the SMF body stops sliding and regains its equilibrium ($t = 120$ s).

Unlike the almost instantaneous generation of earthquake-tsunamis, the SMF-induced tsunami generation is a time-dependent evolutionary process. In the case of the Hirondelle SMF, after ~60 s from the initiation of the motion of the landslide body (Fig. 6b) a significant perturbation of the sea surface is caused. The wave amplitude reaches about 40 m at this stage of the SMF motion. Due to the large volume involved and the fact that the sediments do not run-out far from the source area, the numerical simulations shows that the SHL reaches the equilibrium after ~2 min of motion (see Fig. 6c). At this stage the tsunami generation is completed and the wave reaches 38 m in amplitude.

The computed sea-surface perturbation shows that a mega-tsunami is generated following the failure of a sediments volume of about 500 km^3 at the Hsm. This tsunami can cause significant impact when propagating towards the surrounding coastal stretches that are relatively close to the SMF source zone.

In Fig. 7 we plot the modelled velocity field of the SHL during its motion down slope. The velocity snapshots are presented at $t = 30$ s (Fig. 7a), at $t = 60$ s (Fig. 7b), and at $t = 90$ s (Fig. 7c) after the landslide failure. The peak velocity value of about 70 m·s^{-1} is reached at $t = 90$ s in some parts of the SHL that have high material concentrations and sliding down steep slopes. At $t = 90$ s, the velocity averaged over the whole SHL body is ~40 m·s^{-1}. These velocity values, peak and average, are relatively low at the initiation stage of the failure (at $t = 30$ s, in Fig. 7a) and became lower when the SHL approaches its equilibrium stage that is reached at $t = 120$ s.

3.2.2. Tsunami propagation and coastal hazard

The tsunami hazard posed by the Hirondelle SMF is evaluated by means of simulating numerically the whole source-to-coast tsunami process. This includes numerical simulations of the tsunami propagation and the maximum wave heights distribution along the coasts (pre-run-up) using 600 m-resolution gridded data. The 600 m-resolution bathymetry model is generated from two different data sets: the SWIM bathymetry compilation (Zitellini et al., 2009) and the General Bathymetric Chart of the Oceans (GEBCO) 30-arc sec gridded data (available at: http://www.gebco.net/). Fig. 8 depicts the snapshots of tsunami propagation from the source zone towards the surrounding coastal zones. The analysis of these results shows that after 5 min of propagation, tsunami waves of high amplitudes (>15 m) start travelling from the source area towards the target coasts of Iberia and north Morocco (Fig. 8a). After 40 min of tsunami propagation the waves reach the coasts in Cape S. Vicente and Madeira with amplitudes ranging from 2 to 3 m (Fig. 8b). During this propagation time, the tsunami encounters the shallow water area over the top of the Gorringe Bank, which relatively slows down the propagation and reflects a part of the incident waves (Fig. 8b). The first waves' impact along the south-western coast of Portugal, from Cape S. Vicente to Lisbon, occurred in about 1 h (Fig. 8c). The amplitude of the first incident waves along this coastal segment is about 2–3 m (Fig. 8c). Towards the African coast, the tsunami takes more time to arrive because it encounters the shallow water areas that mark the off-shore extension of the

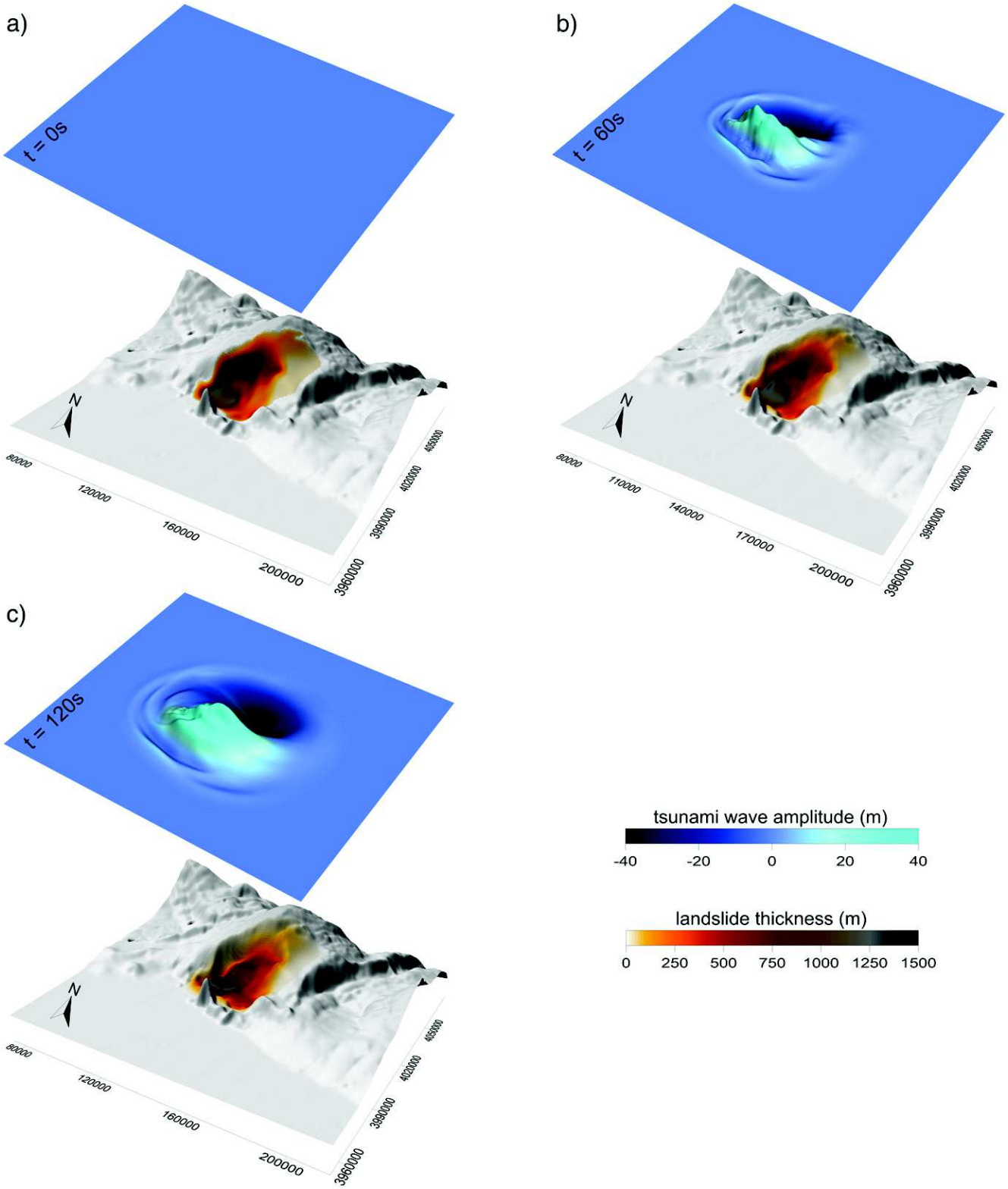

Fig. 6. Potential of tsunami generation. Snapshots of Hirondelle SMF motion (lower layer) and the subsequent tsunami generation (upper layer): a) at $t = 0$ s, the initiation of the landslide failure; b) after 60 s of the landslide failure; c) after 120 s of the landslide failure. The maps coordinates system is UTM – Zone 29 N, Datum WGS-84.

continental shelf (Fig. 8c). 95 min after the tsunami generation, the tsunami waves impact all the coasts of Portugal and Morocco, and reach the Azores Islands with amplitudes of about 3 m (Fig. 8d). The second crest generated propagates towards north with amplitude maxima of 8 m.

In Fig. 9 we present the energy patterns, in term of maximum wave amplitudes, of the tsunami caused by the failure of the South Hirondelle Landslide. The analysis of these results clearly indicates that most tsunami energy is steered towards the northern and southern sides of the Hirondelle Seamount (Fig. 9). At first order, around the generation area, the tsunami amplitude is maximal, ~40 m, in the direction of the SMF movement as well as in the opposite direction of this motion. Away from the source area, the waves undergo attenuation when

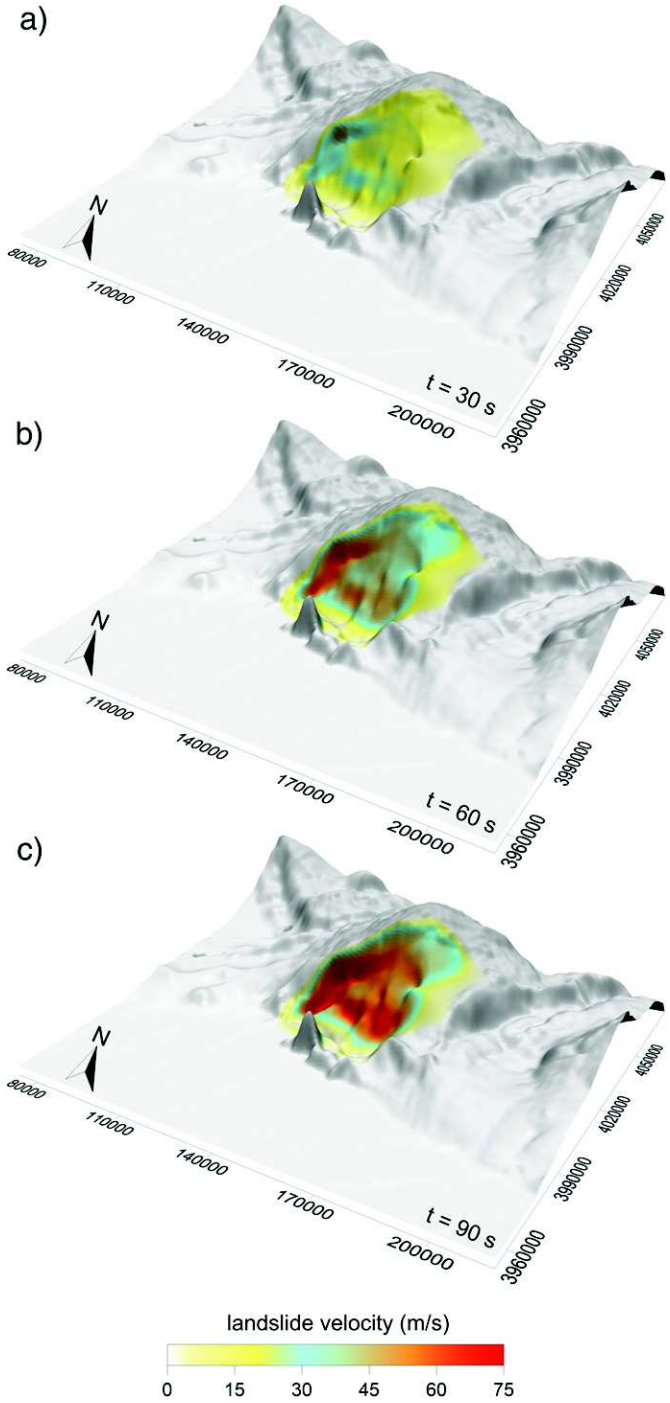

Fig. 7. Snapshots of the Hirondelle SMF velocity field: a) at $t = 30$ s after the landslide failure; b) after 60 s of the landslide failure; c) after 90 s of the landslide failure. The maps coordinates system is UTM – Zone 29 N, Datum WGS-84.

travelling towards the coasts. It is clear that the bathymetry of the region controls the maximum wave amplitudes distribution, acting, when shallow, to guide the energy towards the coast. When interacting with the coastal bathymetry the shoaling effects lead to an increase of wave height. The coastal segment north of Lisbon and along the Moroccan coast are characterized by shallow water due to the offshore extension of the continental shelf, which results in an amplification of the incident waves at those zones. Close to Lisbon the computed maximum wave amplitude reaches 14 m. Along the coast of Morocco numerical modelling predicts a maximum wave amplitude of about 15 m. The SHL-induced tsunami also reaches the Madeira, Azores and Canary Islands with wave amplitudes of 6 m, 7 m and 10 m, respectively.

4. Discussion

4.1. Landslide trigger mechanism and age of the South Hirondelle Landslide

The SHL lies within the Eurasia-Africa plate boundary zone in the Atlantic Ocean as defined by Zitellini et al. (2009), where instrumental clusters of seismicity have been recorded (Fig. 1). Instrumental earthquake events with $M_w > 7$ and epicenters within a distance of ~160 km from the SHL source area were recorded in the last decades (Buforn et al., 1988). Also one $M_w = 8.4$ event took place at ~230 km from the source of the SHL (Buforn et al., 1988). The largest historical earthquake event in western Europe, the 1st November 1755 Lisbon earthquake with estimated magnitude 8.4–8.9, with controversial seismogenic source, was also generated along this plate boundary or its close vicinity (Gutscher et al., 2002; Zitellini et al., 2009), with suggested sources that vary in distance to the SHL from ~100 km to 300 km (Terrinha et al., 2009).

Considering that the minimum water depth of the Hirondelle Seamount exceeds 2000 m and that there is no continuous morphologic connection between the SHL and the nearest continental slope and shelf, it does not seem reasonable to invoke mechanisms associated with storms or sea level variations as a probable cause for the trigger mechanism. Hence, considering that the whole sedimentary sequence is affected by the slide movement, it is here suggested that the possible source is a single earthquake event along this plate boundary or close vicinity. Although the study by ten Brink et al. (2009) refers to the geological setting and attenuation laws of the U.S. East coast, it is reported that $M_w = 7$ events generate landslides at a maximum distance of 160 km with a slope angle of 9°. The SHL displays surface slopes that can exceed 10° and the detachment slope is ~9°.

Although a seismic source is the most plausible mechanism, an aseismic source could also be envisaged due to tilting and differential sedimentary load. An alternative aseismic source could be instability caused by building-up of the continuous tectonic deformation of the sedimentary package caused by the propagation of faults at the corner zone formed by the Gorringe thrust and the Hirondelle Seamount. It was shown by Rosas et al. (2012) that faults connecting strike-slip faults and thrusts form on the foot-wall of the thrust and become parallel to the strike-slip faults as they approach them (Fig. 2). The case study used by Rosas et al. (2012) was based on numerical and physical modelling of a natural analogue of the intersection of the Horseshoe fault and SWIM faults in the close vicinity of the Hirondelle Seamount. Alternatively, it is a possibility that the mantle rooted blind faults connecting the Gorringe thrust and the Hirondelle Seamount may account for the observed seismicity (Figs. 1 and 2).

An accurate age of the SHL should be based on the study of seafloor sediments, which has not been done. However, because the post-Lower Miocene seismo-stratigraphy does not show unconformities within UIV it seems that the Quaternary record is continuous, probably made up of hemipelagic sedimentation. Since the whole stratigraphic package is deformed by the landslide movement a Quaternary age is suggested, possibly a Late Pleistocene age as reported for other events by Gràcia et al. (2010) and Lo Iacono et al. (2012) for the Marquês de Pombal landslides and for the North Gorringe Landslide shown in Fig. 2.

4.2. Tsunamigenic potential of the South Hirondelle Landslide and propagation patterns

The generation of a tsunami from a submarine landslide is, in general, controlled by intrinsic characteristics, such as the volume, the type and density of the material, the lithologic composition, the thickness, the kinematic viscosity (Chaytor et al., 2009; Geist et al., 2009), and

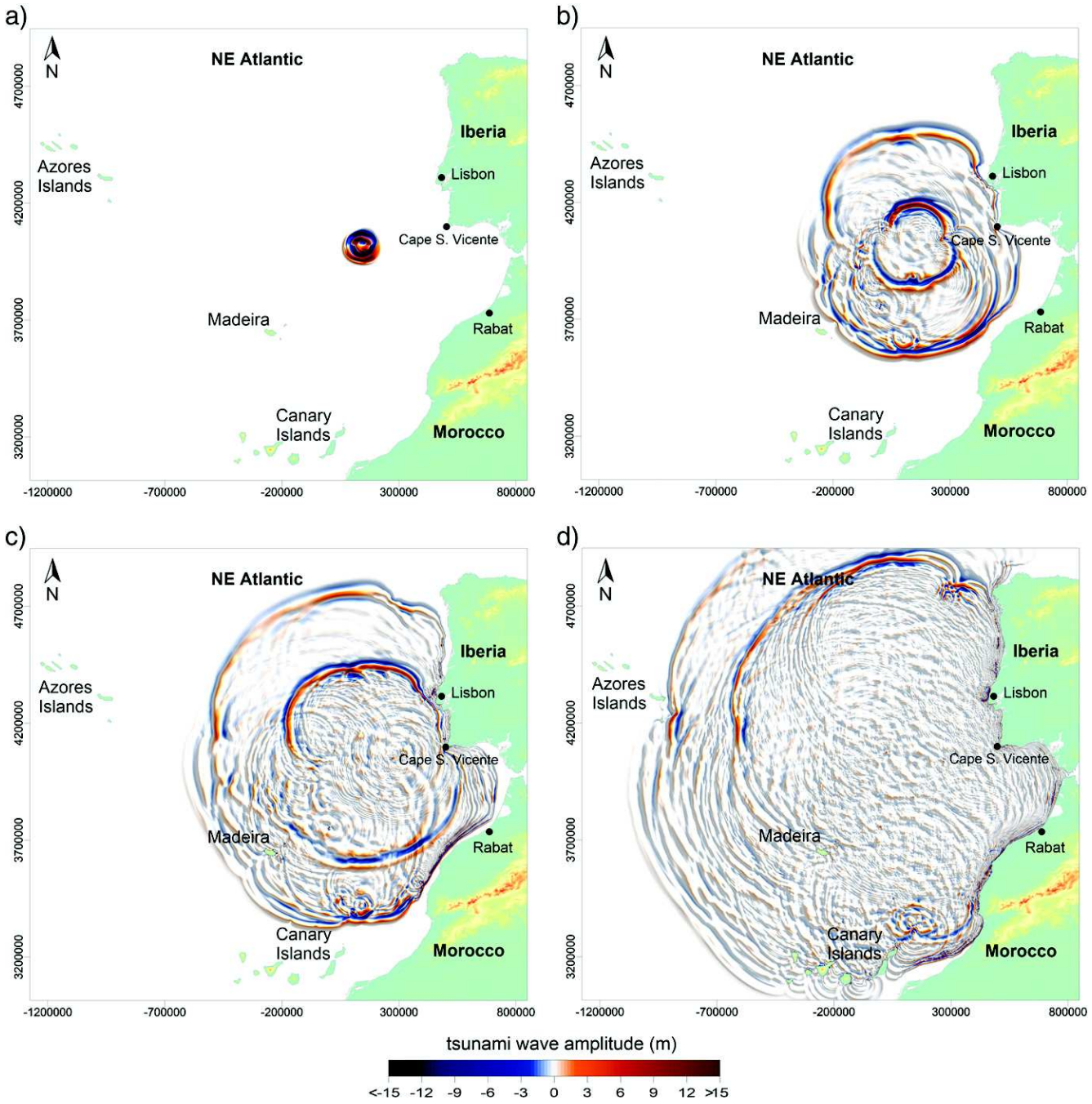

Fig. 8. Tsunami waves propagation in the NE Atlantic region following the failure of the Hirondelle submarine landslide. The propagation snapshots are plotted after: a) 5 min of propagation; b) 45 min of propagation; c) 60 min of propagation; d) 95 min of propagation. The maps coordinates system is UTM – Zone 29 N, Datum WGS-84.

the environmental constraints in which the failure occurs, such as the water depth and the slope gradient (Pelinovsky and Poplavsky, 1996). Even though deep-water submarine landslides have less potential in generating strong tsunami waves (Masson et al., 2006; Harbitz et al., 2006), we have shown through numerical simulations that the SHL, located at a depth between approximately 2.5 and 4.7 km, may have generated a large tsunami. This is mainly due to the fact that the failure of SHL involves a volume of hundred cubic kilometres of sediments (~500 km^3) with large thickness (max of ~1500 m) that starts sliding over a relatively steep slope (between 10° and 3.5°, see Fig. 2b, and reaching 16°). All these factors led to a fast failure of the SHL, average velocity over the whole landslide body reached ~40 $m \cdot s^{-1}$ at 90 s after the failure, resulting in a significant vertical displacement of the sea-floor and therefore in a generation of a large tsunami.

The tsunami hazard is addressed here through the worst-case scenario assuming a unique failure of the SHL. Although it is likely that the SHL corresponds to a single event, we cannot exclude the possibility of a sequence of small failures emplaced over a short period. To account for this possibility, we simulate the SHL-induced tsunami considering two additional SMF scenarios: i) the failure of a half of the volume considered for the SHL, and ii) a sequence of two failures, half of SHL volume each, with a time lag of 2.5 min. Results of tsunami modelling for these two scenarios are depicted in Figs. 10 and 11. The failure of the half of the volume considered for the SHL would generate a tsunami wave up to 20 m in amplitude (Fig. 10a) that hit the SW Iberian and Moroccan coasts with wave reaching 6 m (Fig. 10b). Simulations of the tsunami caused by the failure of SHL in a sequence of two SMFs indicate the generation of two successive waves with a maximum amplitude up to 25 m

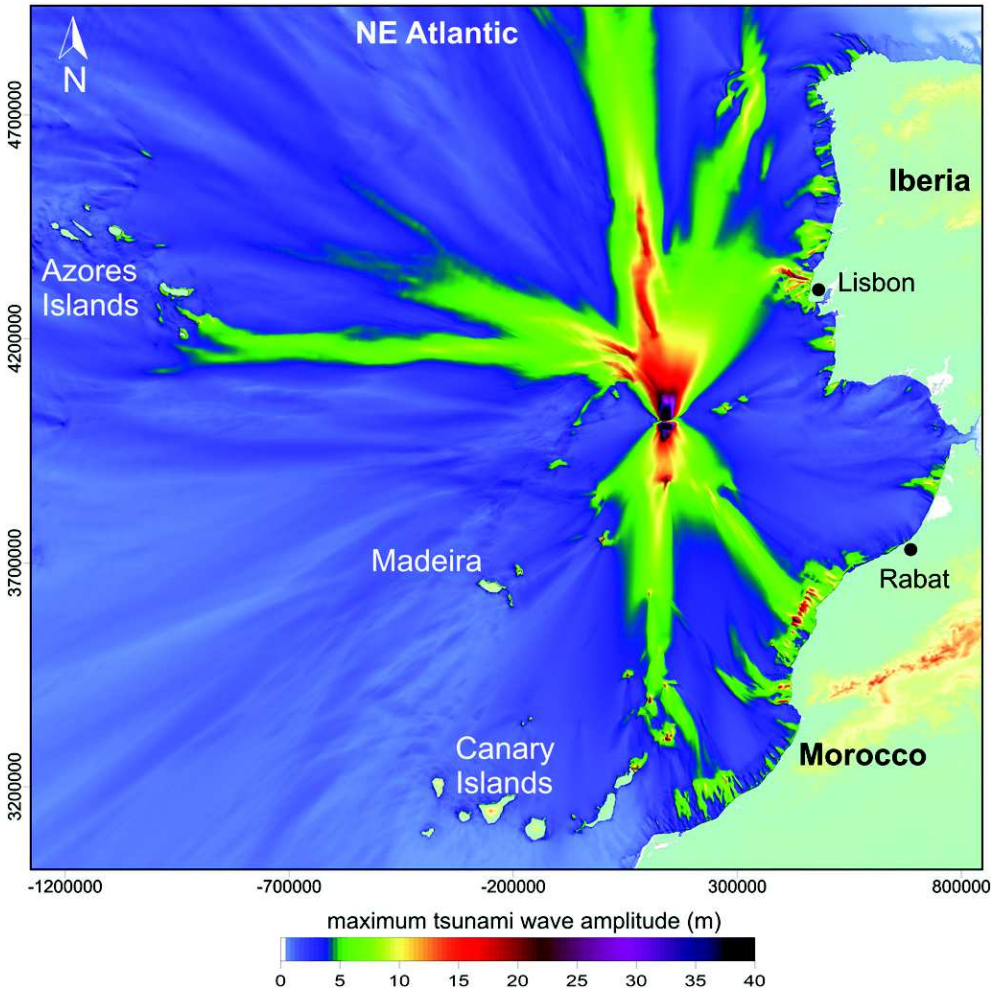

Fig. 9. Tsunami maximum wave amplitudes distribution in the NE Atlantic region due to the occurrence of the South Hirondelle submarine landslide. The map coordinates system is UTM – Zone 29 N, Datum WGS-84.

(Fig. 11a). The overall effect of the tsunami impact from this scenario (Fig. 11b) shows that the NE Atlantic coasts may experience waves up to 7 m at some locations. Therefore, smaller landslide volumes still present a significant threat for the SW Iberian and Moroccan coasts, and cannot be neglected in coastal geo-hazard assessment for the NE Atlantic region.

The Hirondelle Seamount is surrounded by a number of oceanic features, namely the Gorringe Bank to the east, the Coral Patch Ridge to the south and the Madeira-Tore Rise to the west (Fig. 1a for location). All these bathymetric structures affect the SHL-induced tsunami propagation. The presence of the Gorringe Bank at the eastern side of the SHL slows down the tsunami propagation and reflects a part of the incident waves, which can result in a loss of tsunami energy steered towards the south-western coasts of Iberia. Towards the south, the tsunami waves encounter the Coral Patch Ridge that leads to significant reflections of the waves. This ridge appears to play the role of a barrier that partially protects the southern Moroccan coast. At the west of the SHL, the Madeira-Tore Rise also seems to play the same role in protecting the coasts of the Madeira Islands.

The tsunami caused by the SHL seems to have a regional impact as the waves travelled with relatively large amplitudes from the source area towards various coastal zones of the NE Atlantic. Despite the fact that the tsunamis caused by the submarine landslides undergo a significant attenuation of the waves when travelling far-away from the source area (Okal and Synolakis, 2004; Harbitz et al., 2006), as it is the case of the SHL, an important tsunami energy remains steered particularly towards the north. Also, when the tsunami reaches the shallow water areas, it encounters the continental shelf extended along various coastal zones, which lead to an important amplification of the incident waves. These shoaling effects occur in particular north of Lisbon-Portugal and along the coast of Morocco. Another effect is due to the shallow water areas along the Gloria Fault that channel the wave energy towards the Azores Islands.

In the NE Atlantic only few studies addressed the landslide-induced tsunami hazard on the coasts of Iberia and Morocco. Lo Iacono et al. (2012) investigated the Gorringe Bank deep-water landslide and showed that it may cause a major tsunami waves reaching the coasts of Portugal. The Gorringe Bank landslide has an estimated volume of ~80 km^3 that is distributed between the depths of 2900 m and 5100 m. The numerical simulations predict an initial wave of ~20 m and an impact along the Portuguese coasts with waves reaching 7 to 20 m after 30 min of propagation. On the other hand, our case of SHL has similar depth but different volume and source characteristics when compared to the Gorringe Bank landslide. These differences result in the generation of a bigger tsunami that takes more time (~45 min) to reach the coast of Portugal. Even though both events present different characteristics, the GB landslide is a rock fall involving different tsunami generation mechanism, we find a similarity in the wave energy distribution, in particular in the near-shore mainly due to the morphologic configuration of the area.

It is important to mention here that this study suffers from some limitations regarding the models considered. The main simplification concerns the rheological model adopted to represent the landslide material and its dynamics, which mainly affects the tsunami generation.

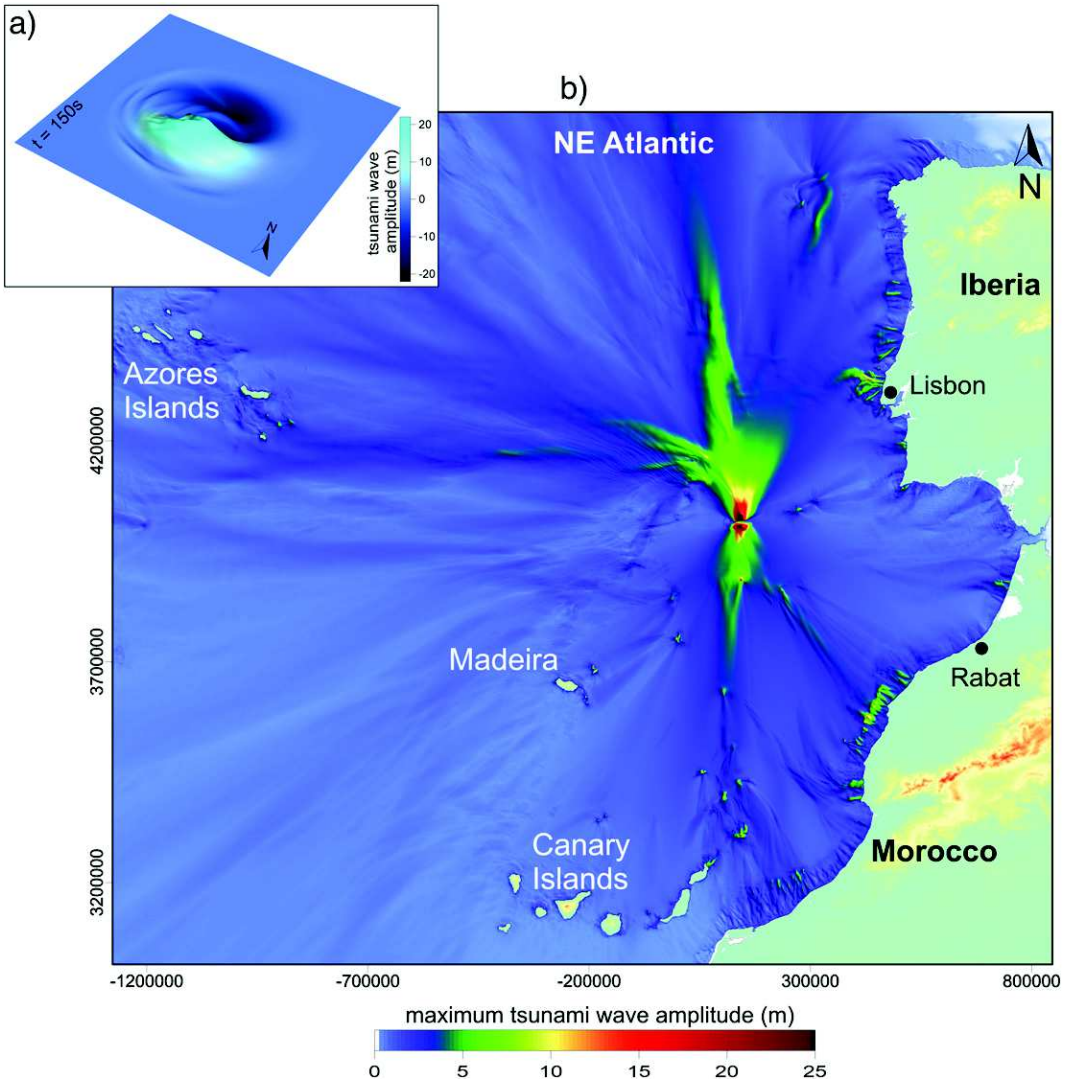

Fig. 10. Tsunami simulation results due to the occurrence of a smaller landslide, half of the volume considered for the South Hirondelle Landslide: a) Tsunami generation; and b) Tsunami maximum wave amplitudes distribution in the NE Atlantic region. The map coordinates system is UTM – Zone 29 N, Datum WGS-84.

A better representation of the landslide rheological model requires geotechnical analyses of sediment cores, which are extremely expensive to collect and are seldom available. Also, the reconstruction of the pre-event landslide was based on the interpretation of only one multichannel profile in addition to the scar observed in the bathymetry. Despite these limitations, this study is an important contribution to assess the landslide generated tsunami hazard in the NE Atlantic region.

In addition to the Hsm and GB, the NE Atlantic region in the Eurasia-Africa plate boundary area comprehends a number of seamounts (e.g., the Josephine, the Marquês de Pombal, and the Coral Patch). These oceanic features have similar vigorous morphology, with average slopes dipping ~3.8° to 4.7° that strongly contrasts with the surrounding abyssal plains that have slopes of <0.1°. Within these seamounts, it is well known that many of the triggered landslides occurred in Late Pleistocene and Holocene times (Gràcia et al., 2010). The pre-conditioning and triggering mechanisms of SMFs, mainly consisting of moderate to high magnitude seismicity and tectonic driven gravity instability, still persist in the region, and therefore, favor the triggering of future large SMFs. This study and the study by Lo Iacono et al. (2012) clearly show the significant tsunamigenic potential of such SMFs occurring in deep-water seamounts. Both studied features, Hsm and GB landslides, can form a starting point to construct a reliable deep-water tsunamigenic SMFs database for the region. This database must be completed with more quantitative information on the rheological properties and chronology of the existent SMFs for a comprehensive geo-hazard assessment in the region. Moreover, slope stability analysis for the main deep-water seamounts in the region requires more attention in order to mitigate future failures as well as their possible tsunamigenic potential.

5. Conclusions

In this paper we investigated the possible tsunami and its coastal impact caused by a deep water submarine mass failure in the NE Atlantic. The Hirondelle Seamount case study, located at water depths >2000 m, has a large mass transported deposit. The main findings of this work are:

i. The occurrence of a large submarine landslide (SHL) involving a volume 500 km^3 of sediments deposit and the mapping of its corresponding scar and source area.
ii. The SHL occurred as one single landslide event as sustained from inspection of multichannel reflection seismic profile.
iii. The SHL caused a significant tsunami despite being located in a deep-water region.
iv. The SHL had a regional impact along the surrounding coasts of the NE Atlantic region, in particular along the coasts of Morocco and Iberia.

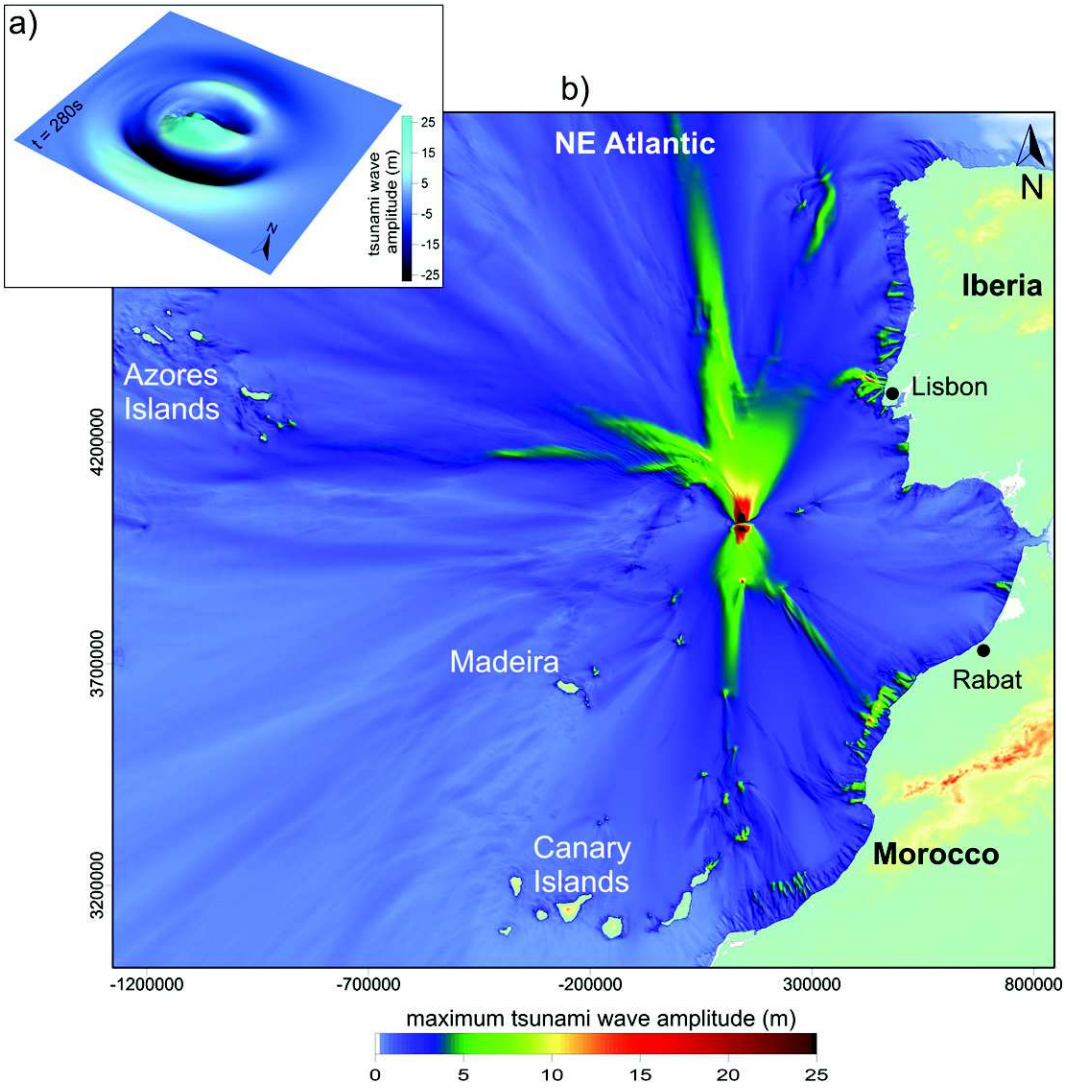

Fig. 11. Tsunami simulation results due to the occurrence of the South Hirondelle Landslide as a sequence of two landslides emplaced over 2.5 min period: a) Tsunami generation; and b) Tsunami maximum wave amplitudes distribution in the NE Atlantic region. The map coordinates system is UTM – Zone 29 N, Datum WGS-84.

v. The SHL-induced tsunami took tens of minutes (45–60 min) to reach the Portuguese and Moroccan coasts.

In summary, this paper presents a contribution to the study of the tsunami hazard associated to non-seismic sources in the NE Atlantic. In addition, it is suggested that in the NE Atlantic more attention should be given to tsunami hazard assessment due to the landslides occurring in the deep-water seamounts.

Acknowledgements

This work is funded by the EU project ASTARTE - Assessment, Strategy And Risk Reduction for Tsunamis in Europe, Grant 603839, 7th FP (ENV.2013.6.4-3) and by the Portuguese Foundation for Science and Technology – FCT project CONDRIBER, Grant PTDC/GEO-GEO/4430/2012. The support by Landmark Graphics Corporation via the Landmark University Grant Program is also acknowledged. The authors would like to thank the Editor M. Rebesco, C. Lo Iacono and an anonymous reviewer for their timely and helpful reviews, which improved the manuscript.

References

Assier-Rzadkiewicz, S.A., Mariotti, C., Heinrich, P., 1997. Numerical simulation of submarine landslides and their hydraulic effects. J. Waterw. Port Coast. Ocean Eng. 123 (4), 149–157.

Auzende, J.M., Charvet, J., Le Lann, A., Le Pichon, X., Monteiro, J.H., Nicolas, A., Olivet, J.L., Ribeiro, A., 1978. Le Banc de Gorringe: résultats de la campagne CYAGOR (août 1977). Bull. Soc. Géol. 545–556 (7 serie, t. XXI, n 5).

Bondevik, S., Løvholt, F., Harbitz, C., Mangerud, J., Dawson, A., Inge Svendsen, J., 2005. The Storegga Slide tsunami-comparing field observations with numerical simulations. Mar. Pet. Geol. 22 (1), 195–208.

Bird, P., Kagan, Y.Y., 2004. Plate-tectonic analysis of shallow seismicity: apparent boundary width, Beta, corner magnitude, coupled lithosphere thickness, and coupling in seven tectonic settings. Bull. Seismol. Soc. Am. 94 (6), 2380–2399.

Buforn, E., Udías, A., Colombás, M.A., 1988. Seismicity, source mechanisms and tectonics of the Azores-Gibraltar plate boundary. Tectonophysics 152 (1–2), 89–118.

Chaytor, J.D., Uri, S., Solow, A.R., Andrews, B.D., 2009. Size distribution of submarine landslides along the US Atlantic margin. Mar. Geol. 264 (1), 16–27.

Clague, J.J., 2001. Tsunamis. A Synthesis of Geological Hazards in Canada. Vol. 548, pp. 27–42.

De Alteriis, G., Passaro, S., Tonielli, R., 2003. New, high resolution swath bathymetry of Gettysburg and Ormonde Seamounts (Gorringe Bank, eastern Atlantic) and first geological results. Mar. Geophys. Res. 24 (3–4), 223–244.

Fine, I.V., Rabinovich, A.B., Bornhold, B.D., Thomson, R.E., Kulikov, E.A., 2005. The Grand Banks landslide-generated tsunami of November 18, 1929: preliminary analysis and numerical modeling. Mar. Geol. 45–57 (215 (1-2 SPEC ISS).

Fine, I.V., Rabinovich, A.B., Thomson, R.E., Kulikov, E.A., 2003. Numerical Modeling of Tsunami Generation by Submarine and Subaerial Landslides. In: Yalciner, A.C.,

Pelinovsky, E.N., Synolakis, C.E., Okal, E. (Eds.), Submarine Landslides and TsunamisNATO Advanced Series. Kluwer Academic Publication, Dordrecht, pp. 69–88.
Geissler, W.H., Matias, L., Stich, D., Carrilho, F., Jokat, W., Monna, S., IbenBrahim, A., Mancilla, F., Gutscher, M.-A., Sallarès, V., Zitellini, N., 2010. Focal mechanisms for sub-crustal earthquakes in the Gulf of Cadiz from a dense OBS deployment. Geophys. Res. Lett. 37 (18).
Geist, E.L., Lynett, P.J., Chaytor, J.D., 2009. Hydrodynamic modeling of tsunamis from the Currituck landslide. Mar. Geol. 264 (1), 41–52.
Girardeau, J., Cornen, G., Agrinier, P., Beslier, M.-O., Dubuisson, G., Le Gall, B., Monnier, C., Pinheiro, L., Ribeiro, A., Whitechurch, H., 1998. Preliminary results of Nautile dives on the Gorringe Bank (West Portugal). Comp. Rend. Acad. Scie. Ser. IIA Earth Planet. Scie. 4 (326), 247–254.
Gràcia, E., Vizcaino, A., Escutia, C., Asioli, A., Rodes, A., Pallas, R., Garcia-Orellana, J., Lebreiro, S., Goldfinger, C., 2010. Holocene earthquake record offshore Portugal (SW Iberia): testing turbidite paleoseismology in a slow-convergence margin. Quat. Sci. Rev. 29 (9), 1156–1172.
Gràcia, E., Danobeitia, J., Vergés, J., Bartolomé, R., Córdoba, D., 2003. Crustal architecture and tectonic evolution of the Gulf of Cadiz (SW Iberian margin) at the convergence of the Eurasian and African plates. Tectonics 22 (4).
Gutscher, M.A., Malod, J., Rehault, J.P., Contrucci, I., Klingelhoefer, F., Mendes-Victor, L., Spakman, W., 2002. Evidence for active subduction beneath Gibraltar. Geology 30 (12), 1071–1074.
Harbitz, C.B., Lovholt, F., Pedersen, G., Masson, D.G., 2006. Mechanisms of tsunami generation by submarine landslides: a short review. Nor. J. Geol. 86, 255–264.
Harbitz, C.B., 1992. Model simulations of tsunamis generated by the Storegga slides. Mar. Geol. 105, 1–21.
Hayes, D.E., Pimm, A.C., Beckmann, J.P., Benson, W.E., Berger, W.H., Roth, P.H., Supko, P.R., von Rad, U., 1972. Initial Reports of the Deep Sea Drilling Project, Site DSDP. p. 135 http://dx.doi.org/10.2973/dsdp.proc.14.102.1972.
Hayward, N., Watts, A.B., Westbrook, G.K., Collier, J.S., 1999. A seismic reflection and GLORIA study of compressional deformation in the Gorringe Bank Region, Eastern North Atlantic. Geophys. J. Int. 138, 831–850.
Heinrich, P., Piatensai, A., Okal, E., Hebert, H., 2000. Near-field modelling of the July 17, 1998 tsunami in Papua New Guinea. Geophys. Res. Lett. 27, 3037–3040 (2.3.4).
Hernández-Molina, F.J., Llave, E., Preu, B., Ercilla, G., Fontan, A., Bruno, M., Serra, N., Gomiz, J.J., Brachenridge, R.E., Sierro, F.J., Stow, D.A.V., García, M., Juan, C., Sandoval, N., Arnaiz, A., 2014. Contourite processes associated with the Mediterranean outflow water after its exit from the Strait of Gibraltar: global and conceptual implications. Geology 42 (3), 227–230.
Imamura, F., Hashi, K., Imteaz, M., 2001. Modeling for Tsunamis Generated by Landsliding and Debris Flow. Tsunami Research at the End of a Critical Decade. Springer Netherlands, pp. 243–282.
Jiang, L., LeBlond, P.H., 1994. Three-dimensional modeling of tsunami generation due to a submarine mudslide. J. Phys. Oceanogr. 24 (3), 559–572.
Jiménez-Munt, I., Fernàndez, M., Vergés, J., Afonso, J.C., Garcia-Castellanos, D., Fullea, J., 2010. Lithospheric structure of the Gorringe Bank: insights into its origin and tectonic evolution. Tectonics 29 (5), TC5019. http://dx.doi.org/10.1029/2009TC002458.
Kawata, Y., Benson, B.C., Borrero, J.L., Davies, H.L., de Lange, W.P., Imamura, F., Nott, J., Synolakis, C.E., 1999. Tsunami in Papua New Guinea was as intense as first thought. Eos 80 (101), 102–103.
Lo Iacono, C., Gràcia, E., Zaniboni, F., Pagnoni, G., Tinti, S., Bartolomé, R., Masson, D.G., Russell, B.W., Lourenço, N., Abreu, M.P., Dañobeitia, J.J., Zitellini, N., 2012. Large, deep water slope failures: implications for landslide-generated tsunamis. Geology 40 (10), 931–934.
Martinez-Loriente, S., Gràcia, E., Bartolome, R., Sallarès, V., Connors, C., Perea, H., Iacono, L., Klaeschen, D., Terrinha, P., Dañobeitia, J.J., Zitellini, N., 2013. Active deformation in old oceanic lithosphere and significance for earthquake hazard: seismic imaging of the Coral Patch Ridge area and neighboring abyssal plains (SW Iberian Margin). Geochem. Geophys. Geosyst. 14 (7), 2206–2231. http://dx.doi.org/10.1002/ggge.20173.
Masson, D.G., Harbitz, C.B., Wynn, R.B., Pedersen, G., Løvholt, F., 2006. Submarine landslides: processes, triggers and hazard prediction. Phil. Trans. R. Soc. A 364 (1845), 2009–2039.
McSaveney, M.J., Goff, J.R., Darby, D.J., Goldsmith, P., Barnett, A., Elliott, S., Nongkas, M., 2000. The 17 July 1998 tsunami, Papua New Guinea: evidence and initial interpretation. Mar. Geol. 170 (1), 81–92.
Medialdea, T., Vegas, R., Somoza, L., Vazquez, J.T., Maldonado, A., Diaz-del Rio, V., Maestro, A., Cordoba, D., Fernandes-Puga, M.C., 2004. Structure and evolution of the "Olistostrome" complex of the Gibraltar Arc in the Gulf of Cádiz (eastern Central Atlantic): evidence from two long seismic cross-sections. Mar. Geol. 209 (1), 173–198.
Murty, T.S., 1977. Seismic sea waves: tsunamis (No. 198). Department of Fisheries and the Environment. Fish. Mar. Ser.
Okal, E.A., Synolakis, C.E., 2004. Source discriminants for near-field tsunamis. Geophys. J. Int. 158 (3), 899–912.
Pelinovsky, E., Poplavsky, A., 1996. Simplified model of tsunami generation by submarine landslides. Phys. Chem. Earth 21 (1), 13–17.
Rabinovich, A.B., Thomson, R.E., Bornhold, B.D., Fine, I.V., Kulikov, E.A., 2003. Numerical modelling of tsunamis generated by hypothetical landslides in the Strait of Georgia, British Columbia. Pure Appl. Geophys. 160 (7), 1273–1313.
Roque, C., Duarte, H., Terrinha, P., Valadares, V., Noiva, J., Cachão, M., Ferreira, J., Legoinha, P., Zitellini, N., 2012. Pliocene and Quaternary depositional model of the Algarve margin contourite drifts (Gulf of Cadiz, SW Iberia): seismic architecture, tectonic control and paleoceanographic insights. Mar. Geol. 303, 42–62.
Roque, C., 2007. Tectonostratigrafia Do Cenozóico Das Margens Continentais Sul e Sudoeste Portuguesas: Um Modelo de correlação sismostratigráfica (PhD thesis) Department of Geology, University of Lisbon (in Portuguese, 310 pp.).
Rosas, F.M., Duarte, J.C., Neves, M.C., Terrinha, P., Silva, S., Matias, L., Gràcia, E., Bartolomé, R., 2012. Thrust–wrench interference between major active faults in the Gulf of Cadiz (Africa–Eurasia plate boundary, offshore SW Iberia): tectonic implications from coupled analog and numerical modeling. Tectonophysics 548, 1–21.
Ryan, W.B.F., Hsü, K.J., Cita, P.D., M.B., Lort, J., Maync, W., Nesteroff, W.D., Pautot, G., Stradner, H., Wezel, F.C., 1973. Site DSDP 120. Initial Rep. Deep Sea Drill. Proj. http://dx.doi.org/10.2973/dsdp.proc.13.102.1973.
Sallarès, V., Martínez-Loriente, S., Prada, M., Gràcia, E., Ranero, C.R., Gutscher, M.A., Bartolome, R., Gailler, A., Dañobeitia, J.J., Zitellini, N., 2013. Seismic evidence of exhumed mantle rock basement at the Gorringe Bank and the adjacent horseshoe and Tagus abyssal plains (SW Iberia). Earth Planet. Sci. Lett. 365, 120–131. http://dx.doi.org/10.1016/j.epsl.2013.01.021.
Sartori, R., Torelli, L., Zitellini, N., Peis, D., Lodolo, E., 1994. Eastern segment of the Azores–Gibraltar line (central–eastern Atlantic): an oceanic plate boundary with diffuse compressional deformation. Geology 22, 555–558.
Schmincke, H.-U., Weaver, P.P.E., Firth, J.V., 1995. Background, Objectives, and Principal Results of Drilling the Clastic Apron of Gran Canaria (VICAP). In: Schmincke, H.-U., Weaver, P.P.E., Firth, J.V. (Eds.), Proc. ODP, Init. Repts. Vol. 157. Ocean Drilling Program, College Station, TX, pp. 11–25. http://dx.doi.org/10.2973/odp.proc.ir.157.1995
Seton, M., Müller, R.D., Zahirovic, S., Gaina, C., Torsvik, T., Shephard, G., Talsma, A., Gurnis, M., Turner, M., Maus, S., Chandler, M., 2012. Global continental and ocean basin reconstructions since 200 Ma. Earth Sci. Rev. 113 (3–4), 212–270.
Synolakis, C.E., Bardet, J.P., Borrero, J.C., Davies, H.L., Okal, E.A., Silver, E.A., Sweet, S., Tappin, D.R., 2002. The slump origin of the 1998 Papua New Guinea tsunami. Proc. R. Soc. Lond. A 458, 763–789.
Tappin, D.R., Watts, P., McMurty, G.M., Lafoy, Y., Matsumoto, T., 2001. The Sissano, Papua New Guinea tsunami of July 1998—offshore evidence on the source mechanism. Mar. Geol. 175, 1–24. http://dx.doi.org/10.1016/S0025-3227(01)00131-1.
ten Brink, U.S., Lee, H.J., Geist, E.L., Twichell, D., 2009. Assessment of tsunami hazard to the U.S. East Coast using relationships between submarine landslides and earthquakes. Mar. Geol. 264 (1), 65–73.
Terrinha, P., Matias, L., Vicente, J., Duarte, J., Luis, J., Pinheiro, L., Lourenço, N., Diez, S., Rosas, Magalhães, V., Valadares, V., Zitellini, N., Roque, C., MATESPRO Team, 2009. Morphotectonics and strain partitioning at the Iberia–Africa plate boundary from multibeam and seismic reflection data. Mar. Geol. 267 (3), 156–174.
Terrinha, P., Pinheiro, L.M., Henriet, J.-P., Matias, L., Ivanov, M.K., Monteiro, J.H., Akhmetzhanov, A., Volkonskaya, A., Cunha, T., Shaskin, P., Rovere, M., The TTR10 Shipboard Scientific Party, 2003. Tsunamigenic-seismogenic structures, neotectonics, sedimentary processes and slope instability on the southwest Portuguese Margin. Mar. Geol. 195 (1), 55–73. http://dx.doi.org/10.1016/S0025-3227(02)00682-5.
Thomson, R.E., Rabinovich, A.B., Kulikov, E.A., Fine, I.V., Bornhold, B.D., 2001. On Numerical Simulation of the Landslide-Generated Tsunami of November 3, 1994 in Skagway Harbor, Alaska. Tsunami Research at the End of a Critical Decade. Springer Netherlands, pp. 243–282.
Torelli, L., Sartori, R., Zitellini, N., 1997. The giant chaotic body in the Atlantic Ocean off Gibraltar: new results from a deep seismic reflection survey. Mar. Pet. Geol. 14 (2), 125–138.
Zitellini, N., Gràcia, E., Matias, L., Terrinha, P., Abreu, M.A., DeAlteriis, G., Heriet, J.P., Dañobeitia, J.J., Masson, D.G., Mulderi, T., Ramella, R., Somoza, L., Diez, S., 2009. The quest for the Africa–Eurasia plate boundary west of the Strait of Gibraltar. Earth Planet. Sci. Lett. 280 (1), 13–50.
Zitellini, N., Rovere, M., Terrinha, P., Chierici, F., Matias, L., Team, B., 2004. Neogene through Quaternary tectonic reactivation of SW Iberian passive margin. Pure Appl. Geophys. 161 (3), 565–587.

CHAPTER

8

The Gloria Transform Fault—NE Atlantic: Seismogenic and Tsunamigenic Potential

Rachid Omira[*,†], *Marta Neres*[*,†], *Luis Batista*[*,†]

[*]Portuguese Institute for Sea and Atmosphere, IPMA, Lisbon, Portugal [†]Dom Luiz Institute, IDL, Faculty of Sciences, University of Lisbon, Lisbon, Portugal

OUTLINE

1 INTRODUCTION

The Azores-Gibraltar fracture zone (AGFZ) marks the western plate boundary between the Eurasian and Nubian plates. It extends eastwards from the Mid-Atlantic Ridge in the Azores toward the Strait of Gibraltar (Fig. 1). The central domain of the AGFZ, called Gloria Fault (GF), follows a prominent morphological feature. The GF was first mapped by Laughton et al. (1972) and presents a relatively slow, ~5mm/year, interplate motion (Fernandes et al., 2003) dominated by dextral strike-slip faulting. Seismically, it is characterized by low seismic activity, although exhibiting a large variation between its eastern, central and western segments. The lack of seismic activity in the eastern GF segment suggests that the low-magnitude earthquakes are probably not detectable by the available seismic network.

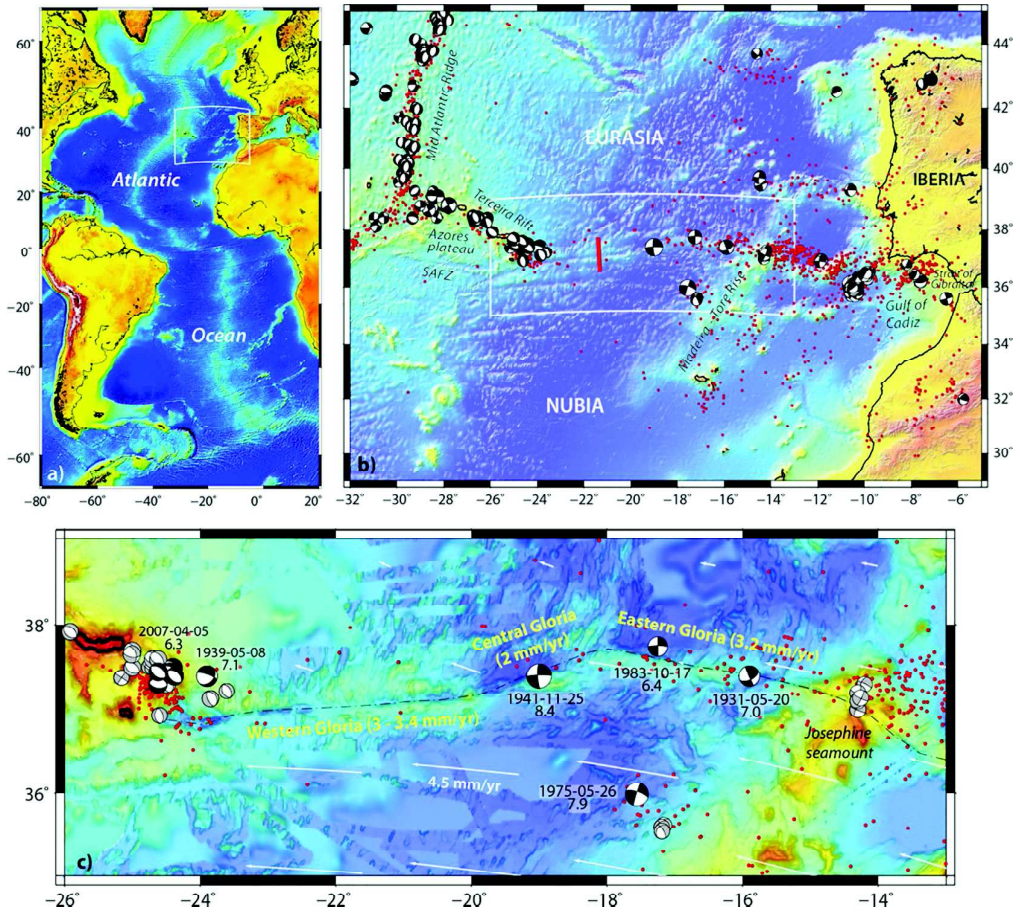

FIG. 1 (A) Location of the study area in the Atlantic Ocean. The Azores-Gibraltar fracture zone (AGFZ) is the only fracture-transform zone in the Atlantic Ocean that constitutes a relatively discrete major plate boundary. (B) The AGFZ and its regional context. *Red dots* are epicenters of $M > 4$ earthquakes from the International Seismological Center (ISC) for the period 1970–2017. Focal mechanisms from the database compiled by Custódio et al. (2016) ($M > 5$). *Red line* locates the seismic refraction and multichannel seismic reflection profiles by Batista et al. (2017) (Fig. 2). SAFZ: South Azores fracture zone. (C) The Gloria Fault. *Red dots*: $M > 4$ epicenters. Focal mechanisms (Custódio et al., 2016 database) for earthquakes $M > 5$ (in *gray*) and $M > 6$ (in *black*, labels indicate date and magnitude). *White arrows*: vectors from the relative NU-EU velocity field as modeled by the neotectonic model of Neres et al. (2016). *Yellow* labels: Gloria Fault segments and respective slip rates as inferred by Neres et al. (2016) (note that the model allows for fault slip and continuum strain rate).

Alternatively, this could indicate that the GF in this area is locked and loading for the next big earthquake. This later hypothesis is supported by the occurrence of past large strike-slip earthquake events within the GF or in its vicinities.

During the 20th century, three large earthquakes ($M > 7$) took place along the GF or in its proximity (Fig. 1C). All have generated tsunamis that were recorded by the regional

tide-gauge network. The Ms 7.1, May 8, 1939, earthquake occurred near the Azores (see Fig. 1C) with an epicenter located close to the end of the GF (Buforn et al., 1988; Reis et al., 2017). It caused a small tsunami that was recorded by the Ponta Delgada (Azores) tide gauge (Reis et al., 2017). On November 25, 1941, an M 8.4 earthquake occurred in the central segment of the GF (see Fig. 1C, Udias et al., 1976; Baptista et al., 2016). It was considered the largest strike-slip event ever recorded (Bird and Kagan, 2004) until the April 11, 2012 Sumatra earthquake, Mw 8.6 (Meng et al., 2012). The 1941 GF earthquake was followed by a tsunami recorded by sea-level stations in Portugal mainland, Morocco, Madeira, and Azores islands, with a maximum wave height of about 0.2 m in Ponta Delgada (Azores) (Baptista et al., 2016). Another high-magnitude event, the M 7.9 May 26, 1975, earthquake had its source 100 km south from the eastern segment of the GF (see Fig. 1C, Buforn et al., 1988; Kaabouben et al., 2008). This strike-slip earthquake also generated a small tsunami that was recorded by the Portuguese, Spanish, and the Moroccan tide-gauge networks (Kaabouben et al., 2008). The spatial distribution of these large events suggests that there is no unique discrete structure running from the Azores to Gibraltar that can be considered as the locus of seismic slip, but rather some degree of fault-segment delocalization accounting for the observed earthquake dispersion (Baptista et al., 2017).

In this chapter, we provide, as a starting point, an overview of the geodynamic setting of the AGFZ. We then focus on the Gloria transform fault by describing the main geometry and interpreted kinematics of this major tectonic structure, as well as its main associated seismicity. Furthermore, we use numerical modeling of tsunami propagation to provide new insight into the tsunamigenesis of the GF, and discuss the implications of its tsunamigenic potential on the NE Atlantic, the Mediterranean, and Connected Seas Tsunami Warning System (NEAM TWS).

2 GEODYNAMIC SETTING

The AGFZ is a complex structure bordering Nubia and Eurasia in the Atlantic that underwent a complex tectonic evolution (Fig. 1A and B). It runs from the Azores plateau (in the west) to the Strait of Gibraltar (in the east) across three distinct morphotectonic domains: the Azores triple junction zone, the GF, and the southwest Iberian Margin (SWIM) (Fig. 1B). Within each domain, different kinematic and stress regimes occur, mostly determined by the Nubia-Eurasia (NU-EU) relative motion (e.g., Fernandes et al., 2003; Serpelloni et al., 2007; Neres et al., 2016).

The Azores triple junction zone is the westernmost domain of the AGFZ where the North American, African (Nubia), and the Eurasian plates meet, and where the NU-EU boundary shows a divergent relative motion (Fig. 1B). This domain comprises a zone of distributed transtensional deformation close to the Mid-Atlantic Ridge that connects to the NW-SE-oriented Terceira spreading ridge (e.g., Miranda et al., 2014, 2015). Along the Terceira Rift, extensional tectonics generate intense normal regime seismicity of low to moderate magnitude that accounts for most of the NU-EU relative motion, also suggested by the absence of seismicity at the South Azores fracture zone (SAFZ, see Fig. 1B).

The easternmost domain of the AGFZ runs from the Strait of Gibraltar to the Madeira-Tore Rise across the SWIM (Fig. 1B). Here, Nubia and Eurasia show a convergent movement along

an apparently seismically diffuse plate boundary, but with some degree of earthquake clustering. Deformation is characterized by large-scale strain partitioning along differently orientated major dextral strike-slip and thrust faults, as attested by the diversity of focal mechanisms. Most of the active structures are inherited from previous tectonic episodes (e.g., Mesozoic rifting) and were reactivated since the initiation of the Alpine compressive tectonics (e.g., Zitellini et al., 2009; Terrinha et al., 2009).

The central domain of the AGFZ, comprised between the eastern tip of the Terceira Rift (24°W) and the Josephine seamount in the Madeira-Tore Rise (14°W) (see Fig. 1B and C), is dominated by a prominent morphological feature, the expression of the GF (Fig. 1C) that is generally assumed to constitute a pure transform plate boundary segment.

3 THE GLORIA TRANSFORM FAULT

The GF is commonly described as a composite of three main segments (Fig. 1C). Between 24°W and 19°30′W (western Gloria—see Fig. 1C) it strikes parallel to the average direction of NU-EU motion, so this is essentially accommodated by strike-slip faulting (Neres et al., 2016). Between 19°30′W and 18°W (central Gloria—see Fig. 1C) it jogs to ENE-WSW, slightly oblique to the kinematic vectors and likely prone to some dextral transpressive strain. From 18°W to 14°30′W (eastern Gloria—see Fig. 1C) it strikes again parallel to the NU-EU motion. Morphologically, the GF is a 15–20-km wide depression with more than 1 km of vertical offset (Fig. 1C), with E-W elongated basins developed between elongated ridges.

The crustal structure of the GF has recently been investigated by Batista et al. (2017) across a 150-km-long N-S seismic profile (Fig. 2A). Their interpretation (Fig. 2A) shows that the basins overlying the GF have a maximum depth of ~1 km with steepened bounding fault planes dipping ~75 degrees. This study also evidenced the differences in the bulk sedimentation and tectonic deformation between the north and the south side of the GF, that is, Eurasian and Nubian plates. The northern side of the GF shows evidences of minor tectonic movements (Fig. 2A) and a sequence of north-south trending parallel ridges that deflect to NNE-SSW as we move eastwards. In the southern side of the GF, these ridges are not so pronounced and most of the deformation associated with the GF strike-slip tectonic movement is accommodated there. Moreover, the analysis of wide-angle data, by Batista et al. (2017), has showed a five-layer *V*p velocity model (L1–L5 in Fig. 2B). L1 comprises both pelagic sediments and basaltic flows or volcanic sedimentary complex and corresponds to seismo-stratigraphic units U1 + U2 (Fig. 2A); L2 (~3 km thick) presents a basaltic composition normally referred to as oceanic upper crust; L3 (~5 km thick) is in agreement with a gabbroic composition normally referred to as oceanic lower crust; L4 (~4 km thick) was interpreted as partial serpentinization of the upper lithospheric mantle; and L5 corresponds to upper mantle. From this experiment Batista et al. (2017) inferred that the thickness of the crust is ~8 km in the GF strike and ~7 km toward north and south of the GF strike.

The assumption of the GF as a localized transform plate boundary is challenged by the characteristics of the seismicity record. The seismic events (plotted in Fig. 1) show significant moderate seismic activity in the Azores and SWIM domains but less activity along the Gloria domain. The eastern Gloria is the most active segment, while seismic event is almost absent in

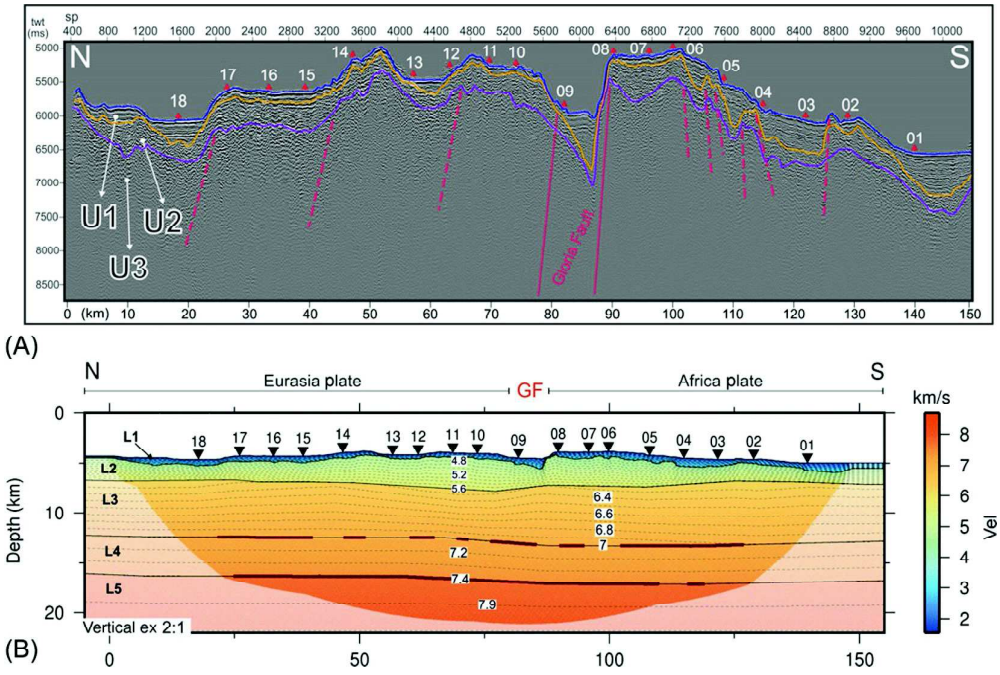

FIG. 2 Morphology and structure across the Gloria Fault, after Batista et al. (2017) (profile located with a *red line* in Fig. 1). (A) Interpreted MCS profile w51: U1—pelagic sediments interbedded with gravity-driven deposition; U2—volcanic or volcanic-sedimentary complex; U3—magmatic crustal material. (B) *V*p velocity model from wide-angle seismic refraction: GF—Gloria Fault; L1–L5—modeled layers; *dark red lines* show reflected waves. Contours are spaced 0.1 km/s. Numbers and triangles represent positions of OBS.

the western Gloria segment. Moreover, the epicenters of the few recorded earthquakes do not follow the Gloria trend but appear to be spread around it. This may result from inaccurate localization of the events, due to the long distance to the seismic networks, as well as to the low azimuthal coverage of this oceanic area. Nonetheless, three large instrumental strike-slip events (M8.4, M7.0, and M6.4) have been recorded within the Gloria domain and all are located very close to its morphological structure. This suggests that large events/ruptures would preferably localize along the main structure, irrespective of a possible more spread location of the small events. The M8.4 Gloria earthquake of 1941 (Buforn et al., 1988; Baptista et al., 2016) was the largest strike-slip earthquake recorded until the Mw8.6 Sumatra earthquake in 2012. Such a large magnitude might have implied a long rupture propagating for multiple segments, eventually until the western Gloria domain. This large rupture has been evoked as a possible justification for the lack of seismicity on the GF: it may now be locked and loading for a next big event. Another challenging fact for the definition of the GF as a pure transform plate boundary is the 1975 M7.9 strike-slip earthquake (Fig. 1C). This large magnitude event, located about 100 km south of Gloria, in the prolongation of an arguably inactive fracture zone, may suggest that Gloria is not the only active plate boundary

structure along this domain (Baptista et al., 2017). It may rather consist of a plate boundary zone with transform motion distributed among several fracture zones. An alternative explanation for the 1975 event may involve the close presence of the crustal-thickened Madeira-Tore Rise, which certainly affects and deflects the nearby stress and strain fields.

4 TSUNAMIGENIC POTENTIAL OF GLORIA FAULT

In this chapter, the evaluation of the tsunamigenic potential of the GF follows a number of steps which include: (i) definition of the tsunami sources; (ii) characterization and parameterization of the maximum credible tsunamigenic scenarios; (iii) modeling of tsunami generation; and (iv) simulation of the tsunami propagation and the resulting coastal wave heights.

Our definition of the tsunami sources for the GF is based on the available earthquakes information, particularly for the 1941 and 1975 events, and on the recently published works (e.g., Kaabouben et al., 2008; Baptista et al., 2016, 2017; Batista et al., 2017). This leads to distinguish a maximum credible tsunami scenario within each one of the three main GF segments, namely the western GF, the central GF, and the eastern GF. Additionally, a tsunamigenic scenario corresponding to the rupture of a 250-km fault length, located 100 km south of the GF, is also considered to include the fault where the 1975 event may have occurred.

Table 1 depicts the earthquake fault parameters for the maximum credible scenarios considered in this work. These parameters are used to compute the tsunami generation following the earthquake occurrence.

To model the generation of the tsunami, we use the Okada's (1985) half-space elastic model to calculate the earthquake-induced sea-bottom coseismic deformation that it is assumed to mimic the sea-surface deformation. Then, we propagate the tsunami from the source to the target coast of the NE Atlantic by solving the nonlinear shallow water equations using staggered-grid finite difference scheme (Omira et al., 2016a; Baptista et al., 2017 and references therein). As the simulation of the tsunami inundation is beyond the scope of this work, we use a coarse resolution bathymetric/topographic grid (800×800 m) in our simulations of tsunami propagation. This bathymetric model was generated using multisource height/depth data from the GEBCO 30-arcs gridded data, and from the SWIM bathymetry compilation (Zitellini et al., 2009).

TABLE 1 Earthquake Fault Parameters for the Selected Tsunamigenic Scenarios of the GF

Rupture Segment	Max. Mag (Mw)	Length (km)	Width (km)	Slip (m)	Strike (°)	Dip (°)	Rake (°)
Western GF	8.6	300	45	10	265	75	161
Central GF	8.4	200	45	8	255	88	161
Eastern GF	8.4	200	45	8	282	88	161
1975-Fault	8.5	250	45	8	277	88	161

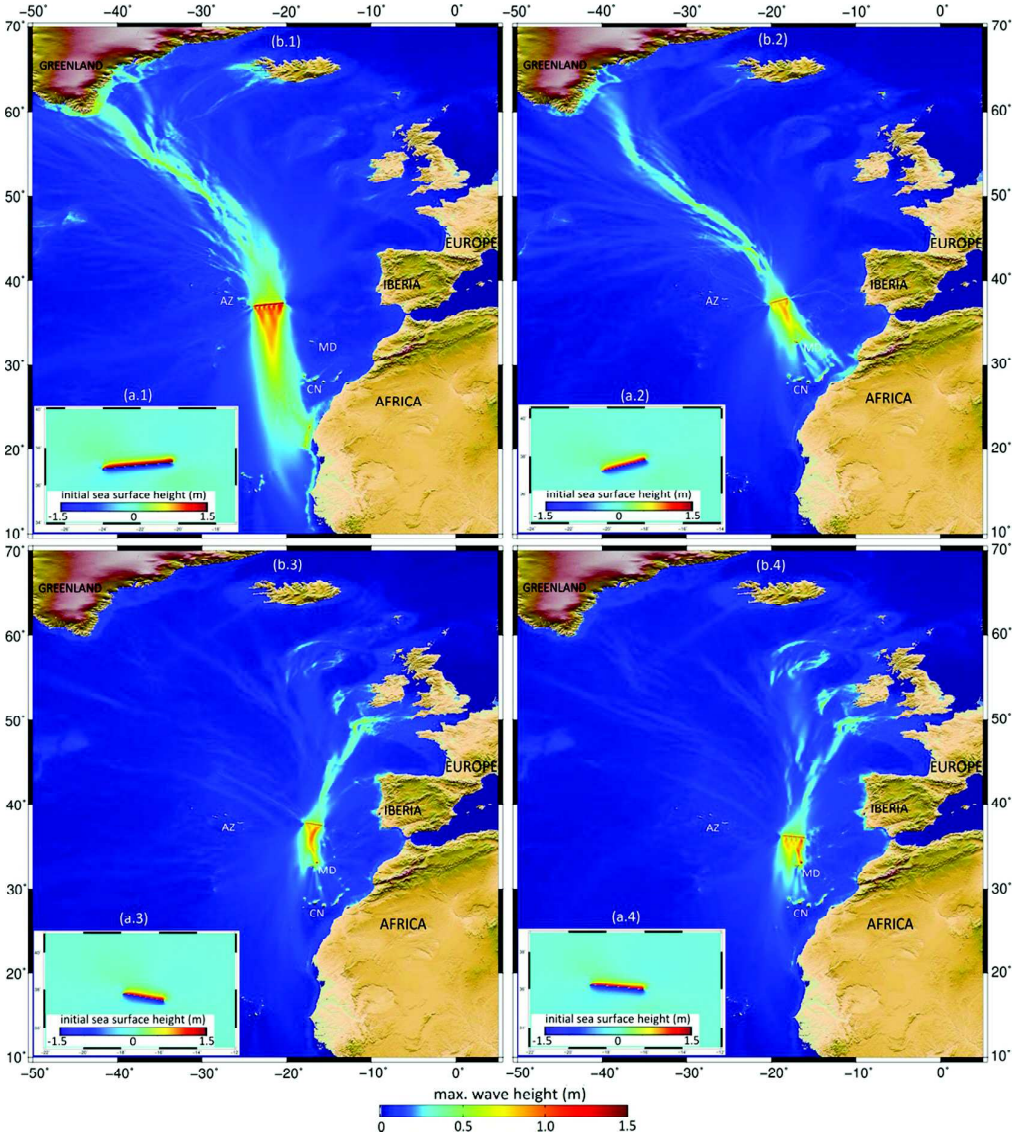

FIG. 3 Tsunami numerical models for the four-selected maximum credible earthquake scenarios of the GF. (A) The initial sea-surface perturbations that follow the sea-bottom coseismic deformations from: (1) the western GF, (2) the central GF, (3) the eastern GF, and (4) the 1975-fault earthquake scenarios. (B) The maximum tsunami wave heights distributions in the NE Atlantic region from: (1) the western GF, (2) the central GF, (3) the eastern GF, and (4) the 1975-fault tsunami scenarios. *AZ*, Azores; *CN*, Canary Islands; *MD*, Madeira.

Fig. 3 depicts the tsunami models for the maximum credible earthquake scenarios of the GF. The analysis of the initial sea-surface perturbation (Fig. 3A1–4) clearly shows that the Mw8.4–8.6 GF earthquakes lead to the generation of relatively small tsunamis, with maximum wave heights in the range of 0.8–1.2 m. This is mainly due to the mechanism of the earthquake ruptures, which are mainly dominated by a strike-slip motion, causing a small vertical deformation of the sea bottom.

The tsunamis from the GF's maximum credible earthquake scenarios pose a low threat along the most of the NE Atlantic coast (Fig. 3B, 1–4). Results of maximum wave heights computations show values of less than 1 m (Fig. 3). They are in good agreement with the observed tsunami heights from the past events in the region (Kaabouben et al., 2008; Baptista et al., 2016, 2017). The tsunami energy distribution from the selected scenarios meets the reasonable expectations, being, at first order, maximal in the direction perpendicular to the fault strike. However, when the tsunami propagates away from the source it encounters shallow water zones that affects its waveforms and amplifies its wave heights. For such a reason, we observe the effect of the Mid-Atlantic Ridge bathymetry channeling the tsunami energy (Fig. 3B, 1 and 2) which results in a noticeable impact along the coast of Greenland, even though it is located far from the source zone.

Results also show that the location of the earthquake source within the GF can help identify the coastal regions that are mostly threatened by a potential tsunami. The Mw8.6 eastern GF scenario steers most of the tsunami energy toward the Azores and Greenland coasts, with a maximum wave height of up to 0.8 m (Fig. 3B, 1), whereas, only small waves, less than 0.25 m, reach the Iberian coast. Moving westward, the coasts of Madeira and Canary Islands are the most affected by the Mw8.4 event generated on the central GF segment. Simulated maximum wave heights along Madeira's northern coast are in the range of 1 m (Fig. 3B, 2). Both the eastern GF and the 1975-fault scenarios, Mw8.4 and Mw8.5 respectively, are the most effective in steering tsunami energy toward the Iberian and African coasts. However, the incident tsunami remains relatively small with waves up to 0.4 m in height.

5 DISCUSSION

The tsunamigenic potential of the GF has been studied in a number of recent works (Omira et al., 2015, 2016b; Baptista et al., 2017). Omira et al. (2015, 2016b) considered the GF as one of the main tsunamigenic source zones in the NE Atlantic to derive probabilistic tsunami hazard maps at regional and local scales. Baptista et al. (2017) produced a tsunami catalog using an earthquake synthetic catalog compatible with the plate kinematic constraints of the area. This work, on the other hand, focuses on the tsunamigenesis of the GF from the perspective of the maximum credible earthquake scenarios. While the approach used here is considered the simplest, in comparison to the previously mentioned works, the outcomes of this chapter are easy to interpret and, therefore, can better serve the tsunami warning purpose in the NE Atlantic.

Understanding how tsunamis are generated in the GF domain and propagated toward the NE Atlantic coast helps decision makers in the tsunami warning centers (TWCs) to determine how future tsunamis in the region can be mitigated. In the NE Atlantic region, TWCs use the

Tsunami Decision Matrix (TDM), proposed by the ICG/NEAMTWS (Intergovernmental Coordination Groups/NEAMTWS), to quickly forecast the tsunami threat from large earthquakes. The TDM is an easy-to-use table establishing a link between the earthquake parameters and the possible ensuing tsunami. However, the fact that the TDM only considers the basic earthquake parameters (location, magnitude, and depth) without any information on the rupture mechanism limits the effectiveness of this tool.

To examine the adequacy of the TDM for the potentially tsunamigenic earthquakes of the GF, we compared its performance with the numerical model for the proposed scenario (Fig. 4). For the Mw8.6 western GF scenario, the TDM leads to the maximum tsunami warning level, that is, "Watch," for the entire NE Atlantic coast, which is in disagreement with the numerical modeling results that show only very small tsunami waves along most of the coastal zones of the region. This comparison clearly indicates that the NEAMTWS's TDM overestimate the tsunami threat from the large earthquakes of the GF. This suggests a review of the TDM tool to reduce probable false warning following the GF earthquakes.

Tinti et al. (2012) have investigated the applicability of the TDM to the Italian tsunamis and reached similar conclusions on the need of substantial improvements in this forecast tool to meet early warning requirements. Moreover, they proposed diverse ways of TDM improvements including: (1) to keep the concept as it is and perform a sensitivity analysis to define the boundaries that provide the best performance; (2) integrate additional earthquake parameters, such as the focal mechanism; (3) discard the concept of the TDM and use the

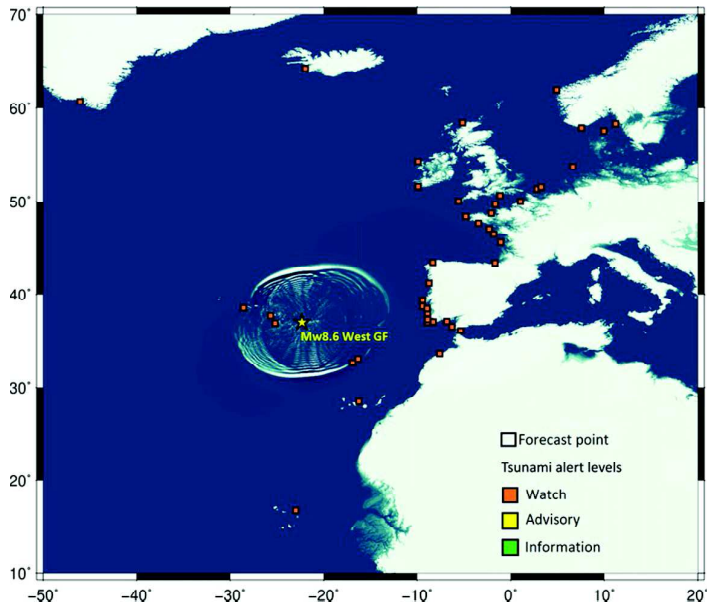

FIG. 4 Application of the Tsunami Decision Matrix for the Mw 8.6 western GF scenario and the resulting tsunami warning levels at the official forecast points along the NE Atlantic coasts.

precomputed scenarios database to forecast earthquake-induced tsunamis. These propositions can form the basis for a further review of the TDM in the NE Atlantic region.

6 CONCLUSIONS

This chapter presents an overview of the seismogenic and tsunamigenic potential of the GF, a domain of the AGFZ that marks the western Eurasia-Nubia plate boundary.

The following main conclusions are drawn:

1. The GF is underexplored, and substantial further work is needed to understand its general tectonic framework and evolution.
2. Despite the lack of recorded seismic activity in some parts of the GF, the occurrence of large seismic events favors the hypothesis that GF is locked and loading for the next big earthquake.
3. Tsunamis from the GF pose low hazard for most of the NE Atlantic coasts.
4. The forecast procedure in-use at the TWCs of the NE Atlantic region overestimates the tsunami threat from the GF.

Acknowledgments

This work was supported by the project ASTARTE—Assessment, STrategy And Risk Reduction for Tsunamis in Europe, Grant 603839, 7th FP (ENV.2013.6.4-3), and by the FCT project UID/GEO/50019/2013, Instituto Dom Luiz. Portuguese Task Group for the Extension of the Continental Shelf (EMEPC) is thanked for making available the high-resolution multibeam bathymetry around the GF. The authors wish to thank the Editor João Duarte and the Reviewer Filipe Rosas for their timely reviews, which improved the manuscript.

References

Baptista, M.A., Miranda, J.M., Batlló, J., Lisboa, F., Luis, J., Maciá, R., 2016. New study on the 1941 Gloria Fault earthquake and tsunami. Nat. Hazards Earth Syst. Sci. 16 (8), 1967–1977.

Baptista, M.A., Miranda, J.M., Matias, L., Omira, R., 2017. Synthetic tsunami waveform catalogs with kinematic constraints. Nat. Hazards Earth Syst. Sci. 17 (7), 1253.

Batista, L., Hübscher, C., Terrinha, P., Matias, L., Afilhado, A., Lüdmann, T., 2017. Crustal structure of the Eurasia–Africa plate boundary across the Gloria Fault, North Atlantic Ocean. Geophys. J. Int. 209, 713–729.

Bird, P., Kagan, Y.Y., 2004. Plate-tectonic analysis of shallow seismicity: apparent boundary width, beta, corner magnitude, coupled lithosphere thickness, and coupling in seven tectonic settings. Bull. Seismol. Soc. Am. 94 (6), 2380–2399.

Buforn, E., Udias, A., Colombas, M.A., 1988. Seismicity, source mechanisms and tectonics of the Azores-Gibraltar plate boundary. Tectonophysics 152 (1–2), 89–118.

Custódio, S., Lima, V., Vales, D., Cesca, S., Carrilho, F., 2016. Imaging active faulting in a region of distributed deformation from the joint clustering of focal mechanisms and hypocentres: application to the Azores–western Mediterranean region. Tectonophysics 676, 70–89.

Fernandes, R., Ambrosius, B.A.C., Noomen, R., Bastos, M., Wortel, M., Spakman, W., Govers, R., 2003. The Relative Motion Between Africa and Eurasia as Derived From ITRF2000 and GPS Data. Geophys. Res. Lett. 30, 1828.

Kaabouben, F., Brahim, A.I., Toto, E., Baptista, M.A., Miranda, J.M., Soares, P., Luis, J.F., 2008. On the focal mechanism of the 26.05.1975 North Atlantic event contribution from tsunami modeling. J. Seismol. 12, 575–583.

Laughton, A.S., Whitmarsh, R.B., Rusby, J.S.M., Somers, M.L., Revie, J., McCartney, B.S., Nafe, J.E., 1972. A continuous east west fault on the Azores-Gibraltar Ridge. Nature 237, 217–220. https://doi.org/10.1038/237217a0.

Meng, L., Ampuero, J.P., Stock, J., Duputel, Z., Luo, Y., Tsai, V.C., 2012. Earthquake in a maze: compressional rupture branching during the 2012 Mw 8.6 Sumatra earthquake. Science 337 (6095), 724–726.

Miranda, J.M., Luis, J.F., Lourenço, N., Goslin, J., 2014. Distributed deformation close to the Azores Triple "Point" Mar. Geol. 355, 27–35.

Miranda, J.M., Luis, J.F., Lourenço, N., Fernandes, R.M.S., 2015. The structure of the Azores Triple Junction: implications for São Miguel Island. In: Geological Society, London, Memoirs. vol. 44, pp. 5–13. https://doi.org/10.1144/M44.2 (Chapter 2).

Neres, M., Carafa, M.M.C., Fernandes, R.M.S., Matias, L., Duarte, J.C., Barba, S., Terrinha, P., 2016. Lithospheric deformation in the Africa-Iberia plate boundary: improved neotectonic modeling testing a basal-driven Alboran plate. J. Geophys. Res. Solid Earth 121, 6566–6596.

Okada, Y., 1985. Surface deformation due to shear and tensile faults in a half-space. Bull. Seismol. Soc. Am. 75 (4), 1135–1154.

Omira, R., Baptista, M.A., Matias, L., 2015. Probabilistic tsunami hazard in the Northeast Atlantic from near-and far-field tectonic sources. Pure Appl. Geophys. 172 (3–4), 901–920.

Omira, R., Baptista, M.A., Lisboa, F., 2016a. Tsunami characteristics along the Peru–Chile trench: analysis of the 2015 Mw8. 3 Illapel, the 2014 Mw8. 2 Iquique and the 2010 Mw8. 8 Maule tsunamis in the near-field. Pure Appl. Geophys. 173 (4), 1063–1077.

Omira, R., Matias, L., Baptista, M.A., 2016b. Developing an event-tree probabilistic tsunami inundation model for NE Atlantic coasts: application to a case study. Pure Appl. Geophys. 173 (12), 3775–3794.

Reis, C., Omira, R., Matias, L., Baptista, M.A., 2017. On the source of the 8 May 1939 Azores earthquake–tsunami observations and numerical modelling. Geomat. Nat. Hazards Risk 8 (2), 328–347.

Serpelloni, E., Vannucci, G., Pondrelli, S., Argnani, A., Casula, G., Anzidei, M., Baldi, P., Gasperini, P., 2007. Kinematics of the Western Africa-Eurasia plate boundary from focal mechanisms and GPS data. Geophys. J. Int. 169, 1180–1200.

Terrinha, P., Matias, L., Vicente, J., Duarte, J., Luís, J., Pinheiro, L., Lourenço, N., Diez, S., Rosas, F., Magalhães, V., Valadares, V., Zitellini, N., Roque, C., Víctor, L.M., 2009. Morphotectonics and strain partitioning at the Iberia-Africa plate boundary from multibeam and seismic reflection data. Mar. Geol. 267, 156–174.

Tinti, S., Graziani, L., Brizuela, B., Maramai, A., Gallazzi, S., 2012. Applicability of the decision matrix of North Eastern Atlantic, Mediterranean and connected seas Tsunami Warning System to the Italian tsunamis. Nat. Hazards Earth Syst. Sci. 12, 843–857.

Udias, A., Arroyo, A.L., Mezcua, J., 1976. Seismotectonic of the Azores-Alboran region. Tectonophysics 31 (3–4), 259–289.

Zitellini, N., Gràcia, E., Matias, L., Terrinha, P., Abreu, M.A., DeAlteriis, G., Henriet, J.P., Dañobeitia, J.J., Masson, D.G., Mulder, T., Ramella, R., Somoza, L., Diez, S., 2009. The quest for the Africa-Eurasia plate boundary west of the Strait of Gibraltar. Earth Planet. Sci. Lett. 280, 13–50.

frontiers in Earth Science

REVIEW
published: 19 March 2019
doi: 10.3389/feart.2019.00039

Marine Transform Faults and Fracture Zones: A Joint Perspective Integrating Seismicity, Fluid Flow and Life

Christian Hensen[1], Joao C. Duarte[2], Paola Vannucchi[3,4], Adriano Mazzini[5], Mark A. Lever[6], Pedro Terrinha[2,7], Louis Géli[8], Pierre Henry[9], Heinrich Villinger[10], Jason Morgan[3], Mark Schmidt[1], Marc-André Gutscher[11], Rafael Bartolome[12], Yama Tomonaga[13], Alina Polonia[14], Eulàlia Gràcia[12], Umberta Tinivella[15], Matteo Lupi[16], M. Namık Çağatay[17], Marcus Elvert[18], Dimitris Sakellariou[19], Luis Matias[2], Rolf Kipfer[13], Aristomenis P. Karageorgis[19], Livio Ruffine[8], Volker Liebetrau[1], Catherine Pierre[20], Christopher Schmidt[1], Luis Batista[2,7], Luca Gasperini[14], Ewa Burwicz[1], Marta Neres[2,7] and Marianne Nuzzo[21]*

[1] GEOMAR Helmholtz Centre for Ocean Research Kiel, Kiel, Germany, [2] Instituto Dom Luiz (IDL), Faculdade de Ciências da Universidade de Lisboa, Lisbon, Portugal, [3] Earth Sciences Department, Royal Holloway, University of London, Egham, United Kingdom, [4] Dipartimento di Scienze della Terra, Università di Firenze, Firenze, Italy, [5] Centre for Earth Evolution and Dynamics (CEED), University of Oslo, Oslo, Norway, [6] Department of Environmental Systems Science, ETH Zürich, Zurich, Switzerland, [7] IPMA- Portuguese Institute for Atmosphere and Ocean, Lisbon, Portugal, [8] Institut Français de Recherche pour l'Exploitation de la Mer (IFREMER), Département Ressources Physiques et Ecosystèmes de Fond de Mer, Unité des Géosciences Marines, Plouzané, France, [9] Aix Marseille Univ, CNRS, IRD, INRA, Coll France, CEREGE, Aix-en-Provence, France, [10] Department of Geosciences, University of Bremen, Bremen, Germany, [11] CNRS, IUEM, Laboratoire Géosciences Océan, University of Western Brittany, Brest, France, [12] Barcelona-CSI, Institut de Ciències del Mar (CSIC), Barcelona, Spain, [13] Eawag, Swiss Federal Institute of Aquatic Science and Technology, Dübendorf, Switzerland, [14] CNR, Institute of Marine Sciences (ISMAR), Bologna, Italy, [15] Istituto Nazionale di Oceanografia e di Geofisica Sperimentale, Trieste, Italy, [16] Department of Earth Sciences, University of Geneva, Geneva, Switzerland, [17] EMCOL and Faculty of Mining, Department of Geological Engineering, İstanbul Technical University, Istanbul, Turkey, [18] MARUM – Center for Marine Environmental Sciences, University of Bremen, Bremen, Germany, [19] Hellenic Centre for Marine Research, Institute of Oceanography, Anavyssos, Greece, [20] LOCEAN, UPMC, Sorbonne Université, Paris, France, [21] Integrated Geochemical Interpretation Ltd., The Granary, Hallsannery, Bideford, United Kingdom*

OPEN ACCESS

Edited by:
Alessandro Tibaldi, University of Milano-Bicocca, Italy

Reviewed by:
Shinsuke Kawagucci, Japan Agency for Marine-Earth Science and Technology, Japan
Wolfgang Rabbel, University of Kiel, Germany

***Correspondence:**
Christian Hensen
chensen@geomar.de

Specialty section:
This article was submitted to Structural Geology and Tectonics, a section of the journal Frontiers in Earth Science

Received: *22 November 2018*
Accepted: *18 February 2019*
Published: *19 March 2019*

Citation:
Hensen C, Duarte JC, Vannucchi P, Mazzini A, Lever MA, Terrinha P, Géli L, Henry P, Villinger H, Morgan J, Schmidt M, Gutscher M-A, Bartolome R, Tomonaga Y, Polonia A, Gràcia E, Tinivella U, Lupi M, Çağatay MN, Elvert M, Sakellariou D, Matias L, Kipfer R, Karageorgis AP, Ruffine L, Liebetrau V, Pierre C, Schmidt C, Batista L, Gasperini L, Burwicz E, Neres M and Nuzzo M (2019) Marine Transform Faults and Fracture Zones: A Joint Perspective Integrating Seismicity, Fluid Flow and Life. Front. Earth Sci. 7:39. doi: 10.3389/feart.2019.00039

Marine transform faults and associated fracture zones (MTFFZs) cover vast stretches of the ocean floor, where they play a key role in plate tectonics, accommodating the lateral movement of tectonic plates and allowing connections between ridges and trenches. Together with the continental counterparts of MTFFZs, these structures also pose a risk to human societies as they can generate high magnitude earthquakes and trigger tsunamis. Historical examples are the Sumatra-Wharton Basin Earthquake in 2012 (M8.6) and the Atlantic Gloria Fault Earthquake in 1941 (M8.4). Earthquakes at MTFFZs furthermore open and sustain pathways for fluid flow triggering reactions with the host rocks that may permanently change the rheological properties of the oceanic lithosphere. In fact, they may act as conduits mediating vertical fluid flow and leading to elemental exchanges between Earth's mantle and overlying sediments. Chemicals transported upward in MTFFZs include energy substrates, such as H_2 and volatile hydrocarbons, which then sustain chemosynthetic, microbial ecosystems at and below the seafloor. Moreover, up- or downwelling of fluids within the complex system

of fractures and seismogenic faults along MTFFZs could modify earthquake cycles and/or serve as "detectors" for changes in the stress state during interseismic phases. Despite their likely global importance, the large areas where transform faults and fracture zones occur are still underexplored, as are the coupling mechanisms between seismic activity, fluid flow, and life. This manuscript provides an interdisciplinary review and synthesis of scientific progress at or related to MTFFZs and specifies approaches and strategies to deepen the understanding of processes that trigger, maintain, and control fluid flow at MTFFZs.

Keywords: transform faults, fractures zones, coupling of seismicity and fluid flow, microbial life, heat flow, fluid geochemistry, seafloor observation systems, seismic precursors

INTRODUCTION TO MARINE TRANSFORM FAULTS AND FRACTURE ZONES (MTFFZS)

Transform faults are one of the three basic types of plate boundaries in plate tectonics. They are so called "conservative" plate boundaries as – unlike at divergent spreading centers and convergent subduction/collision zones – plate material is neither created nor destroyed. Kinematically, transform faults are strike-slip faults that usually link the other two types of plate boundaries. The discovery of transform plate boundaries (Wilson, 1965) played a fundamental role in the development of the theory of plate tectonics as they were recognized to follow the trace of "small circles" according to the spherical Eulerian geometry (Morgan, 1968). Transform faults can be oceanic or continental, depending on the type of crust they crosscut. On the ocean floor transform faults are in most cases linked to plate growth structures (e.g., Gerya, 2010, 2013a,b; Giustiniani et al., 2015; for exceptions see Hey et al., 1980) as they commonly accommodate the progressive horizontal movements between two adjacent mid-ocean ridges – ridge-ridge transform faults (RRTF; **Figure 1**). Besides the most abundant RRTF, there are also ridge-trench (e.g., Mendocino Transform Fault) and trench-trench (e.g., Alpine Fault or the North Scotia Ridge) transform faults.

Oceanic transform faults have a strong morphological signature on the ocean floor with narrow valleys and steep walls that can reach more than 2,000 m of relief (**Figure 1**) and water depths of >5000 m [Vema > 5100 m, Cannat et al., 1991; Romanche Trench > 7700 m, Bonatti et al., 1994; see overviews by Hekinian (1982) and Wolfson-Schwehr and Boettcher (2019)]. However, this characteristic morphology usually continues for thousands of kilometers to "scar" the ocean floor beyond the active plate boundary segment between mid-ocean ridges (see **Figure 2**). These scars, called fracture zones, were known as morphological features even before transform faults were recognized, and they correspond to the intra-plate traces of oceanic transform faults on the sides of mid-ocean ridges. Transform fault/fracture zone systems can extend for several thousand kilometers on the ocean floor and can show large offsets – the Romanche Fracture Zone in the Central Atlantic, for example, stretches over 5,000 km and reaches about 950 km of displacement (e.g., Hekinian, 1982; Wolfson-Schwehr and Boettcher, 2019; and online compilations[1,2]).

Fracture zones were historically viewed as tectonically inactive structures (Isacks et al., 1968). We now recognize that several of these fracture zones are seismically active (Lay, 2019), and have been generating large-scale earthquakes like the Sumatra-Wharton Basin Earthquake in 2012 (Mb8.6; Hill et al., 2015) or along the Atlantic Azores-Gibraltar Fracture Zone in 1755 (Great Lisbon Earthquake; Mw > 8.5; Gutscher, 2004) and in 1941 (M8.4; Lay, 2019). Oceanic transform plate boundaries may also act as pathways for hydrothermal circulation. A well-known example where off-axis seismicity is linked to hydrothermal fluid flow is the Lost City Hydrothermal Field (Atlantis Massif, Central North Atlantic), where faulting in combination with serpentinization-driven expansion of uplifted mantle rocks provides open pathways for hydrothermal circulation and associated water-rock interactions (Kelley et al., 2001). Serpentinization produces high concentrations of CH_4 and H_2 in the fluids (e.g., Kelley et al., 2001) that provide energy for chemosynthetic biota at the seafloor, and possibly below (see **Figure 3**). Hydrothermal fluids of deep crustal origin have also been suggested to play a role in mud volcanism (Hensen et al., 2015).

Three decades of continuous ocean exploration have led to the awareness that subsurface fluid-related processes (e.g., fluid formation, fluid-rock interaction, fluid transport) are key phenomena affecting and controlling geodynamic processes, because fluids affect almost every physical, chemical, mechanical, and thermal property of the seabed and upper crust (e.g., Judd and Hovland, 2007). Yet, an integrated understanding of how fluid-related geodynamic, geochemical, and biological processes interact is still missing, in particular in transform faults and fracture zones. The aim of this review is thus to present an overview of how crustal structure, fault stability, heat flow, fluid generating processes, geochemical conditions, and microbial life interact at Marine Transform Faults and associated Fracture Zones (MTFFZ). In the context of this manuscript, MTFFZ comprise typical oceanic transform faults and fracture zones, but also include other types of submerged (i.e., marine) parts of continental strike-slip faults/boundaries

[1] https://en.wikipedia.org/wiki/Fracture_zone

[2] https://www.britannica.com/science/submarine-fracture-zone

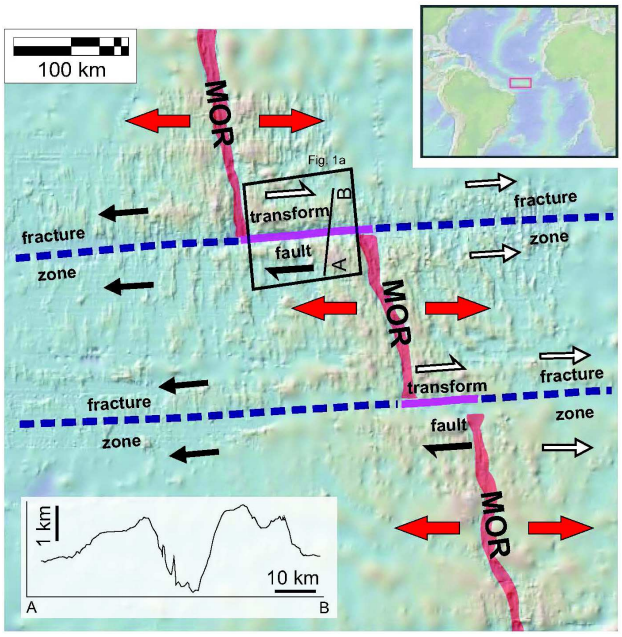

FIGURE 1 | Bathymetric map of the Central Atlantic showing main morphological features of typical ridge-ridge transform fault sections (RRTF; bathymetric data were from GeoMapApp; Ryan et al., 2009).

(e.g., the North Anatolian Fault (NAF) in the Marmara Sea). Terrestrial settings are generally excluded; exceptions are made with respect to specific findings where appropriate in the context. Overall, this manuscript is inspired by many discussions during the EU-funded network FLOWS[3]; 2013–2018). The objective of FLOWS was to merge the expertise of a large number of research groups and further interdisciplinary knowledge on how seep fluid (bio)geochemistry relates to seismicity.

GEODYNAMICS OF MARINE TRANSFORM FAULTS AND FRACTURE ZONES (MTFFZS)

Tectonics and Lithospheric Structure

The key characteristic of transform faults is that they are plate boundaries and thus cut through the lithosphere (see e.g., Bartolome et al., 2012 showing deep strike-slip seismicity nucleating at lithospheric mantle depths of 10 s of kms; see also Gerya, 2016 for a more general review). Continental transform faults may re-use pre-existing fault zones such as sutures and often have multiple sub-parallel strands that define wide areas of strike-slip deformation (see recent reviews by Norris and Toy, 2014; Gerya, 2016; Şengör et al., 2019). In oceanic environments transform faults are typically associated with serpentinization, because large vertical and horizontal temperature gradients and existing, fault-related pathways allow the circulation of large volumes of sea water through the oceanic mantle (e.g., Francis, 1981; Ebert et al., 1983; Cannat et al., 1991; Escartin and Cannat, 1999; Früh-Green et al., 2016; **Figure 3**). Although some volcanism might be present – for example in "leaky" transform faults – transform faults are commonly characterized by absent volcanism. The inside corner of a ridge-transform intersection is a region where crustal-scale normal faulting often shows the intrusive lower crust and lenses of upper mantle material along exposed fault surfaces known as oceanic core complexes (Cann et al., 1997). Core complexes can be associated with hydrothermal fields in which unusual, serpentine-linked geochemical reactions occur, leading to the formation of carbonate-dominated vent systems such as the Lost City Hydrothermal Field in the North Atlantic. Although fluid percolation arguably has a profound effect on the strength of the lithosphere, the depth distribution and lateral extent of serpentinization in transform faults is yet to be determined.

RRTFs on the oceanic crust represent stable features. In contrast to these oceanic systems, spectacular surface expressions of transform faults on land, such as the San-Andreas Fault in Southern California, typically arise from changes in plate configuration, allowing them to grow or shrink with time (Atwater and Menard, 1970). Transform plate boundaries can also connect ridges and orogenic belts *de facto* intersecting both oceanic and continental crust. An example is the Owen Fracture Zone system connecting the Carlsberg Ridge to the Himalayan Orogeny. This fault structure is generally characterized by broad and discontinuous zones of deformation. In cases where a strike-slip fault terminates within a continent (e.g., East Antarctica; Storti et al., 2007), the maximum offset can be located in its center – while "typical" transform faults have constant offsets throughout their entire length.

Despite the fact that transform faults are often defined as conservative plate boundaries, horizontal movement in a system of strike-slip faults may locally cause (i) uplift and folding due to lateral transpression (crustal shortening perpendicular to the fault plane) and has been hypothesized as a precursor for subduction initiation (Casey and Dewey, 1984), (ii) transtension (crustal extension perpendicular to the fault plane) associated with volcanic activity (=leaky transform fault; Garfunkel, 1981), (iii) or the formation of pull-apart basins (e.g., Lonsdale, 1986).

Transform faults often lie within a transform valley, in which their surface expression is a zone only tens of meters wide (Maia, 2019). The limited dimensions of these narrow valleys, the accumulation of tens of kilometers to hundreds of kilometers of displacement over millions of years, and the young, hot, and rheologically weak lithosphere of RRTFs would suggest the development of a fairly smooth, primary fault strand. Transforms are therefore commonly envisaged as single well-localized faults, even though a closer examination often reveals a more complex geometry with multiple strands (Ligi et al., 2002). Fracture zones maintain the surface expression of transform faults and these valleys become major structures that can span over entire ocean basins (**Figure 2**). Spacing of transform faults intersecting mid-ocean ridges correlates with spreading rates: transform faults and fracture zones are more widely spaced in fast spreading centers like in the Pacific (600 ± 300 km) than in slow spreading

[3]https://www.flows-cost.eu/

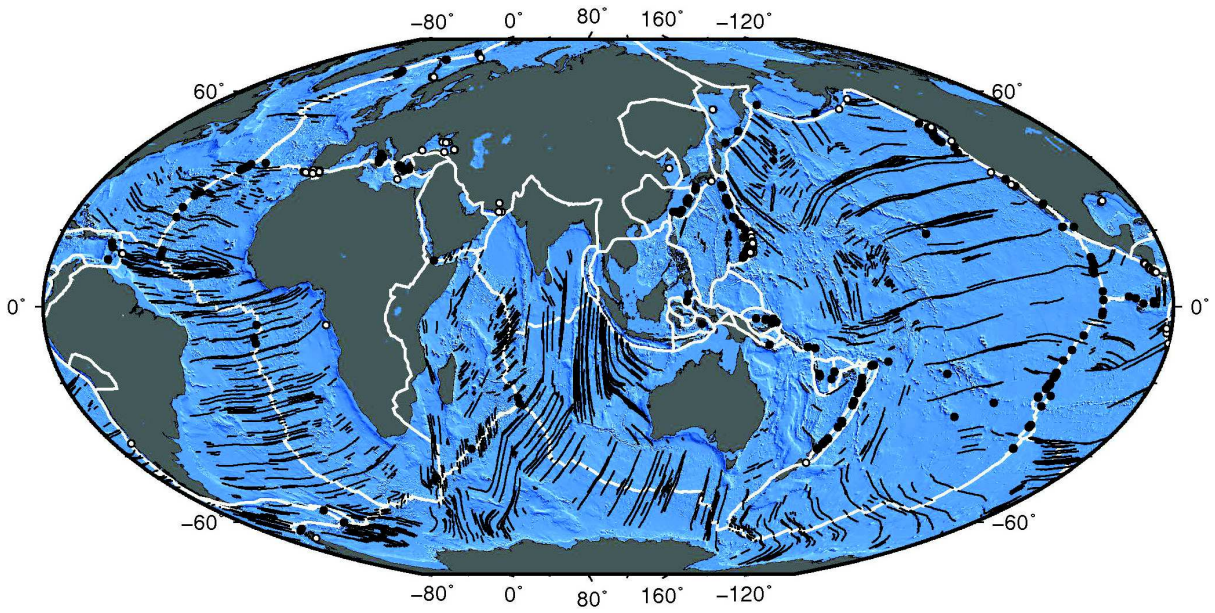

FIGURE 2 | Global bathymetric map with major plate boundaries highlighting active transform faults and oceanic fracture zones (Bird, 2003; Müller et al., 2008; Wessel et al., 2015). Active sites of seafloor hydrothermal venting (solid black circles; Beaulieu and Szafranski, 2018) as well as low temperature seeps (white circles; Hensen et al., 2018) are indicated.

centers like in the Atlantic (400 ± 200 km), while overlaps exist (Macdonald, 1998).

Transform faults are structures that originate to relieve thermal stress (Sandwell, 1986). Along transform faults, lithospheres of different age, and thus with different thermal regimes, get in contact, which is evoked as the primary reason for the possible reactivation of fracture zones. The different negative buoyancies of differently aged plates may, in fact, impart some physical imbalance between the two sides of the fracture zone that may persist during their entire lifetime, keeping the fracture zone "active." Furthermore, the fact that transform faults are generally orthogonal to spreading centers means that their strike-slip motion does not obey the classical Anderson's theory of faulting. At the extensional mid-ocean ridges normal faulting events predominate at ridge segments (Lay and Wallace, 1995), which according to Anderson means that on the horizontal plane the maximum principal stress is perpendicular to the strike of the transform fault. Transform plate boundaries are dominated by strike slip faults (thus strike slip events characterize transform faults; Lay and Wallace, 1995). According to Anderson's theory of faulting the maximum principal stress should be at an angle of 30–45 degrees to them, but in fact is perpendicular to their strike. Faults that move under an unfavorable stress are typically weak, enable fluid circulation, and thus stimulate mineral transformation processes, which, specifically at transform faults, is in agreement with the occurrence of serpentinization. However, although sustained by observations or modeling, all these processes are still poorly known as transform faults and fracture zones have not been thoroughly investigated and their evolution is poorly understood (see Gerya, 2016 and references therein).

Tectonic Analog and Numerical Modeling

Analog models of transform faults have been carried out since the 1970s, including models with and without accreting plates. Examples of models of transform faulting with non-accreting material have been attempted by Dauteuil et al. (2002) and Marques et al. (2007). Examples of thermal+dynamical models with accreting plates are the ones by Oldenburg and Brune (1972, 1975) using freezing wax that reproduced ridge orthogonal transform faults (see Gerya, 2012, 2016 for a detailed review and discussion of this type of experiment). Interestingly, freezing wax experiments are the ones that reproduce best the main characteristics of RRTF, such as the development of "inactive" fracture zones, overlapping spreading centers, rotating microplates and transform faults orthogonal to spreading centers. These models showed that the stability of transform faults is dependent on the thermal state and strain-rate of the system and it is controlled by the almost lack of shear strength of the fault. Moreover, transform faults did not develop in experiments using paraffin suggesting that transform faults are highly dependent on rheology. Analog models with the injection of fluids have also been carried out to study the role of magmatic intrusions and diapirism, most of them using silicone putty (e.g., Corti et al., 2005) or vegetable oil (e.g., Galland et al., 2006). Analog models were also carried out to understand the tectonic consequences of fluid overpressure and seepage forces, demonstrating that gradients in fluid overpressure cause seepage forces, capable of modifying the total stress distribution and the geometry of the faults (Mourgues and Cobbold, 2003, 2006).

Progress in numerical modeling of transform faults has been recently reviewed by Gerya (2012, 2016). Numerical modeling efforts also began in the late 1970s. Due to computer limitations,

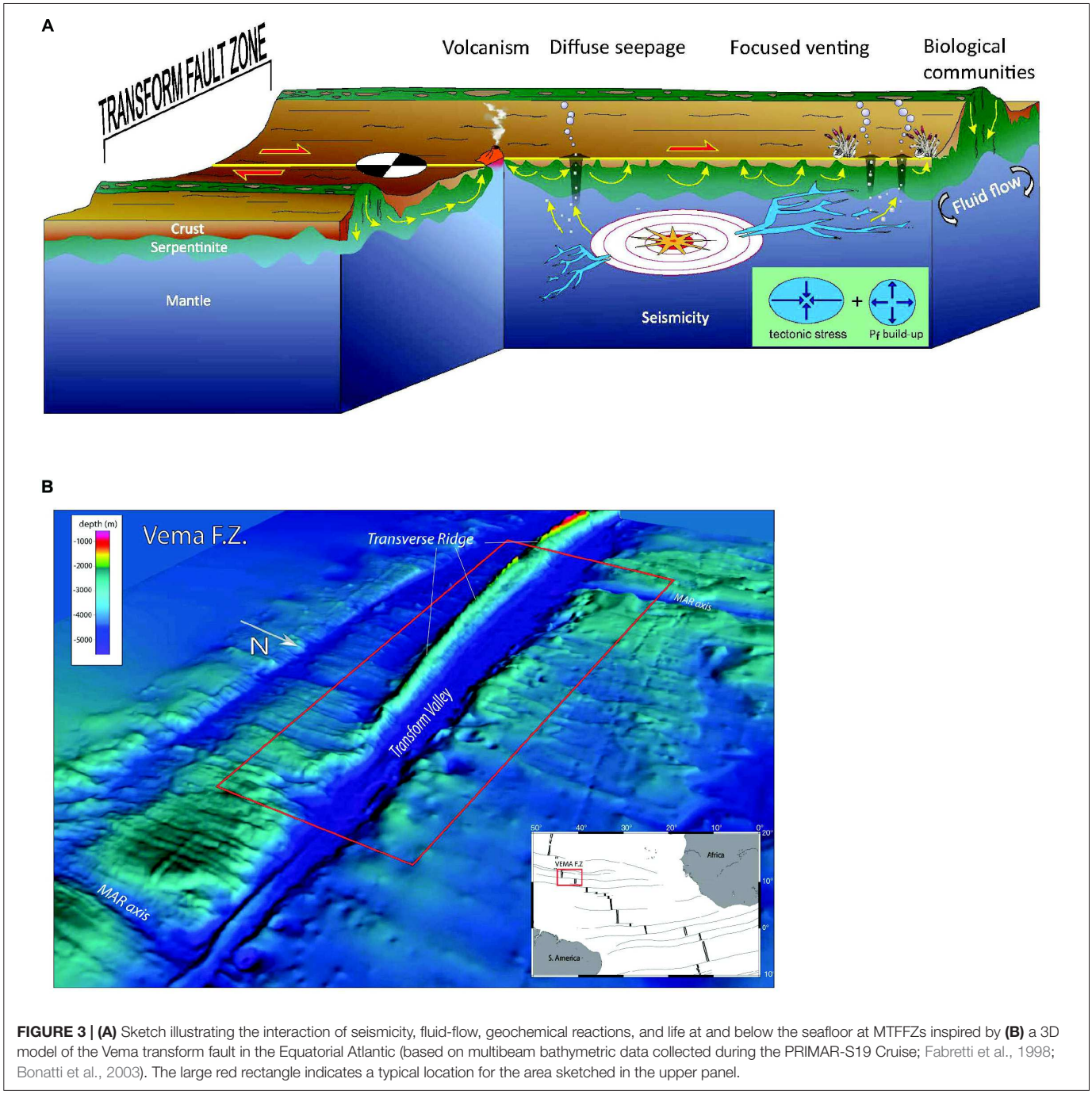

FIGURE 3 | (A) Sketch illustrating the interaction of seismicity, fluid-flow, geochemical reactions, and life at and below the seafloor at MTFFZs inspired by **(B)** a 3D model of the Vema transform fault in the Equatorial Atlantic (based on multibeam bathymetric data collected during the PRIMAR-S19 Cruise; Fabretti et al., 1998; Bonatti et al., 2003). The large red rectangle indicates a typical location for the area sketched in the upper panel.

the first models idealized the lithosphere as a "plane stress" membrane in which horizontal stresses were uniform with depth. This approximation allowed a ridge-transform-ridge system to be approximated with a 2-D model. Early investigations showed that ridge and transform boundaries needed to be much weaker than the lithosphere itself for their geometry to be "plate-like," and also highlighted that stresses become concentrated in the "inside corner" at a ridge-transform intersection (Fujita and Sleep, 1978). The tensile stresses associated with resistance to extension at a ridge needed to be ∼3–5 times higher than shear stresses associated with slip on the transform in order to explain the observed toward-the-transform rotation of diking and normal faults near the ridge-transform intersection (Morgan and Parmentier, 1984). Full 3-D models of stresses and deformation along an oceanic transform were not explored until the 21st century. The first models assumed that the rheological structure of the transform was 2-D, e.g., invariant along the transform, and focused on continental transform systems (Sobolev et al., 2005). Gerya (2016) summarize major efforts toward a better understanding of the evolutionary generation of spreading-parallel transform faults from initially oblique rifted offsets.

Fault Behavior and Seismicity

Transform faults are seismically active (**Figures 1**, **3**) and shearing is typically associated with the hydration of the upper lithospheric units driving the serpentinization of ultramafic rocks. Interestingly, earthquakes are more frequent along the active strike-slip transform segment than along the adjacent normal faulting mid-ocean ridge segments (Hanson and Bowman, 2005).

The seismogenic activity of transform faults in oceanic lithosphere has specific characteristics (Wolfson-Schwehr and Boettcher, 2019). It is generally acknowledged that the base of the seismogenic zone is limited by the 600°C isotherm (Abercrombie and Ekström, 2001; Boettcher and Jordan, 2004). For RRTF, this depth will thus depend on fault length, rate and on the intensity of hydrothermal convection (Roland et al., 2010). In general, RRTF also do not produce great earthquakes (>M8); in particular, if they cut intermediate- to fast-spreading ridges (>40 mm/yr), and have a low seismic coupling ratio (seismic moment release rate versus moment release rate expected from fault kinematics and locking depth; Bird and Kagan, 2004). A component of long-term creep on these transform faults may account for this relatively low level of seismic activity. Examples are known from the repeated occurrence of small earthquakes (e.g., Mendocino Fracture Zone; Materna et al., 2018) as well as from the relative regular occurrence of larger earthquakes on moderate and fast-moving segments (Boettcher and McGuire, 2009). From the seismological point of view, early work showed the anomalously large excitation of long-period waves by ocean transform earthquakes. Some transform earthquakes exhibit long-period seismic anomalies that are best explained by episodes of slow, smooth deformation, several hundred seconds before the high-frequency origin time (Kanamori and Stewart, 1976; Okal and Stewart, 1982; Ihmlé and Jordan, 1994). Because the possibility of anomalously slow rupture preceding normal speed rupture could be useful for short-term prediction, the seismological behavior of oceanic transform faults prior to large earthquakes has recently become the subject of active investigation. It is meanwhile recognized that large earthquakes on RRTFs are commonly preceded by foreshocks and by precursory changes in the seismic properties of the fault zone that could be linked to fluid-related processes (e.g., Dziak et al., 2003; McGuire et al., 2005, 2012). Hydrothermal fluids become (at constant temperature) significantly more compressible with decreasing pressure (Bischoff and Rosenbauer, 1985). Hence, the observed seismic precursors near the intersection of the mid-ocean ridge and the oceanic transform faults could be caused by an increase in fluid compressibility in response to fault core dilatancy just before rupture (Géli et al., 2014). In contrast, transforms in old oceanic lithosphere can produce great earthquakes, such as in the Gloria Fault in the Azores-Gibraltar Fracture Zone (Bezzeghoud et al., 2014) or in the Macquarie Fault Zone (Romanowicz, 1992). Fracture zones were historically thought to be seismically inactive, because the two segments flanking each fracture zone are part of the same plate and move in the same direction. Yet, seismologists have now documented major earthquakes on these structures (e.g., Bohnenstiehl et al., 2004; Lay, 2019). Examples include rupture events in highly stressed lithosphere in the diffuse deformation zone of the India/Australia plate boundary (Robinson et al., 2001; Bohnenstiehl et al., 2004; Hill et al., 2015; Lay, 2019) and in the Pacific Plate in the vicinity of the Alaska subduction and Yakutat terrane collision (Lahr et al., 1988; Lay, 2019). Moreover, the subduction of highly hydrated fracture zones and subsequent dewatering at depth may have an important role in changing the coupling between the lower and the upper plates, with potential consequences for interplate seismicity and back-arc volcanism (Dzierma et al., 2012) or the formation of fluid escape structures in the forearc (see section "Pore Fluid Geochemistry of Seafloor Seeps"). In addition, altered mantle rocks along transform faults or fracture zone may be transferred within subduction systems by plate convergence processes, enhancing shear processes and disruption of the lithosphere during the final closure of the oceans. Inherited discontinuities constituted by fracture zones might also control neotectonic activity, seismicity and location/reactivation of seismogenic structures, e.g., Eastern Mediterranean Sea (Granot, 2016) and Ionian Sea (Polonia et al., 2017).

Marine faults, unlike their continental equivalents, are characterized by the presence of a permanent supply of seawater from above, which is expected to influence geochemical processes within the fault zone itself. Heterogeneity in fault zone properties attributed to interaction with fluids and associated mantle hydration and serpentinization, has been proposed to control the segmentation of moderate and fast-moving RRTFs, and – as previously mentioned – the occurrence of foreshock swarms (e.g., McGuire et al., 2012; Géli et al., 2014). The characteristics of slow and reactivated transforms are less well known. Drilling through plate boundary faults e.g., (NanTroSEIZE; IODP 314/315/316, 338, Kinoshita et al., 2009; Strasser et al., 2014[4]; J-Fast, IODP 343, Chester et al., 2013; SAFOD, Zoback et al., 2011) has shown that the composition of the gouge material in the fault core is an important controlling factor on frictional properties, and on frictional instability leading to earthquakes. Laboratory experiments further showed the complexity of frictional dependence on velocity and temperature, and that this complexity could explain earthquake sequences observed in subduction zones (e.g., Noda et al., 2017). The case of the Tohoku 2011 earthquake has notably suggested that seismic rupture, once initiated, can propagate in smectite rich fault gouge that displays velocity weakening at high slip velocities (Ujiie et al., 2013). Hydrated chrysotile (a serpentine group mineral) can display low friction coefficients and velocity strengthening behavior at low velocities, comparable to that of smectite (Moore et al., 1997). However, frictional properties of serpentinite-bearing fault gouge is complicated by serpentine mineral group polymorphism (antigorite being the most common) and by the presence of other minerals such as saponite, talc or brucite formed under hydrothermal conditions (Moore and Rymer, 2007; Holdsworth et al., 2011; Sone et al., 2012). In partially serpentinized mantle, or weathered oceanic crust, highly variable frictional behaviors are thus expected depending on mineral composition and temperature. In addition, thermo-mechanical coupling with the fluid phase may involve dilatancy

[4]http://publications.iodp.org/index.html

strengthening as well as fault gouge weakening by fluid pressure increase from gouge compaction and/or thermal pressurization. However, serpentinite fault gouges may be more permeable than clay gouges, limiting thermal pressurization effect on friction (Sone et al., 2012). Moreover, below the hydrated zone, the wide range of temperature of the seismogenic zone in oceanic lithosphere (up to 600°C) may result in important variations of fluid compressibility with further consequences of fault stability (Géli et al., 2014). The diversity of behaviors observed at oceanic transform faults – and notably the apparent dependency on plate age and fault slip rate – can only be understood by integrating thermal regime, compositional variations, properties of materials, and interaction with the fluid phase.

Examples From the Southern European Margin

Based on the general information provided so far, this section is dedicated to a more detailed, exemplary description of two different types of MTFFZs, located at the southern European plate margin. These two prominent transform systems are the oceanic Azores-Gibraltar Fracture Zone, which includes the Gloria Fault and the SWIM Fault Zone, forming large parts of the in the central eastern Atlantic, and the submerged, continental NAF running through the Sea of Marmara and the northern Aegean Sea (**Figure 4**). Both systems have been thoroughly and interdisciplinarily investigated in the past and are target areas of ongoing research work. Below, the following sections provide a general description and generic characteristics of these areas, while subsequent sections will pick up on specific findings related to fluid geochemistry and life.

Azores-Gibraltar Fracture Zone (AGFZ)

The term AGFZ has been used for decades to designate the Africa-Eurasia plate boundary in the Atlantic Ocean. It extends for more than 1500 km from the eastern tip of the Azores plateau to the Strait of Gibraltar, accomodating a relative interplate displacement of ∼ 4.5 mm/yr (**Figures 4**, **5**; Bird, 2003; Neres et al., 2016). The lithospheric structure, geometry, kinematics and tectonics of this plate boundary are not simple. Instead, the AGFZ can be subdivided in two major segments: (i) the Gloria Fault and (ii) the Southwest Iberia Margin Fault Zone (SWIM FZ). The Gloria Fault is ∼800 km long and sub-divided in three near-linear segments connecting the Azores plateau to the Madeira-Tore Rise (**Figure 5**).

The Eastern and Western segments are sub-parallel to the movement of Africa with respect to Eurasia, at a small angle that generates transpression along a 50 km wide narrow belt of deformation. The Central segment is at a high angle to the motion of Africa with respect to Eurasia, creating a restraining bend of compressive deformation. The Gloria Fault West segment is characterized by a record of low seismic activity, which may be an expression fault locking or slow creeping. The Central and Eastern segments have a record of high to very high magnitude earthquakes, including the M8.4 event of 1941 and the M7.1 of 1931 (**Figure 5**). The 1941 event was, until the 2012 Sumatra earthquake in the Indo-Australian plate, the largest strike-slip event ever recorded. Interestingly, another very high magnitude event (M8.1) was recorded 200 km south of the plate boundary, probably reactivating an old fracture zone (Lay, 2019). This suggests that the deformation may be distributed over a wide zone rather than localized along a single fault trace.

Recent work on the western segment by Batista et al. (2017) showed the existence of a 4 km thick layer between 12 to 16 km below sea level suggesting the existence of hydrated mantle and implying seawater circulation along fractures to depths of 12 km below seafloor. Faults imaged in shallow reflection seismic profiles are compatible with a present day active transpressive flower-structure that is responsible for creating a linear positive ridge along the whole length of the Gloria fault.

To the East of the Madeira-Tore Rise (MTR) the Africa-Eurasia plate boundary has been described as diffuse on the basis that tectonic deformation is accommodated along several active structures within a 200 km wide (∼600 km long) zone of transpressive deformation between two main thrust systems (Sartori et al., 1994): the Gorringe Bank thrust that involves lithospheric mantle (Sallarès et al., 2013) and the Coral Patch Seamount thrust that involves oceanic crust (Martínez-Loriente et al., 2014). The main dextral strike-slip movement, caused by the oblique motion of Africa with respect to Eurasia, is materialized by the existence of a set of faults, the SWIM Faults, which seem to mark the present-day plate boundary between the MTR and the Strait of Gibraltar (Rosas et al., 2009; Zitellini et al., 2009). However, these faults do not show significant seismicity, which may suggest creeping, related with rheological weakening induced by fluid circulation and mantle hydration (Silva et al., 2017). The SWIM Faults control the location of mud volcanoes within and off the Gulf of Cadiz Accretionary Wedge. Fluid geochemistry of mud volcanoes in this area suggest that seawater circulation along the SWIM Faults reach the oceanic basement, ca. 5 km below seafloor (see section "Pore Fluid Geochemistry of Seafloor Seeps"; Hensen et al., 2015). The SWIM strike-slip faults propagate into crustal thrust faults and the intersections of these faults are also the loci of seismicity clusters (Silva et al., 2017). A recent study shows evidence for large-scale, tsunamigenic landslides in the Quaternary at the Hirondelle seamount (Hs), which is bound by splays of the SWIM Faults (Omira et al., 2016).

The SW Iberian Margin is characterized by shallow to deep earthquakes of low to moderate magnitude with a variety of focal mechanisms (Mw < 5.5; Buforn et al., 1991; Stich et al., 2003, 2007; Custódio et al., 2016). Notwithstanding, this region is also the source of the largest and most destructive earthquakes that have affected Western Europe (AD 1531, 1722, 1755, and 1969; Fukao, 1973). The 1755 Great Lisbon Earthquake (Mw > 8.5) destroyed Lisbon and was accompanied by tsunamis that devastated the SW Iberian and NW African coasts (Baptista et al., 1998; Baptista and Miranda, 2009). On the basis of geological evidence, geophysical data and tsunami modeling, different geodynamic models and mechanisms have been proposed for the source of the Lisbon Earthquake (cf. Gutscher, 2004; Gutscher et al., 2002, 2006; Gràcia et al., 2003; Zitellini et al., 2004, 2009; Stich et al., 2007; Terrinha et al., 2009). However, none of these models

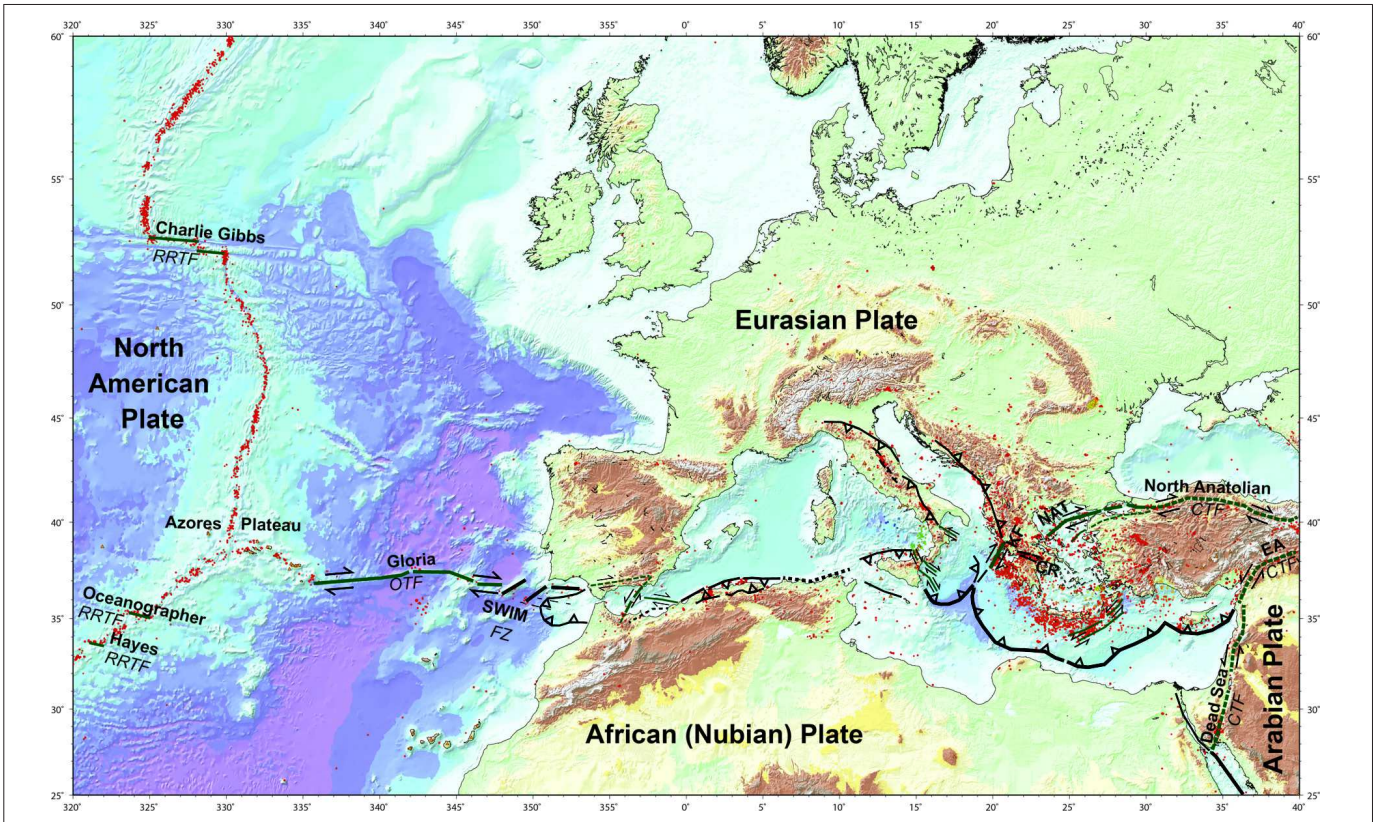

FIGURE 4 | Relief, seismicity (small red dots), plate boundaries and major active faults in the European – Mediterranean region, including the Azores and NE Atlantic. Sense of motion shown on major faults by arrows and symbols (thrust teeth, normal barbs). RRTF, Ridge Ridge Transform Fault; OTF, Oceanic Transform Fault (shown as solid green lines), CTF, Continental Transform Fault (shown as tightly dashed green lines). SWIM FZ – South West Iberian Margin Fault Zone, EA – East Anatolian, NAT – North Aegean Trough, CR – Corinth Rift, KF – Kephalonia Fault. Dashed black lines indicate uncertain/debated faults or plate boundary segments.

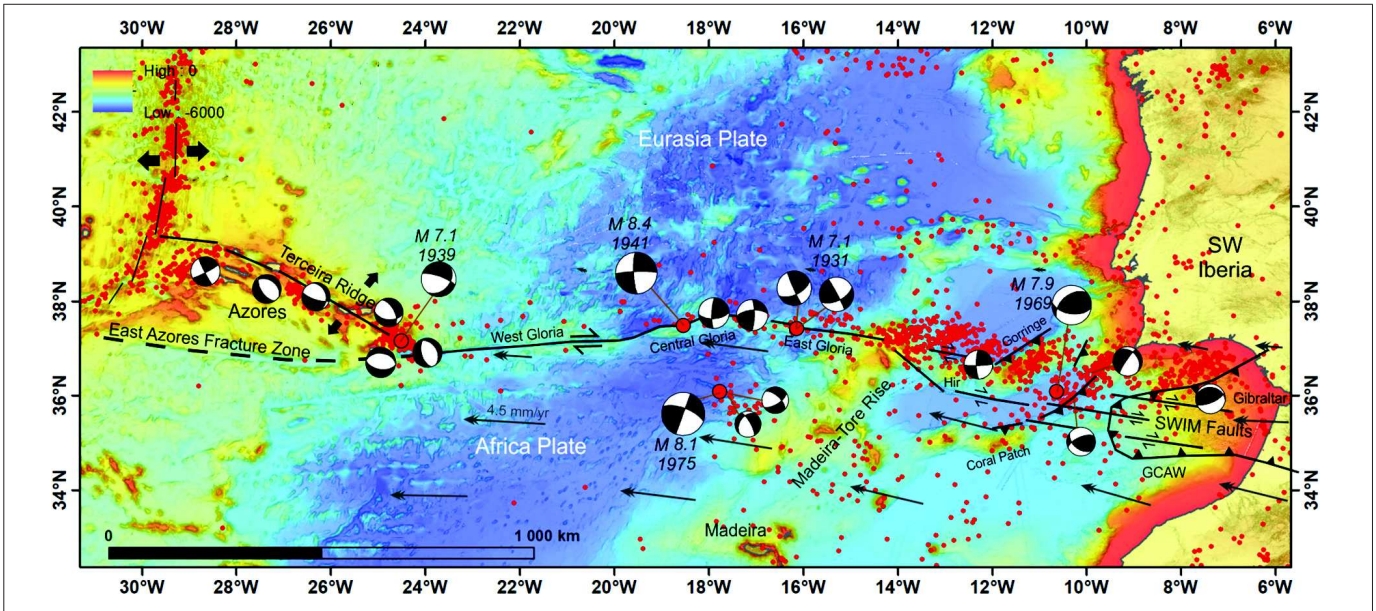

FIGURE 5 | Bathymetric map of the AGFZ region showing major structural units and seismic events. Hir, Hirondelle Seamount; GCAW, Gulf of Cadiz Accretionary Wedge; Red dots are epicenters of $M > 4$ earthquakes from the International Seismological Centre (ISC) for the period 1970–2017. Focal mechanisms from the database compiled by Custódio et al. (2016) ($M > 5.5$). Gray arrows represent vectors from the relative Africa-Eurasia velocity field as modeled by the neotectonic model of Neres et al. (2016).

satisfactorily accounts for the estimated magnitude of the earthquake and tsunami arrival times at the different localities onshore, which suggests interference of various processes from mantle to surface, such as multiple rupture across the lithosphere and crust and slip along inter-connected strike-slip and thrust faults (Rosas et al., 2009; Silva et al., 2017) and large scale landsliding in the epicentral area (Gràcia et al., 2003; Terrinha et al., 2003; Lo Iacono et al., 2012; Omira et al., 2016). The AD 1969 thrust earthquake (M 7.9) that occurred within the flat Horseshoe Abyssal Plain can be a recent reactivation of fracture zone-thrust fault interference (**Figure 5**; Rosas et al., 2016).

The North Anatolian Fault in the Sea of Marmara and the Aegean Sea

The NAF is a right lateral, strike-slip fault separating the Eurasian and the Anatolian Plates. The NAF extends over 1500 km, from the Eurasia-Anatolia-Arabia triple junction near Karliova (∼41°E) in eastern Turkey into the North Aegean Trough in the Aegean Sea and terminates in the 1600 m deep Sporadhes Basin at the eastern margin of the mainland of Greece (**Figure 6**; e.g., McKenzie, 1978; Armijo et al., 1999; Barka, 1999; Le Pichon et al., 2001, 2015; Şengör et al., 2014 Çağatay and Uçarkuş, 2019).

The North Aegean Trough has been very early associated with the westward prolongation of the NAF and considered to represent the northern boundary of the deforming Aegean region (McKenzie, 1978; Le Pichon and Angelier, 1979, 1981; Armijo et al., 1999). The main NAF zone consists of many segments running along the southern steep margin of the North Aegean Trough and give rise to transpressional ridges and transtensional basins between them (Sakellariou et al., 2018; Sakellariou and Tsampouraki-Kraounaki, 2019). GPS campaigns have confirmed the dextral shear along the NAF in the North Aegean Sea with strike-slip motion rates between 7 and 21 mm per year decreasing from east to west (Müller et al., 2013). Within the dominant NE-SW dextral shear regime, the Mw 6.4 Skyros 2001 earthquake related to strike-slip motion along the NAF in the North Aegean Trough (Ganas et al., 2005 and references therein). Moreover, the propagation of the NAF into the Northern Aegean Sea and the interaction with the Hellenic subduction in the Southern Aegean has strongly influenced the distribution of the volcanic centers (Armijo et al., 1999; Sakellariou and Tsampouraki-Kraounaki, 2019; **Figure 6**).

The submerged segment within the NAF is considered to be a natural laboratory for studying the coupling between fluid motion and fault slip (seismic and aseismic). In addition, the NAF is set along a former oceanic suture that holds ophiolitic bodies, which may influence both mechanical properties and fluid geochemistry (Tryon et al., 2010; Burnard et al., 2012). Since 1939, the NAF has produced a unique sequence of $M > 7$ earthquakes, starting from eastern Anatolia and propagating to the west toward Istanbul (e.g., Armijo et al., 1999; Parsons et al., 2000). Prior to this sequence, which ended in 1999 with the devastating earthquakes of Izmit and Düzce (causing more than 20,000 casualties at the eastern end of the Sea of Marmara) the fault ruptured in 1912. This earlier rupture developed in the west at the transition into the North Aegean, leaving the Marmara section of the NAF as the only part of the fault not having generated a major earthquake in the past 250 years. The Istanbul-Marmara region between the 1912 and 1999 ruptures is thus generally considered to represent a seismic gap with a potential for earthquake generation of up to M7.4 (Aochi and Ulrich, 2015 and references therein). As a consequence, the assessment of a seismic hazard for the densely populated (>15 million) greater Istanbul region is a matter of continuous investigation. Probabilistic interseismic models constrained by published GPS data sets, suggest that the Ganos and Çınarcık segments are locked, while creep is detected in the central portion of the Marine Marmara Fault (MMF; Ergintav et al., 2014; Klein et al., 2017). Submarine, acoustic-based geodetic data rather suggest locking along the Central segment (Sakic et al., 2016) and creeping along the Western High segment (Yamamoto et al., 2018). Thus, further geodetic studies are needed to provide a more complete picture.

Submarine paleoseismological techniques have been extensively applied at various key locations along the two submerged branches of the NAF in the Sea of Marmara. These reveal an average slip rate of 10 mm/year over the last ∼10 ka and long-term sedimentary records of earthquakes in the Sea of Marmara (e.g., Polonia et al., 2004; Sarı and Çağatay, 2006; McHugh et al., 2006, 2014; Gasperini et al., 2010, 2011; Drab et al., 2012; Çağatay et al., 2012). Slip rates are smaller than those determined by the GPS geodetic measurements, which are 18–20 mm/yr for the Northern branch (i.e., the MMF) and 5–7 mm/yr for the middle branch (McClusky et al., 2000; Meade et al., 2002). The discrepancy between the geological and geodetic slip rates could be explained by (i) changing rates of deformation over time, (ii) the deformation being accommodated by other faults in the region, (iii) or by the difficulties in modeling GPS data due to the water cover. Along with submarine paleoseismology, the correlation between the seismoturbidite records and the historical records over the last 2500 years reveals an average recurrence time of 250–300 years for the northern branch of the NAF (Sarı and Çağatay, 2006; McHugh et al., 2006, 2014; Beck et al., 2007; Drab et al., 2012; Çağatay et al., 2012), in agreement with the geodetic measurements (McClusky et al., 2000; Meade et al., 2002). The extensive seismological studies conducted over the last two decades have considerably improved our knowledge of the seismicity along the NAF. Since 2011, the identification of a precursory sequence of slow slip occurring at the base of the brittle crust, 44 min prior to the Mw 7.6 Izmit earthquake (Bouchon et al., 2011), has fostered the acquisition of new data in search of seismic tremors. The seismicity along the MMF is now well known to exhibit strong lateral variability (Schmittbuhl et al., 2016).

The Marmara Fault System is also characterized by an intense fluid activity at the seabed (Halbach et al., 2004; Armijo et al., 2005; Kuşçu et al., 2005; Géli et al., 2008; Zitter et al., 2008; Dupré et al., 2015) since it provides a major pathway for the seafloor expulsion of thermogenic hydrocarbons generated in Eocene-Oligocene Thrace Basin source rocks (Bourry et al., 2009; Ruffine

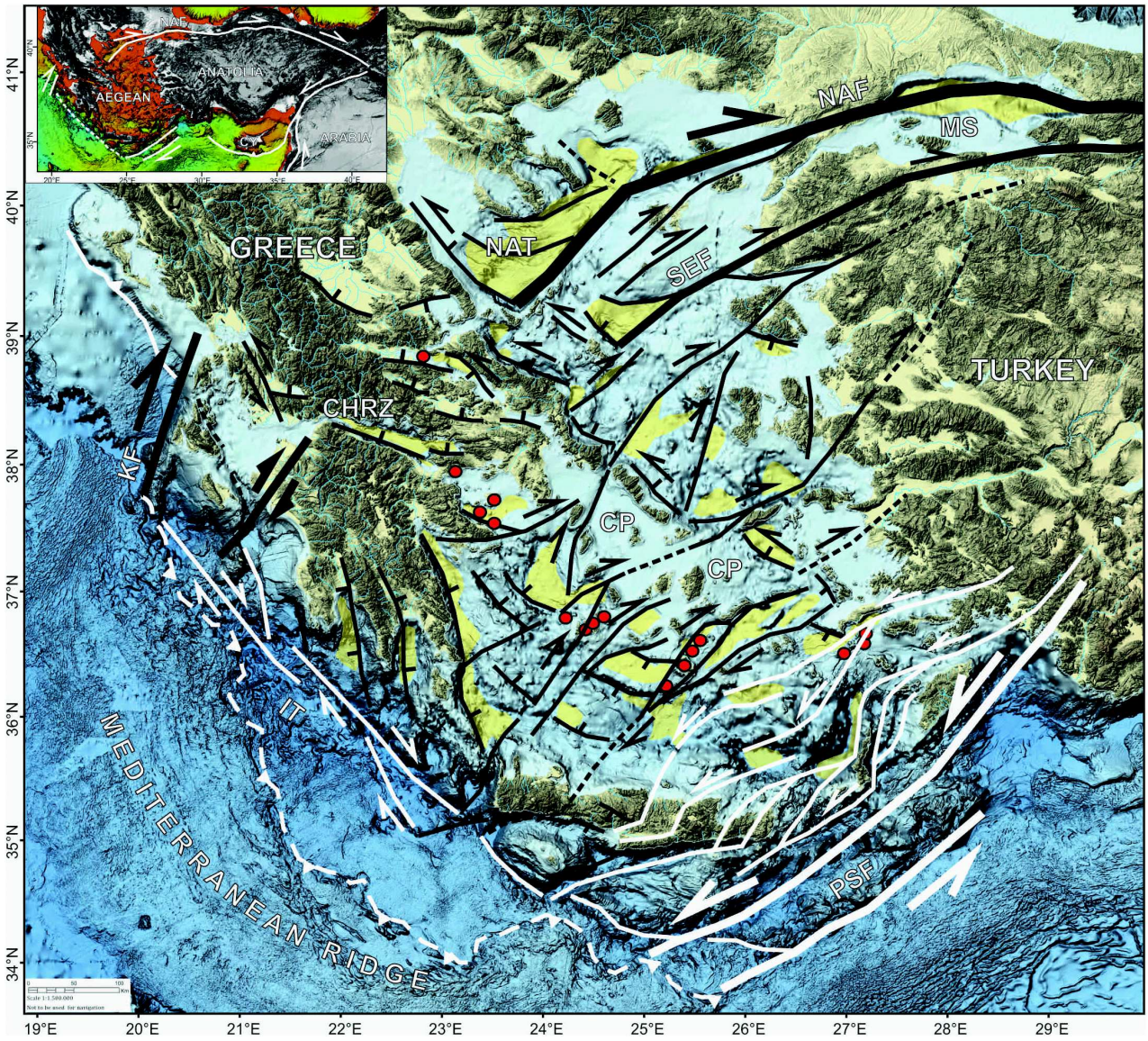

FIGURE 6 | Tectonic and kinematic map of the NAF and the Aegean region based on interpretations by Sakellariou and Tsampouraki-Kraounaki (2019). The NAF, the Skyros-Edremit Fault (SEF) and major dextral, NE-SW trending fault zones in the Aegean along with their conjugate faults are drawn in black. The Pliny and Strabo Fault zones (PSF) and the sinistral fault zones in the Southeast Aegean are drawn in white. Yellow: Plio-Quaternary basins. Red dots: volcanoes of the South Aegean Volcanic Arc. KF: Kephallinia Fault; CP: Cyclades Plateau; IT: Ionian Trench; MS: Marmara Sea.

et al., 2018a), possibly generating gas-induced seismicity (Batsi et al., 2018; Géli et al., 2018). These aspects will be discussed in more depth subsequently in Section "Pore Fluid Geochemistry of Seafloor Seeps" along with more detailed information of seep locations and fluid sources.

HEAT AND FLUID FLOW AT MARINE TRANSFORM FAULTS AND FRACTURE ZONES (MTFFZS)

Based on the structural and geodynamic framework provided above, this chapter compiles the current knowledge on heat and focused fluid flow at MTFFZs, depicting some of the most interesting regions, and highlighting important processes and mechanisms affecting fluid geochemistry, and how they stimulate and sustain chemosynthetic life in the deep sea.

Heat Flow

As the lithosphere created at mid-ocean ridges (MORs) cools and subsides during lateral seafloor spreading, heat flow from the lithosphere to the ocean decreases. Models of a conductively cooling lithosphere predict that heat flow decreases linearly with the inverse square root of age, and that at the same time the depth of the ocean basins (subsidence) increases linearly with square root of age [further details in Davis and Elderfield (2004);

Hasterok (2013); and references therein]. Heat flow at ridge flanks is highly variable but systematically lower than predicted by conductive cooling models. This heat deficit on ridge flanks is attributed to an incomplete or thin sediment cover, which allows a direct exchange of energy and mass between ocean and upper crust. Once the sediment cover is continuous and the hydraulic impedance of the sediment layer is above a critical threshold (about tens of meters), advective exchange between ocean and crust is significantly reduced (Spinelli et al., 2004). Consequently, at about a crustal age of about 65 ± 10 Ma, observed and predicted heat flow values are approximately equal, which indicates that crustal permeability is reduced below a level where advection of fluids is no longer possible (Manning and Ingebritsen, 1999). This crustal age is commonly referred to as "sealing age" (Stein and Stein, 1994). Heat flow on ocean crust >100 Ma is generally uniform (45–50 mW m^{-2}; Davis et al., 1984; Lister et al., 1990) suggesting that the thermal structure of the lithosphere has stabilized in terms of energy input at its base from the convecting asthenosphere.

Investigations on the well-sedimented ridge flank in the Cascadia Basin (NE Pacific) revealed that faults and seamounts may act as places where seawater recharges into or discharges from the upper crust (Fisher, 2005). Recharge sites are characterized by a wide and clear depression in heat flow around the site (cooling halo) whereas discharge sites show very localized heat flow values up to a magnitude higher than regional values. Fisher (2005) summarized this concept of off-axis hydrothermal circulation and termed it "hydrothermal siphon," a widespread phenomenon on Pacific crust (Hutnak et al., 2007; Kuhn et al., 2017; Villinger et al., 2017) as well as on Atlantic crust (Lucazeau et al., 2006; Le Gal et al., 2018). Moreover, a comparison of observed heat flow pattern and modeled heat flow based on known sediment thickness (depth to basement) reveals the pattern and strength of hydrothermal circulation in the upper crust. Therefore, seafloor heat flow measurements are a powerful, and currently the only tool to image hydrothermal circulation in the upper crust (Davis et al., 1997; Fisher and Harris, 2010; Le Gal et al., 2018).

Due to the structural weakness and permeability of transform faults and fracture zones, significant seafloor heat flow anomalies and possibly hydrothermal activity are to be expected. However, only very few detailed heat flow surveys across a fracture zone or a transform fault have been made up to now (von Herzen et al., 1970; Kolandaivelu et al., 2017). Published data from Khutorskoi and Polyak (2017) from the Vema fracture zone in the equatorial North Atlantic indicate remarkably uniform and high heat flow, with values between 100 and 250 mW m^{-2} (coinciding with similar results by Langseth and Hobart, 1976). Rather than focussing on MTFFZs, most of the offshore data from the Global Heat Flow Database (data from 1965 to 1985; **Figure 7**) were collected in order to characterize the marine heat flow pattern in conjunction with plate tectonics, and hence the cooling of the oceanic lithosphere. Only very few profiles were dedicated to fracture zones and transform faults. The latest compilation and interpretation of such data sets was recently published

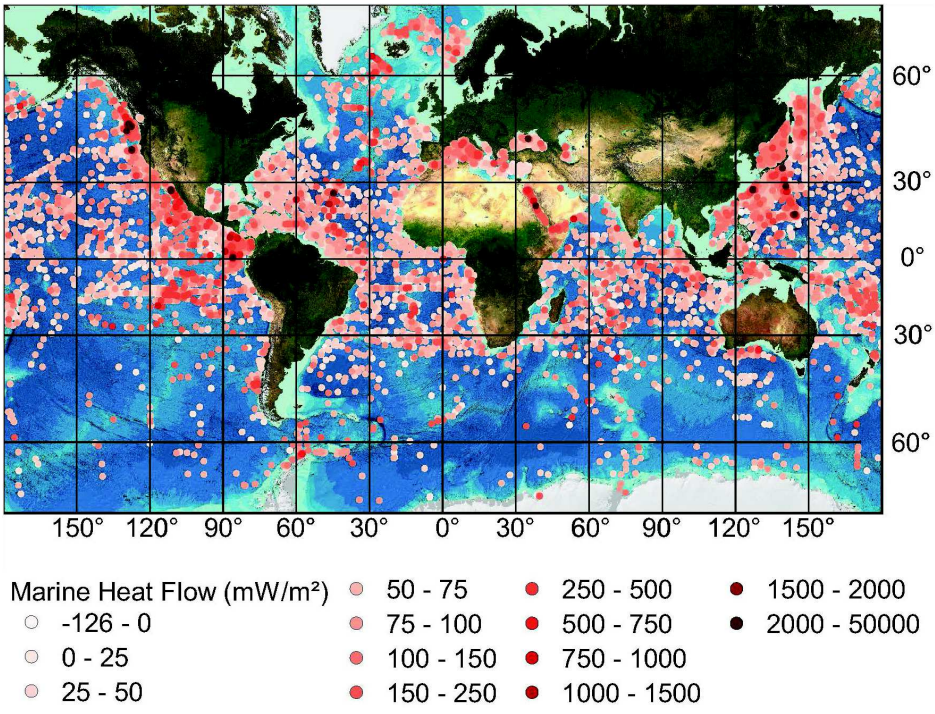

FIGURE 7 | Global distribution of heat flow measurements at water depths >500 m (Global Heat Flow Compilation Group, 2013; https://doi.pangaea.de/10.1594/PANGAEA.810104). Highest values are found at active spreading centers. To date, no systemic deviations along/across MTFFZs have been observed (background map is reproduced from the GEBCO world map 2014, www.gebco.net).

(Khutorskoi and Polyak, 2017), however, the original articles from which the data came from do not contain locations of these measurements.

Compared to direct heat flow measurements, more research has been done involving modeling of heat flow at MTFFZs. Numerous articles on numerical or analytical models on the thermal-mechanical structure and behavior of a transform fault were published in the last 30 years with Roland et al. (2010) being the latest one containing a rich bibliography of research done in this field. Their 3D numerical model incorporates viscoplastic rheology, shear heating, and hydrothermal circulation in the upper crust and predicts elevated heat flow across transform faults. The model of Roland et al. (2010) was applied to the Blanco Transform Fault (Northeast Pacific) and the results are constrained by maximum earthquake depth, which the authors associate with the 600°C isotherms. Gerya (2012) and Gerya (2013a,b) reviewed the modeling of ridge segmentation and hence the development of transform faults and fracture zones. The emphasis of their modeling attempts is, however, on the seafloor expression of the underlying processes and the comparison with the observed bathymetry.

Overall, the presented literature and database search revealed that heat flow investigations at transform faults and fracture zones are a neglected research field. Yet, none of the published numerical models calculate seafloor heat flow, which would be, apart from the maximum depth of earthquakes, another helpful constraint for the models.

Pore Fluid Geochemistry of Seafloor Seeps

Fluid discharge at the seafloor is known from hot vents at mid-ocean ridges (e.g., Elderfield and Schultz, 1996; Von Damm, 2013; German and Seyfried, 2014), cold seeps and mud volcanoes at continental margins (e.g., Suess, 2014; Mazzini and Etiope, 2017), serpentinite-hosted fluid systems (e.g., Mottl et al., 2004; Okumura et al., 2016), as well as low-temperature discharge at seamounts (Wheat and Mottl, 2000; Wheat and Fisher, 2008). This distribution is well documented by numerous publications and illustrated in **Figure 2**, while reported findings from transform plate boundaries remain sparse (e.g., Martin et al., 1997). Hydrothermal circulation has been recognized as an important factor in global geochemical cycles and exchange processes between the lithosphere and the hydrosphere (e.g., Elderfield and Schultz, 1996; Davis and Elderfield, 2004). Flow rates at cold seeps are much lower and geochemical deviations from seawater, typically depending on the geological setting, source depth, etc., are mostly less pronounced when compared to hot vents. Whereas hydrothermal activity at spreading axes and ridge flanks has been relatively well investigated (e.g., Von Damm, 1990; Elderfield et al., 1999; Humphris and Klein, 2018; Le Gal et al., 2018), almost nothing is known about crust-seawater exchange on old oceanic crust.

As detailed above, heat flow data imply a general decline of hydrothermal circulation at crustal ages of >60 Ma due to cooling, cementation of pore space, and sealing by increasing sediment coverage. Due to this paradigm the vast area between spreading axes and the continents has largely remained unexplored with regard to fluid exchange and fluid seepage. Research over the past 15 years has, however, shown that hydrothermal circulation can even occur in oceanic crust that is older than 60 Ma (Von Herzen, 2004; Fisher and Von Herzen, 2005). Yet, a hydrological connection that results in significant exchange of energy between the permeable upper crust and the seafloor may only develop under specific conditions where seamounts or active faults provide suitable pathways through otherwise impermeable sediment layers.

In addition to seamounts, favorable structural settings for such fluid exchange between the crustal lithosphere and hydrosphere include transform faults and fracture zones. Currently, most examples are from active transform fault settings in young oceanic crust. Examples range from low-temperature hydrothermal systems with barite chimneys and associated mineralizations (Blanco Fracture Zone; Hein et al., 1999), or cold seeps with vigorous methane flow from the subsurface (Mendocino Transform Fault: Stakes et al., 2002; Guaymas Basin: Paull et al., 2007). In the Atlantic, shallow fluid circulation through ultramafic oceanic crust at the Lost City Hydrothermal Field (Atlantis Massif: Kelley et al., 2001, 2005) causes active serpentinization and thus an energy source for chemosymbiotic fauna (see section "Chemosynthesis-Based Ecosystems"). Indications for chemoautotrophic life have also been reported for the active Vema transform fault (Cannat et al., 1991; Krylova et al., 2010). Recently, this evidence was confirmed by pore water anomalies along an E-W transect, indicating the advection of methane-rich fluids in this area (**Figure 8**; Devey et al., 2018).

Some recent evidence for fluid flow through older crust and discharge related to MTFFZs comes from deep-sea mud volcanoes in the Gulf of Cadiz (Eastern AGFZ; **Figure 6**). During RV Meteor cruise M86/5 in 2012, previously unknown mud volcanoes were discovered at great water depth of about 4500 m in a geo-tectonically atypical area, located roughly 90 km west of the deformation front of the accretionary wedge of the Gulf of Cadiz (**Figure 9**). Seismic data suggest that fluid flow is mediated by a >400-km-long strike-slip fault system proposed to represent a nascent plate boundary between Africa and Eurasia,

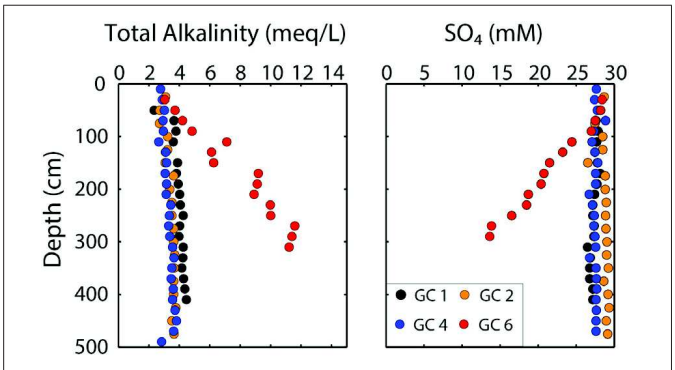

FIGURE 8 | Pore water profiles of total alkalinity [from Devey et al. (2018)] and SO_4 along an E-W transect on the Vema TFFZ (for locations see **Figure 9**).

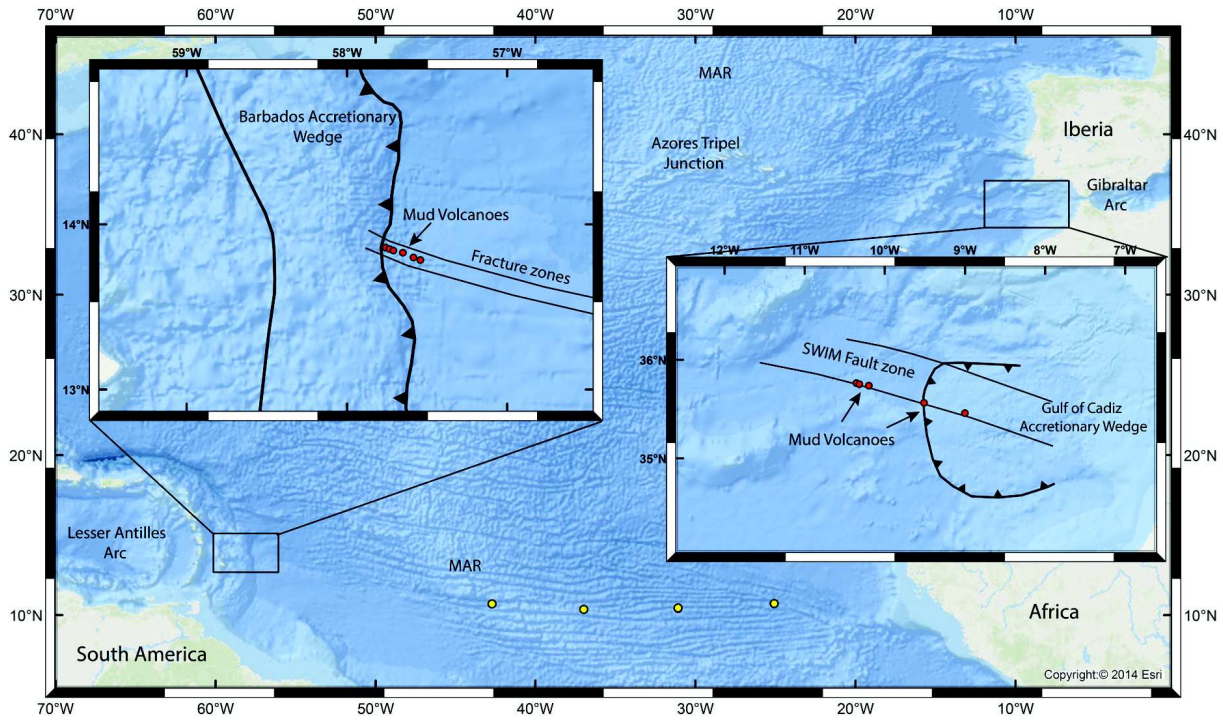

FIGURE 9 | Mud volcanoes related to active strike-slip faulting in the western Gulf of Cadiz and aligned along the Mercurus Fracture zone offshore Barbados [adapted from Godón et al. (2004); Hensen et al. (2015)]. Yellow dots along the Vema TFFZ indicate the location of gravity cores shown in **Figure 8** (bathymetric map was created using ArcGIS® software by Esri (www.esri.com).

reactivating old (Jurassic) oceanic fracture zones (Zitellini et al., 2009). In addition, geochemical data of pore fluids sampled at the mud volcanoes reveal that those fluids carry diagenetic signals from the oldest stratigraphic units and have at least partially interacted with the oceanic basement, hence, implying the existence of a hydrological connection from the seafloor to the oceanic crust (Scholz et al., 2009, 2010; Hensen et al., 2015; Schmidt et al., 2018; Nuzzo et al., 2019). The exact mechanism causing fluid migration is not known yet, but the recent findings (Hensen et al., 2015; Schmidt et al., 2018) indicate active fluid percolation through old (>140 Ma) oceanic crust, potentially induced by nearby crustal highs and adding further evidence to the notion that fluid circulation can continue at a crustal age of >65 Ma.

Mud volcanoes expelling geochemically distinct fluids off the Barbados accretionary wedge (Dia et al., 1995; Godón et al., 2004) are found in a tectonic setting comparable to that in the Gulf of Cadiz. The mud volcanoes are aligned along the Mercurus fracture zone, which is running westward into the accretionary wedge of the subduction zone (**Figure 9**). By now, fluid mobilization and geochemical signals have been ascribed to subduction-related dewatering processes and associated mineral-water interactions. However, Sumner and Westbrook (2001) hypothesized that the mud volcanism along the Mercurus fracture zone was initiated by changes in plate motion along this fracture. Thus, processes similar to those in the Gulf of Cadiz might drive or at least contribute to the emergence of mud volcanoes off the Barbados accretionary wedge.

The fluid geochemistry of the mud volcanoes in Gulf of Cadiz and off Barbados is illustrated in **Figure 10**. Due to their location near continental margins, fluid geochemistry in both systems is dominated by sediment-water reactions (such as clay-mineral dehydration), illustrated by pronounced B-enrichment and Cl-depletion (e.g., Hensen et al., 2004). Similar B-enrichments are known from sediment-hosted hydrothermal systems, such as the Guaymas Basin. Here the dilution component is lacking, because B is extracted from sediments by percolation of saline, and thus Cl-rich, hydrothermal water. In non-sedimented systems the concentration of B is typically close to seawater or even depleted due to serpentinization. The lithospheric imprint becomes obvious by low (non-radiogenic) $^{87}Sr/^{86}Sr$ ratios and is most pronounced in hot hydrothermal systems. In the Gulf of Cadiz, the $^{87}Sr/^{86}Sr$ values are a combined signal from ancient (Mesozoic) carbonates and oceanic crust. For Barbados, there are no specific investigations available, but the interpretation of the $^{87}Sr/^{86}Sr$ is further complicated by widespread abundance of volcanogenic sediments.

Intense fluid emissions at the seafloor have also been detected in the continental margin setting along the NAF in the Sea of Marmara. In the shallow domain, within the Izmit Bay, the intimate link between fluid (gas) release and earthquake has been evidenced from seafloor inspections after the 1999 Izmit earthquake where sediment fluidization and cracks have been observed at locations above gas-charged sediments (Kuşçu et al., 2005; Gasperini et al., 2012). However, direct evidence for the coupling of seismicity and fluid flow remains difficult

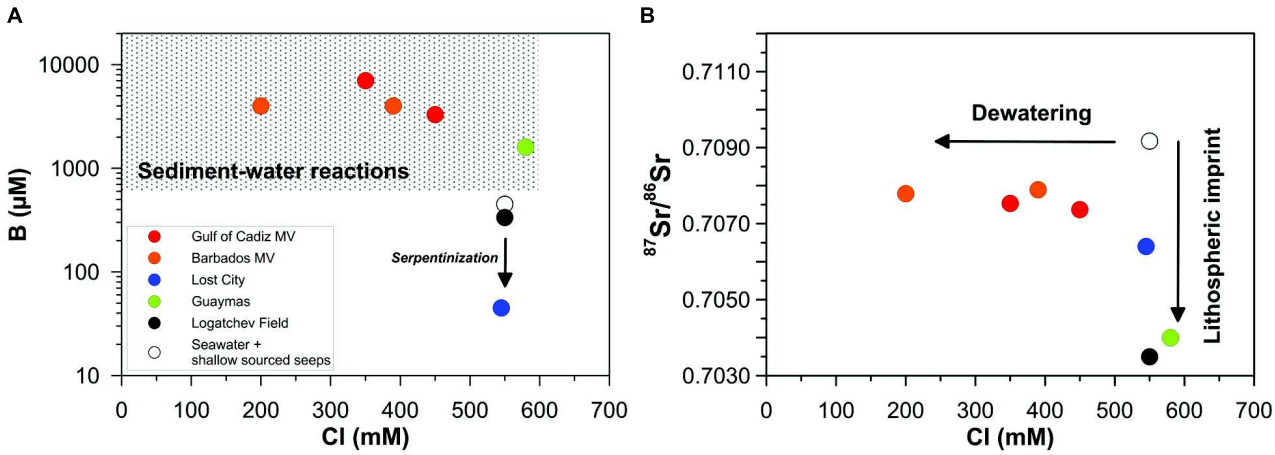

FIGURE 10 | Cross plots of B vs. Cl **(A)** and $^{87}Sr/^{86}Sr$ vs. Cl **(B)** of fluid endmembers from mud volcanoes in the Gulf of Cadiz and off Barbados compared to endmembers from different hydrothermal systems; Lost City, off-axis, serpentinization; Logatchev Field, ridge-crest, high temperature; Guaymas, sediment hosted, high temperature. Data from: Von Damm et al. (1985), Palmer (1991), Godón et al. (2004), Schmidt et al. (2007), Foustoukos et al. (2008), Scholz et al. (2009), Hensen et al. (2015) and Seyfried et al. (2015).

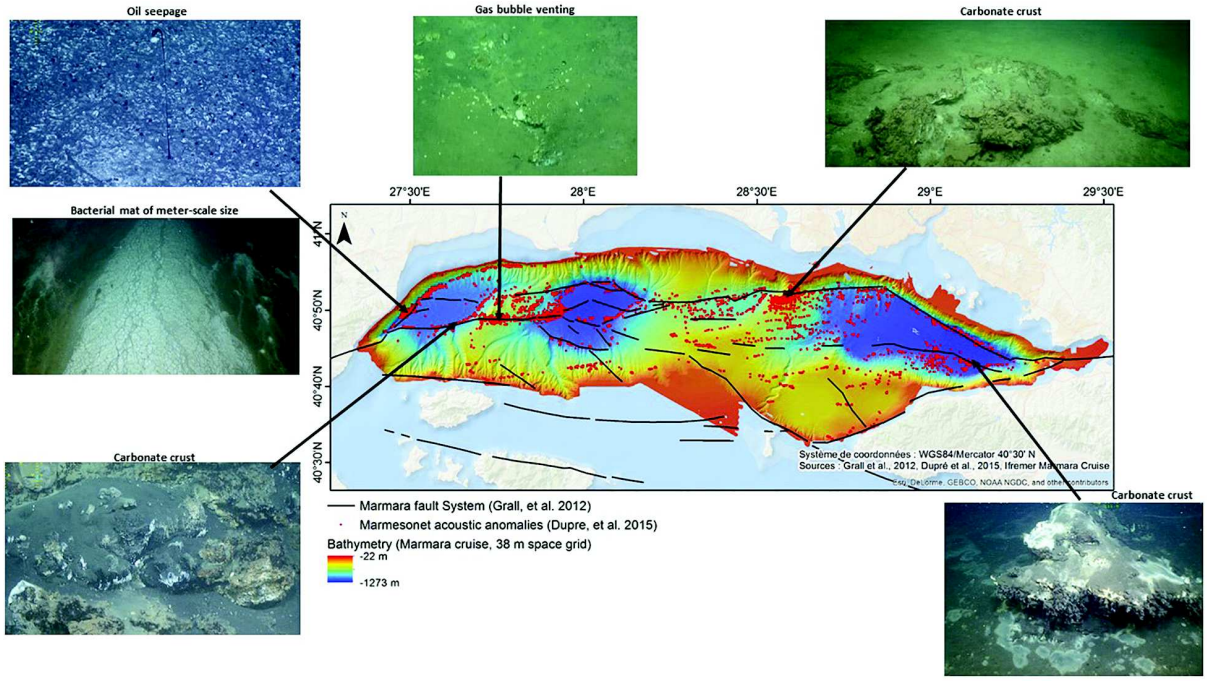

FIGURE 11 | Bathymetric map of the Sea of Marmara highlighting the link between structural features and gas emissions [data from Grall et al. (2012, 2018a), Ruffine and Geli (2014), Dupré et al. (2018)]. A large variety of carbonate crusts and seeps (oil and gas) are widespread along the fault network. Fluid discharge sustains the development of bacterial mats at the seafloor.

to prove (Embriaco et al., 2014; findings and state of research of this aspect are further explored in section "Fluid Flow and Chemical Indicators Related to Seismic Activity"). In the deeper parts of the Sea of Marmara, the nature and sources of fluids and gases were investigated during a number of cruises within the past two decades, specifically dedicated to a deeper understanding of how geodynamic processes along the NAF may control fluid flow in the subsurface (e.g., Géli et al., 2008; Bourry et al., 2009; Dupré et al., 2010, 2015; Grall et al., 2018a,b; Ruffine et al., 2018a,b; **Figure 11**). Emitted hydrocarbon gases indicate that deeper thermogenic sources are tapped in the western basin while microbial gases prevail in the eastern basin. In the western basin, there is also evidence for mantle-derived helium (Burnard et al., 2012; Ruffine et al., 2018a) and pore water data shown by Tryon et al. (2010) allow speculations about ongoing serpentinization in the deeper

subsurface. Aseismic slip in the western Sea of Marmara may effectively maintain high permeability conduits in the NAF zone. In contrast, the long-term seismic quiescence (since 1766) and recent low seismicity along the Istanbul segment suggest that this segment is currently locked, providing a primary factor for the relative scarce gas emissions. Because hydrocarbon occurrence is a widespread phenomenon at ocean margins, the relation between gas emissions, seismicity and crustal creeping opens new perspectives for improving our understanding of fault behavior and geohazard assessment in gas-prone, submarine environments.

Reports of mud volcanoes in deep-sea settings related to MTFFZs are still quite rare, but existing findings encourage further exploration. Evidence for methane-rich fluid venting has been reported e.g., from the eastern part of the Mendocino fracture zone in the Northeast Pacific (Stakes et al., 2002). Globally, transform-type plate boundaries are of similar length as convergent plate boundaries (∼50,000 km; Bird, 2003), which are known for intense seepage activity. Recently, Coogan and Gillis (2018) provided evidence that fluid fluxes at off-axis hydrothermal systems are likely important factors modulating ocean chemistry, but additional studies are indispensable to substantiate current estimates. Taking also into account the vast stretches of fracture zones, MTFFZ might bear a considerable potential for fluid discharge at the seafloor. However, based on the available data, we can only speculate about the role of MTFFZs as pathways for fluid exchange between the lithosphere and the deep ocean. Hence, systematic efforts are required to estimate the potential impact on geochemical cycles and life in the abyssal ocean.

Chemosynthesis-Based Ecosystems

The global impact of transform faults and fracture zones on life is still poorly understood. Several studies have shown that transform faults act as barriers to seafloor invertebrate dispersal (Johnson et al., 2006), including the dispersal of larvae of hydrothermal vent macrofauna (Young et al., 2008). This is because transform faults act as topographic breaks to the ridge axes formed during seafloor spreading, and as such interfere with the predominant along-axis water flow in spreading centers. The resulting cross-axis water flow through the transform fault and fracture zone can obstruct genetic exchange between adjacent sides of the ridge axis, and thus promote genetic drift and speciation, both among typical deep sea macrobenthos and highly specialized chemosymbiotic hydrothermal vent macrofauna (O'Mullan et al., 2001; Hurtado et al., 2004).

In locations where lithosphere-derived fluids are actively transported to the seafloor, transform faults are furthermore hotspots of life. First evidence for the support of chemosynthetic, biological communities by abiotically produced chemical compounds at transform faults came from the Lost City Hydrothermal Field. Fluids advecting out of the seafloor in this location are characterized by high pH (9–11), moderately warm temperatures within the temperature limits of life (40–90°C), and high concentrations of H_2 (Kelley et al., 2001, 2005) produced by subseafloor serpentinization (Früh-Green et al., 2003). High concentrations of dissolved hydrocarbons, in particular methane, and organic acids, in particular formate, are also present in these fluids (Kelley et al., 2001, 2005; Lang et al., 2018), and have been explained with Fischer-Tropsch-Type or Sabatier-Type synthesis reactions involving serpentinization-derived H_2 and mantle-derived inorganic carbon that is released by the weathering of host rocks (McCollom and Seewald, 2007; Prokurowski et al., 2008; Bradley and Summons, 2010). Analyses of methane isotopologues have suggested methane in aqueous fluids of the Lost City Hydrothermal Field to be formed under equilibrium temperature conditions around 310°C (Wang et al., 2018). In contrast, methane-carbon isotope analyses from lower temperature onshore serpentinizing environments such as found in Costa Rica and Turkey revealed that methane may be also partially formed biologically (Crespo-Medina et al., 2017; Zwicker et al., 2018). Evidence is based on carbon isotope fractionation being severely reduced under high partial pressure of H_2 and its availability (Penning et al., 2005; Londry et al., 2008), thus eventually mimicking abiotic or thermogenic methane formation. Furthermore, under conditions similar to those found in the subsurface of the Lost City Hydrothermal Field, abiotic amino acid synthesis is thermodynamically favorable (Shock, 1990; Schulte and Shock, 1995). Aliphatic amino acids could be synthesized through Strecker-type reactions involving cyanide (HCN) and aldehydes or ketones (Holm and Neubeck, 2009; Konn et al., 2015), while aromatic amino acids could be abiotically produced via Friedel-Crafts reactions involving aromatic hydrocarbons as reactants and iron-rich saponite clays as catalysts (Ménez et al., 2018). Both types of abiotic amino acid synthesis reactions may help sustain chemoorganotrophic life at and below the seafloor of the Lost City Hydrothermal Field and in other ultramafic systems.

The mixing of deeply sourced fluids that are rich in electron donors, such as H_2, methane, and organic acids, with bottom seawater containing high concentrations of the electron acceptors O_2 and sulfate sustains a high biomass of aerobic and anaerobic H_2-, methane-, and sulfur-metabolizing microbial communities in seafloor carbonate chimneys of the Lost City Hydrothermal Field (Kelley et al., 2005; Brazelton et al., 2006, 2012). Archaeal communities are dominated by H_2-consuming methanogens and Anaerobic Methane-oxidizing archaea (ANMEs). Stable carbon isotope compositions of diagnostic archaeal lipid biomarkers imply extraordinary isotopic fractionations during carbon fixation in this environment (Bradley et al., 2009; Méhay et al., 2013). Sulfate-reducing bacteria also play an important role, possibly being the main consumers of abiotically produced formate (Lang et al., 2018). Macrofauna that are characteristic of high-temperature, "black smoker-type" hydrothermal vent environments (e.g., large tubeworms, Pompeii worms, mussels) are absent; instead a high biomass of sponges and corals is present (Kelley et al., 2001).

In addition to the Lost City Hydrothermal Field, several other locations within MTFFZs have been discovered, in which deeply sourced fluids are supporting abundant life at the seafloor. On the Gorda Escarpment in the Mendocino Fracture Zone off northern California, thriving chemosynthetic microbial and macrofaunal communities occur in areas where low-temperature methane-rich fluids are venting at exposed basement rock

(Stakes et al., 2002). Macrofaunal communities are dominated by siboglinid tube worms (*Lamellibrachia barhami*) and vesicomyid clams. Both types of macrofauna are also found in cold seep environments along continental margins and forearcs, and are known to harbor aerobic sulfide-oxidizing bacteria as endosymbionts (Stakes et al., 2002; Levin, 2005; Dubilier et al., 2008; Ohara et al., 2012; Onishi et al., 2018). Along the Sonora Margin Transform Fault of the Guaymas Basin, there are cold seeps where dissolved inorganic carbon and methane of thermogenic origin are transported to the seafloor (Paull et al., 2007). Here, areas at the base of carbonate formations also have a high biomass of chemosymbiotic vestimentiferan tube worms and vesicomyid clams, whereas authigenic carbonates in places with fluid seepage are covered by sulfide-oxidizing microbial mats (*Beggiatoa* spp.) and harbor abundant populations of gastropods (Paull et al., 2007). Nearby sediments are also covered by *Beggiatoa*, which here coexist with a high diversity and abundance of ANMEs (Vigneron et al., 2013). Within cold seeps of the Sea of Marmara, high abundances of macro- and meiofauna, including symbiont-bearing bivalves (*Vesicomyidae, Lucinidae, Mytilidae*), are present at carbonate crusts and within soft sediments (Ritt et al., 2010). Methane seepage supports a high biomass of ANMEs (ANME-2a and -2c) and symbiotic sulfate-reducing Deltaproteobacteria (*Desulfosarcina, -coccus, and -bulbus*) in shallow subsurface sediments (Chevalier et al., 2011, 2013). High abundances of macrofauna (*Siboglinidae*) and high rates of anaerobic oxidation of methane coupled to sulfate reduction have furthermore been found in mud volcanoes of the Gulf of Cadiz (Niemann et al., 2006; Sommer et al., 2009). Yet, despite their locations in MTFFZs, most of the methane transported to the seafloor in both the Mendocino Fracture Zone and the Sonora Margin Transform Fault is likely of biogenic or thermogenic sedimentary rather than abiotic crustal origin.

The limited number of published studies already shows clearly that transport of deeply sourced fluids containing high concentrations of microbial energy substrates to the seafloor in MTFFZs can locally sustain a high diversity and biomass of microbial and macrofaunal life. Yet, the importance of serpentinization and other deep rock-fluid reactions as a source of these energy substrates in MTFFZs remains elusive, and more exploratory research on MTFFZs, including fracture zones that are located far off-axis relative to oceanic spreading centers, is needed. An additional important research aim will be to investigate the distribution of life below the seafloor in MTFFZs. Published studies indicate that microbial methane production and sulfate reduction – possibly supported by serpentinization – can occur at moderate temperatures (65° C) in olivine-rich, young (3.5 Ma) subseafloor basalt on the Juan de Fuca ridge flank (Lever et al., 2013). Similarly, active methane- and acetate-producing microbial communities have been linked to the turnover of H_2 produced by serpentinization in deep subseafloor sediments of the Kumano mud volcano in the Nankai accretionary complex (Ijiri et al., 2018). Yet, currently nothing is known about the presence or activities of microbial communities in the subsurface of MTFFZs. In some places, these subsurface microorganisms could be an important but unknown sink for abiotically produced H_2, methane, and organic acids, and consume these compounds before they reach the seafloor. As in other subseafloor environments (Hoehler and Jørgensen, 2013; Lever et al., 2015; LaRowe et al., 2017), the distribution of life in subseafloor environments within MTFFZs is most likely limited by the balance of catabolic energy obtained from the transformation of chemical compounds and the energetic cost of survival; the latter is largely driven by temperature-controlled rates of biomolecule damage, and other factors, e.g., pH and salinity, which affect the energetic cost of maintaining cellular homeostasis (Head et al., 2003; Harrison et al., 2013; Lever et al., 2015). Future investigations will reveal how the combination of locally high energy inputs, e.g., in areas of active fluid flow, affects the ability of microorganisms to cope with subsurface stressors, such as elevated temperature, highly alkaline pH, fluid compositions very different from those within cells, and whether a yet undiscovered, uniquely adapted, or globally important deep biosphere exists below the seafloor in MTFFZs.

COUPLING OF SEISMICITY AND FLUID FLOW

In the previous sections, we provided an overview on the current knowledge of fluid flow related processes at MTFFZs. Although, promising findings have been made, it is also obvious that large knowledge gaps exist, which need to be filled. This section provides an overview on the general relationship between seismic activity, faulting, fluid flow, and geochemical activity beyond the evidence from MTFFZs, also exploring the potential use of geochemical signals as precursors for seismic activity.

Fluid Flow and Chemical Indicators Related to Seismic Activity

The release of seismic energy and the associated static stress variations imposed by large magnitude earthquakes may cause abrupt changes in the near- and far-field of the fault. Hydrothermal systems, mud volcanoes, and magmatic volcanoes are geological environments particularly sensitive to dynamic and static stress variations because of their near-critical state at depth. Pore pressure deviating from hydrostatic conditions is a key condition to determine whether incoming seismic energy and long-term variations of the local stress field may promote a response. Triggered activity occurs over a range of timescales and distances spanning from seconds to decades and from the near- to the far-field (Hill et al., 2002; Delle Donne et al., 2010; Mazzini and Etiope, 2017; Miller and Mazzini, 2018).

The effect of earthquakes on pore pressures may cause processes such as rectified diffusion, gas exsolution, and/or unclogging of migration pathways (Hill et al., 1995; Manga and Brodsky, 2006). Reported phenomena are changes in groundwater flow rates (e.g., Tsunogai and Wakita, 1995; Brodsky, 2003), temperature fluctuations at mid ocean ridges (Johnson et al., 2000), water level changes in deep wells (Roeloffs et al., 2003), or variations in geyser periodicity (Husen et al., 2004). Examples of fault reactivation have been reported, among others, on Iceland after the Mw 6.6 2000 earthquake (Pagli, 2003), in Indonesia after the Mw 6.3 Yogyakarta earthquake

(Mazzini et al., 2009), and in Costa Rica after the Mw 7.6 Nicoya earthquake (Lupi et al., 2014). In the Costa Rican forearc, the occurrence of seismic swarms in the subducting plate has been related to upward fluid flow eventually feeding seafloor seepage structures (Thorwart et al., 2014). Triggered fault slips are frequently connected to elevated fluid pressures at depth that induce rapid fluid flow along the fault plane (Miller et al., 2004; Lupi et al., 2011a) and may result in phenomena like flash vaporization of interstitial fluids (Weatherley and Henley, 2013).

In this context, seismically active areas have been studied in the past decades with the goal of associating gas anomalies to the occurrence of seismic events, e.g., earthquakes have been related to the release of seafloor hydrocarbons (Mau et al., 2007; Tsunogai et al., 2012; Fischer et al., 2013; Geersen et al., 2016). The most commonly investigated concentrations of elements were radon, helium, hydrogen, mercury, carbon dioxide, and several other volatiles (King, 1986). Geochemical anomalies preceding seismic activity, e.g., at fault junctions or above fractured reservoirs, may last from a few hours to several days (Claesson et al., 2007; Walia et al., 2009; Skelton et al., 2014). For instance, co-seismic geochemical variations in springs and gaseous vents were recorded during the 1997 seismic crisis in Italy (Miller et al., 2004). In Taiwan, Yang et al. (2006) identified significant variations in CO_2 and CH_4 emissions from mud pools along regional fracture zones so that monitoring of CO_2 and CH_4 seems to represent a potentially valuable tool for detecting intimate relationships between seismic activity and fluids. Helium (Sano et al., 1986, 2014), argon (Mamyrin and Tolstikhin, 1984) and radon concentrations (Fu et al., 2008; Attanasio and Maravalle, 2016) have been used in continental settings to analyze the response of terrestrial fluid emanation with respect to seismic activity. It is important to note in this context that the relationship between gas emissions and earthquakes seems to rely mostly on the gas flux variability (Kita et al., 1982; Field and Jennings, 1987; Hirose et al., 2011). Sano et al. (2014) reported ^{3}He anomalies in relation to the catastrophic 2011 Tohoku-Oki earthquake (M9.0) suggesting the emission of mantle fluids along the subduction zone offshore Japan. Enrichment in ^{3}He was also measured in gases from hot springs after the 1984 Nagano earthquake (M6.8; Sano et al., 1986) and related to deep-seated fluids being forced upward by earthquake-induced tectonic stress. However, the opposite pattern (^{4}He enrichment, resulting in lower ^{3}He/^{4}He ratios) was observed after the 1995 Kobe earthquake (M7.2) and attributed to the generation of micro-fractures releasing radiogenic ^{4}He from the rock matrix. Hence, the interpretation of volatile anomalies in relation to seismic events depends strongly on the geological setting and the available geochemical information. For instance, terrigeneous fluids in sediments of Lake Van (Turkey) located at the eastward extension of the NAF showed crustal He enrichments prior to the occurrence of the devastating M7.2 earthquake in 2011 (Tomonaga et al., 2011, 2012, 2014). Recently, Sano et al. (2016) could relate radiogenic ^{4}He anomalies to the strain change in an active strike-slip fault system produced by the 2016 Kumamoto earthquake (M7.3), emphazising the potential use of such monitoring approach in other geological settings.

Mud volcanoes seem to be geological phenomena particularly sensitive to external forcing. The onset of mud volcanism is in fact often related to seismic activity, with many examples of earthquakes affecting or triggering onshore and offshore mud volcanoes (e.g., Kopf and Deyhle, 2002; Brodsky, 2003; Husen et al., 2004; Hieke, 2004; Manga and Brodsky, 2006; Mellors et al., 2007; Manga et al., 2009; Lupi et al., 2013; Miller and Mazzini, 2018). Bonini (2009) pointed out that the Nirano mud volcanic field in Italy showed a remarkable increase of fluid emission after the 15th of May 1873 earthquake that occurred at the Pede-Apennines margin, near Reggio-Emilia. Lupi et al. (2015) showed precursory seismic signals in the same region occurring before the 2013 Lunigiana earthquake. Mazzini and Etiope (2017) report on several recent onshore and offshore mud volcanic eruptions related to seismic activity. Specifically, the spectacular Lusi eruption (NE Java), following the 2006 M6.3 Yogyakarta strike-slip earthquake, represents one of the most recent events of a newborn, sediment-hosted hydrothermal system (Mazzini et al., 2012) triggered by a remote earthquake (Miller and Mazzini, 2018).

Among the most spectacular, the newly formed mud island offshore of Gwadar (Pakistan) erupting few hours after the September 2013 M7.7 earthquake occurring 410 km far from the coast. Dynamic triggering was also observed in a mud volcano in the Marmara Sea after the May 24, 2014, Mw 6.9 strike-slip earthquake that occurred in the northern Aegean Sea, about 250 km away (Lupi et al., 2018).

In addition to observations from fluid seepage sites, numerical modeling provides a powerful tool to identify links between fluid migration, active faults and earthquakes. Interconnected high permeability zones (e.g., fractures) may efficiently transfer pore fluids from deep sources toward the seafloor. For accurate simulations of the fluid system in response to pressure pulses, it is important to use realistic physical parametrization (e.g., permeability, capillary entry pressure) and mass transport mechanisms, like Darcy flow in porous media or Stokes flow in fractured media. Recently, basin-scale, numerical models of this type have been used to constrain fluid sources of mud volcanoes in the Gulf of Cadiz (Schmidt et al., 2018). Enhancing this type of model will result in the performance of realistic simulations on how deep fluid signals are transferred to the seafloor and an assessment of the response time between seismic events and fluid pulses prior and after the seismic events. Sophisticated modeling approaches including the three-dimensional representation of fault planes (e.g., Burwicz et al., 2017) already provide realistic predictions of fluid migration in natural geological settings in tectonically active regions.

Archives of Seafloor Fluid Discharge

At mud volcanoes or, more generally, cold seeps, authigenic carbonate crusts and chimneys are often precipitated due to the anaerobic oxidation of methane, the latter mediated by the presence of microbial communities such as sulfate-reducing bacteria and methanotrophic archea, leading to sequestration of methane-derived carbon (Chevalier et al., 2011; Akhoudas et al., 2018). Their size varies from a few centimeters to more than one-meter, with a variety of shapes and variable

spatial extent, and they are mainly composed of calcite, Mg-calcite, aragonite, and dolomite (e.g., Zitter et al., 2008; Pierre et al., 2012; Çağatay et al., 2018; Ruffine et al., 2018b). Locations of carbonate-chimneys were first detected by use of shipborne multibeam echosounders, further constrained by microbathymetry AUV surveys, and finally by ROV or manned submersible dives allowing for visual observation and sampling (e.g., Zitter et al., 2008; Dupré et al., 2010, 2015; Gasperini et al., 2012).

Authigenic carbonate precipitates can be considered as archives for the activity of fluid flow and may thus provide important tools for deciphering the long-term relationship between fluid geochemistry and seismic activity (e.g., dating of seismic events). With these properties, the precipitates could be even more useful than seismo-turbidite archives that were described above for the Sea of Marmara (e.g., Drab et al., 2012; Çağatay et al., 2012; McHugh et al., 2014) and other tectonically active regions such as the Calabrian Arc Subduction Complex, SW Iberia, and New Zealand (e.g., Gràcia et al., 2010; Pouderoux et al., 2012; Polonia et al., 2013). Hence, extending this paleo-perspective on the coupling of seismicity to changes in geochemistry and intensity of fluid flow, authigenic precipitates may serve as long-term evolving recorder. Depending on setting and type, especially methane-derived authigenic carbonates (MDACs) may provide well-preserved archives of tectonically driven variations in fluid emanation (e.g., Kutterolf et al., 2008; Liebetrau et al., 2010, 2014; Magalhães et al., 2012; Teichert et al., 2018; Çağatay et al., 2018) as well as for major environmental changes in bottom and pore water chemistry (e.g., Bayon et al., 2009; Cremiere et al., 2013). However, the use of authigenic carbonates as paleo-earthquake and paleo-fluid geochemistry archives requires systematic studies involving U-Th dating, stable isotope and biomarker analyses (Çağatay et al., 2018). In this regard, a high-resolution multi-proxy study carried out by Teichert et al. (2018) in the Sea of Marmara provides a promising example for the use of authigenic carbonates as archives of past seismic activity. As future perspective, carbonate archives from different MTFFZs could be used to get new insights into their evolution and impact on chemical fluxes. In addition to these high sensitivity calibration attempts, paleorecords provide a useful approach to improve the systematics of major control processes and their impact in time and space. More examples as described for the Sea of Marmara are available for other long-term tectonically active regions like Calabrian Arc Subduction Complex, SW Iberia and New Zealand, e.g., Polonia et al. (2015), Gràcia et al. (2010), and Pouderoux et al. (2012), respectively.

In summary, to date, no geochemical proxies have been unequivocally identified which can be used either as records of past seismic events or as precursors for seismic activity. This is a scientific endeavor for future studies in order to develop more robust relationships between seismically imposed dynamic stress and the release of fluids from depth. Currently, available results, but also technical approaches are quite limited. Below, we address a number of useful developments that could help bridging the knowledge gap.

Seismic Imaging of Geological Structures and Subsurface Fluids

As it can be deduced from the previous sections, seismic records are of utmost importance for the fundamental understanding of subsurface structures and related geological processes. Seismic processing is typically used for characterizing variations in lithology and petrophysical properties. The imaging of complex geological structures, like faults or the occurrence of overpressured fluids requires sophisticated processing schemes, such as wave equation datuming (WED) or amplitude versus offset (AVO; e.g., Tinivella et al., 2005, 2017; Giustiniani et al., 2015, 2018; **Figure 12**). The AVO technique can be used to detect the presence of anomalous fluid content, mainly free gas (e.g., Ostrander, 1984), and anomalous pore pressures (e.g., Tinivella, 2002). Essentially, AVO analyses provide information about the compressional (P) and shear wave (S) velocity (V) contrasts at interfaces, which give indications about the pore fluid content. The joint analysis of both parameters yields information about the main geological features and the fluid presence and circulation (e.g., Accaino et al., 2005; Tinivella et al., 2005). Moreover, it is possible to estimate the pore pressure by comparing the seismic and the theoretical velocity and the resulting density decrease (Tinivella et al., 2005). More recently, full-waveform inversion (FWI) has been applied to extract petrophysical information from shallow seismic data, showing promising application also for crustal data (Virieux and Operto, 2009). **Figure 12** shows an example of joint use of different seismic analysis to detect fluid presence in anomalous pressure condition. Another approach of high potential for assessing pore fluid dynamics is the analysis of the dynamics of seismicity clouds and seismic swarms, from which the propagation of pore pressure and hydraulic permeability can be inferred (e.g., Shapiro, 2000). An application of this method to marine tectonic settings can be found in Thorwart et al. (2014) providing evidence for the coupling of seismicity and fluid flow (see section "Fluid Flow and Chemical Indicators Related to Seismic Activity").

In summary, specific seismic processing schemes offer the opportunity of differentiating between lithology and fluid content as well as fluid-rock interactions. The improvement of such techniques, specifically in combination with geochemical methods is clearly suitable to strengthen our current knowledge on structural control on fluid mobilization processes and its relation to seismicity.

Sea-Floor Observatories and Emerging Monitoring Technologies

The deep ocean still remains a frontier for scientific exploration and discovery. Although the operation of research vessels has been providing a wealth of scientific knowledge, these platforms are clearly limited with respect to the exploration of processes at and below the deep seafloor over extended intervals of time. To address the frontier, research challenges in oceanographic science for the 21st century, permanent, multidisciplinary seafloor observatory networks are required for recording long-term time series measurements.

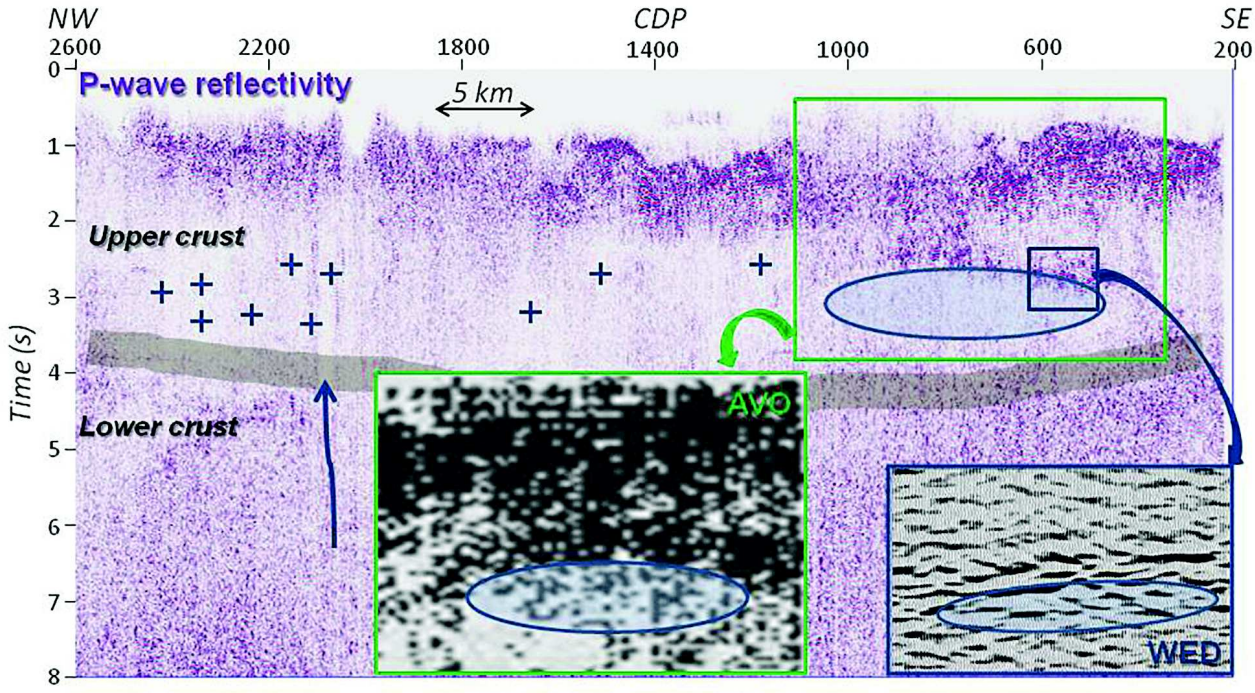

FIGURE 12 | Example of P-wave reflectivities from the Tuscan geothermal field [data from Tinivella et al. (2005)] demonstrating the advantage of the joint use of seismic methods. A combined analysis of P- and S-wave reflectivities (AVO) within the green-framed area of the P-wave reflectivity plot shows general evidence for fluid overpressure (white spots). The high P-wave amplitude contrast is well imaged in the seismic line after the application of WED [blue box; data from Giustiniani et al., 2015)]. Light-blue zones: fluids. Blue arrow: vertical channel. Blue crosses: magmatic intrusions. The gray area indicates a regional reflecting zone related to lithologic change and may correspond to the brittle-ductile transition zone.

Considerable efforts in developing seafloor observatory networks have been made over the last two decades (Favali et al., 2015). In Japan, most advanced submarine cabled observatory networks for earthquake and tsunami observation have been established (DONET: Nankai Trough; S-Net: Japan Trench[5]; Kaneda, 2014; Kanazawa et al., 2015; Kamogawa et al., 2016). In Canada (e.g., Barnes et al., 2015), a regional cabled Ocean Observatory (Neptune Canada) for ocean sciences has been established in the Northeast Pacific Ocean[6]. In the United States, other observatories are also operated, as part of the Ocean Observatory Initiative (OOI: oceanobservatories.org). In Europe, the European Multidisciplinary Seafloor and water column Observatory (EMSO, emso.eu) is a relatively new science infrastructure under European Research Infrastructure Consortium (ERIC; Best et al., 2016). It consists of a system of distributed, regional facilities placed at key sites around Europe, from the Atlantic (Azores), through the Mediterranean to the Black Sea (e.g., Ruhl et al., 2011). Overall, ongoing activities clearly document the progress in monitoring technologies, which is important for many branches within ocean sciences, such as marine eco-systems, climate change, and geohazards. The understanding of seismic fault activity is one of the main challenges facing Earth Science. On land, substantial progress has been made by combining geophysical instrumentation (seismometers, GPS, tiltmeters) with the use of remote sensing facilities). Almost nothing comparable to this exists for the deep ocean. Except at specific sites (e.g., offshore Japan and in the NW Pacific Cascadia subduction zone), observing stations are deployed on land, far away from the areas where active processes are at work.

In submarine nearshore environments, amphibious approaches are a useful alternative (e.g., Guerrero Seismic Gap, off Mexico; Cruz-Atienza et al., 2018). Alternative solutions to fixed cabled observatories are in progress and will likely be more affordable and versatile. Overall, the emergence of new technologies offers a promising future, as for instance:

(1) Telecommunication optical fiber cables can detect seismic events when combined with state-of-the-art frequency metrology techniques ("distributed acoustic sensing," DAS; e.g., Lindsey et al., 2017; Marra et al., 2018 and references herein).
(2) Laser reflectometry using Brillouin Optical Time Domain Reflectometry (BOTDR), commonly used for the monitoring of engineering structures can measure very small strains (<1 mm) at very large distances (10–200 km). This technique is currently tested witin the FOCUS project to demonstrate the feasibility of measuring small (1–2 cm)

[5]https://www.jamstec.go.jp/donet/e/rd/index.html
[6]http://www.oceannetworks.ca/observatories/pacific

displacements across the tectonically active North Alfeo fault offshore eastern Sicily (Gutscher et al., 2018).

(3) New developments in high-resolution Absolute Pressure Gauges and Triaxial Accelerometers, based on in-situ calibration allows long-term measurements of geodesy[7]; Davis et al., 2017).

(4) *In situ* Raman sensor technology has been proven to monitor methane and other organic geochemical tracers subsea (e.g., Kolomijeca et al., 2013).

(5) Dissolved gases in seawater and seeping fluids can be determined by using *in situ* sensors operated by ROV, AUV, Seafloor-Landers, and from towed platforms (e.g., Linke et al., 2015; Schmidt et al., 2015).

(6) Mass spectrometry is a valuable tool for detecting and monitoring seeping fluids from the seafloor (e.g., Sommer et al., 2015). *In situ*, mass spectrometry for gas analyses at the seafloor is currently under development (e.g., Gentz, 2015).

(7) Noble gases have been shown to be a useful and robust tracer for fluid flow, fluid sources, and potentially as precursor for seismic activity, but state-of-the-art sampling approaches only allow collection of a very limited number of samples. Recently, mass spectrometers with a membrane inlet separating gases from water have been tested successfully (GE-MIMS; Mächler et al., 2012, 2014). Experimental developments in this field of research are currently pursued (Brennwald et al., 2016) and aim at the combined acquisition and integration in short- and long-term observatories (e.g., autonomously operated seafloor instruments).

PERSPECTIVE

This manuscript has been developed to provide a comprehensive overview of the state-of-the-art and current research at MTFFZs beyond a geodynamic viewpoint. The key motivation was to provide an integrated view on current research linking plate tectonics, fluid flow, and life at MTFFZs. MTTFZs cover vast stretches of the seafloor in the deep oceans and offer an exciting field of research for cross-disciplinary studies, which is currently underrepresented in the research landscape. A number of findings suggest that the deep-sea areas between the spreading axis and the continental margins are more active in terms of heat and fluid flow than previously thought. To date, existing evidence, e.g., along oceanic fracture zones, comes from isolated observations, such as seismic records or heat flow measurements, indicating deviations from theory or empirically derived patterns. A deeper understanding of such regional or localized anomalies now requires comprehensive, multidisciplinary monitoring and research approaches. These may include investigations on seismic activity coupled with groundtruthing techniques through heat flow measurements, geochemical, and/or microbiological studies. An important first step to overcome was the conduction of interdisciplinary, sea-going expeditions. Given that MTFFZs cover vast areas of the seafloor, a comprehensive investigation even of some key regions will require long-lasting efforts, which will be supported by ongoing technological developments and new monitoring concepts e.g., for simultaneous records of seismic activity and fluid flow. This article aims at stimulating such future interdisciplinary research along MTFFZs in order to further our understanding of the still underexplored regions of the deep ocean.

[7] http://paroscientific.com/pdf/P20_Seismic_Oceanic_Sensors_(SOS).pdf

DATA AVAILABILITY

All datasets generated for this study are included in the manuscript and/or the supplementary files.

AUTHOR CONTRIBUTIONS

All authors actively contributed to various parts of the manuscript and agree with its contents. CH, JD, PV, AM, ML, PT, LG, PH, HV, JM, MS, and M-AG developed the concept of the manuscript. Figures were provided and or developed by AM, PV, M-AG, JD, LG, LGa, RB, CH, LB, DS, HV, CS, MS, LR, and UT.

FUNDING

This study was the outcome of interdisciplinary research and intense, pan-European, scientific exchange within the EU-funded COST Action FLOWS (ES1301; https://www.flows-cost.eu/) since 2013, supported by COST (European Cooperation in Science and Technology; www.cost.eu).

ACKNOWLEDGMENTS

The authors wish to thank all members of the FLOWS consortium (https://www.flows-cost.eu/de/members) for fruitful discussions and ongoing knowledge exchange. Additional thanks for fruitful collaboration go to colleagues of the InterRidge working group on Oceanic Transform Faults (https://www.interridge.org/WG_Transform_Faults), the Deep Carbon Observatory (https://deepcarbon.net/), and the MARSITE Programme [EU Grant agreement N° (308417)]. The manuscript benefited from critical and insightful comments by Shinsuke Kawagucci and Wolfgang Rabbel. JD acknowledges an FCT Researcher contract, an exploratory project grant ref. IF/00702/2015, and the FCT project UID/ GEO/50019/2013-IDL. LG acknowledges the bilateral ANR/TÜBITAK collaborative research project MAREGAMI (ANR-16-CE03-0010-02 and Tübitak Project 116Y371). AM acknowledges the European Research Council under the Seventh Framework Programme (grant agreement 308126, LUSI LAB) and the Research Council of Norway (Centers of Excellence funding scheme 223272).

REFERENCES

Abercrombie, R. E., and Ekström, G. (2001). Earthquake slip on oceanic transform faults. *Nature* 410, 74–77. doi: 10.1038/35065064

Accaino, F., Tinivella, U., Rossi, G., and Nicolich, R. (2005). "Geofluid evidence from analysis of deep crustal seismic data (Southern Tuscany, Italy), structures in the continental crust and geothermal resources," in *Journal of Volcanology and Geothermal Research*, Vol. 148, eds D. Liotta and G. Ranalli (Duivendrecht: Elsevier), 46–59.

Akhoudas, C., Chevalier, N., Blanc-Valleron, M. M., Klein, V., Mendez-Millan, M., Demang, J., et al. (2018). Methane derived stromatolitic carbonate crust from an active fluid seepage in the western basin of the Sea of Marmara: mineralogical, isotopic and molecular geochemical characterization. *Deep Sea Res. II* 153, 110–120. doi: 10.1016/j.dsr2.2017.12.022

Aochi, H., and Ulrich, T. (2015). A probable earthquake scenario near Istanbul determined from dynamic simulations. *Bull. Seismol. Soc. Am.* 105, 1468–1475. doi: 10.1785/0120140283

Armijo, R., Meyer, B., Hubert, A., and Barka, A. (1999). Westward propagation of the north Anatolian into the northern Aegean: timing and kinematics. *Geology* 27, 267–270. doi: 10.1130/0091-7613(1999)027<0267:WPOTNA>2.3.CO;2

Armijo, R., Pondard, N., Meyer, B., Mercier de Lepinay, B., Uçarkus, G., Malavieille, J., et al. (2005). Submarine fault scarps in the Sea of Marmara pull-apart (North Anatolian Fault): implications for seismic hazard in Istanbul. *Geochem. Geophys. Geosyst.* 6:Q06009. doi: 10.1029/2004GC000896

Attanasio, A., and Maravalle, M. (2016). Some considerations between radon and earthquakes in the crater of L'Aquila. *Nat. Hazards* 81, 1971–1979. doi: 10.1007/s11069-016-2169-4

Atwater, T., and Menard, H. W. (1970). Magnetic lineations in the Northeast Pacific. *Earth Planet. Sci. Lett.* 7, 445–450. doi: 10.1016/0012-821X(70)90089-0

Baptista, M. A., and Miranda, J. M. (2009). Revision of the Portuguese catalog of tsunamis. *Nat. Hazards Earth Syst. Sci.* 9, 25–42. doi: 10.5194/nhess-9-25-2009

Baptista, M. A., Miranda, P. M. A., Miranda, J. M., and Victor, L. M. (1998). Constrains on the source of the 1755 Lisbon tsunami inferred from numerical modelling of historical data. *J. Geodyn.* 25, 159–174. doi: 10.1016/S0264-3707(97)00020-3

Barka, A. A. (1999). The 17 August 1999 Izmit earthquake. *Science* 285, 1858–1859. doi: 10.1126/science.285.5435.1858

Barnes, C. R., Best, M. M. R., Johnson, F. R., and Pirenne, B. (2015). "NEPTUNE Canada: installation and initial operation of the world's first regional cabled ocean observatory," in *Seafloor Observatories: A New Vision of the Earth from the Abyss*, eds P. Favali, L. Beranzoli, and A. De Santis (Berlin: Springer), 415–437. doi: 10.1007/978-3-642-11374-1_16

Bartolome, R., Gràcia, E., Stich, D., Martínez-Loriente, S., Klaeschen, D., Mancilla, F. L., et al. (2012). Evidence for active strike-slip faulting along the Eurasia-Africa convergence zone: implications for seismic hazards on the SW Iberian Margin. *Geology* 40, 495–498. doi: 10.1130/G33107.1

Batista, L., Hubscher, C., Terrinha, P., Matias, L., Afilhado, A., and Ludmann, T. (2017). Crustal structure of the Eurasia–Africa plate boundary across the Gloria Fault, North Atlantic Ocean. *Geophys. J. Int.* 209, 713–729. doi: 10.1093/gji/ggx050

Batsi, E., Lomax, A., Tary, J. B., Klingelhoefer, F., Riboulot, V., Murphy, M., et al. (2018). An alternative view of the microseismicity along the western main marmara fault. *Bull. Seismol. Soc. Am.* 108, 2650–2674. doi: 10.1785/0120170258

Bayon, G., Henderson, G. M., and Bohn, M. (2009). U-Th stratigraphy of a cold seep carbonate crust. *Chem. Geol.* 260, 47–56. doi: 10.1016/j.chemgeo.2008.11.020

Beaulieu, S. E., and Szafranski, K. (2018). *InterRidge Global Database of Active Submarine Hydrothermal Vent Fields, Version 3.4. World Wide Web Electronic Publication*. Available at: http://vents-data.interridge.org/

Beck, C., Mercier de Lépinay, B., Schneider, J.-L., Cremer, M., Çağatay, N., Wendenbauma, E., et al. (2007). Late Quaternary co-seismic sedimentation in the Sea of Marmara's deep basins. *Sediment. Geol.* 199, 65–89. doi: 10.1016/j.sedgeo.2005.12.031

Best, M. M. R., Favali, P., Beranzoli, L., Blandin, J., Çağğatay, M. N., Cannat, M., et al. (2016). The EMSO-ERIC pan-european consortium: data benefits and lessons learned as the legal entity forms. *Mar. Technol. Soc. J.* 50, 8–15. doi: 10.4031/MTSJ.50.3.13

Bezzeghoud, M., Adam, C., Buforn, E., Borges, J. F., and Caldeira, B. (2014). Seismicity along the Azores-Gibraltar region and global plate kinematics. *J. Seismol.* 18, 205–220. doi: 10.1007/s10950-013-9416-x

Bird, P. (2003). An updated digital model of plate boundaries. *Geochem. Geophys. Geosyst.* 4:1027. doi: 10.1029/2001GC000252

Bird, P., and Kagan, Y. Y. (2004). Plate-tectonic analysis of shallow seismicity: apparent boundary width, beta, corner magnitude, coupled lithosphere thickness, and coupling in seven tectonic settings. *Bull. Seismol. Soc. Am.* 94, 2380–2399. doi: 10.1785/0120030107

Bischoff, J. L., and Rosenbauer, R. J. (1985). An empirical equation of state for hydrothermal seawater (3.2 percent NaCl). *Am. J. Sci.* 285, 725–763. doi: 10.2475/ajs.285.8.725

Boettcher, M. S., and Jordan, T. H. (2004). Earthquake scaling relations for mid-ocean ridge transform faults. *J. Geophys. Res.* 109:B12302. doi: 10.1029/2004JB003110

Boettcher, M. S., and McGuire, J. J. (2009). Scaling relations for seismic cycles on mid-ocean ridge transform faults. *Geophys. Res. Lett.* 36:L21301. doi: 10.1029/2009GL040115

Bohnenstiehl, D. R., Tolstoy, M., and Chapp, E. (2004). Breaking into the plate: a 7.6 Mw fracture-zone earthquake adjacent to the Central Indian Ridge. *Geophys. Res. Lett.* 31:L02615. doi: 10.1029/2003gl018981

Bonatti, E., Ligi, M., Brunelli, D., Cipriani, A., Fabretti, P., Ferrante, V., et al. (2003). Mantle thermal pulses below the Mid-Atlantic Ridge and temporal variations in the formation of oceanic lithosphere. *Nature* 423, 499–505. doi: 10.1038/nature01594

Bonatti, E., Ligi, M., Gasperini, L., Peyve, A., Raznitsin, Y., and Chen, Y. J. (1994). Transform migration and vertical tectonics at the Romanche fracture zone, equatorial Atlantic. *J. Geophys. Res. Solid Earth* 99, 21779–21802. doi: 10.1029/94JB01178

Bonini, M. (2009). Mud volcano eruptions and earthquakes in the Northern Apennines and Sicily, Italy. *Tectonophysics* 474, 723–735. doi: 10.1016/j.tecto.2009.05.018

Bouchon, M., Karabulut, H., Aktar, M., Ozalabey, S., Schmittbuhl, J., and Bouin, M.-P. (2011). Extended nucleation of the 1999 M 7.6 izmit earthquake. *Science* 331, 877–880. doi: 10.1126/science.1197341

Bourry, C., Chazallon, B., Charlou, J. L., Pierre Donval, J., Ruffine, L., Henry, P., et al. (2009). Free gas and gas hydrates from the Sea of Marmara, Turkey: chemical and structural characterization. *Chem. Geol.* 264, 197–206. doi: 10.1016/j.chemgeo.2009.03.007

Bradley, A. S., Hayes, J. M., and Summons, R. E. (2009). Extraordinary 13C enrichment of diether lipids at the Lost City Hydrothermal Field indicates a carbon-limited ecosystem. *Geochim. Cosmochim. Acta* 73, 102–118. doi: 10.1016/j.gca.2008.10.005

Bradley, A. S., and Summons, R. E. (2010). Multiple origins of methane at the Lost City Hydrothermal Field. *Earth Planet. Sci. Lett.* 297, 34–41. doi: 10.1016/j.epsl.2010.05.034

Brazelton, W. J., Nelson, B., and Schrenk, M. O. (2012). Metagenomic evidence for H2 oxidation and H2 production by serpentinite-hosted subsurface microbial communities. *Front. Microbiol.* 2:268. doi: 10.3389/fmicb.2011.00268

Brazelton, W. J., Schrenk, M. O., Kelley, D. S., and Baross, J. A. (2006). Methane- and sulfur-metabolizing microbial communities dominate the Lost City Hydrothermal Field ecosystem. *Appl. Environ. Microbiol.* 72, 6257–6270. doi: 10.1128/AEM.00574-06

Brennwald, M. S., Schmidt, M., Oser, J., and Kipfer, R. (2016). A portable and autonomous mass spectrometric system for on-site environmental gas analysis. *Environ. Sci. Technol.* 50, 13455–13463. doi: 10.1021/acs.est.6b03669

Brodsky, E. E. (2003). A mechanism for sustained groundwater pressure changes induced by distant earthquakes. *J. Geophys. Res.* 108:2390. doi: 10.1029/2002JB002321

Buforn, E., Udias, A., and Madariaga, R. (1991). Intermediate and deep earthquakes in Spain. *Pure Appl. Geophys.* 136, 375–393. doi: 10.1007/BF00878576

Burnard, P., Bourlange, S., Henry, P., Géli, L., Tryon, M. D., Natal'in, B., et al. (2012). Constraints on fluid origins and migration velocities along the Marmara Main Fault (Sea of Marmara, Turkey) using helium isotopes. *Earth Planet. Sci. Lett.* 341–344, 68–78. doi: 10.1016/j.epsl.2012.05.042

Burwicz, E., Reichel, T., Wallmann, K., Haeckel, M., and Hensen, C. (2017). 3-D basin-scale reconstruction of natural gas hydrate system of the Green

Canyon, Gulf of Mexico. *Geochem. Geophys. Geosyst.* 18, 1959–1985. doi: 10.1002/2017GC006876

Çağatay, M. N., Erel, L., Bellucci, L. G., Polonia, A., Gasperini, L., Eriş, K. K., et al. (2012). Sedimentary earthquake records in the Ýzmit Gulf, Sea of Marmara, Turkey. *Sediment. Geol.* 282, 347–359. doi: 10.1016/j.sedgeo.2012.10.001

Çağatay, M. N., and Uçarkuş, G. (2019). "Morphotectonics of the Sea of Marmara: basins and highs on the North Anatolian continental transform plate boundary," in *Transform Plate Boundaries and Fracture Zones*, ed. J. C. Duarte (Amsterdam: Elsevier), 397–416. doi: 10.1016/B978-0-12-812064-4.00016-5

Çağatay, M. N., Yıldız, G., Bayon, G., Ruffine, L., and Henry, P. (2018). Seafloor authigenic carbonate crusts along the submerged part of the North Anatolian Fault in the Sea of Marmara: mineralogy, geochemistry, textures and genesis. *Deep Sea Res. Part II* 153, 92–109. doi: 10.1016/j.dsr2.2017.09.003

Cann, J. R., Blackman, D. K., Smith, D. K., McAllister, E., Janssen, B., Mello, S., et al. (1997). Corrugated slip surfaces formed at ridge-transform intersections on the Mid-Atlantic Ridge. *Nature* 385, 329–332. doi: 10.1038/385329a0

Cannat, M., Mamaloukas-Frangoulis, V., Auzende, J.-M., Bideau, D., Bonatti, E., Honnorez, J., et al. (1991). A geological cross-section of the Vema Fracture Zone transverse ridge, Atlantic Ocean. *J. Geodyn.* 13, 97–118. doi: 10.1016/0264-3707(91)90034-C

Casey, J. F., and Dewey, J. F. (1984). Initiation of subduction zones along transform and accreting plate boundaries, triple-junction evolution, and forearc spreading centres - Implications for ophiolitic geology and obduction. *Geol. Soc. Spec. Publ.* 13, 269–290. doi: 10.1144/GSL.SP.1984.013.01.22

Chester, F. M., Mori, J., Eguchi, N., and Toczko, S. (2013). *Proc. IODP, 343/343T*. Tokyo: Integrated Ocean Drilling Program Management International. doi: 10.2204/iodp.proc.343343T.2013

Chevalier, N., Bouloubassi, I., Birgel, D., Crémière, A., Taphanel, M. H., and Pierre, C. (2011). Authigenic carbonates at cold seeps in the Marmara Sea (Turkey): a lipid biomarker and stable carbon and oxygen isotope investigation. *Mar. Geol.* 288, 112–121. doi: 10.1016/j.margeo.2011.08.005

Chevalier, N., Bouloubassi, I., Birgel, D., Taphanel, M.-H., and López-García, P. (2013). Microbial methane turnover at Marmara Sea cold seeps: a combined 16S rRNA and lipid biomarker investigation. *Geobiology* 11, 55–71. doi: 10.1111/gbi.12014

Claesson, L., Skelton, A., Graham, C., and Morth, C. M. (2007). The timescale and mechanisms of fault sealing and water-rock interaction after an earthquake. *Geofluids* 7, 427–440. doi: 10.1111/j.1468-8123.2007.00197.x

Coogan, L. A., and Gillis, K. M. (2018). Low-temperature alteration of the seafloor: impacts on ocean chemistry. *Ann. Rev. Earth Planet. Sci.* 46, 21–45. doi: 10.1146/annurev-earth-082517-010027

Corti, G., Bonini, M., Innocenti, F., and Manetti, P. (2005). Extension of a continental lithosphere weakened by impregnation of asthenospheric melts: analogue modelling approach. *Ofioliti* 30:159.

Cremiere, A., Bayon, G., Ponzevera, E., and Pierre, C. (2013). Paleo-environmental controls on cold seep carbonate authigenesis in the Sea of Marmara. *Earth Planet. Sci. Lett.* 376, 200–211. doi: 10.1016/j.epsl.2013.06.029

Crespo-Medina, M., Twing, K. I., Sánchez-Murillo, R., Brazelton, W. J., McCollom, T. M., and Schrenk, M. O. (2017). Methane dynamics in a tropical serpentinizing environment: the Santa Elena Ophiolite, Costa Rica. *Front. Microbiol.* 8:916. doi: 10.3389/fmicb.2017.00916

Cruz-Atienza, V. M., Ito, Y., Kostoglodov, V., Hjörleifsdóttir, V., Iglesias, A., Tago, J., et al. (2018). A seismogeodetic mphibious network in the Guerrero seismic gap, Mexico. *Seismol. Res. Lett.* 89, 1435–1449. doi: 10.1785/0220170173

Custódio, S., Lima, V., Vales, D., Cesca, S., and Carrilho, F. (2016). Imaging active faulting in a region of distributed deformation from the joint clustering of focal mechanisms and hypocentres: application to the Azores–western Mediterranean region. *Tectonophysics* 676, 70–89. doi: 10.1016/j.tecto.2016.03.013

Dauteuil, O., Bourgeois, O., and Mauduit, T. (2002). Lithosphere strength controls oceanic transform zone structure: insights from analogue models. *Geophys. J. Int.* 150, 706–714. doi: 10.1046/j.1365-246X.2002.01736.x

Davis, E. E., and Elderfield, H. (2004). *Hydrology of the Oceanic Lithosphere*, eds E. Davis and H. Elderfield (Cambridge: Combridge University Press), 706. doi: 10.1016/j.epsl.2017.01.042

Davis, E. E., Heesemann, M., Lambert, A., and He, J. (2017). Seafloor tilt induced by ocean tidal loading inferred from broadband seismometer data from the Cascadia subduction zone and Juan de Fuca Ridge. *Earth Planet. Sci. Lett.* 463, 243–252. doi: 10.1016/j.epsl.2017.01.042

Davis, E. E., Kelin, W., Jiangheng, H., Chapman, D. S., Villinger, H., and Rosenberger, A. (1997). An unequivocal case for high Nusselt number hydrothermal convection in sediment-buried igneous oceanic crust'. *Earth Planet. Sci. Lett.* 146, 137–150. doi: 10.1016/S0012-821X(96)00212-9

Davis, E. E., Lister, C. R., and Sclater, J. G. (1984). Towards determining the thermal state of old ocean lithosphere: heat-flow measurements from the Blake–Bahama outer ridge, north-westem Atlantic. *Geophys. J. R. Astron. Soc.* 78, 507–545. doi: 10.1111/j.1365-246X.1984.tb01962.x

Delle Donne, D., Harris, A. J. L., Ripepe, M., and Wright, R. (2010). Earthquake-induced thermal anomalies at active volcanoes. *Geology* 38, 771–774. doi: 10.1130/G30984.1

Devey, C. W., Augustin, N., Brandt, A., Brenke, N., Köhler, J., Lins, L., et al. (2018). Habitat characterization of the Vema Fracture Zone and Puerto Rico Trench. *Deep Sea Res. Part II Top. Stud. Oceanogr.* 148, 7–20. doi: 10.1016/j.dsr2.2018.02.003

Dia, A. N., Castrec, M., Boulègue, J., and Boudou, J. P. (1995). Major and trace element and Sr isotope constraints on fluid circulations in the Barbados accretionary complex. Part I: fluid origin. *Earth Planet. Sci. Lett.* 134, 69–85. doi: 10.1016/0012-821X(95)00102-I

Drab, L., Hubert Ferrari, A., Schmidt, S., and Martinez, P. (2012). The earthquake sedimentary record in the western part of the Sea of Marmara, Turkey. *Nat. Hazards Earth Syst. Sci.* 12, 1235–1254. doi: 10.5194/nhess-12-1235-2012

Dubilier, N., Bergin, C., and Lott, C. (2008). Symbiotic diversity in marine animals: the art of harnessing chemosynthesis. *Nat. Rev. Microbiol.* 6, 725–740. doi: 10.1038/nrmicro1992

Dupré, S., Scalabrin, C., Augustin, J.-M., Guérin, C., Ogor, A., and Clouet, H. (2018). *Distribution Spatiale des Sorties de Fluides en mer de Marmara (4 Novembre au 14 Decembre 2009)*. Barcelona: SEANOE. doi: 10.17882/54983

Dupré, S., Scalabrin, C., Grall, C., Augustin, J.-M., Henry, P., Şengör, A. M. C., et al. (2015). Tectonic and sedimentary controls on widespread gas emissions in the Sea of Marmara: results from systematic, shipborne multibeam echo sounder water column imaging. *J. Geophys. Res. Solid Earth* 120, 2891–2912. doi: 10.1002/2014JB011617

Dupré, S., Woodside, J., Klaucke, I., Mascle, J., and Foucher, J. P. (2010). Widespread active seepage activity on the Nile Deep Sea Fan (offshore Egypt) revealed by high-definition geophysical imagery. *Mar. Geol.* 275, 1–19. doi: 10.1016/j.margeo.2010.04.003

Dziak, R. P., Chadwick, W. W. Jr., Fox, C. G., and Embley, R. W. (2003). Hydrothermal temperature changes at the Southern Juan de Fuca Ridge associated with Mw 6.2 Blanco Transform Earthquake. *Geology* 31, 119–122. doi: 10.1130/0091-7613(2003)031<0119:HTCATS>2.0.CO;2

Dzierma, Y., Rabbel, W., Thorwart, M., Koulakov, I., Wehrmann, H., Hoernle, K., et al. (2012). Seismic velocity structure of the slab and continental plate in the region of the 1960 Valdivia (Chile) slip maximum - Insights into fluid release and plate coupling. *Earth Planet. Sci. Lett.* 331–332, 164–176. doi: 10.1016/j.epsl.2012.02.006

Ebert, R., Bideau, D., and Hekinian, R. (1983). Ultramafic and mafic rocks from the Garret transform fault near 13°30'S on the East Pacific Rise: igneous petrology. *Earth Planet. Sci. Lett.* 65, 107–125. doi: 10.1016/0012-821X(83)90193-0

Elderfield, H., and Schultz, A. (1996). Mid-Ocean Ridge hydrothermal fluxes and the chemical composition of the ocean. *Ann. Rev. Earth Planet. Sci.* 24, 191–224. doi: 10.1146/annurev.earth.24.1.191

Elderfield, H., Wheat, C. G., Mottl, M. J., Monnin, C., and Spiro, B. (1999). Fluid and geochemical transport through oceanic crust: a transect across the eastern flank of the Juan de Fuca Ridge. *Earth Planet. Sci. Lett.* 172, 151–165. doi: 10.1016/S0012-821X(99)00191-0

Embriaco, D., Marinaro, G., Frugoni, F., Monna, S., Etiope, G., Gasperini, L., et al. (2014). Monitoring of gas and seismic energy release by multiparametric benthic observatory along the North Anatolian Fault in the Sea of Marmara (NW Turkey). *Geophys. J. Int.* 196, 850–866. doi: 10.1093/gji/ggt436

Ergintav, S., Reilinger, R. E., Çakmak, R., Floyd, M., Cakir, Z., Doğan, U., et al. (2014). Istanbul's earthquake hot spots: geodetic constraints on strain accumulation along faults in the Marmara seismic gap. *Geophys. Res. Lett.* 41, 5783–5788. doi: 10.1002/2014GL060985

Escartin, J., and Cannat, M. (1999). Ultramafic exposures and gravity signature of the lithosphere near the Fifteen-Twenty Fracture Zone (Mid-Altlantic Ridge,

14°-16.5°N). *Earth Planet. Sci. Lett.* 171, 411–424. doi: 10.1016/S0012-821X(99)00169-7

Fabretti, P., Bonatti, E., Peyve, A., Brunelli, D., Cipriani, A., Dobrolubova, X., et al. (1998). First results of cruise S19 (PRIMAR Project): petrological and structural investigations of the Vema Transverse Ridge (equatorial Atlantic). *G. Geol.* 60, 3–16.

Favali, P., Beranzoli, L., and De Santis, A. (2015). *Seafloor Observatories: A New Vision of the Earth from the Abyss*. Berlin: Springer. doi: 10.1007/978-3-642-11374-1

Field, M. E., and Jennings, A. E. (1987). Seafloor gas seeps triggered by a northern California earthquake. *Mar. Geol.* 77, 39–51. doi: 10.1016/0025-3227(87)90082-X

Fischer, D., Mogollon, J. M., Strasser, M., Pape, T., Bohrmann, G., Fekete, N., et al. (2013). Subduction zone earthquake as potential trigger of submarine hydrocarbon seepage. *Nat. Geosci.* 6, 647–651. doi: 10.1038/ngeo1886

Fisher, A. T. (2005). Marine hydrogeology: recent accomplishments and future opportunities. *Hydrogeol. J.* 13, 69–97. doi: 10.1007/s10040-004-0400-y

Fisher, A. T., and Harris, R. N. (2010). Using seafloor heat flow as a tracer to map subseafloor fluid flow in the ocean crust. *Geofluids* 10, 142–160.

Fisher, A. T., and Von Herzen, R. P. (2005). Models of hydrothermal circulation within 106 Ma seafloor: constraints on the vigor of fluid circulation and crustal properties, below the Madeira Abyssal Plain. *Geochem. Geophys. Geosyst.* 6:Q11001. doi: 10.1029/2005GC001013

Foustoukos, D. I., Savov, I. P., and Janecky, D. R. (2008). Chemical and isotopic constraints on water/rock interactions at the Lost City Hydrothermal Field, 30°N Mid-Atlantic Ridge. *Geochim. Cosmochim. Acta* 72, 5457–5474. doi: 10.1016/j.gca.2008.07.035

Francis, T. J. G. (1981). Serpentinization faults and their role in the tectonics of slow spreading ridges. *J. Geophys. Res. Solid Earth* 86, 11616–11622. doi: 10.1029/JB086iB12p11616

Früh-Green, G. L., Kelley, D. S., Bernasconi, S. M., Karson, J. A., Ludwig, K. A., Butterfield, D. A., et al. (2003). 30,000 years of hydrothermal activity at the Lost City Vent Field. *Science* 301, 495–498. doi: 10.1126/science.1085582

Früh-Green, G. L., Orcutt, B. N., Green, S. L., and Cotterill, C. (2016). "Atlantis massif serpentinization and life," in *Proceedings of the International Ocean Discovery Program*, (College Station, TX: International Ocean Discovery Program), 357. doi: 10.14379/iodp.proc.357.2017

Fu, C.-C., Yang, T. F., Du, J., Walia, V., Chen, Y.-G., Liu, T.-K., et al. (2008). "Variations of helium and radon concentrations in soil gases from an active fault zone in southern Taiwan," in *Proceedings of the 23rd International Conference on Nuclear Tracks in Solids*, Vol. 43, Beijing, S348–S352. doi: 10.1016/j.radmeas.2008.03.035

Fujita, K., and Sleep, N. H. (1978). Membrane stresses near mid-ocean ridge-transform intersections. *Tectonophysics* 50, 207–221. doi: 10.1016/0040-1951(78)90136-1

Fukao, Y. (1973). Thrust faulting at a lithospheric plate boundary, the Portugal earthquake of 1969. *Earth Planet. Sci. Lett.* 18, 205–216. doi: 10.1016/0012-821X(73)90058-7

Galland, O., Cobbold, P. R., Hallot, E., de Bremend d'Ars, J., and Delavaud, G. (2006). Use of vegetable oil and silica powder for scale modelling of magmatic intrusion in a deforming brittle crust. *Earth Planet. Sci. Lett.* 243, 786–804. doi: 10.1016/j.epsl.2006.01.014

Ganas, A., Drakatos, G., Pavlides, S. B., Stavrakakis, G. N., Ziazia, M., Sokos, E., et al. (2005). The 2001 Mw = 6.4 Skyros earthquake, conjugate strike-slip faulting and spatial variation in stress within the central Aegean Sea. *J. Geodyn.* 39, 61–77. doi: 10.1016/j.jog.2004.09.001

Garfunkel, Z. (1981). Internal structure of the Dead Sea leaky transform (rift) in relation to plate kinematics. *Tectonophysics* 80, 81–108. doi: 10.1016/0040-1951(81)90143-8

Gasperini, L., Polonia, A., Bortoluzzi, G., Henry, P., Le Pichon, X., Tryon, M., et al. (2010). How far did the surface rupture of the 1999 İzmit earthquake reach in Sea of Marmara? *Tectonics* 30:TC1010. doi: 10.1029/2010TC002726

Gasperini, L., Polonia, A., Çağatay, M. N., Bortoluzzi, G., and Ferrante, V. (2011). Geological slip rates along the North Anatolian Fault in the Marmara region. *Tectonics* 30:TC6001. doi: 10.1029/2011TC002906

Gasperini, L., Polonia, A., Del Bianco, F., Etiope, G., Marinaro, G., Favali, P., et al. (2012). Gas seepage and seismogenic structures along the North Anatolian Fault in the eastern Sea of Marmara. *Geochem. Geophys. Geosyst.* 13:Q10018. doi: 10.1029/2012GC004190

Geersen, J., Scholz, F., Linke, P., Schmidt, M., Lange, D., Behrmann, J. H., et al. (2016). Fault zone controlled seafloor methane seepage in the rupture area of the 2010 Maule earthquake, Central Chile. *Geochem. Geophys. Geosyst.* 17, 4802–4813. doi: 10.1002/2016GC006498

Géli, L., Henry, P., Grall, C., Tary, J. B., Lomax, A., Batsi, E., et al. (2018). Gas and seismicity within the Istanbul seismic gap. *Sci. Rep.* 8:6819. doi: 10.1038/s41598-018-23536-7

Géli, L., Henry, P., Zitter, T., Dupré, S., Tryon, M., Çağatay, M. N., et al. (2008). Gas emissions and active tectonics within the submerged section of the North Anatolian Fault zone in the Sea of Marmara. *Earth Planet. Sci. Lett.* 274, 34–39. doi: 10.1016/j.epsl.2008.06.047

Géli, L., Piau, J.-M., Maury, V., Fitzenz, D., Dziak, R., Coutellier, Q., et al. (2014). Seismic precursors linked to highly compressible fluids at oceanic transform faults. *Nat. Geosci.* 7, 757–761. doi: 10.1038/ngeo2244

Gentz, T. (2015). "Improvements in under water mass spectrometry," in *Workshop on Harsh-Environment Mass Spectrometry Proceedings of the Meeting 13 September 2015 - 16 September 2015*, (Baltimore, MD: University of Maryland School of Pharmacy).

German, C. R., and Seyfried, W. E. (2014). "8.7 - hydrothermal processes," in *Treatise on Geochemistry*, 2nd Edn, eds H. D. Holland and K. K. Turekian (Oxford: Elsevier), 191–233. doi: 10.1016/B978-0-08-095975-7.00607-0

Gerya, T. V. (2010). Dynamical instability produces transform faults at mid-ocean ridges. *Science* 329, 1047–1050. doi: 10.1126/science.1191349

Gerya, T. V. (2012). Origin and models of oceanic transform faults. *Tectonophysics* 522–523, 34–54. doi: 10.1016/j.tecto.2011.07.006

Gerya, T. V. (2013a). Initiation of transform faults at rifted continental margins: 3D petrological–thermomechanical modeling and comparison to the Woodlark Basin. *Petrology* 21, 550–560. doi: 10.1134/S0869591113060039

Gerya, T. V. (2013b). Three-dimensional thermomechanical modeling of oceanic spreading initiation and evolution. *Phys. Earth Planet. Interiors* 214, 35–52. doi: 10.1016/j.pepi.2012.10.007

Gerya, T. V. (2016). "Origin, evolution, seismicity, and models of oceanic and continental transform boundaries," in *Plate Boundaries and Natural Hazards, AGU Geophysical Monograph Series 219*, eds J. C. Duarte and W. P. Schellart (Hoboken, NJ: Wiley), 39–76.

Giustiniani, M., Tinivella, U., and Nicolich, R. (2015). Reflection seismic sections across the Geothermal Province of Tuscany from reprocessing CROP profiles. *Geothermics* 53, 498–507. doi: 10.1016/j.geothermics.2014.09.003

Giustiniani, M., Tinivella, U., and Nicolich, R. (2018). Crustal structure of central sicily. *Tectonophysics* 722, 299–313. doi: 10.1016/j.tecto.2017.08.034

Global Heat Flow Compilation Group (2013). *Component Parts of the World Heat Flow Data Collection*. Bremen: PANGAEA.

Godón, A., Jendrzejewski, N., Castrec-Rouelle, M., Dia, A., Pineau, F., Boulegue, J., et al. (2004). Origin and evolution of fluids from mud volcanoes in the Barbados accretionary complex. *Geochim. Cosmochim. Acta* 68, 2153–2165. doi: 10.1016/j.gca.2003.08.021

Gràcia, E., Dañbeitia, J., Vergés, J., and Bartolomé, R. (2003). Crustal architecture and tectonic evolution of the Gulf of Cadiz (SW Iberian margin) at the convergence of the Eurasian and African plates. *Tectonics* 22:1033. doi: 10.1029/2001TC901045

Gràcia, E., Vizcaino, A., Escutia, C., Asioli, A., Rodés, A., Pallàs, R., et al. (2010). Holocene earthquake record offshore Portugal (SW Iberia): testing turbidite paleoseismology in a slow-convergence margin. *Quat. Sci. Rev.* 29, 1156–1172. doi: 10.1016/j.quascirev.2010.01.010

Grall, C., Dupré, S., Guerin, C., Normand, A., Gaillot, A., Fleury, J., et al. (2018a). *Processed AsterX AUV Data from the Sea of Marmara: High-Resolution Bathymetry and Seafloor Backscatter Images*. Barcelona: SEANOE. doi: 10.17882/55744

Grall, C., Henry, P., Dupré, S., Géli, L., Scalabrin, C., Zitter, T. A. C., et al. (2018b). Upward migration of gas in an active tectonic basin: an example from the sea of Marmara. *Deep Sea Res. Part II Top. Stud. Oceanogr.* 153, 17–35. doi: 10.1016/j.dsr2.2018.06.007

Grall, C., Henry, P., Tezcan, D., Mercier de Lepinay, B., Bécel, A., Géli, L., et al. (2012). Heat flow in the Sea of Marmara Central Basin: possible implications for the tectonic evolution of the North Anatolian fault. *Geology* 40, 3–6. doi: 10.1130/G32192.1

Granot, R. (2016). Palaeozoic oceanic crust preserved beneath the eastern Mediterranean. *Nat. Geosci.* 9, 701–705. doi: 10.1038/ngeo2784

Gutscher, M.-A. (2004). What caused the great lisbon earthquake? *Science* 305, 1247–1248. doi: 10.1126/science.1101351

Gutscher, M.-A., Baptista, M. A., and Miranda, J. M. (2006). The Gibraltar Arc seismogenic zone (part 2): constraints on a shallow east dipping fault plane source for the 1755 Lisbon earthquake provided by tsunami modeling and seismic intensity. *Tectonophysics* 426, 153–166. doi: 10.1016/j.tecto.2006.02.025

Gutscher, M.-A., Malod, J., Rehault, J.-P., Contrucci, I., Klingelhoefer, F., Mendes-Victor, L., et al. (2002). Evidence for active subduction beneath Gibraltar. *Geology* 30, 1071–1074. doi: 10.1130/0091-7613(2002)030<1071:EFASBG>2.0.CO;2

Gutscher, M.-A., Royer, J.-Y., Graindorge, D., Murphy, S., Klingelhoefer, F., Cattaneo, A., et al. (2018). *Benefitting from Cabled Observatories to Study Active Submarine Faults: the FOCUS Project (FOCUS = Fiber Optic Cable Use for Seafloor Studies of Earthquake Hazard and Deformation)*. Vienna: EGU General Assembly.

Halbach, P., Holzbecher, E., Reichel, T., and Moche, R. (2004). Migration of the sulphate - methane reaction zone in marine sediments of the Sea of Marmara - can this mechanisms be tectonically induced? *Chem. Geol.* 205, 73–82. doi: 10.1016/j.chemgeo.2003.12.013

Hanson, J. A., and Bowman, J. R. (2005). Indian Ocean ridge seismicity observed with a permanent hydroacoustic network. *Geophys. Res. Lett.* 32:L06301. doi: 10.1029/2004GL021931

Harrison, J. P., Gheeraert, N., Tsigelnitskiy, D., and Cockell, C. S. (2013). The limits of life under multiple extremes. *Trends Microbiol.* 21, 204–212. doi: 10.1016/j.tim.2013.01.006

Hasterok, D. (2013). Global patterns and vigor of ventilated hydrothermal circulation through young seafloor. *Earth Planet. Sci. Lett.* 380, 12–20. doi: 10.1016/j.epsl.2013.08.016

Head, I. M., Jones, D. M., and Larter, S. R. (2003). Biological activity in the deep subsurface and the origin of heavy oil. *Nature* 426, 344–352. doi: 10.1038/nature02134

Hein, J. R., Koski, R. A., Embley, R. W., Reid, J., and Chang, S.-W. (1999). Diffuse-flow hydrothermal field in an oceanic fracture zone setting, Northeast Pacific: deposit composition. *Explor. Min. Geol.* 8, 299–322.

Hekinian, R. (1982). Petrology of the ocean floor. chapter 7 oceanic fracture zones. *Elsevier Oceanogr. Ser.* 33, 219–222, 223, 227–249. doi: 10.1016/S0422-9894(08)70949-8

Hensen, C., Mazzini, A., and Bartolome, R. (2018). *Data Compilation of Locations of Seafloor Seeps*. Bremen: PANGAEA.

Hensen, C., Scholz, F., Nuzzo, M., Valadares, V., Gràcia, E., Terrinha, P., et al. (2015). Strike-slip faults mediate the rise of crustal-derived fluids and mud volcanism in the deep sea. *Geology* 43, 339–342. doi: 10.1130/G36359.1

Hensen, C., Wallmann, K., Schmidt, M., Ranero, C. R., and Suess, E. (2004). Fluid expulsion related to mud extrusion off Costa Rica continental margin - a window to the subducting slab. *Geology* 32, 201–204. doi: 10.1130/G20119.1

Hey, R., Duennebier, F. K., and Morgan, W. J. (1980). Propagating rifts on midocean ridges. *J. Geophys. Res.* 85, 3647–3658. doi: 10.1029/JB085iB07p03647

Hieke, W. (2004). The August 27, 1886 earthquake in Messenia (Peloponnesus) and reported flames over the Ionian Sea—a Mediterranean Ridge gas escape event? *Mar. Geol.* 207, 259–265. doi: 10.1016/j.margeo.2004.03.007

Hill, D., Johnston, M., Langbein, J., and Bilham, R. (1995). Response of long valley caldera to the M = 7.3 landers, California, earthquake. *Geophys. Res. Lett.* 100, 12985–13005. doi: 10.1029/95JB00860

Hill, D., Pollitz, F., and Newhall, C. (2002). Earthquake-volcano interactions. *Phys. Today* 55, 41–47. doi: 10.1063/1.1535006

Hill, E. M., Yue, H., Barbot, S., Lay, T., Tapponnier, P., Hermawan, I., et al. (2015). The 2012 Mw 8.6 Wharton Basin sequence: a cascade of great earthquakes generated by near-orthogonal, young, oceanic mantle faults. *J. Geophys. Res. Solid Earth* 120, 3723–3747. doi: 10.1002/2014JB011703

Hirose, T., Kawagucci, S., and Suzuki, K. (2011). Mechanoradical H2 generation during simulated faulting: implications for an earthquake-driven subsurface biosphere. *Geophys. Res. Lett.* 38:L17303. doi: 10.1029/2011GL048850

Hoehler, T. M., and Jørgensen, B. B. (2013). Microbial life under extreme energy limitation. *Nature Rev. Microbiol.* 11, 83–94. doi: 10.1038/nrmicro2939

Holdsworth, R. E., van Diggelen, E. W. E., Spiers, C. J., de Bresser, J. H. P., Walker, R. J., and Bowen, L. (2011). Fault rocks from the SAFOD core samples: implications for weakening at shallow depths along the San Andreas Fault, California. *J. Struct. Geol.* 33, 132–144. doi: 10.1016/j.jsg.2010.11.010

Holm, N. G., and Neubeck, A. (2009). Reduction of nitrogen compounds in oceanic basement and its implications for HCN formation and abiotic organic synthesis. *Geochem. Trans.* 10, 9–20. doi: 10.1186/1467-4866-10-9

Humphris, S. E., and Klein, F. (2018). Progress in deciphering the controls on the geochemistry of fluids in seafloor hydrothermal systems. *Annu. Rev. Mar. Sci.* 10, 315–343. doi: 10.1146/annurev-marine-121916-063233

Hurtado, L. A., Lutz, R. A., and Vrijenhoek, R. C. (2004). Distinct patterns of genetic differentiation among annelids of eastern Pacific hydrothermal vents. *Mol. Ecol.* 13, 2603–2615. doi: 10.1111/j.1365-294X.2004.02287.x

Husen, S., Wiemer, S., and Smith, R. B. (2004). Remotely triggered seismicity in the Yellowstone National Park region by the 2002 Mw 7.9 Denali Fault earthquake, Alaska. *Bull. Seismol. Soc. Am.* 94, S317–S331. doi: 10.1785/0120040617

Hutnak, M., Fisher, A. T., Stein, C. A., Harris, R., Wang, K., Silver, E., et al. (2007). "The thermal state of 18–24 ma upper lithosphere subducting below the nicoya peninsula, northern costa rica margin," in *Interplate Subduction Zone Seismogenesis, MARGINS Theoretical Institute*, eds T. Dixon and C. Moore (New York, NY: Columbia University Press), 86–122.

Ihmlé, P., and Jordan, T. H. (1994). Teleseismic search for slow precursors to large earthquakes. *Science* 266, 1547–1551. doi: 10.1126/science.266.5190.1547

Ijiri, A., Inagaki, F., Kubo, Y., Adhikari, R. R., Hattori, S., Hoshino, T., et al. (2018). Deep-biosphere methane production stimulated by geofluids in the Nankai accretionary complex. *Sci. Adv.* 4:eaao4631. doi: 10.1126/sciadv.aao4631

Isacks, B., Oliver, J., and Sykes, L. R. (1968). Seismology and the new global tectonics. *J. Geophys. Res.* 73, 5855–5899. doi: 10.1029/JB073i018p05855

Johnson, H. P., Hutnak, M., Dziak, R. R. P., Fox, C. C. G., Urcuyo, I., Cowen, J. P. J., et al. (2000). Earthquake-induced changes in a hydrothermal system on the Juan de Fuca mid-ocean ridge. *Nature* 407, 174–177. doi: 10.1038/35025040

Johnson, S. B., Young, C. R., Jones, W. J., Warén, A., and Vrijenhoek, R. C. (2006). Migration, isolation, and speciation of hydrothermal vent limpets (Gastropoda; Lepetodrilidae) across the Blanco Transform Fault. *Biol. Bull.* 210, 140–157. doi: 10.2307/4134603

Judd, A. G., and Hovland, M. (2007). *Seabed Fluid Flow. The Impact on Geology, Biology and the Marine Environment*. Cambridge: Cambridge University Press, 293. doi: 10.1017/CBO9780511535918

Kamogawa, M., Orihara, Y., Tsurudome, C., Tomida, Y., Kanaya, T., Ikeda, D., et al. (2016). A possible space-based tsunami early warning system using observations of the tsunami ionospheric hole. *Sci. Rep.* 6:37989. doi: 10.1038/srep37989

Kanamori, H., and Stewart, G. S. (1976). Mode of the strain release along the gibbs fracture zone, mid-atlantic ridge. *Phys. Earth Planet. Int.* 11, 312–332. doi: 10.1016/0031-9201(76)90018-2

Kanazawa, T., Uehira, K., Mochizuki, M., Shinbo, T., Noguchi, S., and Fujimoto, H. (2015). "The Japan Trench earthquake and tsunami monitoring network project of cable-linked 150 seafloor observatories: the S-net project," in *Proceedings of the CTBTO Science and Technology Conference 2015*, Vienna, 22–26.

Kaneda, Y. (2014). Introduction to ocean floor networks and their scientific application. *Mar. Geophys. Res.* 35, 177–180. doi: 10.1007/s11001-014-9232-x

Kelley, D. S., Karson, J. A., Blackman, D. K., Früh-Green, G. L., Butterfield, D. A., Lilley, M. D., et al. (2001). An off-axis hydrothermal vent field near the Mid-Atlantic Ridge at 30°N. *Science* 412, 145–149.

Kelley, D. S., Karson, J. A., Früh-Green, G. L., Yoerger, D. R., Shank, T. M., Butterfield, D. A., et al. (2005). A serpentinite-hosted ecosystem: the Lost City Hydrothermal Field. *Science* 307, 1428–1434. doi: 10.1126/science.1102556

Khutorskoi, M. D., and Polyak, B. G. (2017). Special features of heat flow in transform faults of the North Atlantic and Southeast Pacific. *Geotectonics* 51, 152–162. doi: 10.1134/S0016852117010022

King, C.-Y. (1986). Gas geochemistry applied to earthquake prediction: an overview. *J. Geophys. Res.* 91, 12269–12281. doi: 10.1029/JB091iB12p12269

Kinoshita, M., Tobin, H., Ashi, J., Kimura, G., Lallemant, S., Screaton, E. J., et al. (2009). *Proc. IODP, 314/315/316*. Washington, DC: Integrated Ocean Drilling Program Management International. doi: 10.2204/iodp.proc.314315316.2009

Kita, I., Matsuo, S., and Wakita, H. (1982). H2 generation by reaction between H2O and crushed rock: an experimental study on H2 degassing from the active fault zone. *J. Geophys. Res. Solid Earth* 87, 10789–10795. doi: 10.1029/JB087iB13p10789

Klein, E., Duputel, Z., Masson, F., Yavasoglu, H., and Agram, P. (2017). Aseismic slip and seismogenic coupling in the Marmara Sea: what can we learn from onland Geodesy? *Geophys. Res. Lett.* 44, 3100–3108. doi: 10.1002/2017GL072777

Kolandaivelu, K. P., Harris, R. N., Lowell, R. P., Alhamad, A., Gregory, E. P. M., and Hobbs, R. W. (2017). Analysis of a conductive heat flow profile in the Ecuador Fracture Zone. *Earth Planet. Sci. Lett.* 467, 120–127. doi: 10.1016/j.epsl.2017.03.024

Kolomijeca, A., Roland, F., Leon, P., and Kronfeldt, H.-D. (2013). Autonomous In-situ Raman sensor, suitable for surface enhanced Raman spectroscopy (SERS) for detection of chemicals in the Sea. *Univers. J. Appl. Sci.* 1, 38–43. doi: 10.13189/ujas.2013.010202

Konn, C., Charlou, J. L., Holm, N. G., and Mousis, O. (2015). The production of methane, hydrogen, and organic compounds in ultramafic-hosted hydrothermal vents of the Mid-Atlantic Ridge. *Astrobiology* 15, 381–399. doi: 10.1089/ast.2014.1198

Kopf, A., and Deyhle, A. (2002). Back to the roots: boron geochemistry of mud volcanoes and its implications for mobilization depth and global B cycling. *Chem. Geol.* 192, 195–210. doi: 10.1016/S0009-2541(02)00221-8

Krylova, E. M., Sahling, H., and Janssen, R. (2010). Abyssogena: a new genus of the family Vesicomyidae (Bivalvia) from deep-water vents and seeps. *J. Molluscan Stud.* 76, 107–132. doi: 10.1093/mollus/eyp052

Kuhn, T., Versteegh, G. J. M., Villinger, H., Dohrmann, I., Heller, C., Koschinsky, A., et al. (2017). Widespread seawater circulation in 18–22 Ma oceanic crust: impact on heat flow and sediment geochemistry. *Geology* 45, 799–802. doi: 10.1130/G39091.1

Kuşçu, İ., Okamura, M., Matsuoka, H., Gökaşan, E., Awata, Y., Tur, H., et al. (2005). Seafloor gas seeps and sediment failures triggered by the August 17, 1999 earthquake in the Eastern part of the Gulf of İzmit, Sea of Marmara, NW Turkey. *Mar. Geol.* 215, 193–214. doi: 10.1016/j.margeo.2004.12.002

Kutterolf, S., Liebetrau, V., Mörz, T., Freundt, A., Hammerich, T., and Garbe-Schönberg, D. (2008). Lifetime and cyclicity of fluid venting at forearc mound structures determined by tephrostratigraphy and radiometric dating of authigenic carbonates. *Geology* 36, 707–710. doi: 10.1130/G24806A.1

Lahr, J. C., Page, R. A., Stephens, C. D., and Christensen, D. H. (1988). Unusual earthquakes in the Gulf of Alaska and fragmentation of the Pacific Plate. *Geophys. Res. Lett.* 15, 1483–1486. doi: 10.1029/GL015i013p01483

Lang, S. O., Früh-Green, G. L., Bernasconi, S. M., Brazelton, W. J., Schrenk, M. O., and McGonigle, J. M. (2018). Deeply-sourced formate fuels sulfate reducers but not methanogens at Lost City Hydrothermal Field. *Sci. Rep.* 8:755. doi: 10.1038/s41598-017-19002-5

Langseth, M. G., and Hobart, M. A. (1976). Interpretation of heat flow measurements in the Vema Fracture Zone. *Geophys. Res. Lett.* 3, 241–244. doi: 10.1029/GL003i005p00241

LaRowe, D. E., Burwicz, E., Arndt, S., Dale, A. W., and Amend, J. P. (2017). Temperature and volume of global marine sediments. *Geology* 45, 275–278. doi: 10.1130/G38601.1

Lay, T. (2019). "Chapter 4 - reactivation of oceanic fracture zones in large intraplate earthquakes?," in *Transform Plate Boundaries and Fracture Zones*, ed. J. C. Duarte (Amsterdam: Elsevier), 89–104. doi: 10.1016/B978-0-12-812064-4.00004-9

Lay, T., and Wallace, T. C. (1995). *Modern Global Seismology*. San Diego, CA: Academic Press, 521.

Le Gal, V., Lucazeau, F., Cannat, M., Poort, J., Monnin, C., Battani, A., et al. (2018). Heat flow, morphology, pore fluids and hydrothermal circulation in a typical Mid-Atlantic Ridge flank near Oceanographer Fracture Zone. *Earth Planet. Sci. Lett.* 482, 423–433. doi: 10.1016/j.epsl.2017.11.035

Le Pichon, X., and Angelier, J. (1979). The Hellenic arc and trench system: a key to the neotectonic evolution of the eastern Mediterranean area. *Tectonophysics* 60, 1–42. doi: 10.1016/0040-1951(79)90131-8

Le Pichon, X., and Angelier, J. (1981). The Aegean Sea. *Philos. Trans. R. Soc. Lond.* 300, 357–372. doi: 10.1098/rsta.1981.0069

Le Pichon, X., Şengör, A. M. C., Demirbağ, E., Rangin, C., Imren, C., Armijo, R., et al. (2001). The active main Marmara fault: comparative anatomy of a continental transform fault in a marine setting. *Earth Planet. Sci. Lett.* 192, 595–616. doi: 10.1016/S0012-821X(01)00449-6

Le Pichon, X., Şengör, A. M. C., Kende, J., İmren, C., Henry, P., Grall, C., et al. (2015). Propagation of a strike slip plate boundary within an extensional environment: the westward propagation of the North Anatolian Fault. *Can. J. Earth Sci.* 53, 1416–1439. doi: 10.1139/cjes-2015-0129

Lever, M. A., Rogers, K., Lloyd, K. G., Overmann, J. O., Schink, B., Thauer, R. K., et al. (2015). Microbial life under extreme energy limitation: a synthesis of laboratory- and field-based investigations. *FEMS Microbiol. Rev.* 39, 688–728. doi: 10.1093/femsre/fuv020

Lever, M. A., Rouxel, O., Alt, J. C., Shimizu, N., Ono, S., Coggon, R. M., et al. (2013). Evidence for microbial carbon and sulfur cycling in deeply buried ridge flank basalt. *Science* 339, 1305–1308. doi: 10.1126/science.1229240

Levin, L. A. (2005). Ecology of cold seep sediments: interactions of fauna with flow, chemistry and microbes. *Oceanogr. Mar. Biol. Ann. Rev.* 43, 1–46. doi: 10.1201/9781420037449.ch1

Liebetrau, V., Augustin, N., Kutterolf, S., Schmidt, M., Eisenhauer, A., Garbe-Schönberg, D., et al. (2014). Cold-seep-driven carbonate deposits at the Central American forearc: contrasting evolution and timing in escarpment and mound settings. *Int. J. Earth Sci.* 103, 1845–1872. doi: 10.1007/s00531-014-1045-2

Liebetrau, V., Eisenhauer, A., and Linke, P. (2010). Cold seep carbonates and associated coldwater corals at the Hikurangi Margin, New Zealand: new insights into fluid pathways, growth structures and geochronology. *Mar. Geol.* 272, 307–318. doi: 10.1016/j.margeo.2010.01.003

Ligi, M., Bonatti, E., Gasperini, L., and Poliakov, A. N. B. (2002). Oceanic broad mutifault transform plate boundaries. *Geology* 30, 11–14. doi: 10.1130/0091-7613(2002)030<0011:OBMTPB>2.0.CO;2

Lindsey, N. J., Martin, E. R., Dreger, D. S., Freifeld, B., Cole, S., James, S. R., et al. (2017). Fiber-optic network observations of earthquake wavefields. *Geophys. Res. Lett.* 44, 11,792–11,799. doi: 10.1002/2017GL075722

Linke, P., Schmidt, M., Rohleder, M., Al-Barakati, A., and Al-Farawati, R. (2015). Novel online digital video and high-speed data broadcasting via standard coaxial cable onboard marine operating vessels. *Mar. Technol. Soc. J.* 49, 7–18. doi: 10.4031/MTSJ.49.1.2

Lister, C. R. J., Sclater, G., Davis, E. E., Villinger, H., and Nagihara, S. (1990). Heat flow maintained in ocean basins of great age: investigations in the north-equatorial West Pacific. *Geophys. J. Int.* 102, 603–630. doi: 10.1111/j.1365-246X.1990.tb04586.x

Lo Iacono, C., Gràcia, E., Zaniboni, F., Pagnoni, G., Tinti, S., Bartolomé, R., et al. (2012). Large, deepwater slope failures: implications for landslide-generated tsunamis. *Geology* 40, 931–934. doi: 10.1130/G33446.1

Londry, K. L., Dawson, K. G., Grover, H. D., Summons, R. E., and Bradley, A. S. (2008). Stable carbon isotope fractionation between substrates and products of *Methanosarcina barkeri*. *Org. Geochem.* 39, 608–621. doi: 10.1016/j.orggeochem.2008.03.002

Lonsdale, P. (1986). Tectonic and magmatic ridges in the Eltanin fault system, South Pacific. *Mar. Geophys. Res.* 8, 203–242. doi: 10.1007/BF00305484

Lucazeau, F., Bonneville, A., Escartìn, J., Von Herzen, R. P., Gouze, P., Carton, H., et al. (2006). Heat-flow variations on a slowly accreting ridge: constraints on the hydrothermal and conductive cooling for the lucky strike segment (mid Atlantic ridge, 37°N). *Geochem. Geophys. Geosyst.* 7:Q07011. doi: 10.1029/2005GC001178

Lupi, M., Fallahi, M. J., Mazzini, A., Polonia, A., D'Alessandro, A., D'Anna, G., et al. (2018). "Seismic activity of mud volcanoes in the Marmara Sea, Turkey," in *Proceedings of the 20th EGU General Assembly, EGU2018* (Vienna: Geophysical Research Abstracts), 14482.

Lupi, M., Fuchs, F., and Pacheco, J. F. J. (2014). Fault reactivation due to the M 7.6 Nicoya earthquake at the Turrialba-Irazú volcanic complex, Costa Rica: effects of dynamic stress triggering. *Geophys. Res. Lett.* 41, 4142–4148. doi: 10.1002/2014GL059942

Lupi, M., Geiger, S., and Graham, C. M. (2011a). Numerical simulations of seismicity-induced fluid flow in the Tjörnes Fracture Zone, Iceland. *J. Geophys. Res.* 116:B07101. doi: 10.1029/2010JB007732

Lupi, M., Ricci, T., Suski, B., Kenkel, J., Fuchs, F., Miller, S. A., et al. (2015). Subsurface fluid distribution and possible seismic precursory signal at the Salse di Nirano mud volcanic field, Italy. *Geophys. J. Int.* 204, 907–917. doi: 10.1093/gji/ggv454

Lupi, M., Saenger, E. H., Fuchs, F., and Miller, S. A. (2013). Lusi mud eruption triggered by geometric focusing of seismic waves. *Nat. Geosci.* 6, 642–646. doi: 10.1038/ngeo2239

Macdonald, K. C. (1998). Linkages between faulting, volcanism, hydrothermal activity and segmentation on fast spreading

centers. *Geophys. Monogr. Ser.* 106, 27–58. doi: 10.1029/GM106p0027

Mächler, L., Brennwald, M. S., and Kipfer, R. (2012). Membrane inlet mass spectrometer for the quasi-continuous on-site analysis of dissolved gases in groundwater. *Environ. Sci. Technol.* 46, 8288–8296. doi: 10.1021/es3004409

Mächler, L., Brennwald, M. S., Tyroller, L., Livingstone, D. M., and Kipfer, R. (2014). Conquering the outdoors with on-site mass spectrometry. *Chimia* 68, 155–159. doi: 10.2533/chimia.2014.155

Magalhães, V. H., Pinheiro, L. M., Ivanov, M. K., Kozlova, E., Blinova, V., Kolganova, J., et al. (2012). Formation processes of methane-derived authigenic carbonates from the Gulf of Cadiz. *Sediment. Geol.* 243–244, 155–168. doi: 10.1016/j.sedgeo.2011.10.013

Maia, M. (2019). "Topographic and morphologic evidences of deformation at oceanic transform faults: far-field and local-field stresses," in *Transform Plate Boundaries and Fracture Zones*, ed. J. C. Duarte (Amsterdam: Elsevier), 61–87. doi: 10.1016/B978-0-12-812064-4.00003-7

Mamyrin, B. A., and Tolstikhin, I. N. (1984). "Helium isotopes in nature," in *Developments in Geochemistry*, Vol. 3, ed. W. S. Fyfe (Amsterdam: Elsevier).

Manga, M., and Brodsky, E. (2006). Seismic triggering of eruptions in the far field: volcanoes and geysers. *Annu. Rev. Earth Planet. Sci.* 34, 263–291. doi: 10.1146/annurev.earth.34.031405.125125

Manga, M., Brumm, M., and Rudolph, M. L. (2009). Earthquake triggering of mud volcanoes. *Mar. Pet. Geol.* 26, 1785–1798. doi: 10.1016/j.marpetgeo.2009.01.019

Manning, C. E., and Ingebritsen, S. (1999). Permeability of the continental crust: implications of geothermal data and metamorphic systems. *Rev. Geophys.* 37, 127–150. doi: 10.1029/1998RG900002

Marques, F. O., Cobbold, P. R., and Lourenço, N. (2007). Physical models of rifting and transform faulting, due to ridge push in a wedge-shaped oceanic lithosphere. *Tectonophysics* 443, 37–52. doi: 10.1016/j.tecto.2007.07.002

Marra, G., Clivati, C., Luckett, R., Tampellini, A., Kronjäger, J., Wright, L., et al. (2018). Ultrastable laser interferometry for earthquake detection with terrestrial and submarine cables. *Science* 361, 486–490. doi: 10.1126/science.aat4458

Martin, J. B., Orange, D. L., Lorenson, T. D., and Kvenvolden, K. A. (1997). Chemical and isotopic evidence of gas influenced flow at a transform plate boundary: monterey Bay, California. *J. Geophys. Res.* 102, 24903–24915. doi: 10.1029/97JB02154

Martínez-Loriente, S., Sallarès, V., Gràcia, E., Bartolome, R., Dañobeitia, J. J., and Zitellini, N. (2014). Seismic and gravity constraints on the nature of the basement in the Africa-Eurasia plate boundary: new insights for the geodynamic evolution of the SW Iberian margin. *J. Geophys. Res. Solid Earth* 119, 127–149. doi: 10.1002/2013JB010476

Materna, K., Taira, T. A., and Bürgmann, R. (2018). Aseismic transform fault slip at the mendocino triple junction from characteristically repeating earthquakes. *Geophys. Res. Lett.* 45, 699–707. doi: 10.1002/2017GL075899

Mau, S., Rehder, G., Arroyo, I. G., Gossler, J., and Suess, E. (2007). Indications of a link between seismotectonics and CH4 release from seeps off Costa Rica. *Geochem. Geophys. Geosyst.* 8:Q04003. doi: 10.1029/2006GC001326

Mazzini, A., and Etiope, G. (2017). Mud volcanism: an updated review. *Earth Sci. Rev.* 168, 81–112. doi: 10.1016/j.earscirev.2017.03.001

Mazzini, A., Etiope, G., and Svensen, H. (2012). A new hydrothermal scenario for the 2006 Lusi eruption, Indonesia - Insights from gas geochemistry. *Earth Planet. Sci. Lett.* 317, 305–318. doi: 10.1016/j.epsl.2011.11.016

Mazzini, A., Nermoen, A., Krotkiewski, M., Podladchikov, Y., Planke, S., and Svensen, H. (2009). Strike-slip faulting as a trigger mechanism for overpressure release through piercement structures - Implications for the Lusi mud volcano, Indonesia. *Mar. Petrol. Geol.* 26, 1751–1765. doi: 10.1016/j.marpetgeo.2009.03.001

McClusky, S., Balassanian, S., Barka, A., Demir, C., Ergintav, S., Georgiev, I., et al. (2000). Global Positioning System constraints on plate kinematics and dynamics in the eastern Mediterranean and Caucasus. *J. Geophys. Res.* 105, 5695–5719. doi: 10.1029/1999JB900351

McCollom, T. M., and Seewald, J. S. (2007). Abiotic synthesis of organic compounds in deep-sea hydrothermal environments. *Chem. Rev.* 107, 382–401. doi: 10.1021/cr0503660

McGuire, J. J., Boettcher, M. S., and Jordan, T. H. (2005). Foreshock sequences and short-term earthquake predictability on East Pacific Rise transform faults. *Nature* 434, 457–461. doi: 10.1038/nature03377

McGuire, J. J., Collins, J. A., Gouédard, P., Roland, E., Lizarralde, D., Boettcher, M. S., et al. (2012). Variations in earthquake rupture properties along the Gofar transform fault, East Pacific Rise. *Nat. Geosci.* 5, 336–341. doi: 10.1038/ngeo1454

McHugh, C. M. G., Braudy, N., Çağatay, M. N., Sorlien, C., Cormier, M.-H., Seeber, L., et al. (2014). Seafloor fault ruptures along the North Anatolia Fault in the Marmara Sea, Turkey: link with the adjacent basin turbidite record. *Mar. Geol.* 353, 65–83. doi: 10.1016/j.margeo.2014.03.005.0025-3227/

McHugh, C. M. G., Seeber, L., Cormier, M. H., Dutton, J., Çağatay, M. N., Polonia, A., et al. (2006). Submarine earthquake geology along the North Anatolia Fault in the Marmara Sea, Turkey: a model for transform basin sedimentation. *Earth Planet. Sci. Lett.* 248, 661–668. doi: 10.1016/j.epsl.2006.05.038

McKenzie, D. P. (1978). Active tectonics of the Alpine Himalayan Belt, the Aegean Sea and surrounding regions. *Geophys. J. Int.* 55, 217–252. doi: 10.1111/j.1365-246X.1978.tb04759.x

Meade, B. J., Hager, B. H., McClusky, S., Reilinger, R., Ergintav, S., Lenk, O., et al. (2002). Estimates of seismic potential in the marmara sea region from block models of secular deformation constrained by global positioning system measurements. *Bull. Seismol. Soc. Am.* 92, 208–215. doi: 10.1785/0120000837

Méhay, S., Früh-Green, G. L., Lang, S. Q., Bernasconi, S. M., Brazelton, W. J., Schrenk, M. O., et al. (2013). Record of archaeal activity at the serpentinite hosted Lost City Hydrothermal Field. *Geobiology* 11, 570–592. doi: 10.1111/gbi.12062

Mellors, R., Kilb, D., Aliyev, A., Gasanov, A., and Yetirmishli, G. (2007). Correlations between earthquakes and large mud volcano eruptions. *J. Geophys. Res.* 112:B04304. doi: 10.1029/2006JB004489

Ménez, B., Pisapia, C., Andreani, M., Jamme, F., Vanbellingen, Q. P., Brunelle, A., et al. (2018). Abiotic synthesis of amino acids in the recesses of the oceanic lithosphere. *Nature* 564, 59–63. doi: 10.1038/s41586-018-0684-z

Miller, S. A., Collettini, C., Chiaraluce, L., Cocco, M., Barchi, M., and Kaus, B. J. P. (2004). Aftershocks driven by a high-pressure CO2 source at depth. *Nature* 427, 724–727. doi: 10.1038/nature02251

Miller, S. A., and Mazzini, A. (2018). More than ten years of Lusi: a review of facts, coincidences, and past and future studies. *Mar. Petrol. Geol.* 90, 10–25. doi: 10.1016/j.marpetgeo.2017.06.019

Moore, D. E., Lockner, D. A., Ma, S., Summers, R., and Byerlee, J. D. (1997). Strengths of serpentinite gouges at elevated temperatures. *J. Geophys. Res. Solid Earth* 102, 14787–14801. doi: 10.1029/97JB00995

Moore, D. E., and Rymer, M. J. (2007). Talc-bearing serpentinite and the creeping section of the San Andreas fault. *Nature* 448, 795–797. doi: 10.1038/nature06064

Morgan, J. P., and Parmentier, E. M. (1984). Lithospheric stress near a ridge-transform intersection. *Geophys. Res. Lett.* 11, 113–116. doi: 10.1029/GL011i002p00113

Morgan, W. J. (1968). Rises, trenches, great faults, and crustal blocks. *J. Geophys. Res.* 73, 1959–1981. doi: 10.1029/JB073i006p01959

Mottl, M. J., Wheat, C. G., Fryer, P., Gharib, J., and Martin, J.-B. (2004). Chemistry of springs across the Mariana forearc shows progressive devolatilization of the subducting plate. *Geochim. Cosmochim. Acta* 68, 4915–4933. doi: 10.1016/j.gca.2004.05.037

Mourgues, R., and Cobbold, P. R. (2003). Some tectonic consequences of fluid overpressures and seepage forces as demonstrated by sandbox modeling. *Tectonophysics* 376, 75–97. doi: 10.1016/S0040-1951(03)00348-2

Mourgues, R., and Cobbold, P. R. (2006). Sandbox experiments on gravitational spreading and gliding in the presence of fluid overpressures. *J. Struct. Geol.* 28, 887–901. doi: 10.1016/j.jsg.2005.12.013

Müller, M. D., Geiger, A., Kahle, H.-G., Veis, G., Billiris, H., Paradissis, D., et al. (2013). Velocity and deformation fields in the North Aegean domain, Greece, and implications for fault kinematics, derived from GPS data 1993–2009. *Tectonophysics* 597–598, 34–49. doi: 10.1016/j.tecto.2012.08.003

Müller, R. D., Sdrolias, M., Gaina, C., and Roest, W. R. (2008). Age spreading rates and spreading asymmetry of the world's ocean crust. *Geochem. Geophys. Geosyst.* 9:Q04006. doi: 10.1029/2007GC001743

Neres, M., Carafa, M. M. C., Fernandes, R. M. S., Matias, L., Duarte, J. C., Barba, S., et al. (2016). Lithospheric deformation in the Africa-Iberia plate boundary: improved neotectonic modeling testing a basal-driven Alboran plate. *J. Geophys. Res. Solid Earth* 121, 6566–6596. doi: 10.1002/2016JB013012

Niemann, H., Duarte, J., Hensen, C., Omoregie, E., Magalhães, V. H., Elvert, M., et al. (2006). Microbial methane turnover at mud volcanoes of the Gulf of Cadiz. *Geochim. Cosmochim. Acta* 70, 5336–5355. doi: 10.1016/j.gca.2006.08.010

Noda, H., Sawai, M., and Shibazaki, B. (2017). Earthquake sequence simulations with measured properties for JFAST core samples. *Philos. Trans. R. Soc. A Math. Phys. Eng. Sci.* 375:20160003. doi: 10.1098/rsta.2016.0003

Norris, R. J., and Toy, V. G. (2014). Continental transforms: a view from the Alpine Fault. *J. Struct. Geol.* 64, 3–31. doi: 10.1016/j.jsg.2014.03.003

Nuzzo, M., Tomonaga, Y., Schmidt, M., Valadares, V., Faber, E., Piñero, E., et al. (2019). Formation and migration of hydrocarbons in deeply buried sediments of the Gulf of Cadiz convergent plate boundary - Insights from the hydrocarbon and helium isotope geochemistry of mud volcano fluids. *Mar. Geol.* 410, 56–69. doi: 10.1016/j.margeo.2019.01.005

Ohara, Y., Reagan, M. K., Fujikura, K., Watanabe, H., Michibayashi, K., Ishii, T., et al. (2012). A serpentinite-hosted ecosystem in the Southern Mariana Forearc. *Proc. Natl. Acad. Sci. U.S.A.* 109, 2831–2835. doi: 10.1073/pnas.1112005109

Okal, E. A., and Stewart, L. M. (1982). Slow earthquakes along oceanic fracture zones: evidence for asthenospheric flow away from hotspots? *Earth Planet. Sci. Lett.* 57, 75–87. doi: 10.1016/0012-821X(82)90174-1

Okumura, T., Ohara, Y., Stern, R. J., Yamanaka, T., Onishi, Y., Watanabe, H., et al. (2016). Brucite chimney formation and carbonate alteration at the Shinkai Seep Field, a serpentinite-hosted vent system in the southern Mariana forearc. *Geochem. Geophys. Geosyst.* 17, 3775–3796. doi: 10.1002/2016GC006449

Oldenburg, D. W., and Brune, J. N. (1972). Ridge transform fault spreading pattern in freezing wax. *Science* 178, 301–304. doi: 10.1126/science.178.4058.301

Oldenburg, D. W., and Brune, J. N. (1975). An Explanation for the orthogonality of ocean ridges and transform faults. *J. Geophys. Res.* 80, 2575–2585. doi: 10.1029/JB080i017p02575

Omira, R., Ramalho, I., Terrinha, P., Baptista, M. A., Batista, L., and Zitellini, N. (2016). Deep-water seamounts, a potential source of tsunami generated by landslides? – The Hirondelle seamount, NE Atlantic. *Mar. Geol.* 379, 267–280. doi: 10.1016/j.margeo.2016.06.010

O'Mullan, G. D., Maas, P. A. Y., Lutz, R. A., and Vrijenhoek, R. C. (2001). A hybrid zone between hydrothermal vent mussels (Bivalvia: Mytilidae) from the Mid-Atlantic Ridge. *Mol. Ecol.* 10, 2819–2831. doi: 10.1046/j.0962-1083.2001.01401.x

Onishi, Y., Yamanaka, T., Okumura, T., Kawagucci, S., Watanabe, H. K., and Ohara, Y. (2018). Evaluation of nutrient and energy sources of the deepest known serpentinite-hosted ecosystem using stable carbon, nitrogen, and sulfur isotopes. *PLoS One* 13:e0199000. doi: 10.1371/journal.pone.0199000

Ostrander, W. J. (1984). Plane-wave reflection coefficients for gas sands at non-normal angles of incidence. *Geophysics* 49, 1637–1648. doi: 10.1190/1.1441571

Pagli, C. (2003). Triggered fault slip on June 17, 2000 on the Reykjanes Peninsula, SW-Iceland captured by radar interferometry. *Geophys. Res. Lett.* 30:1273. doi: 10.1029/2002GL015310

Palmer, M. R. (1991). Boron isotope systematics of hydrothermal fluids and tourmalines: a synthesis. *Chem. Geol.* 94, 111–121. doi: 10.1016/S0009-2541(10)80023-3

Parsons, T., Toda, S., Stein, R. S., Barka, A., and Dieterich, J. H. (2000). Heightenined odds of large earthquake near Istanbul: an interaction-based probability calculation. *Science* 288, 661–666. doi: 10.1126/science.288.5466.661

Paull, C. K., Ussler, W. I. I. I., Peltzer, E. T., Brewer, P. G., Keaten, R., Mitts, P. J., et al. (2007). Authigenic carbon entombed in methane-soaked sediments from northeastern transform margin of the Guaymas Basin, Gulf of California. *Deep Sea Res. II* 54, 1240–1267. doi: 10.1016/j.dsr2.2007.04.009

Penning, H., Plugge, C. M., Galand, P. E., and Conrad, R. (2005). Variation of carbon isotope fractionation in hydrogenotrophic methanogenic microbial cultures and environmental samples at different energy status. *Glob. Chang. Biol.* 11, 2103–2113. doi: 10.1111/j.1365-2486.2005.01076.x

Pierre, C., Blanc-Valleron, M. M., Demange, J., Boudouma, O., Foucher, J. P., Pape, T., et al. (2012). Authigenic carbonates from active methane seeps offshore southwest Africa. *Geo Mar. Lett.* 32, 501–513. doi: 10.1007/s00367-012-0295-x

Polonia, A., Gasperini, L., Amorosi, A., Bonatti, E., Çağatay, N., Capotondi, L., et al. (2004). Holocene slip rate of the North Anatolian Fault beneath the Sea of Marmara. *Earth Planet. Sci. Lett.* 227, 411–426. doi: 10.1016/j.epsl.2004.07.042

Polonia, A., Panieri, G., Gasperini, L., Gasparotto, G., Bellucci, L. G., and Torelli, L. (2013). Turbidite paleoseismology in the Calabrian Arc Subduction Complex (Ionian Sea). *Geochem. Geophys. Geosyst.* 14, 112–140. doi: 10.1029/2012GC004402

Polonia, A., Romano, S., Çağatay, M. N., Capotondi, L., Gasparotto, G., Gasperini, L., et al. (2015). Are repetitive slumpings during sapropel S1 related to paleo-earthquakes? *Mar. Geol.* 361, 41–52. doi: 10.1016/j.margeo.2015.01.001

Polonia, A., Torelli, L., Gasperini, L., Cocchi, L., Muccini, F., Bonatti, E., et al. (2017). Lower plate serpentinite diapirism in the Calabrian Arc subduction complex. *Nat. Commun.* 8:2172. doi: 10.1038/s41467-017-02273-x

Pouderoux, H., Lamarche, G., and Proust, J.-N. (2012). Building an 18 000-year-long paleo-earthquake record from detailed deep-sea turbidite characterisation in Poverty Bay, New Zealand. *Nat. Hazards Earth Syst. Sci.* 12, 2077–2101. doi: 10.5194/nhess-12-2077-2012

Prokurowski, G., Lilley, M. D., Seewald, J. S., Früh-Green, G. L., Olson, E. J., Lupton, J. E., et al. (2008). Abiogenic hydrocarbon production at Lost City Hydrothermal Field. *Science* 319, 604–607. doi: 10.1126/science.1151194

Ritt, B., Sarrazin, J., Caprais, J.-C., Noël, P., Gauthier, O., Pierre, C., et al. (2010). First insights into the structure and environmental setting of cold-seep communities in the Marmara Sea. *Deep Sea Res. Part I Oceanogr. Res. Pap.* 57, 1120–1136. doi: 10.1016/j.dsr.2010.05.011

Robinson, D. P., Henry, C., Das, S., and Woodhouse, J. H. (2001). Simultaneous rupture along two conjugate planes of the Wharton Basin earthquake. *Science* 292, 1145–1148. doi: 10.1126/science.1059395

Roeloffs, E., Sneed, M., Galloway, D. L., Sorey, M. L., Farrar, C. D., Howle, J. F., et al. (2003). Water-level changes induced by local and distant earthquakes at Long Valley caldera, California. *J. Volcanol. Geotherm. Res.* 127, 269–303. doi: 10.1016/S0377-0273(03)00173-2

Roland, E., Behn, M. D., and Hirth, G. (2010). Thermal-mechanical behavior of oceanic transform faults: implications for the spatial distribution of seismicity. *Geochem. Geophys. Geosyst.* 11:Q07001. doi: 10.1029/2010GC003034

Romanowicz, B. (1992). Strike-slip earthquakes on quasi-vertical transcurrent faults: inferences for general scaling relations. *Geophys. Res. Lett.* 19, 481–484. doi: 10.1029/92GL00265

Rosas, F. M., Duarte, J., Terrinha, P., Valadares, V., and Matias, L. (2009). Morphotectonic characterization of major bathymetric lineaments in NW Gulf of Cadiz (Africa-Iberia plate boundary): insights from analogue modelling experiments. *Mar. Geol.* 261, 33–47. doi: 10.1016/j.margeo.2008.08.002

Rosas, F. M., Duarte, J. C., Terrinha, P., and Schellart, W. P. (2016). "Seismic potential of thrust-wrench tectonic interference between major active faults offshore SW iberia: a new explanation for the 1755 great lisbon earthquake?," in *Plate Boudaries and Natural Hazards*, eds J. C. Duarte and W. P. Schellart (New Jersey, NJ: Wiley-Blackwell). doi: 10.1002/9781119054146.ch9

Ruffine, L., Donval, J.-P., Croguennec, C., Burnard, P., Luc, H., Germain, Y., et al. (2018a). Multiple gas reservoirs are responsible for the gas emissions along the Marmara fault network. *Deep Sea Res. Part II* 153, 48–60. doi: 10.1016/j.dsr2.2017.11.011

Ruffine, L., and Geli, L. (2014). *MARSITECruise Report. 2014 1st–13th November – Leg 2*. Issy-les-Moulineaux: Ifremer. doi: 10.13155/56480

Ruffine, L., Ondreas, H., Blanc-Valleron, M.-M., Teichert, B. M. A., Scalabrin, C., Rinnert, E., et al. (2018b). Multidisciplinary investigation on cold seeps with vigorous gas emissions in the Sea of Marmara (MarsiteCruise): strategy for site detection and sampling and first scientific outcome. *Deep Sea Res. Part II Top. Stud. Oceanogr.* 153, 36–47. doi: 10.1016/j.dsr2.2018.03.006

Ruhl, H. A., André, M., Beranzoli, L., Çağatay, M. N., Colaço, A., Cannat, M., et al. (2011). Societal need for improved understanding of climate change, anthropogenic impacts, and geo-hazard warning drive development of ocean observatories in European Seas. *Prog. Oceanogr.* 91, 1–33. doi: 10.1016/j.pocean.2011.05.001

Ryan, W. B. F., Carbotte, S. M., Coplan, J. O., O'Hara, S., Melkonian, A., Arko, R., et al. (2009). Global multi-resolution topography synthesis. *Geochem. Geophys. Geosyst.* 10:Q03014. doi: 10.1029/2008GC002332

Sakellariou, D., Rousakis, G., Morfis, I., Panagiotopoulos, I., Ioakim, C., Trikalinou, G., et al. (2018). "Deformation and kinematics at the termination of the North Anatolian Fault: the North Aegean Trough horsetail structure," in *Proceedings of the 9th International INQUA Meeting on Paleoseismology, Active Tectonics and Archeoseismology, 25-27 June 2018*, Possidi. <doi>

Sakellariou, D., and Tsampouraki-Kraounaki, K. (2019). "Chapter 14 - plio-quaternary extension and strike-slip tectonics in the aegean," in *Transform Plate Boundaries and Fracture Zones*, ed. J. C. Duarte (Amsterdam: Elsevier), 339–374. doi: 10.1016/B978-0-12-812064-4.00014-1

Sakic, P., Piété, H., Ballu, V., Royer, J.-Y., Kopp, H., Lange, D., et al. (2016). No significant steady state surface creep along the North Anatolian Fault offshore

Istanbul: results of 6 months of seafloor acoustic ranging. *Geophys. Res. Lett.* 43, 6817–6825. doi: 10.1002/2016GL069600

Sallarès, V., Martínez-Loriente, S., Prada, M., Gràcia, E., Ranero, C., Gutscher, M.-A., et al. (2013). Seismic evidence of exhumed mantle rock basement at the Gorringe Bank and the adjacent Horseshoe and Tagus abyssal plains (SW Iberia). *Earth Planet. Sci. Lett.* 365, 120–131. doi: 10.1016/j.epsl.2013.01.021

Sandwell, D. (1986). Thermal stress and the spacings of transform faults. *J. Geophys. Res.* 91, 6405–6417. doi: 10.1029/JB091iB06p06405

Sano, Y., Hara, T., Takahata, N., Kawagucci, S., Honda, M., Nishio, Y., et al. (2014). Helium anomalies suggest a fluid pathway from mantle to trench during the 2011 Tohoku-Oki earthquake. *Nat. Commun.* 5:3084. doi: 10.1038/ncomms4084

Sano, Y., Nakamura, Y., Wakita, H., Notsu, K., and Kobayashi, Y. (1986). 3He/4He ratio anomalies associated with the 1984 Western Nagano Earthquake: possibly induced by a diapiric magma. *J. Geophys. Res. Solid Earth* 91, 12291–12295. doi: 10.1029/JB091iB12p12291

Sano, Y., Takahata, N., Kagoshima, T., Shibata, T., Onoue, T., and Zhao, D. (2016). Groundwater helium anomaly reflects strain change during the 2016 Kumamoto earthquake in Southwest Japan. *Sci. Rep.* 6:37939. doi: 10.1038/srep37939

Sarı, E., and Çağatay, M. N. (2006). Turbidites and their association with past earthquakes in the deep Çinarcik Basin of the Marmara Sea. *Geo Mar. Lett.* 26, 69–76. doi: 10.1007/s00367-006-0017-359

Sartori, R., Torelli, L., Zitellini, N., Peis, D., and Lodolo, E. (1994). Eastern segment of the Azores–Gibraltar line (central–eastern Atlantic); an oceanic plate boundary with diffuse compressional deformation. *Geology* 22, 555–558. doi: 10.1130/0091-7613(1994)022<0555:ESOTAG>2.3.CO;2

Schmidt, C., Burwicz, E., Hensen, C., Wallmann, K., Martínez-Loriente, S., and Gràcia, E. (2018). Genesis of mud volcano fluids in the Gulf of Cadiz using a novel basin-scale model approach. *Geochim. Cosmochim. Acta* 243, 186–204. doi: 10.1016/j.gca.2018.09.011

Schmidt, K., Koschinsky, A., Garbe-Schönberg, D., de Carvalho, L. M., and Seifert, R. (2007). Geochemistry of hydrothermal fluids from the ultramafic-hosted Logatchev hydrothermal field, 15°N on the Mid-Atlantic Ridge: temporal and spatial investigation. *Chem. Geol.* 242, 1–21. doi: 10.1016/j.chemgeo.2007.01.023

Schmidt, M., Linke, P., Sommer, S., Esser, D., and Cherednichenko, S. (2015). Natural CO2 seeps offshore Panarea - a test site for subsea CO2 leak detection technology. *Mar. Technol. Soc. J.* 49, 19–30. doi: 10.4031/MTSJ.49.1.3

Schmittbuhl, J., Karabulut, H., Lenligné, O., and Bouchon, M. (2016). Seismicity distribution and locking depth along the Main Marmara Fault, Turkey. *Geochem. Geophys. Geosyst.* 17, 954–965. doi: 10.1002/2015GC006120

Scholz, F., Hensen, C., Lu, Z., and Fehn, U. (2010). Controls on the 129I/I ratio of deep-seated marine interstitial fluids: 'old' organic versus fissiogenic 129-iodine. *Earth Planet. Sci. Lett.* 294, 27–36. doi: 10.1016/j.epsl.2010.02.034

Scholz, F., Hensen, C., Reitz, A., Romer, R. L., Liebetrau, V., Meixner, A., et al. (2009). Isotopic evidence (87Sr/86Sr, δ7Li) for alteration of the oceanic crust at deep-rooted mud volcanoes in the Gulf of Cadiz, NE Atlantic Ocean. *Geochim. Cosmochim. Acta* 73, 5444–5459. doi: 10.1016/j.gca.2009.06.004

Schulte, M., and Shock, E. (1995). Thermodynamics of Strecker synthesis in hydrothermal systems. *Orig. Life Evol. Biosph.* 25, 161–173. doi: 10.1007/BF01581580

Şengör, A. M. C., Grall, C., İmren, C., Le Pichon, X., Görür, N., Henry, P., et al. (2014). The geometry of the North Anatolian transform fault in the Sea of Marmara and its temporal evolution: implications for the development of intracontinental transform faults. *Can. J. Earth Sci.* 51, 222–242. doi: 10.1139/cjes-2013-0160

Şengör, A. M. C., Zabcı, C., and Natal'in, B. A. (2019). "Chapter 9 - continental transform faults: congruence and incongruence with normal plate kinematics," in *Transform Plate Boundaries and Fracture Zones*, ed. J. C. Duarte (Amsterdam: Elsevier), 169–247. doi: 10.1016/B978-0-12-812064-4.00009-8

Seyfried, W. E., Pester, N. J., Tutolo, B. M., and Ding, K. (2015). The Lost City hydrothermal system: constraints imposed by vent fluid chemistry and reaction path models on subseafloor heat and mass transfer processes. *Geochim. Cosmochim. Acta* 163, 59–79. doi: 10.1139/cjes-2013-0160

Shapiro, S. A. (2000). An inversion for fluid transport properties of three-dimensionally heterogeneous rocks using induced microseismicity. *Geophys. J. Int.* 143, 931–936. doi: 10.1046/j.1365-246X.2000.00264.x

Shock, E. L. (1990). Geochemical constraints on the origin of organic compounds in hydrothermal systems. *Orig. Life Evol. Biosph.* 20, 331–367. doi: 10.1007/BF01808115

Silva, S., Terrinha, P., Matias, L., Duarte, J. C., Roque, C., Ranero, C. R., et al. (2017). Micro-seismicity in the Gulf of Cadiz: is there a link between micro-seismicity, high magnitude earthquakes and active faults? *Tectonophysics* 717, 226–241.

Skelton, A., Andrén, M., Kristmannsdóttir, H., Stockmann, G., Mörth, C.-M., Sveinbjörnsdóttir, Á., et al. (2014). Changes in groundwater chemistry before two consecutive earthquakes in Iceland. *Nat. Geosci.* 7, 752–756. doi: 10.1038/ngeo2250

Sobolev, S. V., Petrunin, A., Garfunkel, Z., and Babeyko, A. Y. (2005). Thermo-mechanical model of the Dead Sea Transform. *Earth Planet. Sci. Lett.* 238, 78–95. doi: 10.1016/j.epsl.2005.06.058

Sommer, S., Linke, P., Pfannkuche, O., Schleicher, T., Schneider, V., Deimling, J., et al. (2009). Seabed methane emissions and the habitat of frenulate tubeworms on the Captain Arutyunov mud volcano (Gulf of Cadiz). *Mar. Ecol. Prog. Ser.* 382, 69–86. doi: 10.3354/meps07956

Sommer, S., Schmidt, M., and Linke, P. (2015). Continuous inline tracking of dissolved methane plume at a blowout site in the Northern North Sea UK - water column stratification impedes immediate methane release into the atmosphere. *Mar. Petrol. Geol.* 68, 766–775. doi: 10.1016/j.marpetgeo.2015.08.020

Sone, H., Shimamoto, T., and Moore, D. E. (2012). Frictional properties of saponite-rich gouge from a serpentinite-bearing fault zone along the Gokasho-Arashima Tectonic Line, central Japan. *J. Struct. Geol.* 38, 172–182. doi: 10.1016/j.jsg.2011.09.007

Spinelli, G. A., Giambalvo, E. R., and Fisher, A. T. (2004). "Sediment permeability, distribution and influence on fluxes in oceanic basement," in *Hydrology of the Oceanic Lithosphere*, eds E. E. Davis and H. Elderfield (Cambridge: Cambridge University Press), 151–188.

Stakes, D. S., Trehu, A. M., Goffredi, S. K., Naehr, T. H., and Duncan, R. A. (2002). Mass wasting, methane venting, and biological communities on the Mendocino transform fault. *Geology* 30, 407–410. doi: 10.1130/0091-7613(2002)030<0407:MWMVAB>2.0.CO;2

Stein, C. A., and Stein, S. (1994). Constraints on hydrothermal heat flux through the oceanic lithosphere from global heat flow. *J. Geophys. Res.* 99, 3081–3095. doi: 10.1029/93JB02222

Stich, D., Ammon, C. J., and Morales, J. (2003). Moment-tensor solutions for small and moderate earthquakes in the Ibero-Maghreb region. *J. Geophys. Res.* 108, 21–48. doi: 10.1029/2002JB002057

Stich, D., Mancilla, F. D. L., Pondrelli, S., and Morales, J. (2007). Source analysis of the February 12th 2007, Mw 6.0 horseshoe earthquake: implications for the 1755 Lisbon earthquake. *Geophys. Res. Lett.* 34:L12308. doi: 10.1029/2007GL030012

Storti, F., Salvini, F., Rossetti, F., and Morgan, J. P. (2007). Intraplate termination of transform faulting within the Antarctic continent. *Earth Planet. Sci. Lett.* 260, 115–126. doi: 10.1016/j.epsl.2007.05.020

Strasser, M., Dugan, B., Kanagawa, K., Moore, G. F., Toczko, S., and Maeda, L. (2014). *Proc. IODP*. Yokohama: Integrated Ocean Drilling Program, 338. doi: 10.2204/iodp.proc.338.2014

Suess, E. (2014). Marine cold seeps and their manifestations: geological control, biogeochemical criteria and environmental conditions. *Int. J. Earth Sci.* 103, 1889–1916. doi: 10.1007/s00531-014-1010-0

Sumner, R. H., and Westbrook, G. K. (2001). Mud diapirism in front of the Barbados accretionary wedge: the influence of fracture zones and North America - South America plate motions. *Mar. Petrol. Geol.* 18, 591–613. doi: 10.1016/S0264-8172(01)00010-1

Teichert, B. M. A., Chevalier, N., Gussone, N., Bayon, G., Ponzevera, E., Ruffine, L., et al. (2018). Sulfate-dependent anaerobic oxidation of methane at a highly dynamic bubbling site in the Eastern Sea of Marmara (Çinarcik Basin). *Deep Sea Res. Part II* 153, 79–91. doi: 10.1016/j.dsr2.2017.11.014

Terrinha, P., Matias, L., Vicente, J., Duarte, J., Luíse, J., Pinheiro, L., et al. (2009). Morphotectonics and strain partitioning at the Iberia–Africa plate boundary from multibeam and seismic reflection data. *Mar. Geol.* 267, 156–174. doi: 10.1016/j.margeo.2009.09.012

Terrinha, P., Pinheiro, L. M., Henriet, J.-P., Matias, L., Ivanov, M., Monteiro, J. H., et al. (2003). Tsunamigenic-seismogenic structures, neotectonics, sedimentary

processes and slope instability on the southwest Portuguese Margin. *Mar. Geol.* 195, 55–73. doi: 10.1016/S0025-3227(02)00682-5

Thorwart, M., Dzierma, Y., Rabbel, W., and Hensen, C. (2014). Seismic swarms, fluid flow and hydraulic conductivity in the forearc offshore North Costa Rica and Nicaragua. *Int. J. Earth Sci.* 103, 1789–1799. doi: 10.1007/s00531-013-0960-y

Tinivella, U. (2002). The seismic response to overpressure versus gas hydrate and free gas concentration. *J. Seismic Explor.* 11, 283–305.

Tinivella, U., Accaino, F., Rossi, G., and Nicolich, R. (2005). Petrophysical analysis of CROP-18 crustal seismic data. *Boll. Soc. Geol. Ital.* 3, 205–211.

Tinivella, U., Giustiniani, M., and Vargas-Cordero, I. (2017). Wave equation datuming applied to seismic data in shallow water environment and post-critical water bottom reflection. *Energies* 10:1414. doi: 10.3390/en10091414

Tomonaga, Y., Blättler, R., Brennwald, M. S., and Kipfer, R. (2012). Interpreting noble-gas concentrations as proxies for salinity and temperature in the world's largest soda lake (Lake Van, Turkey). *J. Asian Earth Sci.* 59, 99–107. doi: 10.1016/j.jseaes.2012.05.011

Tomonaga, Y., Brennwald, M. S., and Kipfer, R. (2011). Spatial distribution and flux of terrigenic He dissolved in the sediment pore water of Lake Van (Turkey). *Geochim. Cosmochim. Acta* 75, 2848–2864. doi: 10.1016/j.gca.2011.02.038

Tomonaga, Y., Brennwald, M. S., Meydan, A. F., and Kipfer, R. (2014). Noble gases in the sediments of Lake Van – solute transport and palaeoenvironmental reconstruction. *Quat. Sci. Rev.* 104, 117–126. doi: 10.1016/j.quascirev.2014.09.005

Tryon, M. D., Henry, P., Çağatay, M. N., Zitter, T. A. C., Géli, M. L., Gasperini, L., et al. (2010). Pore fluid chemistry of the North Anatolian Fault Zone in the Sea of Marmara: a diversity of sources and processes. *Geochem. Geophys. Geosyst.* 11:Q0ad03. doi: 10.1029/2010GC003177

Tsunogai, U., Maegawa, K., Sato, S., Komatsu, D. D., Nakagawa, F., Toki, T., et al. (2012). Coseimic massive methane release from a submarine mud volcano. *Earth Planet. Sci. Lett.* 341–344, 79–85. doi: 10.1016/j.epsl.2012.06.004

Tsunogai, U., and Wakita, H. (1995). Precursory chemical changes in ground water: kobe Earthquake, Japan. *Science* 269, 61–63. doi: 10.1126/science.269.5220.61

Ujiie, K., Tanaka, H., Saito, T., Tsutsumi, A., Mori, J. J., Kameda, J., et al. (2013). Low coseismic shear stress on the tohoku-oki megathrust determined from laboratory experiments. *Science* 342, 1211–1214. doi: 10.1126/science.1243485

Vigneron, A., Cruaud, P., Pignet, P., Caprais, J.-C., Cambon-Bonavita, M.-A., Godfroy, A., et al. (2013). Archaeal and anaerobic methane oxidizer communities in the Sonora Margin cold seeps, Guaymas Basin (Gulf of California). *ISME J.* 7, 1595–1608. doi: 10.1038/ismej.2013.18

Villinger, H. W., Pichler, T., Kaul, N., Stephan, S., Pälike, H., and Stephan, F. (2017). Formation of hydrothermal pits and the role of seamounts in the Guatemala Basin (equatorial East Pacific) from heat flow, seismic, and core studies. *Geochem. Geophys. Geosyst.* 18, 369–383. doi: 10.1002/2016GC006665

Virieux, J., and Operto, S. (2009). An overview of full-waveform inversion in exploration geophysics. *Geophysics* 74, WCC1–WCC26. doi: 10.1190/1.3238367

Von Damm, K. L. (1990). Seafloor hydrothermal activity: black smoker chemistry and chimneys. *Ann. Rev. Earth Planet. Sci.* 18, 173–204. doi: 10.1146/annurev.ea.18.050190.001133

Von Damm, K. L. (2013). "Controls on the chemistry and temporal variability of seafloor hydrothermal fluids," in *Seafloor Hydrothermal Systems: Physical, Chemical, Biological, and Geological Interactions*, eds S. E. Humphris, R. A. Zierenberg, L. S. Mullineaux, and R. E. Thomson (Hoboken, NJ: Wiley).

Von Damm, K. L., Edmond, J. M., Measures, C. I., and Grant, B. (1985). Chemistry of submarine hydrothermal solutions at Guaymas Basin, Gulf of California. *Geochim. Cosmochim. Acta* 49, 2221–2237. doi: 10.1016/0016-7037(85)90223-6

Von Herzen, R. (2004). "Evidence for continuing hydrothermal circulation in old crust," in *Hydrogeology of the Oceanic Lithosphere*, eds E. E. Davis and H. Elderfield (Cambridge: Cambridge University Press), 414–447.

von Herzen, R., Simmons, G., and Folinsbee, A. (1970). Heat Flow between the Caribbean Sea and the Mid-Atlantic Ridge. *J. Geophys. Res.* 75, 1973–1984. doi: 10.1029/JB075i011p01973

Walia, V., Yang, T. F., Hong, W.-L., Lin, S.-J., Fu, C.-C., Wen, K.-L., et al. (2009). Geochemical variation of soil-gas composition for fault trace and earthquake precursory studies along the Hsincheng fault in NW Taiwan. *Appl. Radiat. Isot.* 67, 1855–1863. doi: 10.1016/j.apradiso.2009.07.004

Wang, D. T., Reeves, E. P., McDermott, J. M., Seewald, J. S., and Ono, S. (2018). Clumped isotopologue constraints on the origin of methane at seafloor hot springs. *Geochim. Cosmochim. Acta* 223, 141–158. doi: 10.1016/j.gca.2017.11.030

Weatherley, D. K., and Henley, R. W. (2013). Flash vaporization during earthquakes evidenced by gold deposits. *Nat. Geosci.* 6, 294–298. doi: 10.1038/ngeo1759

Wessel, P., Matthews, K. J., Müller, R. D., Mazzoni, A., Whittaker, J. M., Myhill, R., et al. (2015). Semiautomatic fracture zone tracking. *Geochem. Geophys. Geosyst.* 16, 2462–2472. doi: 10.1002/2015GC005853

Wheat, C. G., and Fisher, A. T. (2008). Massive, low-temperature hydrothermal flow from a basaltic outcrop on 23 Ma seafloor of the Cocos Plate: chemical constraints and implications. *Geochem. Geophys. Geosyst.* 9:Q12O14. doi: 10.1029/2008GC002136

Wheat, C. G., and Mottl, M. J. (2000). Composition of pore and spring waters from Baby Bare: global implications of geochemical fluxes from a ridge flank hydrothermal system. *Geochim. Cosmochim. Acta* 64, 629–642. doi: 10.1016/S0016-7037(99)00347-6

Wilson, J. T. (1965). A new class of faults and their bearing on bontinental drift. *Nature* 207, 343–347. doi: 10.1038/207343a0

Wolfson-Schwehr, M., and Boettcher, M. S. (2019). "Chapter 2 - global characteristics of oceanic transform fault structure and seismicity," in *Transform Plate Boundaries and Fracture Zones*, ed. J. C. Duarte (Amsterdam: Elsevier), 21–59. doi: 10.1016/B978-0-12-812064-4.00002-5

Yamamoto, R., Kido, M., Ohta, Y., Takahashi, N., Yamamoto, Y., Ozener, H., et al. (2018). "Partial creep revealed by seafloor geodetic observation along the North Anatolian Fault, beneath the Sea of Marmara," in *Proceedings of the 20th EGU General Assembly, EGU2018, Conference Held 4-13 April, 2018*, Vienna.

Yang, T. F., Fu, C.-C., Walia, V., Chen, C.-H., Chyi, L. L., Liu, T.-K., et al. (2006). Seismo-geochemical variations in SW Taiwan: multi-parameter automatic gas monitoring results. *Pure Appl. Geophys.* 163, 693–709. doi: 10.1007/s00024-006-0040-3

Young, C. R., Fujio, S., and Vrijenhoek, R. C. (2008). Directional dispersal between mid-ocean ridges: deep-ocean circulation and gene flow in Ridgeia piscesae. *Mol. Ecol.* 17, 1718–1731. doi: 10.1111/j.1365-294X.2008.03609.x

Zitellini, N., Gràcia, E., Matias, L., Terrinha, P., Abreu, M. A., DeAlteriis, G., et al. (2009). The quest for the Africa-Eurasia plate boundary west of the Strait of Gibraltar. *Earth Planet. Sci. Lett.* 280, 13–50. doi: 10.1016/j.epsl.2008.12.005

Zitellini, N., Rovere, M., Terrinha, P., Chierici, F., Matias, L., and Team, B. (2004). Neogene through quaternary tectonic reactivation of SW iberian passive margin. *Pure Appl. Geophys.* 161, 565–587. doi: 10.1007/s00024-003-2463-4

Zitter, T. A. C., Henry, P., Aloisi, G., Delaygue, G., Çagatay, M. N., Mercier de Lepinay, B., et al. (2008). Cold seeps along the main Marmara Fault in the Sea of Marmara (Turkey). *Deep Sea Res. Part I* 55, 552–570. doi: 10.1016/j.dsr.2008.01.002

Zoback, M. D., Hickman, S., and Ellsworth, W. (2011). Scientific drilling into the san andreas fault zone – an overview of SAFOD's first five years. *Sci. Drill.* 11, 14–28. doi: 10.2204/iodp.sd.11.02.2011

Zwicker, J., Birgel, D., Bach, W., Richoz, S., Smrzka, D., Grasemann, B., et al. (2018). Evidence for archaeal methanogenesis within veins at the onshore serpentinite-hosted Chimaera seeps, Turkey. *Chem. Geol.* 483, 567–580. doi: 10.1016/j.chemgeo.2018.03.027

Conflict of Interest Statement: The authors declare that the research was conducted in the absence of any commercial or financial relationships that could be construed as a potential conflict of interest.